Modeling South Pacific Ice-Ocean Interactions in the Global Climate System

David M. Holland
Adrian Jenkins and Stanley S. Jacobs

Lamont-Doherty Earth Observatory
of Columbia University

Palisades, NY 10964

Final Report

01 March 1997 – 28 February 2001

Grant # NAG5-4028

Polar Research Program
National Aeronautics and Space Administration

Modeling South Pacific Ice-Ocean Interactions in the Global Climate System

David M. Holland
Adrian Jenkins and Stanley S. Jacobs

Lamont-Doherty Earth Observatory
of Columbia University

Palisades, NY 10964

Final Report

01 March 1997 – 28 February 2001

Grant # NAG5-4028

Polar Research Program
National Aeronautics and Space Administration

Abstract

The objective of this project has been to improve the modeling of interactions between large Antarctic ice shelves and adjacent regions of the Southern Ocean. Our larger goal is to gain a better understanding of the extent to which the ocean controls ice shelf attrition, thereby influencing the size and dynamics of the Antarctic Ice Sheet. Melting and freezing under ice shelves also impacts seawater properties, regional upwelling and sinking and the larger-scale ocean circulation. Modifying an isopycnal coordinate general circulation model for use in sub-ice shelf cavities, we found that the abrupt change in water column thickness at an ice shelf front does not form a strong barrier to buoyancy-driven circulation across the front. Outflow along the ice shelf base, driven by melting of the thickest ice, is balanced by deep inflow. Substantial effort was focused on the Filchner-Ronne cavity, where other models have been applied and time-series records are available from instruments suspended beneath the ice. A model comparison indicated that observed changes in the production of High Salinity Shelf Water could have a major impact on circulation within the cavity. This water propagates into the cavity with an asymmetric seasonal signal that has similar phasing and shape in the model and observations, and can be related to winter production at the sea surface. Even remote parts of the sub-ice shelf cavity are impacted by external forcing on sub-annual time scales. This shows that cavity circulations and products, and therefore cavity shape, will respond to interannual variability in sea ice production and longer-term climate change. The isopycnal model gives generally lower net melt rates than have been obtained from other models and oceanographic data, perhaps due to its boundary layer formulation, or the lack of tidal forcing. Work continues on a manuscript describing the Ross cavity results.

Project Description

We modified the Miami Isopycnal Coordinate Ocean Model (MICOM) for a domain that included the waters beneath an ice shelf and those occupying a portion of the open ocean. A floating ice shelf was incorporated as an upper boundary in the southern part of the domain. To initialize the model ocean, an extrapolation scheme filled the sub-ice cavity with waters similar to those observed during summer expeditions at the ice front. Simulations showed that initial properties were flushed out within a few years. Since year-round sea surface temperature and salinity observations do not exist over the model domain, we restored to summer measurements and to the sea surface freezing point in the open ocean during winter, adding sufficient salt during this period to generate the observed High Salinity Shelf Water.

The sub-ice-shelf part of the domain is isolated from the atmosphere, but influenced by the pressure of the floating ice, and by phase changes that occur at the ice shelf base. Zero surface buoyancy forcing indicated that the introduction of a static pressure induced negligible motion in the underlying water. Nonzero surface buoyancy forcing produces a cyclonic circulation beneath the ice shelf. Following initial idealized simulations, realistic geometries were implemented for the Ross and Filchner-Ronne Ice Shelves and their underlying cavities. The numerical experiments included sensitivity studies to assess the fidelity of the simulations, and to check for natural internal oscillations and variability arising from external forcing. Model tracers were used to gain insight into system behavior.

A key feature of the model is that vertical layering is based on density, with depth becoming a prognostic variable. This approach approximates the behavior of the real ocean, where advection and diffusion occur more readily along than across neutral or isopycnal surfaces. The model also has to accommodate strong buoyancy forcing, requiring that density be allowed to evolve freely in the upper layer. This variable density mixed layer applies both to the open ocean and ice cavity, requiring proper resolving of the transition between the two domains. Models of ocean circulation beneath ice shelves are driven in part by the heat and freshwater fluxes associated with phase changes at the ice-ocean boundary. One of the main differences between models is the treatment of turbulent transfer within the oceanic boundary layer. A comparison of alternative formulations gave results within ~30% of observations beneath sea ice. However, the use of bulk transfer coefficients that specified turbulence can give melt/freeze rates that differ by as much as 5x. With our chosen formulation, net melting tends to be one half to one third of prior estimates. We have yet to include a tidal component, which can represent up to 20 cm/s mean flow in other models.

Simulations of the Ross Ice Shelf cavity show that inflow is strongest on the western side, as would be expected from the denser shelf water in that sector, with a relatively strong outflow near ~175W. Several interior gyres occur in the vicinity of ice and sea floor topographic features, similar to those that have been reported beneath the other large ice shelves. The age of water at 450m is slightly less that the mean age estimated for the cavity from tracer studies in the open ocean. On a typical simulation, basal melting under the Ross Ice Shelf ranged from -0.3 to +0.3 m/yr, with melt patches resulting from peaks in the ice thickness, which are not altered during the model run. Such features might disappear with a higher-resolution ice thickness grid, but they also suggest that net melting is likely to be dominated by thicker ice where it moves off the grounding line. The annual cycle of monthly averaged net melting for the Ross cavity shows a peak in the late winter/early spring, confirming a seasonal cycle that appeared earlier in a 2-D channel model around Roosevelt Island.

As the Antarctic coastline also contains smaller ice shelves and floating glaciers of various sizes and different hydrographic environments, we carried out a simulation for the Pine Island Glacier (PIG) which is located in Pine Island Bay in the Amundsen Sea. Initial estimates of the shape and size of the PIG cavity, coupled with ocean measurements taken during a 1994 field experiment, resulted in a modeled net melt rate of ~14 m/yr. This is ~2 orders of magnitude higher than simulated for the Ross cavity with the same model, but is consistent with independent estimates that range from 10-24 m/yr for the PIG cavity. Sensitivity studies confirmed earlier inferences that the high melt rate was the combined result of the 'warm' (>+1C) Circumpolar Deep Water that penetrates the cavity, and the relatively steep slope of the ice shelf base. A general review of the Pine Island Glacier system did not reveal clear evidence for retreat or collapse over the last few decades.

Products

This report incorporates the primary publications that have resulted in full or in part from NASA support of this project. Those papers and related manuscripts submitted or in preparation are listed in the accompanying bibliography. Presentations of the ongoing work, listed following the bibliography, were made at an AGU meeting in San Francisco, a West Antarctic Ice Sheet Workshop in Sterling VA, a MICOM Workshop in Miami, FL, a Chapman Conference in Orono, ME, a Gordon Research Conference in Ventura, CA, a Ross Sea Oceanography Conference in Ischia, Italy, and at the European Geophysical Society in Nice, France. PI Holland also traveled to other sites for talks and discussions, and co-PI Jenkins was supported for travel-related expenses during time spent at Lamont working on this project.

About midway through the grant, PI Holland assumed a faculty position at the Courant Institute of Mathematics of New York University. This necessitated some realignment of expenses, and travel between NYU and Lamont, where Holland was granted an adjunct appointment to facilitate continued work on the project.

Acknowledgments

We thank the Polar Research Program of the National Aeronautics and Space Administration for support of this work under grant NAG5-4028. Some simulations were carried out on a supercomputer at the University of Alaska. Over the term of the grant we were assisted by NASA program managers Robert Thomas, Prasad Gogenini, Kim Partington and Waleed Abdalati. We were also supported in part by New York University, and by the Lamont-Doherty Earth Observatory of Columbia University.

Bibliography

Jenkins, A. and D.M. Holland. 1997. Ocean circulation beneath ice shelves: first results from an isopycnic coordinate ocean general circulation model, in Filchner-Ronne Ice Shelf Programme, Report No 11, edited by H. Oerter, pp. 19-24, Alfred-Wegener-Institute for Polar and Marine Research, Bremerhaven, FRG.

Holland, D.M. and A. Jenkins. 1999. Modeling thermodynamic ice-ocean interactions at the base of an ice shelf, J. Phys. Oceanogr., 29(8), 1787-1800.

Jenkins, A. and D.M. Holland. 2000. New results from the application of the ocean model MICOM to the Filchner-Ronne Ice Shelf, in Filchner-Ronne Ice Shelf Programme, Report No 13, edited by H. Oerter, pp. 19-25, Alfred-Wegener-Institute for Polar and Marine Research, Bremerhaven, FRG.

Holland, D.M. and A. Jenkins. 2001. Adaptation of an isopycnic coordinate ocean model for the study of circulation beneath ice shelves, Mon. Wea. Rev., 129(8), 1905-1927.

Jenkins, A., H.H. Hellmer and D.M. Holland. 2001. The role of meltwater advection in the formulation of conservative boundary conditions at an ice-ocean interface, J. Phys. Oceanogr., 31(1), 285-296.

Vaughan, D.G., A.M. Smith, H.J.F. Corr, A. Jenkins, C.R. Bentley, M.D. Stenoin, S.S. Jacobs, T.B. Kellogg, E. Rignot and B.K. Lucchitta, A Review of Pine Island Glacier, West Antarctica: Hypotheses of Instability vs. Observations of Change, in: The West Antarctic Ice Sheet, R.B. Alley and R.A. Bindschadler (eds), Ant. Res. Ser, 77, 237-256.

Jenkins, A., D.M. Holland and K.W. Nicholls. In press. Oceanographic conditions beneath Ronne Ice Shelf: A comparison between model and field data, in Filchner-Ronne Ice Shelf Programme, Report No 14, edited by H. Oerter, Alfred-Wegener-Institute for Polar and Marine Research, Bremerhaven, FRG.

Holland, D.M. Accepted. A method for computing marine ice thickness at the base of an ice shelf, J. Glaciol.

Jenkins, A., D.M. Holland, K.W. Nicholls and M. Schroeder. Submitted. Seasonal ventilation of the cavity beneath Filchner-Ronne Ice Shelf simulated with an isopycnic coordinate ocean model, J. Geophys. Res.

Jenkins, A. and D.M. Holland. To be Submitted. A model study of circulation beneath Filchner-Ronne Ice Shelf: implications for bottom water formation, Geophys. Res. Lett.

Holland, D.M., S.S. Jacobs and A. Jenkins. To be submitted. Modeling the Ocean Circulation beneath the Ross Ice Shelf, Ant. Sci.

Presentations

Jacobs, S.S. Ice Shelves and Southern Ocean Ventilation, AGU Chapman Conference on the West Antarctic Ice Sheet, University of Maine, Orono, Maine, September 13-18, 1998.

Jenkins, A., D.M. Holland and S.S. Jacobs, Circulation Beneath Ice Shelves Simulated by an Isopycnic Coordinate Ocean Model, AGU Chapman Conference on the West Antarctic Ice Sheet, University of Maine, Orono, Maine, September 13-18, 1998.

Holland, D.M., S.S. Jacobs and A.Jenkins. Ice-Ocean Modeling of the Ross Sea Continental Shelf Waters using MICOM, Layered Ocean Model User's Workshop, Miami, FL, 22-23 Feb 1999.

Jacobs, S.S. D.M Holland and A. Jenkins. Ross Sea Ice Shelf and Ocean Interaction, Gordon Res. Conf. On Polar Mar. Sci., Ventura, CA, 7-12 Mar 1999.

Holland, D.M. Application of an Isopycnic Coordinate Numerical Model to Ice Shelf Cavities, Physical Mathematics Seminar, Massachusetts Inst. of Technology, Cambridge, 27 Apr 1999.

Jenkins, A. and D.M. Holland, New results from the application of the ocean model MICOM to the southern Weddell Sea, Sixth Annual WAIS Workshop, Sterling, VA, September 16-18, 1999.

Jenkins, A. and D.M Holland, Modelling the Buoyancy-Driven Circulation on the Southern Weddell Sea Continental Shelf, European Geophysical Society, 25th General Assembly, Acropolis, Nice, France, 25-29 April, 2000.

Holland, D.M., S.S. Jacobs and A. Jenkins. Modeling Ross Sea Ice Shelf-Ocean Interaction, EOS, Trans. Am. Geophys. Un., 81(48), abstract, F390, 15-19 Dec 2000.

Holland, D.M., S.S. Jacobs and A. Jenkins. Modeling the Ocean Circulation beneath the Ross Ice Shelf, 2nd Int'l Conf. On the Oceanography of the Ross Sea, Ischia, 8-13 October, 2001.

Ocean circulation beneath ice shelves: first results from an isopycnic coordinate ocean general circulation model

Adrian Jenkins

British Antarctic Survey, Natural Environment Research Council, High Cross, Madingley Road, Cambridge, CB3 0ET, U.K.

David M. Holland

Lamont-Doherty Earth Observatory of Columbia University, Palisades, New York 10964, U.S.A.

Introduction

The cavities beneath the floating ice shelves of Antarctica are regions where the waters of the Southern Ocean come into direct contact with the ice sheet. Exchanges of mass and energy at the ice/ocean interface effect a transformation of water masses flowing into the cavity and contribute to the wastage side of Antarctica's mass balance equation. How sensitive the conditions in the sub-ice cavities are to external changes is a question of some importance, as the past and future evolution of both the ice sheet and the surrounding seas are at least partially linked to the answer. Our understanding of the processes that drive sub-ice-shelf circulation owes much to the application of computer models of varying sophistication to the problem (Williams et al., in press). Recently Grosfeld et al. (1997) presented results from the first model to include both an open ocean and a sub-ice cavity within its domain. They concluded that the wind-forced circulation north of the ice shelf and the buoyancy-forced circulation beneath the ice shelf were largely separate, with the degree of communication being topographically controlled. Here we describe some of the preliminary results we have obtained applying an isopycnic coordinate ocean model to a similar domain.

MICOM

We have used the Miami Isopycnic Coordinate Ocean Model (MICOM; Bleck et al., 1992) for this investigation. The key feature of this model is that the vertical discretisation of the domain is based on density instead of the more usual depth. In the isopycnic formulation depth becomes a prognostic variable. Whereas conventional ocean models calculate the water density at a fixed number of discrete depths, MICOM computes the depth at which a fixed number of discrete densities occur. In practice, the integration is performed layer-wise; that is, the ocean is divided into a number of layers of constant-density water, and the model computes the thickness of the layers at each point of the horizontal grid. The advantage of this approach is that it mimics the behaviour of the real ocean very well. Advection and diffusion in the ocean occur readily along neutral surfaces (which are approximately isopycnal surfaces), but much less easily across them.

The disadvantage is that if a given water density does not occur at certain points in the domain, that particular layer will have regions of zero thickness. A sophisticated numerical scheme is required to handle this situation without generating negative layer thicknesses.

If an isopycnic model is to accept buoyancy forcing, the upper layer must have a freely-evolving density. A mixed layer formulation based on the work of Gaspar (1988) is used for the surface layer in MICOM. The entrainment/detrainment algorithm allows water to be cycled from one isopycnic layer, through the mixed layer, where its properties are modified by the surface boundary conditions, into another isopycnic layer. This procedure mimics the manner in which water mass transformations occur in nature, but herein lies the greatest hurdle to be overcome in the application of MICOM to a sub-ice-shelf cavity. The boundary layer adjacent to the ice shelf base is also a site of buoyancy forcing and water mass modification, so the mixed layer must extend under the ice shelf. We have made extensive changes to the model code to allow this to happen.

Testing the new code

We have run a number of simulations to test the stability and accuracy of our new code:

(i) We have set up an ocean with horizontal isopycnal surfaces in front of and beneath an ice shelf to check that the water can remain stationary if not forced.

(ii) We have placed an isolated patch of light fluid beneath the ice shelf to check that it can flow up the ice shelf base and escape from the cavity.

(iii) We have applied boundary conditions at the ice shelf base that freshen and cool the mixed layer to check that its response is to flow up the ice shelf base and exit the cavity.

All of these tests were applied successfully, both with and without Earth rotation.

Preliminary results

Our first results with the full model have been obtained on a 10° latitude by 15° longitude domain, with a horizontal resolution of 20–35 km and 10 layers in the vertical. The seabed was flat and 1000 m deep everywhere, while an ice shelf covered the southern half of the domain. The ice thickness was zonally invariant, but increased from 0 m at the ice front to 300 m at the southern edge of the domain. The water column was initially 0°C everywhere, with salinity ranging from 34.4–34.8 psu, and the model was spun up for five years.

The basal freezing rate (negative numbers indicate melting) at the base of the ice shelf is illustrated in Figure 1. No freezing occurs because the inflowing water is almost 2°C above the surface freezing point and peak melt rates, in excess of 3.5 m yr^{-1}, occur in the south-eastern corner of the domain. The stream function for the vertically integrated transport shows a single, western-intensified gyre occupying most of the cavity (Figure 2). It extends beyond the ice front, which crosses the domain at 75°S, but the currents to the north of the ice shelf are considerably weaker.

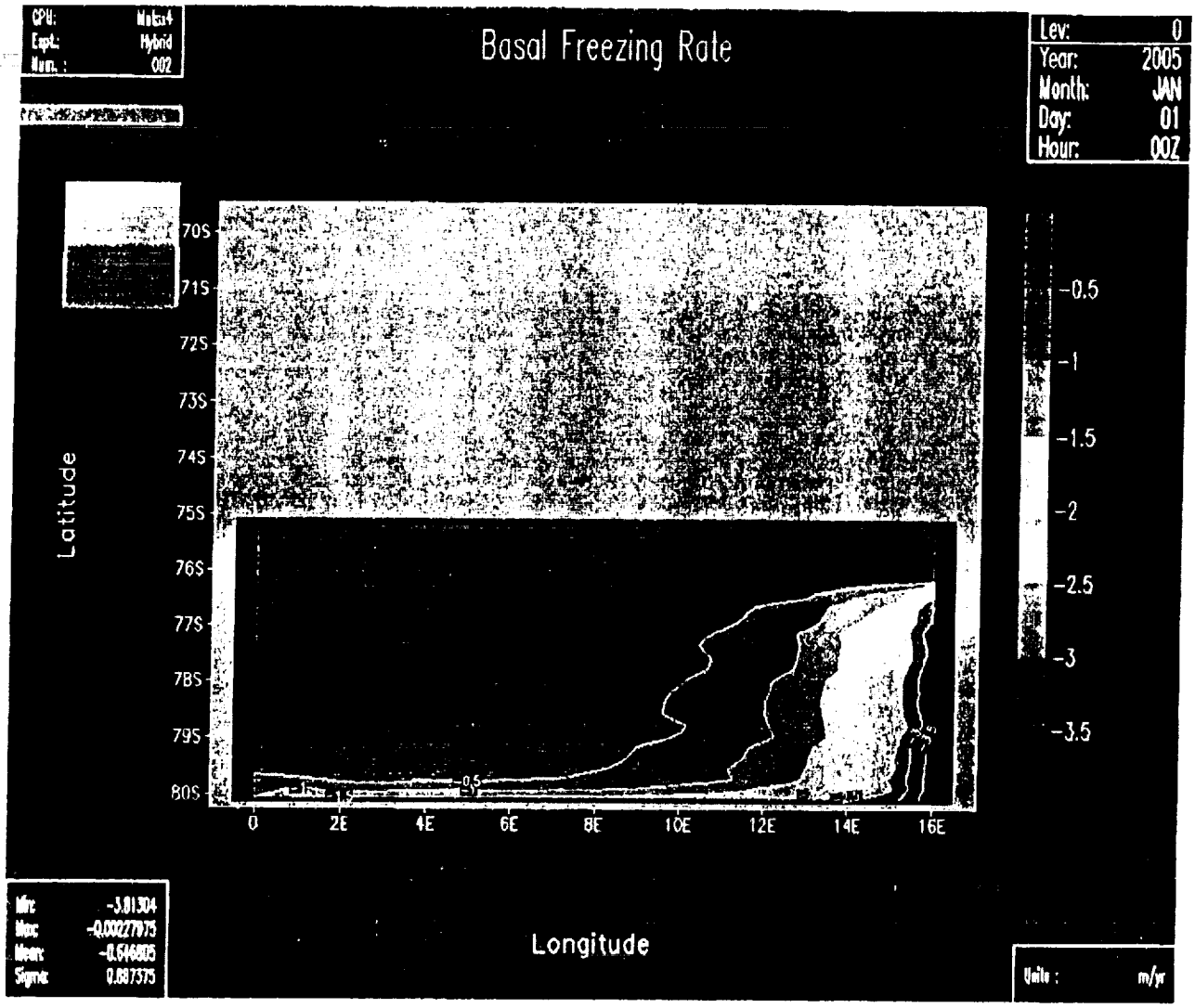

Figure 1: Basal freezing rate (m yr^{-1}) at the ice shelf base.

This circulation pattern is broadly similar to that found by Determann and Gerdes (1994) and Grosfeld et al. (1997). However, we need to look a little closer at the model results in order to be able to explain the pattern of basal melting. If the entire water column were following this gyre we would expect strongest melting immediately to the east of the gyre centre, where the inflowing currents are strongest. The most active layer beneath the ice shelf is the mixed layer, which reacts to the combination of buoyancy and Coriolis forcing by flowing from east to west across the ice shelf base, with a small component to the north generated by the frictional drag (Figure 3). This leads to strong divergence along the eastern boundary and weak divergence along the southern boundary. The resulting upwelling of warm water and entrainment into the mixed layer gives rise to the pattern of melting and sustains the motion. The mixed layer behaves in the manner we would expect of a buoyant, two dimensional plume under the influence of rotation. This suggests that the differences between the circulation produced by one and two dimensional models (eg. Jenkins, 1991; Hellmer and Olbers, 1989) may not be as great as suggested by Williams et al. (in press).

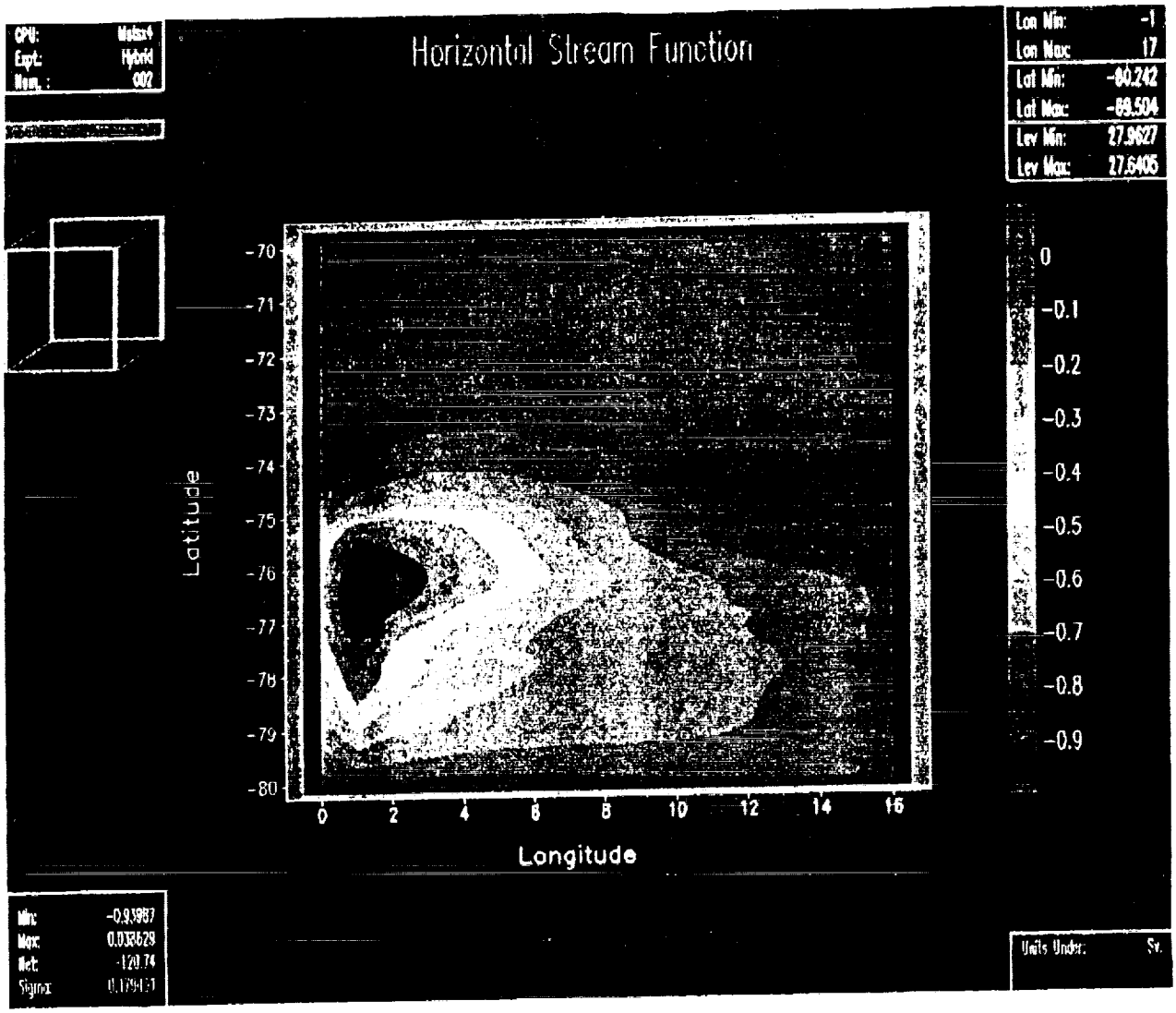

Figure 2: Stream function for the vertically integrated transport (Sv).

More results from this model run can be found on the web site:

http://figgy.ldeo.columbia.edu/~holland/html_float_shelf/idealized/expt_002/expt_descriptor.html

Future work

These preliminary results suggest that our modified version of MICOM can be a useful tool in understanding the intricacies of sub-ice-shelf circulation. In future we hope to apply the model to domains more reminiscent of the southern Weddell Sea, and eventually to use real topography. As MICOM is a free surface model we also hope to be able to include the effects of tidal forcing at a later date.

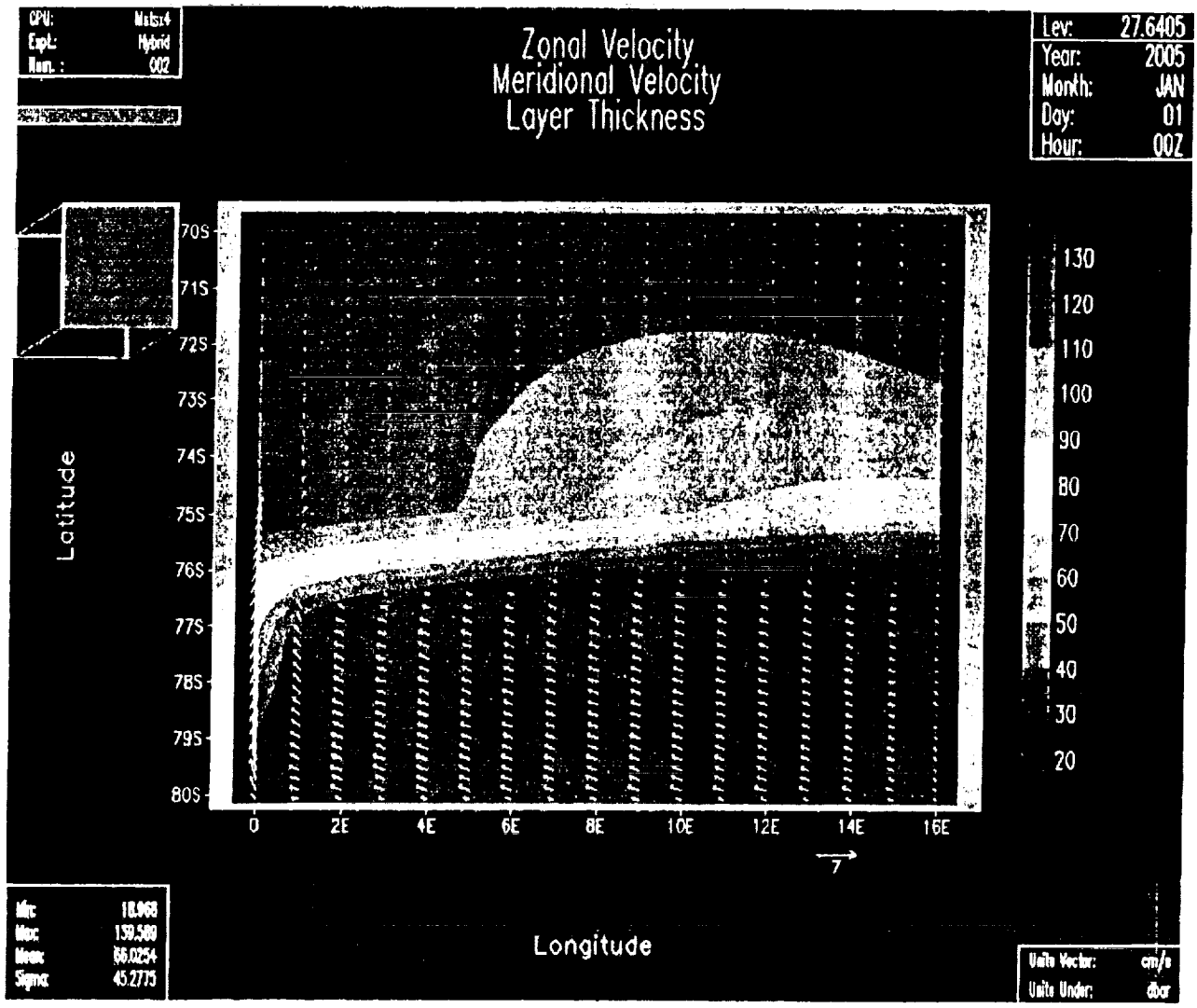

Figure 3: Thickness (dbar) and velocity (cm s^{-1}) of the mixed layer.

Acknowledgements: This work has received financial support from the United States Department of Energy, the European Ice Sheet Modelling Initiative, Cray Research Inc. and the National Aeronautics and Space Administration.

References

Bleck, R., C. Rooth, D. Hu and L.T. Smith. 1992. Salinity-driven thermocline transients in a wind- and thermohaline-forced isopycnic coordinate model of the North Atlantic, *J. Phys. Oceanogr.*, **22**: 1486–1505.

Determann, J. and R. Gerdes. 1994. Melting and freezing beneath ice shelves: implications from a three-dimensional ocean-circulation model, *Ann. Glaciol.*, **20**: 413–419.

Gaspar, P. 1988. Modeling the seasonal cycle of the upper ocean, *J. Phys. Oceanogr.*, **18**: 161–180.

Grosfeld, K., R. Gerdes and J. Determann. 1997. Thermohaline circulation and interaction between ice shelf cavities and the adjacent open ocean, *J. Geophys. Res.*, **102**: 15,595–15,610.

Hellmer, H.H. and D.J. Olbers. 1989. A two-dimensional model for the thermohaline circulation under an ice shelf, *Antarct. Sci.*, **1**: 325–336.

Jenkins, A. 1991. A one-dimensional model of ice shelf-ocean interaction, *J. Geophys. Res.*, **96**: 20,671–20,677.

Williams, M.J.M., A. Jenkins and J. Determann. In press. Physical controls on ocean circulation beneath ice shelves revealed by numerical models, *Antarct. Res. Ser.*

Modeling Thermodynamic Ice–Ocean Interactions at the Base of an Ice Shelf

DAVID M. HOLLAND

Lamont-Doherty Earth Observatory, Palisades, New York

ADRIAN JENKINS

British Antarctic Survey, Cambridge, United Kingdom

(Manuscript received 6 May 1998, in final form 14 August 1998)

ABSTRACT

Models of ocean circulation beneath ice shelves are driven primarily by the heat and freshwater fluxes that are associated with phase changes at the ice–ocean boundary. Their behavior is therefore closely linked to the mathematical description of the interaction between ice and ocean that is included in the code. An hierarchy of formulations that could be used to describe this interaction is presented. The main difference between them is the treatment of turbulent transfer within the oceanic boundary layer. The computed response to various levels of thermal driving and turbulent agitation in the mixed layer is discussed, as is the effect of various treatments of the conductive heat flux into the ice shelf. The performance of the different formulations that have been used in models of sub-ice-shelf circulation is assessed in comparison with observations of the turbulent heat flux beneath sea ice. Formulations that include an explicit parameterization of the oceanic boundary layer give results that lie within about 30% of observation. Formulations that use constant bulk transfer coefficients entail a definite assumption about the level of turbulence in the water column and give melt/freeze rates that vary by a factor of 5, implying very different forcing on the respective ocean models.

1. Introduction

The continental shelf seas surrounding Antarctica most frequently attract attention because they are the source regions of Antarctic Bottom Water. It is commonly assumed that atmospheric forcing of the ocean and ice cover is the primary driving mechanism behind the deep convection that occurs over the continental slope (e.g., Gill 1973). However, poleward of the shelf break, 40% of the sea surface is covered by floating ice shelves, which range in thickness from 100 to 2000 m and therefore completely isolate the ocean from the atmosphere. Circulation beneath the ice shelves and the associated meltwater input have a profound impact on shelf water properties (Foldvik et al. 1985; Jacobs et al. 1985; Fahrbach et al. 1994; Hellmer et al. 1999). Toggweiler and Samuels (1995) suggest that up to 75% of all the ocean's deep waters may retain a signature of this meltwater input.

The interaction between ice shelves and the ocean is thus a potentially important element of the climate system, and in recent years numerical models have been used to evaluate the key processes operating in sub-ice-shelf cavities (Williams et al. 1999). Upper boundary conditions derived from a thermodynamic model of the ice–ocean interaction have been applied to ocean models of varying sophistication. Dynamic models of the ice shelf itself have not been included, so the ice–ocean interface has been treated as a fixed boundary. The disparity of timescales between the slowly flowing ice shelf and the relatively fast flowing waters beneath provides some justification for this approach. Although the specification of the upper boundary conditions represents a computationally small and simple component of most sub-ice-shelf circulation models, it is of crucial importance. A correct estimate of the surfaces fluxes is essential to a realistic simulation of the sub-ice-shelf circulation and to the utility of the results for estimating the mass balance of the ice shelves.

In this paper we focus on the mathematical description of the ice–ocean interaction. We present an hierarchy of models describing the heat and freshwater exchange at and near the ice–ocean interface. Our aim is to compare the behavior of the differing upper boundary formulations that have been used in models of sub-ice-shelf circulation to date and to introduce a new formulation that closely follows the work of McPhee et al. (1987). For a related comparative study, but in the context of sea ice–ocean coupling, the reader is referred to

Corresponding author address: David M. Holland, Courant Institute of Mathematical Sciences, 251 Mercer St., Warren Weaver Hall, 907, New York University, MC 0711, New York, NY 10012.
E-mail: holland@cims.nyu.edu

work by Holland et al. (1997). We also compare the results of the various models with recent observations of heat flux in the turbulent boundary layer beneath sea ice.

The fundamental assumption in all the models is that phase changes occur in thermodynamic equilibrium so that the temperature and salinity at the ice–ocean interface are always related by an expression for the freezing point at the appropriate depth. The problem becomes one of calculating the heat and freshwater fluxes that result from deviations in the far-field ocean properties from freezing point conditions. Our treatments of the processes occurring in the oceanic boundary layer differ only in the sophistication with which turbulent diffusion of heat and salt is modeled. On the ice side of the interface the flow is laminar and only the diffusion of heat need be considered because salt cannot diffuse through the solid ice matrix. The problem is that diagnosis of the temperature gradient at the ice shelf base requires solution of the equation for heat advection and diffusion throughout the ice shelf. As the ice flow is unknown, we require a reduced form of this equation that is tractable but captures the essential features of the full solution.

In common with most models of sub-ice-shelf circulation, we consider all phase changes to occur at the ice–ocean boundary, regardless of whether the far-field ocean conditions are above or below freezing. We do not consider the process of frazil ice growth in supercooled parts of the water column, although observations and modeling (Oerter et al. 1992; Bombosch and Jenkins 1995) suggest that deposition of suspended ice crystals is the dominant mechanism of basal growth beneath ice shelves. Thus, while it is instructive to intercompare the response of the different boundary formulations to supercooling in the ocean, direct comparisons between models and observations are only valid for melting conditions. It is possible to treat the thermodynamics of frazil ice growth in a manner analogous to that outlined below for melting and freezing at a solid boundary, but the incorporation of frazil ice into an ocean model requires the addition of an ice conservation equation (Omstedt and Svensson 1984; Mellor et al. 1986; Jenkins and Bombosch 1995).

2. Thermodynamic models of ice–ocean interaction

The objective of modeling the ice–ocean interaction is to obtain as realistic as possible a melt rate at the ice-shelf base. We now define and solve the necessary equations to achieve this. The far-field quantities are the prescribed interior properties of the ice shelf and the properties of the upper layer or level of the ocean model. We are interested in determining the characteristics exactly at the ice–ocean interface where there are three physical constraints: the interface must be at the freezing point and both heat and salt must be conserved at the interface during any phase changes. This gives a system of up to three equations in up to three unknowns, namely, the interface temperature, salinity, and melt rate.

To assist the discussion below, the relevant layers, temperatures, salinities, and heat and salt fluxes are shown schematically in Fig. 1. The ocean mixed layer has a temperature T_M and salinity S_M, which are not necessarily equal to the respective ice–ocean interface properties T_B and S_B. The gradients in temperature and salinity through the boundary layer drive heat and salt fluxes between the interface and the mixed layer. The temperature gradient in the ice at the base of the ice shelf drives a heat flux from the interface into the ice shelf, which has a surface temperature denoted by T_s and a bulk salinity denoted by S_I.

a. Fundamental equations

1) Freezing point dependence

The freezing point of seawater is a weakly nonlinear function of salinity and a linear function of pressure (Millero 1978). This relationship between temperature and salinity at the ice–ocean interface will be one of three equations that will have to be solved simultaneously, so it is simpler to work with a linearized version:

$$T_B = aS_B + b + cp_B, \tag{1}$$

where p_B is the pressure at the interface. The values of the empirical constants a, b, and c are given in Table 1 along with other constants and parameters used in this study. The formula is valid only in the salinity range 4–40 psu and does not apply to pure freshwater.

2) Heat conservation

At the ice–ocean interface, the divergence of the heat flux balances the sink or source of latent heat caused by melting or freezing:

$$Q_I^T - Q_M^T = Q_{\text{latent}}^T. \tag{2}$$

The latent heat term is given by

$$Q_{\text{latent}}^T = -\rho_M w_B L_f, \tag{3}$$

where $\rho_M w_B$ represents the mass of ice that is melted ($w_B > 0$) or frozen ($w_B < 0$) per unit time. The estimation of the diffusive heat fluxes is discussed in detail below.

3) Salt conservation

An equation analogous to (3) describes the salt flux required to maintain the boundary salinity at S_B in the presence of the "freshwater" flux associated with melting or freezing of ice having a salinity of S_I:

$$Q_{\text{brine}}^S = \rho_M w_B (S_I - S_B). \tag{4}$$

This is balanced by the salt flux divergence at the interface:

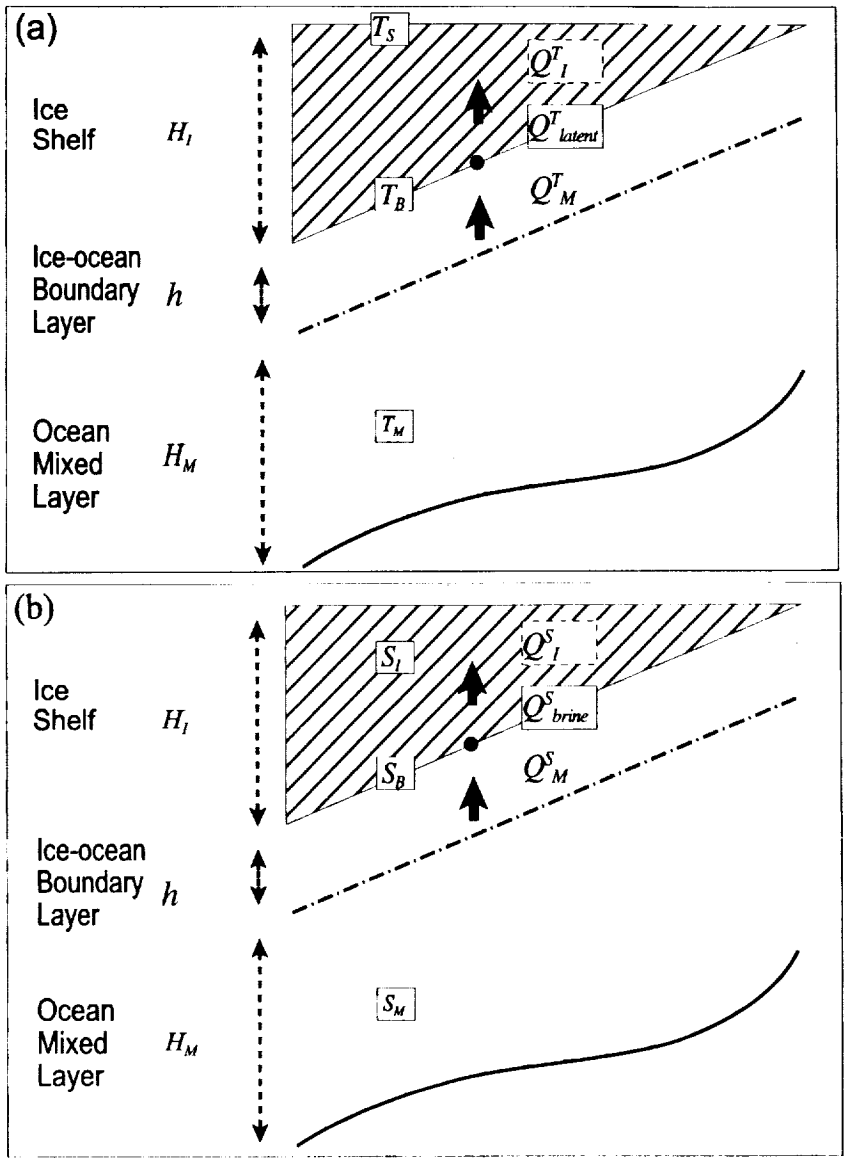

FIG. 1. Schematic representation of (a) the heat and (b) the salt balance at the base of an ice shelf. The slope of the ice shelf base is greatly exaggerated for illustrative purposes.

$$Q^S_I - Q^S_M = Q^S_{\text{brine}}. \quad (5)$$

The diffusive flux of salt into the ice shelf, Q^S_I, is identically zero and will be discussed no further, while the estimation of the diffusive flux through the oceanic boundary layer will be addressed below. Continental ice that melts from the base of an ice shelf has a salinity of zero, but when seawater freezes, brine is usually trapped within the forming ice, giving it a nonzero bulk salinity. Observations of marine ice found at the base of ice shelves with salinities of 0.025 psu (Eicken et al. 1994) indicate that a very effective desalination process must operate. As further evidence, additional observations (Oerter et al. 1992) show very low salinities of approximately 0.100 and suggest that to a good approximation we can treat S_I as zero always.

b. *Modeling the oceanic fluxes*

1) A ONE-EQUATION FORMULATION

The simplest approach recognizes that whatever the details of heat and salt transfer through the oceanic boundary layer, the overall effect is to cause the upper layer of the ocean to relax toward the freezing point. If this relaxation is assumed to occur instantaneously, there is no distinction between interface and mixed layer properties, and the ice–ocean interaction can be de-

TABLE 1. Model parameters and constants.

Parameter	Symbol	Units	Value
Salinity coefficient of freezing equation	a	°C psu^{-1}	-5.73×10^{-2}
Constant coefficient of freezing equation	b	°C	9.39×10^{-2}
Bernoulli numbers	B_n	dimensionless	
Ocean surface buoyancy flux	B_M	m^2 s^{-2}	
Pressure coefficient of freezing equation	c	°C Pa^{-1}	-7.53×10^{-8}
Constants of integration	c_1, c_2	dimensionless	
Momentum exchange coefficient	c_d	dimensionless	1.50×10^{-3}
Specific heat capacity ice shelf	c_{pI}	J kg^{-1} K^{-1}	2009.0
Specific heat capacity mixed layer	c_{pM}	J kg^{-1} K^{-1}	3974.0
Coriolis parameter	f	s^{-1}	-1.00×10^{-4}
Gravitational acceleration	g	m s^{-2}	9.81
Thickness of boundary layer	h	m	
Thickness of viscous sublayer	h_ν	m	~0.001
Thickness of ice shelf	H_I	m	~1000
Thickness of mixed layer	H_M	m	~10
Von Kármán's constant	k	dimensionless	0.40
Latent heat fusion	L_f	J kg^{-1}	3.34×10^5
Obukhov length	L_o	m	
Solutions of characteristic polynomial	m, m_1, m_2	dimensionless	
Nusselt number	Nu	dimensionless	$\gg 1$
Pressure at ice shelf base	p_B	Pa	$\sim 1.0 \times 10^7$
Prandtl number	Pr	dimensionless	13.8
Conductive heat flux through ice shelf	Q_I^T	W m^{-2}	
Latent heat at ice–ocean interface	Q_{latent}^T	W m^{-2}	
Diffusive heat flux in boundary layer	Q_M^T	W m^{-2}	
Diffusive salt flux through ice shelf	Q_I^S	psu m^{-1} s^{-1}	
Salt flux at ice–ocean interface	Q_{brine}^S	psu m^{-1} s^{-1}	
Diffusive salt flux in boundary layer	Q_M^S	psu m^{-1} s^{-1}	
Ratio of melt/freeze rates	r	dimensionless	
Critical flux Richardson number	R_c	dimensionless	0.20
Schmidt number	Sc	dimensionless	2432
Bulk salinity of ice shelf	S_I	psu	0
Salinity at ice–ocean interface	S_B	psu	Prognostic
Salinity of mixed layer	S_M	psu	~34.5
Time coordinate	t	s	
Temperature at ice shelf surface	T_S	°C	~−25.0
Temperature at ice–ocean interface	T_B	°C	Prognostic
Temperature of mixed layer	T_M	°C	~−1.85
Thermal driving	T_*	°C	
Ice shelf flow velocity	U_I	m s^{-1}	
Ocean mixed layer velocity	U_M	m s^{-1}	
Friction velocity ice–ocean	U_*	m s^{-1}	
Melt rate at ice shelf base	w_B	m s^{-1}	Prognostic
Vertical velocity of ice shelf	w_I	m s^{-1}	
Vertical geopotential coordinate	z	m	
Salinity contraction coefficient	β_S	psu^{-1}	
Thermal expansion coefficient	β_T	°C^{-1}	
Molecular thermal conductivity ice shelf	κ_I^T	m^2 s^{-1}	1.14×10^{-6}
Thermal diffusivity of mixed layer	κ_M^T		
Molecular salt conductivity ice shelf	κ_I^S	m^2 s^{-1}	0.0
Salt diffusivity mixed layer	κ_M^S	m^2 s^{-1}	
Ice shelf reference density	ρ_I	kg m^{-3}	920.0
Ocean reference density	ρ_M	kg m^{-3}	1025.0
Ratio of thermal driving to thermal forcing	Θ	dimensionless	
Thermal exchange velocity	γ_T	m s^{-1}	$\sim 1.00 \times 10^{-4}$
Salinity exchange velocity	γ_S	m s^{-1}	$\sim 5.05 \times 10^{-7}$
Kinematic viscosity of sea water	ν	m^2 s^{-1}	1.95×10^{-6}
Péclet number	Υ	dimensionless	
Temperature gradient amplification factor	Π	dimensionless	
Turbulent transfer parameter	Γ_{Turb}	dimensionless	
Thermal molecular transfer parameter	Γ_{Mole}^T	dimensionless	
Salinity molecular transfer parameter	Γ_{Mole}^S	dimensionless	
Stability parameter	η_*	dimensionless	≤ 1
Stability constant	ξ_N	dimensionless	0.052

scribed completely using Eq. (1). Such a formulation has been widely used in large-scale ocean–atmosphere–sea ice models (Holland 1998) and was the basic assumption behind the earliest conceptual and numerical models of ice shelf–ocean interaction (Doake 1976; Robin 1979; MacAyeal 1985; Jenkins and Doake 1991). Despite its simplicity, the application of such a boundary condition to an ocean model may not be straightforward. If the usual prognostic equations for temperature and salinity are solved everywhere, the derived values must subsequently be reset wherever the mixed layer is in contact with ice. The "melt rate" cannot be recovered from the boundary condition but is determined from the change in temperature of the mixed layer. The derived rate is therefore a function of model time step and mixed layer thickness among other things. This is an undesirable feature if the aim is an accurate diagnosis of the melting and, since this formulation is not directly comparable to those presented below, we will discuss it no further.

2) TWO-EQUATION FORMULATIONS

The next approach that we will discuss recognizes that the rate at which the mixed layer temperature relaxes toward the freezing point is governed by the diffusion of heat through the oceanic boundary layer. Equation (2) is introduced and estimates are made of the two heat fluxes that appear on the left-hand side. In their most general form they can be written

$$Q_I^T = -\rho_I c_{pI} \kappa_I^T \left.\frac{\partial T_I}{\partial z}\right|_B \tag{6}$$

and

$$Q_M^T = -\rho_M c_{pM} \kappa_M^T \left.\frac{\partial T_M}{\partial z}\right|_B . \tag{7}$$

In the above equations κ are thermal diffusivities adjacent to the ice–ocean interface, ρ are densities, and c_p are specific heat capacities, while subscript M indicates mixed layer properties and I ice properties. In Eq. (6) the density, specific heat capacity, and thermal diffusivity may all be regarded as constant, and the problem becomes one of estimating the temperature gradient at the base of the ice shelf. To solve Eq. (7) we can treat the density and specific heat capacity as constant, but we need a suitable parameterization of the product of the diffusivity and temperature gradient near the ice shelf base. If the boundary layer were laminar, we would anticipate that the temperature would vary linearly between the interface and mixed layer temperatures, in which case Eq. (7) could be written

$$Q_M^T = -\rho_M c_{pM} \kappa_M^T \frac{(T_B - T_M)}{h}, \tag{8}$$

where h is the boundary layer thickness. Turbulence in the boundary layer means that the temperature profile is nonlinear and the diffusivity is variable, but we can parameterize these complications with the introduction of a Nusselt number, Nu, an empirical parameter having a value greater than 1:

$$Q_M^T = -\rho_M c_{pM} \left(\frac{\mathrm{Nu}\kappa_M^T}{h}\right)(T_B - T_M). \tag{9}$$

We will refer to the first quantity in brackets, which has dimensions of velocity, as a thermal exchange velocity γ_T. The simplest approach would be to choose a constant value for the exchange velocity but, recognizing that it is a result of turbulence in the mixed layer, a more realistic assumption is to make it a function of the friction velocity.

The two-equation formulation offers some advantages over the one-equation formulation. It is still very simple, but it includes a diagnosis of the melt rate. Associated heat and freshwater fluxes can then be applied to the ocean model in an identical manner to all other surface fluxes, and no special treatment of the mixed layer equations is required because of the presence of ice. However, it still lacks some realism, as to solve Eq. (1) it must be assumed that the interface salinity and the mixed layer salinity are identical. This implies infinite salt diffusivity, whereas in reality we would expect salt to diffuse at the same rate as, or slower than, heat. Nevertheless, the only error implied by this assumption is the misdiagnosis of the interface temperature, and as this is a weak function of salinity, we might anticipate relatively small errors. McPhee (1992) and McPhee et al. (1999) show that this formulation produces heat fluxes that agree well with measurements made beneath sea ice having a wide range of roughness characteristics. An analogous formulation, but with a constant thermal exchange velocity and a constant, prescribed interface salinity, has been used in the sub-ice-shelf models of Determann and Gerdes (1994), Grosfeld et al. (1997), and Williams et al. (1998).

3) THREE-EQUATION FORMULATIONS

The most sophisticated formulations make no prior assumptions about conditions at the interface and solve Eqs. (1), (2), and (5) using the known mixed layer and ice properties. By an analogous argument to that used in the derivation of Eq. (9) we can express the surviving term on the left-hand side of Eq. (5) as

$$Q_M^S = -\rho_M \gamma_S (S_B - S_M), \tag{10}$$

where γ_s is the salinity exchange velocity. Once again the exchange velocity can be either assumed constant or assigned a functional dependence on friction velocity. The former approach was followed by Hellmer and Olbers (1989, 1991), Scheduikat and Olbers (1990), and Hellmer and Jacobs (1992). The latter approach has been developed in the sea-ice literature [see Gade (1993) for

a review] and adopted in the ice shelf–ocean interaction models of Jenkins (1991), Jenkins and Bombosch (1995), Hellmer and Jacobs (1995), and Hellmer et al. (1999).

c. *Parameterizing the transfer of heat and salt through the oceanic boundary layer*

The key to diagnosing a realistic melt rate from either the two- or the three-equation formulation lies in the choice of appropriate exchange velocities. In the case of the three-equation model the problem is complicated by the fact that the thermal and salinity diffusivities can only be assumed to be equal in the fully turbulent part of the boundary layer. Close to the ice–ocean interface, the eddy size and hence the turbulent diffusivity are suppressed. Where the suppression is great enough that molecular diffusion becomes the dominant transfer mechanism, heat will diffuse more rapidly than salt. As the exchange velocities need to account for all processes occurring within the boundary layer, γ_s will be smaller than γ_T.

The role of molecular diffusion in governing the rate of heat and mass transfer within a thin, viscous sublayer adjacent to the ice–ocean boundary was recognized by Mellor et al. (1986). Subsequently, McPhee et al. (1987) and Steele et al. (1989) investigated boundary layer parameterizations that explicitly included a viscous sublayer. Jenkins (1991) used an analogous parameterization to calculate exchange velocities at the base of an ice shelf. Assuming the ice–ocean interface in this case to be hydraulically smooth leads to expressions of the form (Kader and Yaglom 1972)

$$\gamma_T = \frac{u_*}{2.12 \ln(u_* h/\nu) + 12.5 \, \mathrm{Pr}^{2/3} - 9} \tag{11}$$

and

$$\gamma_S = \frac{u_*}{2.12 \ln(u_* h/\nu) + 12.5 \, \mathrm{Sc}^{2/3} - 9}. \tag{12}$$

The influence of the molecular sublayer is apparent in the inclusion of the molecular Prandtl number, Pr (the ratio of viscosity to thermal diffusivity), and the molecular Schmidt number, Sc (the ratio of viscosity to salinity diffusivity), in the denominators. The kinematic viscosity of sea water is considered constant and is denoted by the symbol ν. The friction velocity u_* is defined in terms of the shear stress at the ice–ocean interface, a simple parameterization of which involves a dimensionless drag coefficient c_d and the velocity of the mixed layer U_M, the ice being considered stationary:

$$u_*^2 = c_d U_M^2. \tag{13}$$

A potentially important effect not accounted for in (11) and (12) is the impact of the buoyancy flux at the ice–ocean interface on turbulence within the boundary layer. A stabilizing buoyancy flux (i.e., melting) will suppress mixing, while a destabilizing buoyancy flux (i.e., freezing) will enhance mixing (McPhee 1994). We wish to investigate how the stability of the boundary layer might influence melt rates at the base of an ice shelf, so we follow McPhee et al. (1987) in expressing the transfer coefficients as

$$\gamma_{T,S} = \frac{u_*}{\Gamma_{\mathrm{Turb}} + \Gamma^{T,S}_{\mathrm{Mole}}}, \tag{14}$$

where

$$\Gamma_{\mathrm{Turb}} = \frac{1}{k} \ln\left(\frac{u_* \xi_N \eta_*^2}{f h_\nu}\right) + \frac{1}{2\xi_N \eta_*} - \frac{1}{k} \tag{15}$$

and

$$\Gamma^{T,S}_{\mathrm{Mole}} = 12.5(\mathrm{Pr}, \mathrm{Sc})^{2/3} - 6. \tag{16}$$

In Eq. (15) k is von Kármán's constant, f is the Coriolis parameter, ξ_N is a dimensionless constant, and h_ν is the thickness of the viscous sublayer. Values for the first three of these are given in Table 1, while we estimate the sublayer thickness to be (Tennekes and Lumley 1972, p. 160)

$$h_\nu = 5\frac{\nu}{u_*}. \tag{17}$$

In Eqs. (15)–(17) we have assumed the ice–ocean interface to be hydraulically smooth. The influence of the interfacial buoyancy flux is encapsulated in the stability parameter, introduced by McPhee (1981):

$$\eta_* = \left(1 + \frac{\xi_N u_*}{f L_O R_c}\right)^{-1/2}, \tag{18}$$

where R_c is a critical flux Richardson number and L_o is the Obukhov length. If the Obukhov length is negative (i.e., the buoyancy flux is destabilizing) the stability parameter is set to 1. We do not consider how destabilizing buoyancy fluxes influence freezing rates because direct freezing to the ice shelf base is thought to be limited. The formation of frazil ice in the water column, which we do not discuss here, will have a stabilizing effect on the boundary layer (Jenkins and Bombosch 1995).

d. *Modeling the heat flux into the ice shelf*

We now address the problem of estimating the basal temperature gradient in the ice shelf, required in Eq. (6). This requires solution of the heat transport equation in the ice shelf:

$$\frac{\partial T_I}{\partial t} + \mathbf{U}_I \cdot \nabla T_I = \kappa_I^T \nabla^2 T_I. \tag{19}$$

In practice, the solution of the full equation is not possible unless the flow field within the ice shelf is known, so we consider reduced forms.

1) NO ADVECTION, NO DIFFUSION

The simplest of all approximations is that the ice shelf is a perfect insulator. With no diffusion into the ice shelf, the first term on the left-hand side of Eq. (2) is identically zero. Such an approximation has been used by Determann and Gerdes (1994), Jenkins and Bombosch (1995), Grosfeld et al. (1997), and Williams et al. (1998), although it can be justified only if the conducted heat flux is always small compared to the latent heat term.

2) NO ADVECTION, VERTICAL DIFFUSION

In this case (19) reduces to

$$\frac{\partial^2 T_I}{\partial z^2} = 0 \tag{20}$$

for a steady state. The solution is a linear temperature profile throughout the thickness of the ice shelf, so the basal gradient can be expressed as

$$\left.\frac{\partial T_I}{\partial z}\right|_B = \frac{(T_S - T_B)}{H_I}, \tag{21}$$

where H_I is the thickness of the ice shelf and T_S is the surface temperature. Such an approximation has been used in the models of Hellmer and Olbers (1989, 1991), Scheduikat and Olbers (1990), and Hellmer and Jacobs (1992, 1995). This approach is common in sea–ice models, but the thickness of ice shelves and the observed, highly nonlinear temperature profiles make it less satisfactory for modeling ice-shelf thermodynamics.

3) CONSTANT VERTICAL ADVECTION, VERTICAL DIFFUSION

The simplest way to allow a nonlinear temperature profile to develop is to allow for vertical advection within the ice shelf. We will assume that the vertical velocity is constant and equal to the basal melt/freeze rate and that the ice shelf is in a steady state. There is some justification for this approximation in that over the short timescales of interest here, that is, of years to decades, the ice shelves are believed to be in a relatively steady state. Clearly, such an approximation would be unrealistic for consideration of sea ice thermodynamics because of its thinness. This requires that all ice added or removed at the base is balanced by surface ablation or accumulation. In this case Eq. (19) reduces to the equation used by Wexler (1960) (see also discussion by Paterson 1994, p. 204):

$$\frac{\partial^2 T_I}{\partial z^2} + \frac{w_I}{\kappa_I^T}\frac{\partial T_I}{\partial z} = 0, \tag{22}$$

where

$$w_I = \frac{\rho_M}{\rho_I} w_B. \tag{23}$$

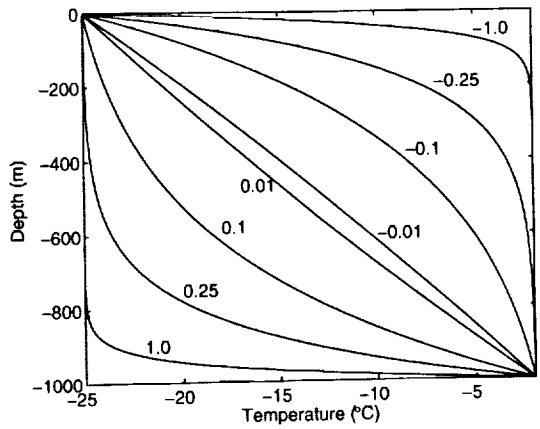

FIG. 2. Temperature–depth profiles through an ice shelf 1000 m thick, calculated assuming a constant vertical velocity. Surface and basal temperatures are −25° and −2°C, respectively. Vertical velocity (in m yr^{-1}) is given for each profile where positive labels indicate basal melting.

We assume a solution of the form $T(z) = e^{mz}$, which yields a quadratic characteristic polynomial of Eq. (22) having the two roots $m_1 = -w_I/\kappa_I^T$ and $m_2 = 0$. The general solution of Eq. (22) is then

$$T_I(z) = c_1 e^{m_1 z} + c_2 e^{m_2 z}, \tag{24}$$

where c_1 and c_2 are constants to be determined by the boundary conditions of fixed temperatures at the ice shelf surface T_S and base T_B. Utilizing these boundary conditions, the temperature profile can be written

$$T_I(z) = \frac{(T_S - T_B)\exp\left(\frac{-w_I z}{\kappa_I^T}\right) + T_B - T_S \exp\left(\frac{w_I H_I}{\kappa_I^T}\right)}{1 - \exp\left(\frac{w_I H_I}{\kappa_I^T}\right)} \tag{25}$$

with $z = 0$ at the surface and $z = -H_I$ at the base. The solution expressed by (25) is shown in Fig. 2 for an ice shelf 1000 m thick experiencing a range of basal melting and freezing rates. Under melting conditions, the temperature gradient near the base of the ice shelf is increased, which increases the conductive heat flux and serves to counteract the melting. Conversely, freezing decreases the temperature gradient and the conductive flux, which leads to a lower freezing rate than would be estimated for a linear temperature profile.

From Eq. (25) we can derive the temperature gradient at the ice shelf base:

$$\left.\frac{\partial T_I}{\partial z}\right|_B = \Pi \frac{(T_S - T_B)}{H_I}. \tag{26}$$

Equation (26) has the same form as Eq. (21) apart from the factor

$$\Pi = \frac{\Upsilon}{e^{\Upsilon} - 1}, \tag{27}$$

which depends on the Péclet number

$$\Upsilon = \frac{-w_I H_I}{\kappa_I^T}. \tag{28}$$

For a melt rate of 1 m yr^{-1} at the base of an ice shelf 1000 m thick we obtain a Péclet number of approximately -30, implying that the temperature gradient amplification factor Π can play an important role in Eq. (26).

Immediately obvious is that Eq. (27) is ill-defined for a melt rate of zero, a problem that may be overcome by rewriting the right-hand side as a power series (Arfken 1970) of the form

$$\frac{\Upsilon}{e^{\Upsilon} - 1} = \sum_{n=0}^{\infty} B_n \frac{\Upsilon^n}{n!}, \tag{29}$$

where B_n represent the sequence of Bernoulli numbers. The first few Bernoulli numbers have values (Abramowitz and Stegun 1972)

$$B_0 = 1, \quad B_2 = -\frac{1}{2}, \quad B_4 = -\frac{1}{30}, \quad B_6 = \frac{1}{42}, \cdots \tag{30}$$

the odd labeled Bernoulli numbers, B_{2n+1} for $n = 1, 2, 3, \ldots$, being identically zero. The series (29) is valid for $\Upsilon < 2\pi$ and is therefore appropriate for small values of the Péclet number (i.e., a near-zero melt/freeze rate). In particular when $\Upsilon = 0$, the expression in (29) equals B_0 and Eq. (26) is then identical to Eq. (21), the purely diffusive solution with no advection. We also note that for sea ice $\Upsilon < 1$ typically, so the purely diffusive solution is a good approximation.

Figure 3 illustrates the behavior of Π as a function of the Péclet number. Under conditions of moderate to high freezing Π is close to zero, while for moderate to high melting it is very close to the absolute value of the Péclet number. This suggests that a possible simplification of Eq. (27) is

$$\Pi = \begin{cases} \dfrac{w_I H_I}{\kappa_I^T} & \text{for melting case when } w_B > 0 \\ 0 & \text{for freezing case when } w_B < 0. \end{cases} \tag{31}$$

This approximation (also shown in Fig. 3) has the advantage of linearizing Eq. (2), and hence simplifying the solution of the ice–ocean boundary equations. Such an approximation was introduced by Nøst and Foldvik (1994) and has been adopted in the model of Hellmer et al. (1999).

4) More complex models

The next stage of complexity in the heat transport problem would be to introduce a vertical velocity that varies linearly from the surface to the base of the ice shelf. This would lead to the classical solution for the temperature profile in an ice column, first introduced by Robin (1955) for ice sheets. However, the solution involves either error functions or Dawson's integrals, and we have little hope of recovering a linear version of Eq. (2). To use such a solution, the basal temperature gradient would have to be calculated as a separate problem and the result introduced directly into Eq. (6). The same applies to models of greater sophistication that could include the horizontal advection of heat. Such a model was used by Jenkins (1991) for a specific region of Ronne Ice Shelf where measurements of ice flow and surface temperature made the computation of a steady-state temperature distribution within the ice shelf possible.

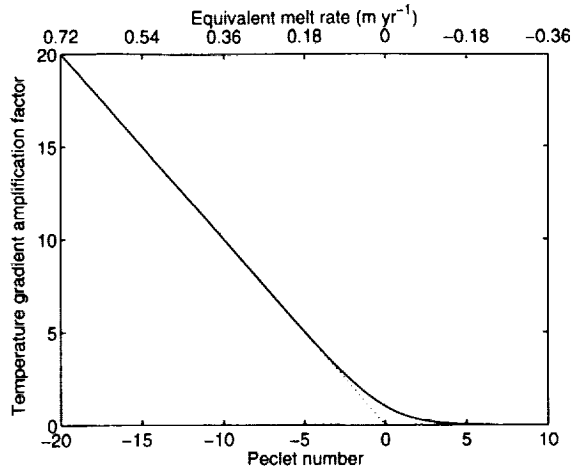

FIG. 3. Temperature gradient amplification factor as a function of Péclet number. The dotted line shows the approximation given in Eq. (31). The upper axis scale indicates equivalent melt rates for an ice shelf 1000 m thick.

3. Comparison of model results

We begin by discussing the behavior of the three-equation formulations, which are the most widely used in the literature on ice shelf–ocean interactions, and we will initially treat the ice shelf as a perfect insulator. With no heat conduction into the ice shelf, the only external parameters that enter into Eqs. (1), (2), and (5) are the friction velocity u_* and the thermal driving T_*, defined as

$$T_* = T_M - (aS_M + b + cp_B). \tag{32}$$

The difference between the various formulations lies in the specification of the exchange velocities for heat and salt, which are illustrated in Fig. 4. The two formulations that include an explicit parameterization of the boundary layer yield heat transfer coefficients that are approximately linear functions of friction velocity, with values that generally differ by no more than about 10% (Fig.

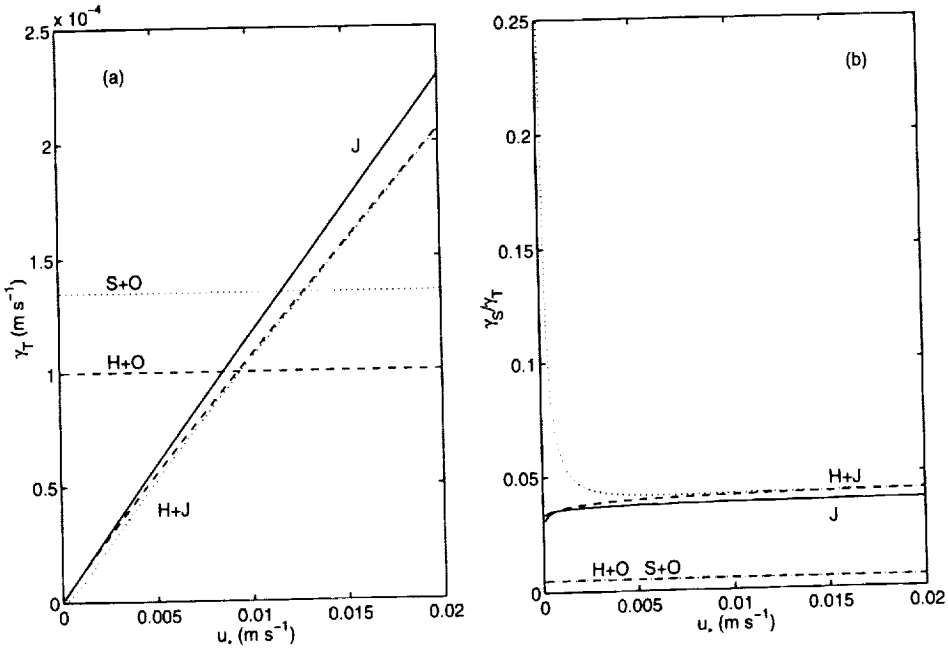

FIG. 4. (a) Heat transfer coefficients introduced by Hellmer and Olbers (1989) (dashed line labeled H+O), by Scheduikat and Olbers (1990) (dotted line labeled S+O), by Jenkins (1991) (solid line labeled J), and in this paper (dotted and dashed lines labeled H+J). In the latter case the dashed line indicates values obtained with the stability parameter of Eq. (18) set to 1, while the dotted line indicates values for a melt rate of 10 m yr^{-1}. (b) Ratio of salt to heat transfer coefficients for the same formulations.

4a). The reason for this close agreement is the dominance of the molecular term, which is the same in all cases, in the denominators of Eqs. (11) and (14). The two models having constant exchange velocities use values of γ_T that are consistent with a friction velocity of about 0.01 m s^{-1}, which corresponds to a mixed layer velocity of about 0.2 m s^{-1}. Although this is higher than most estimates of currents associated with the thermohaline circulation, it is consistent with rms currents associated with strong tidal flow (Makinson and Nicholls 1999). That the ratio of γ_s to γ_T is significantly less than one in all cases, and is relatively constant in most, (Fig. 4b) is evidence of the importance of molecular processes. Heat and salt transfer within the turbulent part of the boundary layer has little impact on the size of the coefficients except in the formulation that considers the influence of gravitational stability, and even in this formulation the effect is only significant under conditions of high thermal driving and low friction velocity.

A model's response to thermal driving is determined by the magnitudes of both the heat and the salt transfer coefficients. Figures 5a–c show the influence of changing the size of both γ_S and γ_T while keeping their ratio constant. Temperature and salinity differences across the boundary layer are set entirely by the thermal driving, with computed melt rates then responding linearly to variations in γ_S and γ_T, as heat and salt are transported with varying ease across the boundary layer. This response is similar to what we would anticipate for a two-equation formulation. However, the salinity difference across the boundary layer (Fig. 5c) means that the corresponding temperature difference (Fig. 5b) is always smaller than the thermal driving. Calculated melt/freeze rates are therefore lower than they would be if the boundary salinity were assumed to be equal to the mixed layer salinity. There is also a slight nonlinearity in the response to thermal driving that arises because the salinity at the ice–ocean interface can increase without limit but can only decrease by ~35 psu before becoming completely fresh.

The role played by salinity diffusion in determining the melt/freeze rates is shown more clearly in Figs. 5d–f, where the effect of varying the ratio of γ_S to γ_T while keeping the latter constant is illustrated. As the ratio tends to infinity, the response becomes that of a two-equation formulation with zero salinity difference across the boundary layer (Fig. 5f), a temperature difference equal to the thermal driving (Fig. 5e), and a melt/freeze rate that is directly proportional to T_* (Fig. 5d). Decreasing the salinity diffusivity increases the salinity difference across the boundary layer, which decreases the temperature difference and with it the melt/freeze rate, while the nonlinearity in the response to T_* becomes more pronounced. With negative thermal driving, the salinity at the boundary can grow until the freezing point depression balances the thermal driving, yielding a temperature difference of zero across the boundary

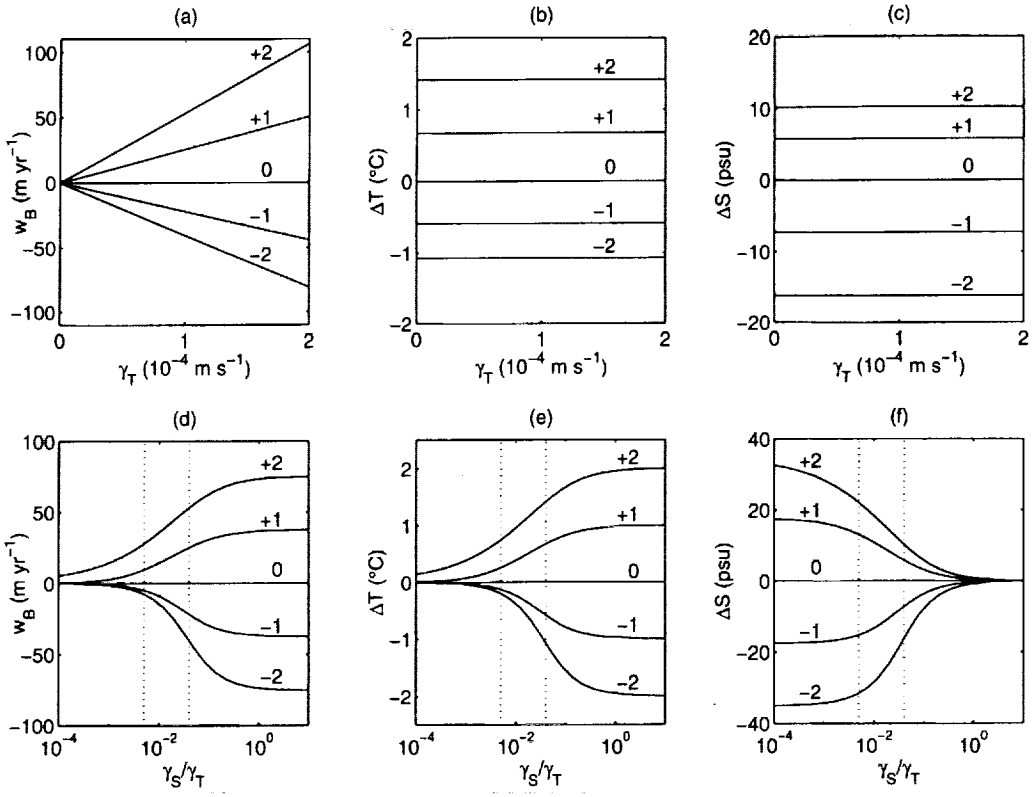

FIG. 5. Response of a three-equation formulation for thermal driving of +2°, +1°, 0°, −1°, and −2°C plotted against the magnitude of the thermal exchange velocity γ_T, (a) melt rate, (b) temperature difference across the boundary layer, (c) salinity difference across the boundary layer. The ratio of the salinity exchange velocity γ_S to γ_T is kept at 0.04. Panels (d), (e), and (f) show the response of the same variables to changes in the ratio of γ_S to γ_T, while the latter is kept constant at 1.0×10^{-4} m s^{-1}. The dotted lines indicate ratios typical of formulations with constant coefficients (0.005) and those based on boundary layer parameterizations (0.04).

layer and hence no freezing, but, given sufficient positive thermal driving, melting can proceed even if the water at the boundary is completely fresh. The two values of γ_S/γ_T found in the literature span a region of high sensitivity. The lower ratio gives rise to melting and freezing rates that are not only smaller (for the same heat transfer coefficient), but also show a more nonlinear response to thermal driving.

The effects discussed above are illustrated quantitatively in Fig. 6, which shows the melt/freeze rates computed by each of the models for a broad range of thermal driving. The two boundary layer parameterizations give rather similar results, suggesting that the precise form of Γ_{Turb} is not critical. This is convenient, as the introduction of the stability parameter into Eq. (15) involves a computationally expensive iteration to derive the melt rates and exchange coefficients. Simply setting the stability parameter to unity does not have a large impact on melt rates computed with this model, except at very low friction velocity (Fig. 7a). For thermal driving less than 0.5°C (i.e., values commonly found in nature) and a friction velocity greater that 0.001 (corresponding to a velocity of about 0.02 m s^{-1}) differences between melt rates computed with and without the stability parameter differ by less than 10%.

A possible refinement to the models discussed above would be the introduction of a conductive heat flux into the ice shelf. The influences of purely diffusive and constant vertical advection/diffusion models are illustrated in Figs. 7b,c. The linear temperature profile assumed by the purely diffusive model causes a net shift toward freezing so that a positive thermal driving is required for zero melting. Only in the region of the melt/freeze transition, where the rates are very small, does this approximation have a noticeable impact on model results (Fig. 7b). The model with constant vertical heat advection in the ice shelf has no effect unless the mixed layer is warmer than the freezing point. It then reduces the computed melt rates by about 10% (Fig. 7c).

McPhee (1992) and McPhee et al. (1999) demonstrated that direct measurements of the turbulent heat flux in the boundary layer beneath drifting sea ice could be well fitted with a two-equation model. This might be anticipated from the approximately linear response of the three-equation models, particularly at the moderate levels of thermal driving that are of most practical

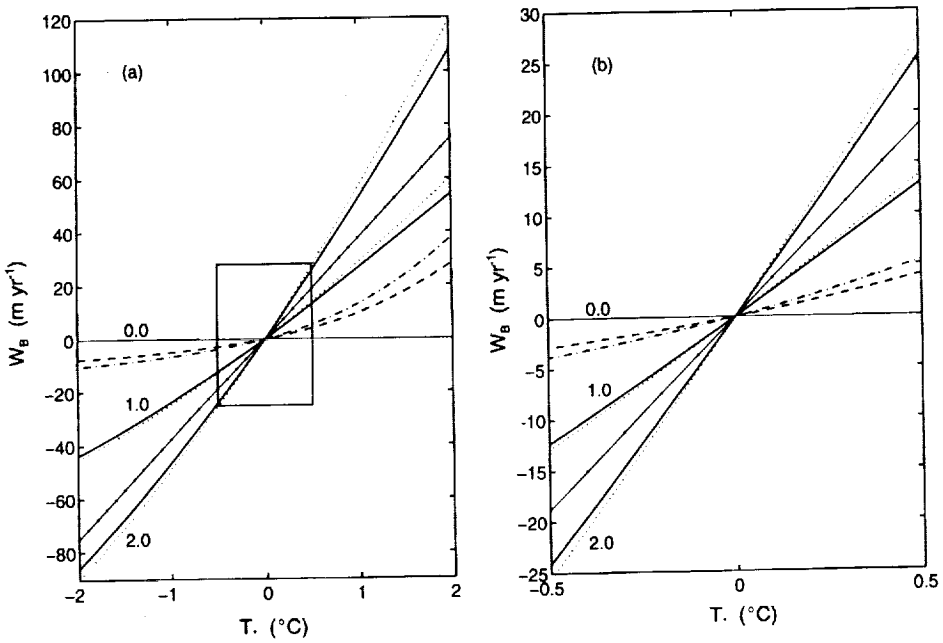

FIG. 6. Melt/freeze rates as a function of thermal driving calculated using exchange velocities given by Eqs. (14)–(18) (solid lines), by Jenkins (1991) (dotted lines), by Hellmer and Olbers (1989) (dashed line), by Scheduikat and Olbers (1990) (dot–dashed line), and by Determann and Gerdes (1994) (solid line with dots). In the Jenkins and Hellmer and Olbers cases, three curves are shown and labeled for friction velocities of 0.0, 1.0, and 2.0 cm s^{-1}. Panel (b) shows an enlargement of the boxed area in panel (a).

interest (Fig. 6b). However, the key to a consistent two-equation formulation lies in the choice of an effective exchange velocity, which accounts approximately for the fact that the finite salinity diffusivity supports a salinity difference across the boundary layer and hence reduces the thermal forcing. Using Eq. (1) we can rewrite Eq. (32) as

$$T_* = (T_M - T_B) - a\,(S_M - S_B) \tag{33}$$

from which we can express the ratio of thermal driving (T_*) to thermal forcing ($T_M - T_B$) as

$$\Theta = 1 - a\frac{(S_M - S_B)}{(T_M - T_B)}. \tag{34}$$

From Eqs. (2) and (5), with all fluxes into the ice shelf ignored, Eq. (34) can be written

$$\Theta = 1 - \frac{aS_B c_{pM}\gamma_T}{L_f \gamma_S}. \tag{35}$$

Provided this factor is approximately constant, a two-equation formulation with an effective transfer coefficient of γ_T/Θ should yield reasonable melt rates. Taking $S_B = 34.5$ psu gives $\Theta = 1.6$ for $\gamma_S/\gamma_T = 0.04$, typical for the models of Jenkins (1991) and McPhee et al. (1987), and $\Theta = 5.7$ for $\gamma_S/\gamma_T = 0.005$, as in the models of Hellmer and Olbers (1989) and Scheduikat and Olbers (1990).

Figure 7d illustrates the differences between melting/freezing rates calculated with the model that includes the stability parameter and those derived from an equivalent two-equation formulation. We find large differences for high thermal driving, particularly at low values of the friction velocity, most of which are a result of ignoring the effect of stability (Fig. 7a). At higher friction velocity, the linear response of the two-equation formulation means that melting rates tend to be underestimated and freezing rates overestimated compared with the results of the full three-equation model. However, for conditions frequently encountered in nature ($|T_*| < 0.5$°C, $u_* > 0.001$) differences between the two- and three-equation formulations are typically less than 10%.

In Fig. 8 we compare the effective transfer coefficients for each of the formulations discussed above, with that derived by McPhee et al. (1999) from observations in the turbulent boundary layer beneath sea ice. The models of McPhee et al. (1987) and Jenkins (1991) reproduce the observed dependency on friction velocity, but overestimate turbulent transfer by about 15% and 30%, respectively. The constant transfer coefficients used by Hellmer and Olbers (1989) and Scheduikat and Olbers (1990) are consistent with currents of 0.06–0.08 m s^{-1}, the right order of magnitude for the thermohaline-forced circulation beneath ice shelves. The effective transfer coefficient of Determann and Gerdes (1994) is much higher, corresponding to a velocity of about 0.35 m s^{-1}, and is therefore appropriate for a cavity subject to vigorous tidal mixing. The melt/freeze rates produced by this latter model are shown in Fig. 6 for comparison.

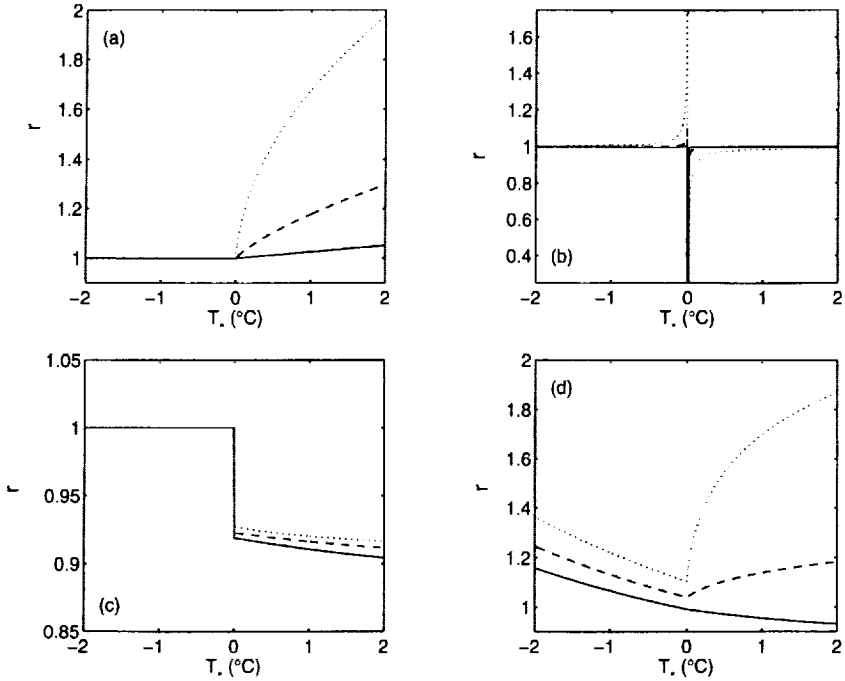

FIG. 7. Ratio of the melt/freeze rate r derived from different formulations to that calculated using the standard three-equation formulation with exchange velocities set according to Eqs. (14)–(18) and no heat conduction into the ice shelf. In each panel, solid lines indicate results obtained with a friction velocity of 1 cm s^{-1}, dashed lines with 0.1 cm s^{-1}, and dotted lines with 0.01 cm s^{-1}. The different formulations are (a) exchange velocities derived from Eqs. (14)–(18) with the stability parameter set to 1, (b) the standard model with vertical heat diffusion in the ice shelf, (c) the standard model with vertical advection and diffusion of heat in the ice shelf, and (d) an equivalent two-equation formulation. Note that the vertical scale differs between panels.

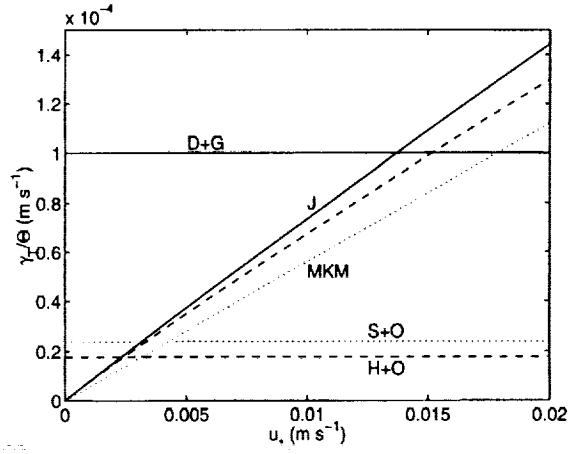

FIG. 8. Effective transfer coefficients for the formulations introduced by Hellmer and Olbers (1989) (dashed line labeled H+O), by Scheduikat and Olbers (1990) (dotted line labeled S+O), by Jenkins (1991) (solid line labeled J), in this paper (unlabeled, dashed line), and by Determann and Gerdes (1994) (solid line labeled D+G). The dotted line labeled MKM illustrates the effective transfer coefficient derived by McPhee et al. (1999) based on observations.

4. Computed buoyancy fluxes

Buoyancy fluxes associated with melting and freezing represent the primary forcing on the ocean beneath an ice shelf. Here we analyze how the differing formulations of the ice–ocean interaction discussed above influence the forcing imparted to an ocean model. The rate of change of mixed layer buoyancy can be written

$$\dot{B}_M = -g\beta_S\dot{S}_M\left(1 - \frac{\beta_T\dot{T}_M}{\beta_S\dot{S}_M}\right), \tag{36}$$

where β_S and β_T are the salinity contraction and thermal expansion coefficients, respectively. The term outside the brackets is directly related to the freshwater flux associated with melting:

$$\dot{S}_M = -\frac{S_M}{H_M}w_B, \tag{37}$$

where H_M denotes the thickness of the mixed layer. The term in brackets can be rewritten

$$\frac{\beta_T\dot{T}_M}{\beta_S\dot{S}_M} = \frac{(\partial T/\partial S)_M}{(\partial T/\partial S)_\sigma}. \tag{38}$$

Melting of ice into the mixed layer causes its T/S properties to evolve along a straight line, the gradient of

which has been derived by Gade (1979), Greisman (1979), and Nøst and Foldvik (1994), and appears as the numerator on the right-hand side of Eq. (38). The denominator is the isopycnal slope in T/S space. Of relevance to the discussion here is that $(\partial T/\partial S)_M$ depends on the assumptions made about the heat flux into the ice shelf (Nøst and Foldvik 1994). In particular, the advection/diffusion model yields a $(\partial T/\partial S)_M$ of 2.8 (for a surface temperature of $-25°C$), while the commonly used model of a perfectly insulating ice shelf gives a value that is lower by 0.33. The overall error in buoyancy forcing is

$$\delta\dot{B}_M = \delta w_B \frac{\partial \dot{B}_M}{\partial w_B} + \delta(\partial T/\partial S)_M \frac{\partial \dot{B}_M}{\partial(\partial T/\partial S)_M} \quad (39)$$

from which we obtain

$$\frac{\delta\dot{B}_M}{\dot{B}_M} = \frac{\delta w_B}{w_B} + \frac{\delta(\partial T/\partial S)_M}{(\partial T/\partial S)_\sigma - (\partial T/\partial S)_M}. \quad (40)$$

As expected, we find that any model that gives an error in the melt rate contributes the same percentage error to the buoyancy forcing. However, if the melt rate is misdiagnosed because of an error in the estimate of the heat conducted into the ice shelf, there is an additional error in the forcing. Figure 7c shows a 10% difference between the melt rates derived from a model having constant vertical advection in the ice shelf and those derived with a model that treats the ice as a perfect insulator. The additional error in buoyancy forcing, arising from the second term on the right-hand side of Eq. (40), is small ($\sim 1\%$) near the surface, where the isopycnals are steep, but rises to about 5% at a depth of 2000 m, which is reached beneath the thickest ice shelves.

5. Summary and conclusions

The main objective of this study has been the presentation of an hierarchy of models describing the thermodynamic interaction between the base of an ice shelf and the underlying ocean waters. We have reviewed the various models that have been used in the literature on ice shelf–ocean interactions and have introduced a parameterization of turbulent transfer in the oceanic boundary layer, based on the work of McPhee et al. (1987), that considers the impact of gravitational stability. We have investigated the behavior of all the models and analyzed their performance in the light of recent studies of the turbulent boundary layer beneath sea ice (McPhee 1992; McPhee et al. 1999). A key finding of the latter authors is that turbulent transfer is apparently independent of the roughness of the ice–ocean interface, a fact that gives us confidence in extrapolating their findings to an ice shelf base of unknown roughness.

Most of the models in the literature conform to the three-equation formulation, although the choice of thermal and salinity transfer coefficients varies. We have shown that the behavior of these models can be approximated by an equivalent two-equation formulation, at least for moderate thermal driving. The nonlinearity in the response of the three-equation models, a feature that does not appear in the simpler formulation, only becomes apparent at high thermal driving. In nature, supercooling can always be damped by the formation of frazil ice within the water column (Jenkins and Bombosch 1995), making model behavior at negative thermal driving greater than $\sim 0.1°C$ of theoretical rather than practical interest. Conditions of high positive thermal driving are unlikely to be encountered beneath the ice shelves of the Ross and Weddell Seas, but measurements from beneath George VI Ice Shelf, in the Bellingshausen Sea, show water more than 1°C above freezing within a few meters of the ice shelf base (K. W. Nicholls 1998, personal communication). A two-equation formulation may be inappropriate under these conditions, which may require the use of the full model of McPhee et al. (1987).

We have discussed various parameterizations of the heat flux into the ice shelf. The only one that manages to capture any of the nonlinearity of the typical ice shelf temperature profile is that which assumes constant vertical advection of ice. Applying this parameterization reduces melting by about 10% but reduces the buoyancy forcing on the ocean by up to 15%, the additional change being the result of the heat loss to the overlying ice. The overall effect is comparable to the differences in buoyancy forcing associated with the various choices of transfer coefficients used in the three-equation models. In nature, the temperature distribution within an ice shelf is determined by the history of melting and freezing that each ice column has experienced, but to introduce this thermal memory of past conditions would require a rather sophisticated dynamic/thermodynamic model of the ice shelf.

Our most important results are summarized in Figs. 6 and 8, which illustrate the behavior of the models used to date in the literature on ice shelf–ocean interactions. The three-equation models of Hellmer and Olbers (1989) and Scheduikat and Olbers (1990) have effective transfer coefficients that are only one-fifth the size of that used by Determann and Gerdes (1994). In the models of Jenkins (1991) and Jenkins and Bombosch (1995), typical friction velocities lie in the range 0.002–0.008 m s^{-1}, yielding effective transfer coefficients ranging in magnitude from that of Hellmer and Olbers (1989) up to half that used by Determann and Gerdes (1994). Whether it is better to use constant coefficients, ones based on assumed tidal velocities, or ones based on computed thermohaline velocities is an open question. However, when comparing model output, it is important to realize that the differing parameterizations of the ice–ocean interaction yield melting rates and hence buoyancy fluxes, that vary over a factor of 5 for the same thermal driving. Our recommendation is that formulations used in future, whether two-equation or three-

equation, should aim to reproduce the behavior observed by McPhee (1992) and McPhee et al. (1999), at least until such time as measurements of turbulent heat flux beneath ice shelves are available.

Acknowledgments. The authors gratefully acknowledge support from the Polar Research Program of the National Aeronautical Space Administration Grant NAG-5-4028. Stan Jacobs and Keith Nicholls provided valuable comments that significantly improved the manuscript.

REFERENCES

Abramowitz, M., and I. A. Stegun, 1972: *Handbook of Mathematical Functions.* Dover p. 810.

Arfken, G., 1970: *Mathematical Methods for Physicists.* Academic Press, p. 279.

Bombosch, A., and A. Jenkins, 1995: Modeling the formation and deposition of frazil ice beneath the Filchner-Ronne Ice Shelf. *J. Geophys. Res.*, **100,** 6983–6992.

Determann, J. M., and R. Gerdes, 1994: Melting and freezing beneath ice shelves: Implications from a three-dimensional ocean-circulation model. *Ann. Glaciol.*, **20,** 413–419.

Doake, C. S. M., 1976: Thermodynamics of the interaction between ice shelves and the sea. *Polar Rec.*, **18,** 37–41.

Eicken, H., H. Oerter, H. Miller, W. Graf, and J. Kipfstuhl, 1994: Textural characteristics and impurity content of meteoric and marine ice in the Ronne Ice Shelf, Antarctica. *J. Glaciol.*, **40,** 386–398.

Fahrbach, E., R. G. Peterson, G. Rohardt, P. Schlosser, and R. Bayer, 1994: Suppression of bottom water formation in the southeastern Weddell Sea. *Deep-Sea Res.*, **41,** 389–411.

Foldvik, A., T. Gammelsrod, and T. Torresen, 1985: Circulation and water masses on the southern Weddell Sea shelf. *Oceanology of the Antarctic Continental Shelf,* S. S. Jacobs, Ed., *Antarct. Res. Ser.*, Vol. **43,** Amer. Geophys. Union, 5–20.

Gade, H. G., 1979: Melting of ice in sea water: A primitive model with applications to the Antarctic ice shelf and icebergs. *J. Phys. Oceanogr.*, **9,** 189–198.

——, 1993: When ice melts in sea water: A review. *Atmos.–Ocean.*, **31,** 139–165.

Gill, A. E., 1973: Circulation and bottom water production in the Weddell Sea. *Deep-Sea Res.*, **20,** 111–140.

Greisman, P., 1979: On meltwater driven by the melt of ice shelves and tidewater glaciers. *Deep-Sea Res.*, **26,** 1051–1065.

Grosfeld, K., R. Gerdes, and J. Determann, 1997: Thermohaline circulation and interaction between ice shelf cavities and the adjacent open ocean. *J. Geophys. Res.*, **102,** 15 595–15 610.

Hellmer, H. H., and D. J. Olbers, 1989: A two-dimensional model for the thermohaline circulation under an ice shelf. *Antarc. Sci.*, **1,** 325–336.

——, and ——, 1991: On the thermohaline circulation beneath the Filchner-Ronne Ice Shelves. *Antarc. Sci.*, **3,** 433–442.

——, and S. S. Jacobs, 1992: Ocean interaction with the base of Amery Ice Shelf, Antarctica. *J. Geophys. Res.*, **97,** 20 305–20 317.

——, and ——, 1995: Seasonal circulation under the eastern Ross Ice Shelf, Antarctica. *J. Geophys. Res.*, **100,** 10 873–10 885.

——, ——, and A. Jenkins, 1999: Oceanic erosion of a floating Antarctic glacier in the Amundsen Sea. *Deep-Sea Res.*, in press.

Holland, D. M., 1998: On the parameterization of basal heat flux for sea-ice modelling. *Geophysica,* **34,** 1–21.

Holland, M. M., J. A. Curry, and J. L. Schramm, 1997: Modeling the thermodynamics of a sea ice thickness distributions 2: Sea ice/ocean interactions. *J. Geophys. Res.*, **102,** 23 093–23 107.

Jacobs, S. S., R. G. Fairbanks, and Y. Horibe, 1985: Origin and evolution of water masses near the Antarctic continental margin: Evidence from $H_2{}^{18}O/H_2{}^{16}O$ ratios in sea water. *Oceanology of the Antarctic Continental Shelf,* S. S. Jacobs, Ed., *Antarctic Res. Ser.*, Vol. 43, Amer. Geophys. Union, 59–85.

Jenkins, A., 1991: A one dimensional model of ice-shelf ocean interaction. *J. Geophys. Res.*, **96,** 20 671–20 677.

——, and C. S. M. Doake, 1991: Ice ocean interaction on Ronne Ice Shelf, Antarctica. *J. Geophys. Res.*, **96,** 791–813.

——, and A. Bombosch, 1995: Modeling the effects of frazil ice crystals on the dynamics and thermodynamics of ice shelf water plumes. *J. Geophys. Res.*, **100,** 6967–6981.

Kader, B. A., and A. M. Yaglom, 1972: Heat and mass transfer laws for fully turbulent wall flows. *Int. J. Heat Mass Transfer,* **15,** 2329–2351.

MacAyeal, D. R., 1985: Evolution of tidally triggered melt water plumes below ice shelves. *Oceanology of the Antarctic Continental Shelf,* S. S. Jacobs, Ed., *Antarctic Res. Ser.*, Vol. 43, Amer. Geophys. Union, 133–143.

Makinson, K., and K. W. Nicholls, 1999: Modeling tidal currents beneath Filchner–Ronne Ice Shelf and on the adjacent continental shelf: Their effects on mixing and transport. *J. Geophys. Res.*, in press.

McPhee, M. G., 1981: An analytical similarity theory for the planetary boundary layer stabilized surface buoyancy. *Bound.-Layer Meteor.*, **21,** 325–339.

——, 1992: Turbulent heat fluxes in the upper ocean under sea ice. *J. Geophys. Res.*, **97,** 5365–5379.

——, 1994: On the turbulent mixing length in the oceanic boundary layer. *J. Phys. Oceanogr.*, **24,** 2014–2031.

——, G. A. Maykut, and J. H. Morison, 1987: Dynamics and thermodynamics of the ice/upper ocean system in the marginal ice zone of the Greenland Sea. *J. Geophys. Res.*, **92,** 7017–7031.

——, C. Kottmeier, and J. H. Morison, 1999: Ocean heat flux in the central Weddell Sea during winter. *J. Phys. Oceanogr.*, **29,** 1166–1179.

Mellor, G. L., M. G. McPhee, and M. Steele, 1986: Ice–seawater turbulent boundary layer interaction with melting and freezing. *J. Phys. Oceanogr.*, **6,** 1829–1846.

Millero, F. J., 1978: Annex 6: Freezing point of seawater. Eighth report of the joint panel of oceanographic tables and standards. *UNESCO Tech. Paper Mar. Sci.*, **28,** 29–31.

Nøst, O. A., and A. Foldvik, 1994: A model of ice shelf ocean interaction with application to the Filchner-Ronne and Ross Ice shelves. *J. Geophys. Res.*, **99,** 14 243–14 254.

Oerter, H., J. Kipfstuhl, J. Determann, H. Miller, D. Wagenbach, A. Minikin, and W. Graf, 1992: Evidence for basal marine ice in the Filchner-Ronne ice shelf. *Nature,* **358,** 399–401.

Omstedt, A., and U. Svensson, 1984: Modeling supercooling and ice formation in an Ekman layer. *J. Geophys. Res.*, **89,** 735–744.

Paterson, W. S. B., 1994: *The Physics of Glaciers.* Pergamon, 480 pp.

Robin, G. de Q., 1955: Ice movement and temperature distribution in glaciers and ice sheets. *J. Glaciol.*, **2,** 523–532.

——, 1979: Formation, flow and disintegration of ice shelves. *J. Glaciol.*, **24,** 259–271.

Scheduikat, M., and D. J. Olbers, 1990: A one-dimensional mixed layer model beneath the Ross Ice Shelf with tidally induced vertical mixing. *Antarc. Sci.*, **2,** 29–42.

Steele, M., G. L. Mellor, and M. G. McPhee, 1989: Role of the molecular sublayer in the melting or freezing of sea ice. *J. Phys. Oceanogr.*, **19,** 139–147.

Tennekes, H., and J. L. Lumley, 1972: *A First Course in Turbulence.* The MIT Press, 300 pp.

Toggweiler, J. R., and B. Samuels, 1995: Effect of sea ice on the salinity of Antarctic bottom waters. *J. Phys. Oceanogr.*, **25,** 1980–1997.

Wexler, H., 1960: Heating and melting of floating ice shelves. *J. Glaciol.*, **3,** 626–645.

Williams, M. J. M., R. C. Warner, and W. F. Budd, 1998: The effect of ocean warming on melting and ocean circulation under the Amery Ice Shelf, East Antarctica. *Ann. Glaciol.*, **27,** 75–80.

——, A. Jenkins, and J. Determan, 1999: Physical controls on ocean circulation beneath ice shelves revealed by numerical models. *Ocean, Ice, and Atmosphere Interactions at the Continental Margin,* S. S. Jacobs and R. Weiss, Eds., *Antarctic Res. Ser.*, Amer. Geophys. Union, 285–300.

New results from the application of the ocean model MICOM to the Filchner-Ronne Ice Shelf

Adrian Jenkins

British Antarctic Survey, Natural Environment Research Council, High Cross, Madingley Road, Cambridge, CB3 0ET, U.K.

David M. Holland

Courant Institute of Mathematical Sciences, New York University, New York City, New York 10012, U.S.A.

Introduction

The seawater-filled cavity beneath Filchner-Ronne Ice Shelf (FRIS) is a region of major importance for both the Antarctic Ice Sheet and the Southern Ocean. High Salinity Shelf Water (HSSW) flowing into the cavity melts ice from the underside of the ice shelf and in the process is transformed into Ice Shelf Water (ISW), a precursor of the coldest and densest form of Antarctic Bottom Water. However, direct observations of conditions in the cavity are restricted to a few isolated sites and there remains considerable uncertainty over the strength of the exchange between the cavity and the open ocean to the north. The production of HSSW over the continental shelf of the southern Weddell Sea varies both spatially and temporally, but the consequences of this variability for the ice shelf-ocean system are presently unknown.

A study of water properties measured near the ice front led Nøst and Foldvik (1994) to the conclusion that ISW in the Filchner Depression is formed from the HSSW found in the Ronne Depression. This indicated a west-to-east circulation beneath the ice shelf, but Nicholls et al. (1997) suggested that most of the inflowing water reaching the deeper parts of the Ronne Depression is unable to cross the relatively shallow seabed to the south of Korff and Henry ice rises and must remain trapped within the depression. More recent observations reported by Nicholls et al. (this volume) suggest strong west-to-east flow around the southern tip of Berkner Island, but the western source region is not clear. Currentmeter measurements discussed by Østerhus at FRISP '99 suggest that some may come from the Berkner Bank. Results from a two-dimensional model of thermohaline circulation beneath FRIS indicated the possibility of flow around Berkner Island (Hellmer and Olbers, 1991), but more recent three-dimensional studies suggest only minor west-to-east exchange, most of the flow being concentrated within gyres that are strongly constrained by the sub-ice topography (Grosfeld and Gerdes, 1998; Gerdes et al., 1999).

Here we describe the first results obtained with an isopycnic coordinate ocean model. Our aim is to investigate the response of the cavity beneath Filchner-Ronne Ice Shelf to the formation of HSSW on the continental shelf to the north. The model domain therefore includes the whole of the continental shelf and is forced only by the restoration of surface temperature and salinity to a prescribed seasonal cycle over the open ocean portion of the domain.

The model

We have adapted the Miami Isopycnic Coordinate Ocean Model (MICOM; Bleck et al., 1992) so that it can be used for sub-ice-shelf investigations. The key feature of this model is that the vertical discretisation of the domain is based on density. The ocean is divided into a number of layers of constant-density water, and the model computes the thickness of these layers at each point of the horizontal grid. The advantage of this approach is that any artificial, numerical diffusion that is present is purely isopycnal. Diapycnal diffusion can be carefully controlled and even eliminated altogether, if desired. For the model to accept buoyancy forcing, the upper layer must have a freely-evolving density, so MICOM uses an embedded mixed layer at the surface. The entrainment/detrainment algorithm allows water to be cycled from one isopycnic layer, through the mixed layer, where its properties are modified by the surface boundary conditions, into another isopycnic layer. Unlike the isopycnic layers that can appear and disappear as required, the surface mixed layer is always present at all grid points, including those beneath the ice shelf. Most of the modifications we have made to the code have been connected with the mixed layer routines.

The model domain (Figure 1) covers 12° of latitude and 60° of longitude and is divided into square grid cells having dimensions equivalent to 0.75° of longitude. This gives a horizontal resolution ranging from 11.5 km along the southern boundary, to 28.5 km along the northern boundary. Ice thickness and seabed depth south of 75°S are taken from Vaughan et al. (1995), while to the north seabed depths come from the ETOPO5 database. Initial conditions are taken from the AWI Hydrographic Atlas (Olbers et al., 1992), with the cavity being filled by extrapolation. The northern and eastern boundaries are solid walls, where scalar variables are restored to Altas values. The only external forcing on the domain is the restoration of temperature and salinity in the mixed layer to the north of the ice front. Winter and summer salinity fields are shown in Figure 2. At each point the variation between the two is a simple

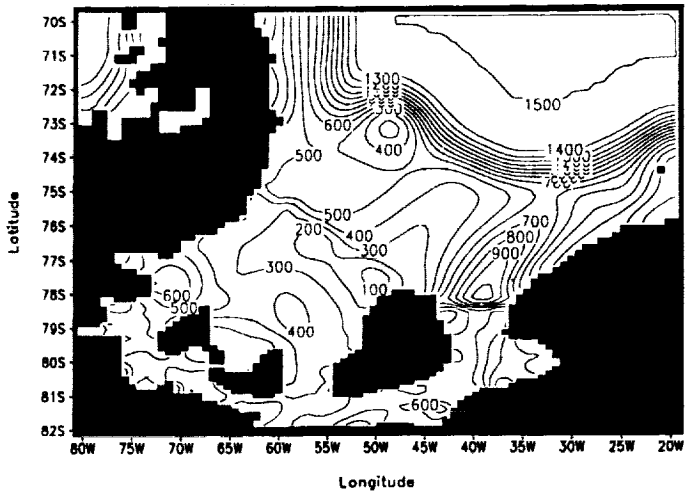

Figure 1: Water column thickness (m) over the southern Weddell Sea domain.

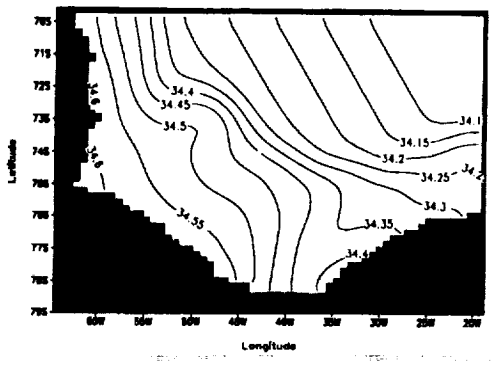

Figure 2a: Mid-summer restoring field for sea surface salinity (psu).

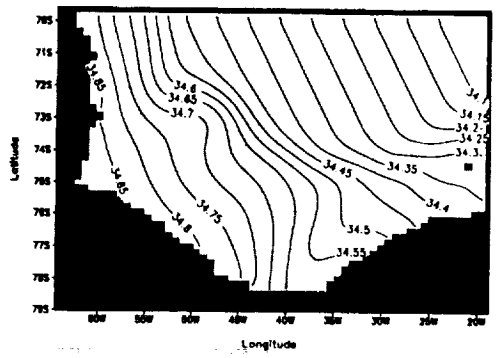

Figure 2b: Mid-winter restoring field for sea surface salinity (psu).

sinusoid. Temperature is restored to the surface freezing point during most of the year, but is ramped up to -1°C in December and January.

Preliminary results

The model has been run out over ten years with the forcing described above. While it would appear that some form of steady state has been reached at this stage (Figure 3), it should be noted that the south and west of the cavity are rather poorly ventilated, and may still by influenced by the initial conditions. In general, the computed melt/freeze rates accord reasonably well with

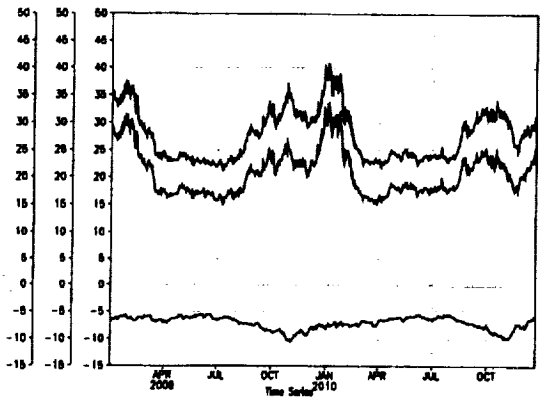

Figure 3: Melt/freeze rates (cm yr^{-1}) averaged over the ice shelf base. The upper line shows the mean of all grid points experiencing melting and the lower line the mean of all points experiencing freezing. The centre line is the overall average of all points in the sub-ice-shelf domain.

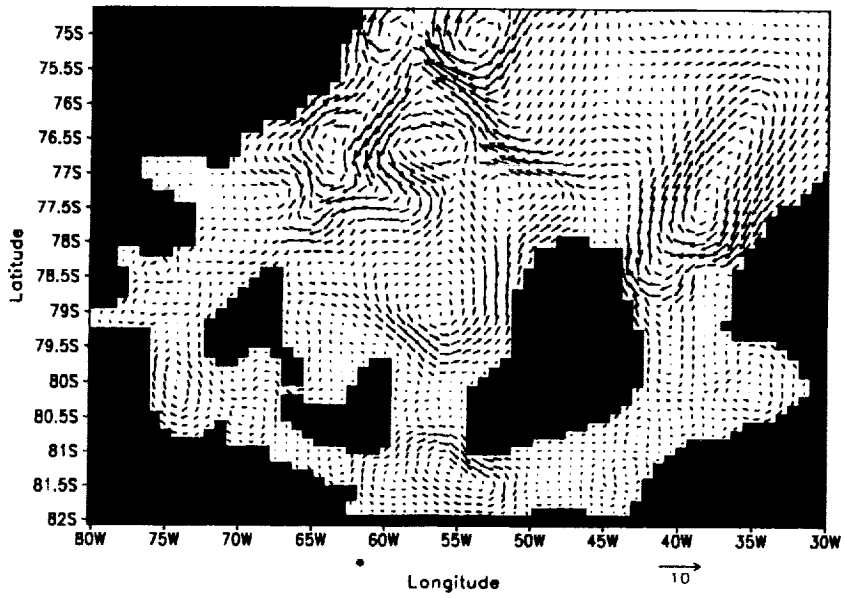

Figure 4a: Depth-averaged velocity (cm s^{-1}) in late summer.

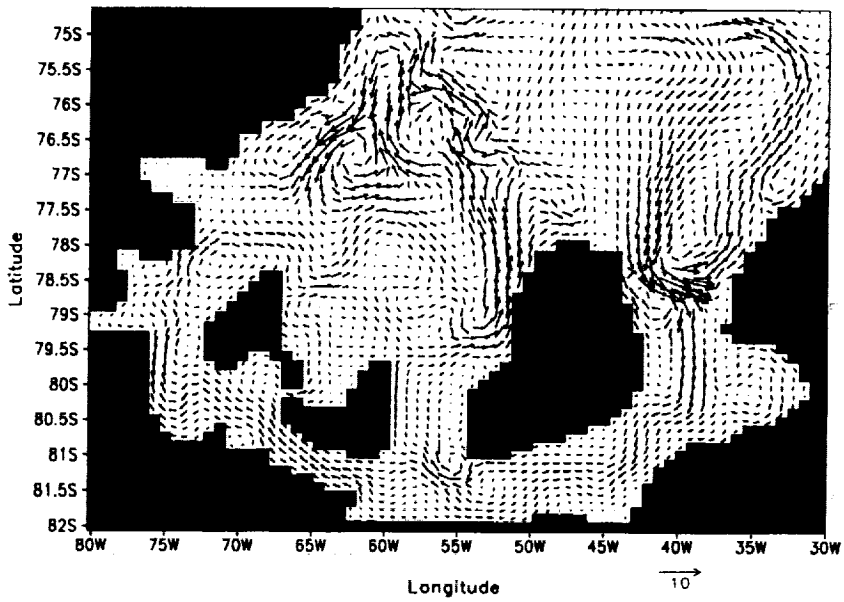

Figure 4b: Depth-averaged velocity (cm s^{-1}) in late winter.

those deduced from observation. Melting is focussed near the grounding lines of the major ice streams, as we would anticipate, but outside of these regions mass exchange between ice and ocean appears to be too weak. This is likely an artefact of the mixed layer entrainment/detrainment routine, which represents the only mechanism by which heat can be brought to the ice shelf base. The peak melt rates in mid-summer (Figure 3) reflect the influence of the warm surface layer on the regions near the ice front. The secondary peak in late winter, at a time when there is an associated peak in freezing, corresponds to the time of maximum external forcing on the cavity circulation. The overall average is a net melt rate of 20 cm yr^{-1}.

The impact of the external forcing, which is strongest in late winter when convection over the open continental shelf reaches its deepest, can clearly be seen in Figure 4. This figure also illustrates that the depth-averaged flow produced by MICOM differs markedly from that reported by Grosfeld and Gerdes (1998) and Gerdes et al. (1999). We see generally weak and variable depth-averaged velocities, which do not form into the strong, coherent gyres described by the above authors. This is because the direct impact of the buoyancy forcing is confined to the mixed layer. The lower layers move only in response to changes in the mixed layer, and the induced motion is often in a direction that differs from that of the mixed layer itself. Bearing this in mind, we should be cautious in interpreting Figure 4, which only illustrates one aspect of the circulation. However, it is clear that the cavity is ventilated primarily via the Ronne and Filchner depressions, and that waters reach the remotest parts of the cavity only indirectly and intermittently.

The biggest seasonal changes in flow occur over the Filchner Depression, and these are a direct result of the surface forcing. In summer, a cyclonic gyre within the depression penetrates only weakly into the cavity, but in winter, convection on the Berkner Bank produces a mixed layer that extends to 800m on the western flank of the depression and induces a strong west-to-east density gradient (Figure 5b). The cyclonic gyre is displaced to the east and strong southward flow develops in the west of the depression. After mid-winter the surface buoyancy forcing weakens and the vertical isopycnals subside. Dense waters drain from the Berkner Bank into the depression, turning to the north, while mid-depth waters move to the west and turn beneath the ice shelf. By mid-summer most of the potential energy has been removed from the water column, and we are left with the domed isopycnals, associated with the cyclonic gyre that has now re-established itself (Figure 5a).

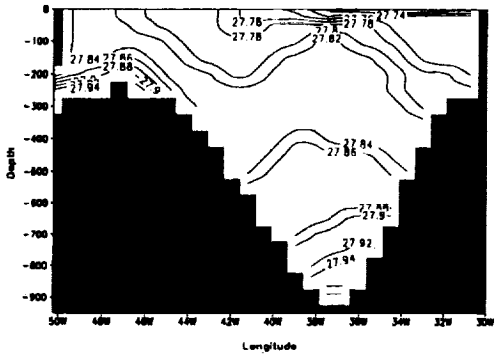

Figure 5a: Late summer potential density (kg m^{-3} - 1000) distribution at 77°S in the Filchner Depression.

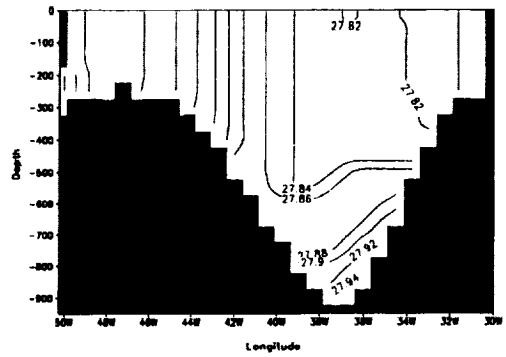

Figure 5b: Late winter potential density (kg m^{-3} - 1000) distribution at 77°S in the Filchner Depression.

The picture of circulation described above is sensitive to the prescribed surface restoring fields. In earlier simulations we used a surface salinity field that differed significantly from the one shown in Figure 2. Lower salinities in the east meant that convective overturning never occurred on the Berkner Bank, and the dominant inflow to the cavity originated in the Ronne Depression. The inflowing waters turned to the east, followed the coast of Berkner Island and finally emerged in the Filchner Depression. The area to the south of Korff and Henry ice rises was also poorly ventilated. The circulation described earlier should therefore not be interpreted as a definitive statement on the current circulation beneath Filchner-Ronne Ice Shelf, but more as the first in a number of sensitivity studies into the response of the cavity to the spatial distribution of HSSW production on the open continental shelf.

Conclusions

Preliminary runs of MICOM on a domain resembling the real topography of the southern Weddell Sea illustrate the sensitivity of the circulation beneath Filchner-Ronne Ice Shelf to the seasonal formation of HSSW to the north of the ice front. Although the circulation throughout the cavity responds to the seasonal forcing, the remotest parts of the cavity remain poorly ventilated. The possibility exists for waters to reach the interior from either the Ronne or the Filchner Depression, depending on the location of convective activity on the open continental shelf. This conclusion is similar to that reached by Hellmer and Olbers (1991), but the reasoning is subtly different. The model of Hellmer and Olbers (1991) responded directly to the density of the waters within the two depressions. In the results described in this paper, the densest HSSW is formed in the Ronne Depression, but stronger inflow develops in the Filchner Depression because of the more pronounced zonal density gradients generated there and the greater depth range over which these gradients persist. Hence, there is more potential energy available to drive shear flow perpendicular to the ice front. These results suggest that changes in the production of HSSW, such as those described by Nøst and Østerhus (1998), could have a major impact on the circulation within the cavity. We plan to investigate this by studying the response of our model to reduced restoring salinities over the Berkner Bank.

Acknowledgements: This work has received financial support from the Polar Research Program of the United States National Aeronautics and Space Administration (grant NAG-5-4028).

References

Bleck, R., C. Rooth, D. Hu and L.T. Smith. 1992. Salinity-driven thermocline transients in a wind- and thermohaline-forced isopycnic coordinate model of the North Atlantic, *J. Phys. Oceanogr.*, **22**: 1486–1505.

Gerdes, R., J. Determann and K Grosfeld. 1999. Ocean circulation beneath Filchner-Ronne Ice Shelf from three-dimensional model results, *J. Geophys. Res.*, **104**, 15827–15842.

Grosfeld, K. and R. Gerdes. 1998. Circulation in the Filchner-Ronne Ice Shelf domain: first

results from a 3D-ocean model, in *Filchner-Ronne Ice Shelf Programme*, Report No. 12, compiled by H. Oerter, pp. 35–39, Alfred-Wegener-Institute, Bremerhaven, Germany.

Hellmer, H.H. and D.J. Olbers. 1991. On the thermohaline circulation beneath the Filchner-Ronne Ice Shelves, *Antarct. Sci.*, **3**: 433–442.

Nicholls, K.W., K. Makinson and M.R. Johnson. 1997. New oceanographic data from beneath Ronne Ice Shelf, Antarctica, *Geophys. Res. Lett.*, **24**, 167–170.

Nøst, O.A. and A. Foldvik. 1994. A model of ice shelf-ocean interaction with application to the Filchner-Ronne and the Ross ice shelves, *J. Geophys. Res.*, **99**: 14243–14254.

Nøst, O.A. and S. Østerhus. 1998. Impact of grounded icebergs on the hydrographic conditions near the Filchner Ice Shelf, in *Ocean, Ice, and Atmosphere: Interactions at the Antarctic Continental Margin, Antarct. Res. Ser.*, Vol. 75, edited by S.S. Jacobs and R.F. Weiss, pp. 267–284, American Geophysical Union, Washington, D.C., U.S.A.

Olbers, D.J., V. Gouretski, G. Seiß and H. Schröter. 1992. *Hydrographic Atlas of the Southern Ocean*, Alfred-Wegener-Institute, Bremerhaven, Germany.

Vaughan, D.G., J. Sievers, C.S.M. Doake, H. Hinze, D.R. Mantripp, V.S. Pozdeev, H. Sandhäger, H.W. Schenke, A. Solheim and F. Thyssen. 1995. Subglacial and seabed topography, ice thickness and water column thickness in the vicinity of Filchner-Ronne Schelfeis, Antarctica, Polarforschung, 64, 75–88.

Adaptation of an Isopycnic Coordinate Ocean Model for the Study of Circulation beneath Ice Shelves

DAVID M. HOLLAND

Courant Institute of Mathematical Sciences, New York, New York

ADRIAN JENKINS

British Antarctic Survey, Cambridge, United Kingdom

(Manuscript received 17 April 2000, in final form 17 January 2001)

ABSTRACT

Much of the Antarctic coastline comprises large, floating ice shelves, beneath which waters from the open ocean circulate. The interaction of the seawater with the base of these ice shelves has a bearing both on the rate at which Antarctic Bottom Water is formed and on the mass balance of the ice sheet. An isopycnic coordinate ocean general circulation model has been modified so as to allow the incorporation of a floating ice shelf as an upper boundary to the model domain. The modified code admits the introduction of an arbitrary surface pressure field and includes new algorithms for the diagnosis of entrainment into, and detrainment from, the surface mixed layer. Special care is needed in handling the cases where the mixed layer, and isopycnic interior layers, interact with surface and basal topography. The modified model is described in detail and then applied to an idealized ice shelf–ocean geometry. Simple tests with zero surface buoyancy forcing indicate that the introduction of the static surface pressure induces an insignificant motion in the underlying water. With nonzero surface buoyancy forcing the model produces a cyclonic circulation beneath the ice shelf. Outflow along the ice shelf base, driven by melting of the thickest ice, is balanced by deep inflow. The abrupt change in water column thickness at the ice shelf front does not form a barrier to buoyancy-driven circulation across the front.

1. Introduction

Eustacy is affected by a variety of factors including the storage of land surface and ground water, the thermal expansion of the oceans, and the mass balance of glaciers and ice sheets. A report by the Intergovernmental Panel on Climate Change (Houghton et al. 1996) has singled out the ice sheets as representing the greatest uncertainty in accounting for past, and predicting future, changes in sea level. Ice sheet mass balance is a combination of surface accumulation and ablation, calving of icebergs from the fronts of ice shelves and tidewater glaciers, and melting and freezing that occurs at the ice–ocean interface. The latter component of the mass budget has no direct impact on sea level, as the vast majority of the melting ice is already freely floating in the ocean, but the ice shelves may play a role in regulating the discharge from some grounded portions of the ice sheet.

Aside from this indirect impact on global sea level, basal melting also has an important influence on the properties of the waters that circulate beneath an ice shelf. Outside the subice cavity the only heat sink available to the ocean is the atmosphere, so seawater cannot be cooled below the surface freezing point of about −1.9°C. The base of an ice shelf represents a heat sink at depths approaching 2000 m where the freezing point may be as low as −3.4°C (Millero 1978), so the waters in contact with the ice shelf may be up to 1.5°C below the freezing point at atmospheric pressure. Such potentially supercooled water is referred to as ice shelf water (ISW). In the Weddell Sea, ISW contributes to the formation of Antarctic Bottom Water (Foldvik and Kvinge 1974), and the exceptionally cold temperatures attained by ISW enhance the density of the product water, through the thermobaric effect. A further consequence of the generation of potentially supercooled water is that if it rises toward the surface it may become supercooled with respect to the in situ freezing point. The result is ice production deep in the water column (Foldvik and Kvinge 1974). Where this happens beneath the ice shelf, the ice accumulates on the base as marine ice (Bombosch and Jenkins 1995), while the freezing of ISW that exits the subice cavity may contribute to the sea-ice budget (Bombosch 1998).

The interaction between ice sheets and oceans is thus an important element of the climate system, and in re-

Corresponding author address: Dr. David M. Holland, Courant Institute of Mathematical Sciences, 251 Mercer Street, New York, NY 10012.
E-mail: holland@cims.nyu.edu

cent years numerical models have been used to evaluate the key processes operating in the subice cavity (Williams et al. 1998). The approach taken has been to use ocean models of varying sophistication and apply upper boundary conditions derived from a thermodynamic model of the ice shelf–ocean interaction (Holland and Jenkins 1999). The calculated heat and freshwater fluxes represent the only surface forcing on the sub–ice shelf water column, since the overlying ice shelf isolates the ocean from wind, evaporation and precipitation, and the direct effects of atmospheric temperature variations. Dynamic models of the ice shelf itself have not been included to date, and the implicit assumption has been made that any ice shelf thickness changes resulting from melting or freezing are offset exactly by the flow of the ice shelf itself. The disparity of timescales between the slowly evolving ice shelf and the rapidly ventilated waters beneath provides some justification for this modeling approach.

In this paper we focus on the mathematical description of an isopycnic coordinate sub–ice shelf ocean model, and in particular the treatment and parameterization of the mixed layer processes. Observations show the presence of a mixed layer in the water column beneath an ice shelf (Nicholls and Makinson 1998) with water properties relatively well mixed near the ice shelf base and sometimes over a significant fraction of the water column. Section 2 presents the conservation equations for the isopycnic layers of the model and describes how the equations differ for the mixed layer. The necessary modifications to the model required for it to function in the oceanographic regime beneath an ice shelf are then presented. The main issues are that of (i) the incorporation of an arbitrary surface pressure field, (ii) the processes of mixed layer entrainment and detrainment, and (iii) the interaction of layers with topography. We also briefly present some additional changes we have made to the code, associated with internal friction, that are not directly related to the ice shelf problem. Finally the modified model is applied to an idealized ice shelf–ocean geometry and the results are discussed.

2. Model description

As a longer-term science objective a coupled numerical model is being developed suitable for investigation of oceanographic processes in polar regions, referred to as the Polar Ocean Land Atmosphere Ice Regional (POLAIR) modeling system. At present this system consists of a viscous-sublayer parameterization describing the thermodynamic interaction between the ice shelf base and the ocean surface (Holland and Jenkins 1999) coupled to an isopycnic ocean general circulation model (Bleck et al. 1992). That ocean component, the Miami Isopycnic Coordinate Ocean Model (MICOM), already contains an embedded mixed layer model based on a turbulent kinetic energy (TKE) budget. In the next stages of development, a sea-ice, atmospheric boundary layer, and dynamical ice shelf model will be added. We now briefly describe the ocean model and its mixed layer submodel prior to elaborating upon the modifications that are addressed in the sections following.

a. Isopycnic interior model

The primitive equation isopycnic coordinate ocean model used (MICOM) has four prognostic equations: one equation for the horizontal velocity vector, a layer thickness tendency equation, and two conservative equations for the buoyancy related variables. Since not all layers are necessarily constant density (e.g., the mixed layer), we first present the equations for a generalized vertical coordinate ξ (Bleck and Boudra 1981; Bleck 1998):

$$\frac{\partial \mathbf{v}}{\partial t_\xi} + \nabla_\xi \frac{\mathbf{v}^2}{2} + (\zeta + f)\hat{\mathbf{k}} \times \mathbf{v} + \left(\frac{\partial p}{\partial \xi}\frac{\partial \xi}{\partial t}\right)\frac{\partial \mathbf{v}}{\partial p} = -\alpha_\theta \nabla_\xi p - \nabla_\xi \phi - g\frac{\partial \boldsymbol{\tau}}{\partial p} + \left(\frac{\partial p}{\partial \xi}\right)^{-1} \nabla_\xi \cdot \left(\kappa_v \frac{\partial p}{\partial \xi}\nabla_\xi \mathbf{v}\right) \tag{2.1}$$

$$\frac{\partial}{\partial t_\xi}\left(\frac{\partial p}{\partial \xi}\right) + \nabla_\xi \cdot \left(\mathbf{v}\frac{\partial p}{\partial \xi}\right) + \frac{\partial}{\partial \xi}\left(\frac{\partial p}{\partial \xi}\frac{\partial \xi}{\partial t}\right) = \nabla_\xi \cdot \left(\kappa_h \nabla_\xi \frac{\partial p}{\partial \xi}\right) \tag{2.2}$$

$$\frac{\partial}{\partial t_\xi}\left(\frac{\partial p}{\partial \xi}C\right) + \nabla_\xi \cdot \left(\mathbf{v}\frac{\partial p}{\partial \xi}C\right) + \frac{\partial}{\partial \xi}\left(\frac{\partial p}{\partial \xi}\frac{\partial \xi}{\partial t}C\right) = \nabla_\xi \cdot \left(\kappa_C \frac{\partial p}{\partial \xi}\nabla_\xi C\right) + \mathcal{F}_C. \tag{2.3}$$

In these relations, $\mathbf{v} = (u, v)$ is the horizontal velocity vector, p the pressure, C represents either one of the model's dynamically active tracers (i.e., potential temperature θ or salinity S) as well as any passive tracers, $\zeta = \partial v/\partial x_\xi - \partial u/\partial y_\xi$ the relative vorticity, α_θ the specific volume, $\phi = gz$ the geopotential, g the gravitational acceleration, f the Coriolis parameter (spatially varying), $\hat{\mathbf{k}}$ the vertical unit vector, κ_v the isopycnic eddy viscosity, κ_h the layer thickness diffusivity, κ_C the tracer diffusivity, $\boldsymbol{\tau}$ the wind- and/or bottom-drag-induced shear stress vector, and $\mathcal{F}_C$ represents the sum of all diabatic forcings on the tracer variable C. The quantity $(\partial p/\partial \xi\, \partial \xi/\partial t)$ represents the vertical mass flux through a surface ξ. The independent variables x, y, and t have their usual meanings and ξ is now the independent variable in the vertical direction.

The above equations are relationships formulated for variables on ξ surfaces, but the ocean model is formulated for layers (i.e., the material bounded between

two ξ surfaces). A point of nomenclature: in the discrete context the individual layers will be denoted by integer subscript k, with the topmost layer assigned index 1 and the bottommost layer assigned index N. Furthermore, in general we will use the notation of a superscript symbol $(-)$ to refer to a quantity at the surface interface of a layer and a superscript symbol $(+)$ at the basal interface of a layer. To obtain averaged equations for the fluid between some upper ξ^- and lower ξ^+ bounding surfaces requires multiplication of each of (2.1) through (2.3) by $\partial p/\partial\xi$, vertical integration of the resulting equations over the coordinate interval $\Delta\xi = \xi^+ - \xi^-$, and division by the pressure jump between the surfaces, $\Delta p = p(\xi^+) - p(\xi^-)$. As a further simplification for use in later sections, we introduce the notation that the layer thickness is exactly defined in terms of the pressure jump as $h = \Delta p$. As the velocity within a layer is vertically constant, it is convenient to also introduce the notation of Δv^-, Δv^+ as the velocity jump across the upper $-$ and lower $+$ interfaces of a layer, respectively.

After these transformations, the horizontal momentum, layer thickness, and buoyancy conservation equations for a layer become

$$\frac{\partial \mathbf{v}}{\partial t} + \nabla\frac{\mathbf{v}^2}{2} + (\zeta + f)\hat{\mathbf{k}} \times \mathbf{v} + \frac{1}{\Delta p}\left[\left(\frac{\partial p}{\partial \xi}\frac{\partial \xi}{\partial t}\right)^+ \Delta \mathbf{v}^+ - \left(\frac{\partial p}{\partial \xi}\frac{\partial \xi}{\partial t}\right)^- \Delta \mathbf{v}^-\right] = -\alpha_\theta \nabla\frac{p(\xi^+) + p(\xi^-)}{2} - \nabla\frac{\phi(\xi^+) + \phi(\xi^-)}{2} - \frac{g}{\Delta p}(\boldsymbol{\tau}^+ - \boldsymbol{\tau}^-) + \frac{\nabla \cdot (\kappa_v \Delta p \nabla \mathbf{v})}{\Delta p} \quad (2.4)$$

$$\frac{\partial \Delta p}{\partial t} + \nabla \cdot (\mathbf{v}\Delta p) + \left[\left(\frac{\partial p}{\partial \xi}\frac{\partial \xi}{\partial t}\right)^+ - \left(\frac{\partial p}{\partial \xi}\frac{\partial \xi}{\partial t}\right)^-\right] = \nabla \cdot (\kappa_h \nabla \Delta p) \quad (2.5)$$

$$\frac{\partial}{\partial t}(\Delta p C) + \nabla \cdot (\mathbf{v}\Delta p C) + \left[\left(\frac{\partial p}{\partial \xi}\frac{\partial \xi}{\partial t}\right)^+ C^+ - \left(\frac{\partial p}{\partial \xi}\frac{\partial \xi}{\partial t}\right)^- C^-\right] = \nabla \cdot (\kappa_C \Delta p \nabla C) + \mathcal{F}_C. \quad (2.6)$$

The topmost layer is not isopycnic, is referred to as the mixed layer, and has a nonzero $(\partial p/\partial\xi\ \partial\xi/\partial t)_1^+$ representing a large flux of mass and properties into and out of an otherwise almost-adiabatic ocean interior. The interior ocean is not exactly adiabatic as there exists subtle diapycnic fluxes $(\partial p/\partial\xi\ \partial\xi/\partial t)_k^+$ between neighboring layers due to the background presence of small-scale turbulence. A detailed treatment of these terms is presented elsewhere (McDougall and Dewar 1998) and no modification of that treatment is undertaken in this study.

For all interior model layers (i.e., excluding the mixed layer) we choose ξ to be surfaces of constant potential density ρ_θ, and for these layers the $(\partial p/\partial\xi\ \partial\xi/\partial t)_k^+$ terms vanish if there are no diapycnic exchanges. For future reference we will define this flux of mass between layers as a general diapycnic flux by introducing the notation $w_k^+ = (\partial p/\partial\xi\ \partial\xi/\partial t)_k^+$. On isopycnic layers the pressure and geopotential gradient terms in (2.4) can be replaced by the gradient of the Montgomery potential (Montgomery 1937):

$$M = \alpha_\theta p + gz. \quad (2.7)$$

Because the Montgomery potential is vertically invariant throughout the depth of a layer, it does not matter at what level within the layer it is evaluated. For adiabatic isopycnic interior layers Eqs. (2.4)–(2.6) reduce to (Bleck 1998)

$$\frac{\partial \mathbf{v}}{\partial t} + \nabla\frac{\mathbf{v}^2}{2} + (\zeta + f)\hat{\mathbf{k}} \times \mathbf{v} = -\nabla M - \frac{g}{\Delta p}[\boldsymbol{\tau}^+ - \boldsymbol{\tau}^-] + \frac{\nabla \cdot (\kappa_v \Delta p \nabla \mathbf{v})}{\Delta p} \quad (2.8)$$

$$\frac{\partial \Delta p}{\partial t} + \nabla \cdot (\mathbf{v}\Delta p) = \nabla \cdot (\kappa_h \nabla \Delta p) \quad (2.9)$$

$$\frac{\partial (\Delta p C)}{\partial t} + \nabla \cdot (\mathbf{v}\Delta p C) = \nabla \cdot (\kappa_C \Delta p \nabla C). \quad (2.10)$$

As these equations are derived, whether for nonisopycnic or isopycnic layers, under the hydrostatic (and Boussinesq) approximation, the vertical component of the momentum balance is a diagnostic equation, which takes on the form (Bleck 1998)

$$\frac{\partial M}{\partial \alpha_\theta} = p. \quad (2.11)$$

b. Mixed layer model

A characteristic problem of pure isopycnic coordinate formulations is an inability to accommodate buoyancy forcing at the ocean surface. The solution adopted in MICOM is to have a variable density mixed layer sitting on top of the pure isopycnic layers that acts as an interface between the adiabatic ocean interior and the buoyancy forcing from the atmosphere. In the present application the surface buoyancy fluxes also arise from thermodynamic interactions at the base of an ice shelf, and so the mixed layer must also exist beneath the ice shelf. While all interior isopycnic layers adhere to the basic conservation equations (2.4)–(2.6), the mixed layer is unique in that its layer thickness is also dependent upon a TKE balance, determined from the input of frictional stress and buoyancy at the surface, and a parameterization of energy dissipation processes (Gaspar 1988). We define the buoyancy in a layer, b, as

$$b = g\frac{\rho_v - \rho_\theta}{\rho_v}, \quad (2.12)$$

where the potential density is $\rho_\theta = 1/\alpha_\theta$ and $\rho_v = 1/\alpha_v$

is a reference density based on a reference specific volume α_o. Then, the rate of entrainment of fluid into the mixed layer, w_1^+, can be expressed by

$$\frac{w_1^+ \Delta b}{2\rho_\theta g} = \frac{\rho_\theta g m_g u_*^3}{\Delta p_1} + \frac{B_M}{2} - \varepsilon_d, \qquad (2.13)$$

where Δb is the change in mixed layer buoyancy resulting from entrainment, m_g is an empirical constant, u_* is the friction velocity, Δp_1 is the thickness of the mixed layer in pressure units, B_M is the buoyancy flux due to surface forcing, and ε_d is the parameterized dissipation of TKE (see Gaspar 1988 for further details). The relation between (2.4)–(2.6) and (2.13) is manifested through the common definition of the diapycnic velocity, w_1^+, which permits mass exchange between the mixed layer and the isopycnic interior layers by moving the interface representing the mixed layer base.

A source of TKE (e.g., strong shear in the flow between the ocean surface and the base of the ice shelf or alternatively brine rejection associated with marine ice growth) leads in general to a deepening of the mixed layer; the reverse being true for a sink of TKE (e.g., input of meltwater during a basal melting event). During times when the mixed layer is deepening, water is entrained from the adiabatic ocean interior into the mixed layer. The exact amount of water entrained is diagnosed by balancing the supply of TKE against the increase in potential energy of the water column resulting from mixing. At times when the mixed layer is shallowing, water is detrained from the mixed layer into the interior isopycnic layer closest in density to that of the detrained water. In this fashion, the waters in the oceanic interior are ventilated by the mixed layer.

c. *Equation of state*

The equation of state we utilize to compute potential density ρ_θ, and its inverse the potential specific volume α_θ, is an approximation of the United Nations Educational, Scientific and Cultural Organization (UNESCO; Millero et al. 1980) equation of state in the form of a polynomial that is cubic in potential temperature, quadratic in pressure, and linear in salinity (Brydon et al. 1999). This polynomial represents a reasonable compromise between accuracy and computational economy as compared to the much higher-order UNESCO polynomial. It also allows for direct analytical "inversion" of the equation of state so that, for instance, potential temperature can be obtained from given values of potential density, salinity, and pressure. The polynomial equation for the density is, expressed in sigma-theta terms,

$$\begin{aligned}\sigma(\theta, S, p_o) = {} & c_1^\sigma(p_o) + c_2^\sigma(p_o)\theta + c_3^\sigma(p_o)S \\ & + c_4^\sigma(p_o)\theta^2 + c_5^\sigma(p_o)S\theta + c_6^\sigma(p_o)\theta^3 \\ & + c_7^\sigma(p_o)S\theta^2, \qquad (2.14)\end{aligned}$$

where the empirical coefficients $C_1^\sigma \cdots C_7^\sigma$ are known functions of ocean reference pressure p_o (Brydon et al. 1999). This equation of state is suitable over the range of temperatures, salinities, and pressures encountered in a sub–ice shelf cavity.

3. Surface pressure

a. *Isostatic assumption*

A common assumption made in the construction of numerical models of ocean circulation is that the surface pressure either is spatially and temporally constant, or varies at most by a fraction of the overlying atmospheric pressure. The ocean surface then deviates only slightly from a surface of constant geopotential and the deviations are always small in comparison with the depth of the water column. However, a floating ice shelf may exert a pressure approaching 200 atm on the underlying ocean, and the associated surface topography is then of the same order of magnitude as the ocean bottom topography. Computing the oceanic response to changes in pressure of this magnitude would be a challenging problem, but the ice shelf thickness evolves on timescales that are much longer than those of interest for the dynamic response of the ocean. We can therefore assume that the surface pressure is static and that the surface elevation is always close to that of the isostatically adjusted sea level. The isostatically adjusted sea surface then plays a role identical to that of a constant geopotential sea surface in conventional ocean models.

In the case of MICOM, the isopycnic interior layers are bounded by interfaces that experience a spatially and temporally varying pressure field and may have an entirely arbitrary interfacial topography. The bottom interface of the bottommost layer is unique in that it has a fixed bottom topography and a bottom pressure that undergoes small, temporal variations according to the total weight of fluid in the overlying water column. The surface interface of the mixed layer is also unique in that it has a small, temporally and spatially variable surface topography and a zero surface pressure. We undertook to transform the model code to allow for an arbitrarily large, static surface pressure field, as might be imposed by a floating ice shelf, which provides the surface interface of the mixed layer with a large, spatially variable surface topography. The surface of the mixed layer continues to undergo small height perturbations about its mean topographic profile—that profile now being the bottom interface of an ice shelf. After the modifications, there still remains no temporal variation in surface pressure, whatsoever.

We define the isostatically adjusted sea level z_1^* by

$$\alpha_1 \nabla p_1 = -g \nabla z_1^*, \qquad (3.1)$$

where α_1 is the specific volume of the mixed layer. In the open-ocean part of the domain p_1 is considered as the sea surface pressure while in the sub–ice shelf cavity

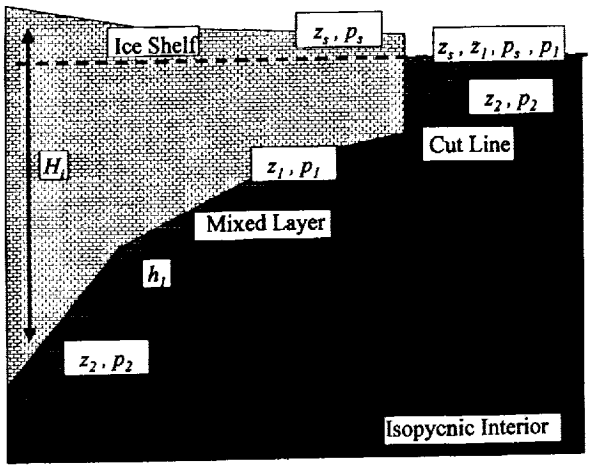

FIG. 1. Side view of horizontally varying surface pressure over the ocean surface due to the presence of an ice shelf. The ice shelf has horizontally varying thickness H_i and it ends abruptly at the ice shelf front, creating the probable situation of the mixed layer becoming horizontally discontinuous (i.e., a cutline) at the ice shelf front. The top surface of the ice shelf and of the open ocean are denoted by elevation and pressure z_s and p_s. The surface of the ocean (i.e., the surface of the mixed layer) has elevation and pressure denoted by z_1 and p_1, while the bottom of the mixed layer is denoted by z_2 and p_2. The heavy dashed line shows for reference the equilibrium elevation for an ocean surface in the absence of an ice shelf that would be, of course, a horizontally uniform geopotential surface.

part of the domain it is the ice shelf bottom pressure. We estimate the surface pressure according to

$$p_1 = \frac{gH_i}{\alpha_i}, \tag{3.2}$$

where α_i and H_i are the mean specific volume and thickness of the overlying ice column, respectively. A schematic of the definition of these and other relevant quantities is given in Fig. 1. The expression (3.1) is based on the assumption that the ice shelf cannot support vertical shear stresses between neighboring columns of ice, and is a good approximation over horizontal scales that are large compared with the ice thickness (~1 km) as is the case in the present application. The sea level z_1^* so defined is the *equilibrium* sea surface position and is not a geopotential surface as is typically the case in ocean modeling. As dynamical motions occur in the ocean, the model sea level, z_1, undergoes small height perturbations relative to its reference value z_1^*.

An important consequence of the definition of the sea surface (3.1), whether it be that residing beneath an ice shelf or that occurring over the open ocean, is that the gradient of the Montgomery potential will correctly vanish for the situation where the horizontal pressure force is zero and no flow is expected. Such a situation being when there is no horizontal gradient of the mixed layer specific volume α_1 and the sea surface elevation is equal to its reference value of z_1^*. In that case ∇M_1 vanishes exactly as seen from combining (3.1) with the definition of the Montgomery potential.

b. Operator splitting

In common with many ocean models, MICOM employs an operator splitting technique to solve the momentum equations in a computationally efficient manner. The solution for the depth-averaged flow is advanced separately from that for the more complex, depth-dependent component. The former is forced by pressure deviations at the seabed, which reflect net convergence or divergence of mass in the overlying water column, while the latter is forced by changes in the vertical density structure, which leave the overall mass of the water column, and hence the pressure at the seabed, unaffected. The details of the operator splitting are described by Bleck and Smith (1990) and Higdon and Bennett (1996), so only the essential modifications will be presented here. The total pressure p is multiplicatively split into "baroclinic" and "barotropic" components according to

$$p = p'(1 + \eta), \tag{3.3}$$

where p' represents the depth-dependent baroclinic component and the dimensionless variable η represents the depth-independent barotropic component as the fractional change in total mass of the water column. At the seabed, the baroclinic component p_b' is time invariant, while spatial gradients in the evolving barotropic component $p_b'\eta$ provide the main forcing on the depth-averaged flow. In the presence of a static surface pressure, Eq. (3.3) becomes

$$p - p_1 = (p' - p_1)(1 + \eta). \tag{3.4}$$

Note that the surface pressure does not decompose, because it is unaffected by any changes (barotropic or baroclinic) in the ocean. The velocity is split according to

$$\mathbf{v} = \overline{\mathbf{v}} + \mathbf{v}', \tag{3.5}$$

where $\overline{\mathbf{v}}$ is the depth-mean flow and the deviations $\mathbf{v}'$ have the property that they integrate to zero over the total water column.

c. Barotropic component

The prognostic equation for the depth-averaged velocity is written

$$\frac{\partial \overline{\mathbf{v}}}{\partial t} + f\hat{\mathbf{k}} \times \overline{\mathbf{v}} = -\nabla \overline{M} + \frac{\partial \overline{\mathbf{v}}^*}{\partial t}, \tag{3.6}$$

where we have introduced and defined notation for the barotropic component of the Montgomery potential as $\overline{M} = \alpha_o(p_b' - p_1)\eta$. The final term on the right-hand side of (3.6) represents all addition forcing terms in (2.8) that have not been explicitly taken into account in (3.6). Applying the pressure and velocity splitting to the layer thickness tendency equation (2.9), we obtain

$$\Delta p' \frac{\partial \eta}{\partial t} + \frac{\partial \Delta p'}{\partial t} + \nabla \cdot (\bar{\mathbf{v}} \Delta p') + \nabla \cdot (\bar{\mathbf{v}}' \Delta p') = \nabla \cdot (\kappa_h \nabla \Delta p'), \quad (3.7)$$

where we have used the facts that $\Delta p = \Delta p'(1 + \eta)$ and that $\eta \ll 1$ so that $1 + \eta$ may be approximated by 1 where it appears as a factor. Summing this expression over all layers and recalling that p_b' and p_1 are constants, not subject to time evolution or diffusion, and that the velocity deviations must integrate to zero, yields a predictive equation for the barotropic pressure component:

$$\frac{\partial \eta}{\partial t} + \frac{\nabla \cdot [\bar{\mathbf{v}}(p_b' - p_1)]}{p_b' - p_1} = 0. \quad (3.8)$$

d. Baroclinic component

The corresponding equations for the depth-dependent layer thickness tendencies is obtained by substituting (3.8) into (3.7),

$$\frac{\partial \Delta p'}{\partial t} + \nabla \cdot (\mathbf{v}' \Delta p') = \frac{\Delta p'}{p_b' - p_1} \nabla \cdot [\bar{\mathbf{v}}(p_b' - p_1)] - \nabla \cdot (\bar{\mathbf{v}} \Delta p'), \quad (3.9)$$

and for the depth-dependent layer momentum by subtracting (3.6) from (2.8),

$$\frac{\partial \mathbf{v}}{\partial t} + \nabla \frac{\mathbf{v}^2}{2} + (\zeta + f)\hat{\mathbf{k}} \times \mathbf{v}' + \zeta \hat{\mathbf{k}} \times \bar{\mathbf{v}} = -\nabla M' - \frac{g}{\Delta p'}(\boldsymbol{\tau}^+ - \boldsymbol{\tau}^-) + \frac{1}{\Delta p'} \nabla \cdot (\kappa_v \Delta p' \nabla \mathbf{v}) - \frac{\partial \bar{\mathbf{v}}^*}{\partial t}, \quad (3.10)$$

where M' is the baroclinic component of the Montgomery potential, defined by $M' = M - \bar{M}$. The baroclinic Montgomery potential is computed for each layer, including the mixed layer, by applying the isopycnic form of the hydrostatic relation, Eq. (2.11). This is achieved by starting at the bottom layer, which has a known reference Montgomery potential, and integrating vertically, as

$$M_k' = M_{k+1}' + (\alpha_k - \alpha_{k+1}) p_k^+ - \bar{M}, \quad (3.11)$$

where again k denotes the layer index, with $k = 1$ corresponding to the mixed layer and $k > 1$ corresponding to the isopycnic interior layers.

Equation (3.10) cannot be directly applied to the mixed layer because the density varies horizontally. We must therefore retain the pressure and geopotential gradients as separate terms, as in (2.4). The forcing term equivalent to $\nabla M'$ in (3.10) for the mixed layer, denoted ∇M_1^*, is

$$\nabla M_1^* = \alpha_1 \nabla \left(\frac{p_1 + p_2}{2} \right) + \nabla \left(\frac{\phi_1 + \phi_2}{2} \right). \quad (3.12)$$

The reference to the geopotential function is eliminated by substitution of the definition of the Montgomery potential so as to express ∇M_1^*, only in terms of quantities explicitly calculated by the model. The final expression for the baroclinic component of the mixed layer Montgomery potential is then

$$\nabla M_1^* = \alpha_1 \nabla \left(\frac{p_1 + p_2}{2} \right) + \nabla \left[\frac{(M_1' + M_2') - (\alpha_1 p_1 + \alpha_2 p_2)}{2} \right], \quad (3.13)$$

where M_1' and M_2' are known from (3.11) and the interface pressure p_2 is known from an evaluation of (3.9).

4. Mixed layer processes

a. Entrainment

An elegant algorithm for entrainment in an isopycnic layer context, consistent with overall energy conservation in the water column, is presently employed in the MICOM code (Bleck et al. 1989). The TKE produced via the surface stress and buoyancy extraction processes is used to mix denser water from the isopycnic interior into the mixed layer, thereby increasing the mixed layer thickness. The resulting increase in potential energy of the water column exactly matches and thus exhausts the supply of TKE over the course of one model time step. The entrainment algorithm we use is based on identical principles, but looks algebraically different, as we have had to generalize the equations to allow for an arbitrary surface pressure field. The derivation follows closely that of Bleck et al. (1989) and a schematic of the relationship between the various densities and combinations of surface buoyancy fluxes for a typical entrainment scenario is presented in Fig. 2.

A point of nomenclature that needs be mentioned, as it applies both to the entrainment procedure of the present section and detrainment procedure of the next section, is that in the overall context of the model's mixed layer algorithm there always exist three mixed layer thicknesses: the initial mixed layer thickness h_1 at the beginning of a time step, an intermediate mixed layer thickness h_g derived from Eq. (2.13) based on the physics of Gaspar (1988) and referred to as the "Gaspar" thickness, and the final mixed layer thickness h_m at the end of a time step.

We need to evaluate the potential energy (PE) of the water column between the two pressure interfaces representing the sea surface p_1 and the unknown depth to which mixing and entrainment occurs p_m. This will be done for both the mixed and unmixed states, with the aim of finding the value of p_m for which the change in PE equals the supply of TKE. Introducing the gravitational acceleration as an explicit factor, the PE per unit horizontal area can be expressed in terms of the Montgomery potential:

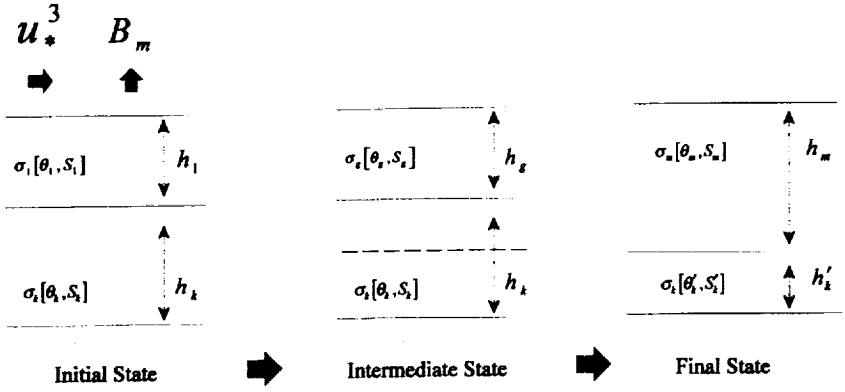

FIG. 2. Schematic of the entrainment of isopycnic-layer waters into the mixed layer due to either free convection as promoted by an unstable vertical density profile or forced convection due to either surface frictional stress u_*^3 or an upward-directed surface buoyancy flux B_m (i.e., buoyancy loss). The leftmost panel shows the *initial state* of the system with the mixed layer density, temperature, salinity, and thickness denoted σ_1, θ_1, S_1, and h_1, respectively. The complementary properties of the isopycnic layer below the mixed layer are indicated by the k subscript. In the presence of an upward surface buoyancy flux B_m, the mixed layer properties are transformed into so-called Gaspar layer properties as shown in the middle panel, and denoted by subscript g. This is an *intermediate state* of the system in that the buoyancy fluxes are applied only over the initial mixed layer thickness, i.e., $h_g = h_1$. This intermediate state includes the possibility that the mixed layer waters have become convectively unstable with respect to the isopycnic layer waters below. The rightmost panel shows the *final state* after entrainment has occurred with the new, deepened mixed layer overlying the partially depleted isopycnic layer. The final mixed layer properties are denoted with m subscripts and the final isopycnic layer properties by prime superscripts.

$$g\mathrm{PE} = \int_{p_1}^{p_m} (M - \alpha p)\, dp. \tag{4.1}$$

As the water column in an isopycnic model is layerwise discretized, the vertical integral transforms into a summation. In the initial, unmixed state this summation gives

$$g\mathrm{PE} = \sum_{k=1}^{n-1} \left[M_k(p_{k+1} - p_k) - \frac{\alpha_k}{2}(p_{k+1}^2 - p_k^2) \right] + \left[M_n(p_m - p_n) - \frac{\alpha_n}{2}(p_m^2 - p_n^2) \right]. \tag{4.2}$$

In the final, mixed state there remains only one layer, having a density α_m equal to the depth-weighted average of all the layers that have been mixed together:

$$\alpha_m(p_m - p_1) = \sum_{k=1}^{n-1} [\alpha_k(p_{k+1} - p_k)] + [\alpha_n(p_m - p_n)]. \tag{4.3}$$

Note that this expression is actually a statement of volume conservation, which only holds for the case of a linear equation of state. However, the small error we make through the use of this approximation in the diagnosis of the entrainment depth is of little concern, given the uncertainties associated with the parameterizations of TKE production and dissipation we have used. Assuming that volume is conserved during mixed layer entrainment also means that the surface elevation remains unchanged, and this allows us to evaluate the Montgomery potential M_m of the final mixed layer as follows:

$$M_m - \alpha_m p_1 = M_1 - \alpha_1 p_1. \tag{4.4}$$

The PE per unit area of the final mixed layer is simply

$$g\mathrm{PE}_m = M_m(p_m - p_1) - \frac{\alpha_m}{2}(p_m^2 - p_1^2), \tag{4.5}$$

and substituting from (4.3) and (4.4) above, this can be written

$$g\mathrm{PE}_m = (p_m - p_1)\left\{ M_1 - \alpha_1 p_1 - \sum_{k=1}^{n-1} \left[\frac{\alpha_k}{2}(p_{k+1} - p_k) \right] - \frac{\alpha_n}{2}(p_m - p_n) \right\}. \tag{4.6}$$

Subtracting the expression for the potential energy of the initial state from this and equating the difference to the TKE supplied by surface stress and buoyancy extraction,

$$g(\mathrm{PE}_m - \mathrm{PE}) = g\mathrm{TKE}, \tag{4.7}$$

leads us to an expression for the pressure at the base of the mixed layer following entrainment:

$$p_m = \frac{g\mathrm{TKE} + p_1(M_1 - \alpha_1 p_1 - F_k) + G_k - p_n\left[M_n - \frac{\alpha_n}{2}(p_1 + p_n)\right]}{(M_1 - \alpha_1 p_1 - F_k) - \left[M_n - \frac{\alpha_n}{2}(p_1 + p_n)\right]}, \tag{4.8}$$

where, for convenience, we have introduced the layerwise functions analogous to those of Bleck et al. (1989):

$$F_k = \sum_{k=1}^{n-1} \frac{\alpha_k}{2}(p_{k+1} - p_k) \quad \text{and} \tag{4.9}$$

$$G_k = \sum_{k=1}^{n-1} \left[M_k(p_{k+1} - p_k) - \frac{\alpha_k}{2}(p_{k+1}^2 - p_k^2)\right]. \tag{4.10}$$

The solution procedure for finding p_m follows exactly that of Bleck et al. (1989). Trial values are found successively for each layer $k = 2 \ldots N$ beneath the mixed layer, and the process is continued as long as the trial value is greater than the pressure at the upper surface of layer k, or the seafloor is reached. The correct value of p_m is the last one that meets this criterion, and once it has been found, updating of layer thicknesses and properties completes the algorithm.

b. Convection

In the MICOM code a separate algorithm deals with the case where buoyancy extraction renders the mixed layer statically unstable with respect to the isopycnic layers beneath. It is assumed that the timescale for convection is small compared to the model time step and thus static instability is removed by an instantaneous rearrangement of the appropriate model layers. Interior layers are incorporated successively into the mixed layer until the density profile is once again statically stable. The process is essentially one of mixed layer entrainment, but since the depth of convective mixing is diagnosed in a manner that is incompatible with the theory outlined in the preceding section, it must be dealt with in a separate routine.

We decided to exploit the similarity between the processes of entrainment and convection and so deal with them both using a single algorithm. In the case of unstable stratification, deepening of the mixed layer lowers the PE of the water column, and the (negative) change in PE between mixed and unmixed states can be found in the manner outlined in the preceding section. The depth of the mixed layer following convection can also be found through the procedure outlined above. In the absence of any TKE supply, the new state will be one with the same PE as the initial state; that is, all the available PE associated with the unstable stratification will have been used for entrainment. With a supply of TKE from surface processes, the mixed layer will deepen further, with the (positive) change in PE between initial and final states equaling the TKE supplied over one time step, as before.

While this procedure is computationally efficient, it suffers one potential disadvantage, in that none of the available PE associated with the unstable water column is dissipated, rather it all contributes to deepening of the mixed layer. However, in a coarse-resolution, hydrostatic model any parameterization of convection is subject to considerable uncertainty. Given that the ultimate aim of a convection routine in such a model is to avoid a situation that cannot be handled by the reduced physics through a somewhat arbitrary reorganization of the vertical structure, there is possibly some advantage in ensuring that this procedure does not represent a sink of energy.

c. Detrainment

In order to maintain the integrity of an isopycnic coordinate system while allowing mass to flux between layers one must ensure that the density of waters received by an isopycnic layer matches its prescribed density. The situation of mixed layer entrainment, discussed in the previous sections, is not of concern in this sense because the mixed layer is nonisopycnic and therefore can receive water of any density. The reverse situation, that is of mixed layer detrainment, is problematic because the density of the waters that are to be detrained into a particular isopycnic layer will not in general match the prescribed density of that layer.

A retreat of the mixed layer occurs whenever the TKE generated by surface stresses is insufficient to maintain the current mixed layer depth in the presence of an input of buoyancy at the surface. In this case the TKE balance of Eq. (2.13) would yield a negative entrainment rate, but since the equation is only valid for zero or positive entrainment, it is used instead to diagnose a new equilibrium depth for the mixed layer. This is the depth for which the supply of TKE is exactly balanced by buoyancy and frictional dissipation, and the entrainment rate is therefore zero. As the mixed layer shoals to this depth and attains a lighter density it leaves beneath it a slab of water of arbitrary density, which we shall refer to as the fossil layer. A schematic of the relationship between the various densities and combinations of surface buoyancy fluxes for a detrainment scenario is presented in Fig. 3.

A variety of solutions to the problem of how to adjoin

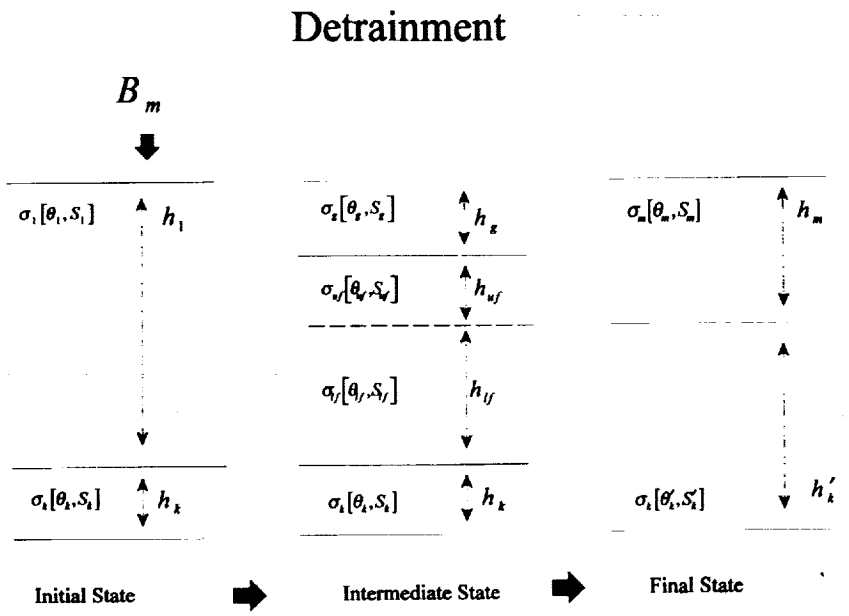

FIG. 3. Schematic of the detrainment of mixed-layer waters into an isopycnic layer as forced by a downward-directed surface buoyancy flux (i.e., buoyancy gain). The leftmost panel shows the initial state of the system with the mixed-layer density, temperature, salinity, and thickness denoted σ_1, θ_1, S_1, and h_1, respectively. The complementary properties of the isopycnic layer below the mixed layer are indicated by the k subscript. The presence of a downward surface buoyancy flux B_m that is strong enough to suppress the TKE supplied by surface stress u_*^3 leads to the creation of a shallow, intermediate state layer referred to as the Gaspar layer over whose depth scale (i.e., the Monin–Obukov length) are distributed the downward surface buoyancy fluxes, i.e., $h_g < h_1$. The relatively shallow Gaspar layer properties are indicated in the middle panel by the subscript g. The difference between the shallow, intermediate state Gaspar layer and the deep, initial state mixed layer leads to the existence of a fossil layer in the intermediate state. This fossil layer is split into two sublayers: the upper fossil layer denoted with subscript *uf*, and a lower fossil layer of subscript *lf*. The final state of the system is shown in the rightmost panel in which the upper fossil layer adjoins with the Gaspar layer to produce the final mixed layer; the lower fossil layer adjoins with the isopycnic layer to produce the final state of the isopycnic layer. The final mixed layer properties are denoted with m subscripts and the final isopycnic layer properties by prime superscripts.

the fossil layer waters to those of the isopycnic interior layers have been proposed, each with its own distinct advantages and disadvantages. One approach is to place all of the fossil water of arbitrary density into the isopycnic layer that most closely matches it in density (Oberhuber 1993). This has the advantage that the mixed layer is fully detrained and has temperature and salinity properties that are in accord with the buoyancy forcing supplied. It has the disadvantage of causing a coordinate drift within the isopycnic layers as they are now receiving water masses that do not exactly match their prescribed densities. Another approach is to introduce a buffer layer sandwiched between the mixed layer and the isopycnic interior, which can hold the fossil layer waters after a detrainment event (Murtugudde et al. 1995) thus preventing coordinate drift of the interior layers. This approach has the disadvantage of curtailing the ventilation of the isopycnic ocean interior while the fossil waters are held in the buffer layer. A third approach is to split the fossil layer into a denser lower part, having a density precisely matching that of an isopycnic interior layer, and a complementary lighter upper part, which rejoins the mixed layer (Bleck et al. 1992). This procedure has the advantage of ventilating the isopycnic interior layers with waters of the correct density, but the disadvantage of having to artificially split the heat and salt content of the fossil layer. While all of these approaches have limitations, these are manifestations of numerical truncation errors, which all diminish in importance as the model resolution is improved.

For our ice shelf–ocean modeling problem, the simplest approach was to follow the MICOM procedure of splitting the fossil layer, but we found that some modification of the algorithm was still necessary. That used in the original MICOM code (Bleck et al. 1992; Sun 1997) has some shortcomings in that under certain conditions of surface forcing it can either create an artificial temperature extremum or prevent detrainment proceeding at all. The problem arises because there are an infinite number of ways in which the fossil layer can be unmixed, and selecting the most appropriate split for

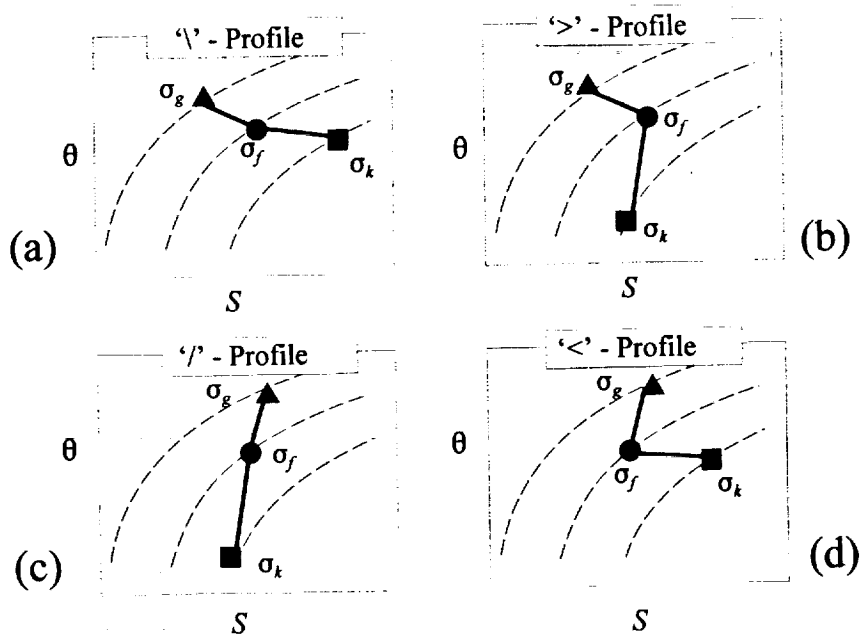

FIG. 4. Temperature–salinity diagram under various scenarios of surface buoyancy-forced mixed-layer detrainment. The density of the Gaspar layer is denoted σ_g and marked by the triangle symbol, that of the fossil layer is denoted σ_f and marked by the circle, and that of the isopycnic layer is denoted σ_k and marked by the square. Depending on whether heating or freshening dominates the surface buoyancy forcing, and whether the isopycnic layer is saltier of fresher than the fossil layer, gives rise to four possible density profiles. These are labeled as the "\," ">," "/," and "<" profiles as suggested by the shape of their vertical structure and are presented in (a), (b), (c), and (d), respectively.

any situation is not straightforward. While the procedures used in MICOM seem to work very well in the warm water sphere, for which they were originally designed, in our high-latitude polar domains their performance appears to degrade.

If there were an infinite number of isopycnic layers, the detrainment algorithm would be straightforward. We would first diagnose the new thickness of the mixed layer from (2.13), then calculate its new temperature and salinity by applying the surface fluxes to this new layer over one time step. The fossil layer would be subducted directly into the interior, having properties identical to those of the mixed layer prior to receiving buoyancy input. Our detrainment algorithm mimics this behavior as closely as possible, given the finite number of isopycnic layers.

1) MICOM ALGORITHM

The original MICOM algorithm for detraining the fossil layer waters into an isopycnic layer involved solely a temperature-based split of the fossil layer into an upper, warmer layer and a cooler, lower layer (Bleck et al. 1992). The salinity of the upper and lower fossil layers was not split but kept the same as the original fossil layer. The upper fossil layer temperature was assigned precisely that of the Gaspar layer. Using these constraints, coupled with an equation of state, and demanding that the lower fossil layer density exactly match that of the isopycnic layer into which the lower fossil layer waters are received, leads to a polynomial equation in one unknown, the thickness of the lower fossil layer.

It was later recognized that splitting the fossil layer solely on temperature was problematic for polar oceans where the density is largely controlled by salinity variations and not temperature. Accordingly, the splitting of the fossil layer was adapted to involve splitting on both temperature and salinity (Sun 1997). In the instance of a density profile of shape as in Fig. 4a, the approach was to assign the lower fossil layer the temperature and salinity properties of the isopycnic layer. The upper fossil layer temperature was still assigned the Gaspar value as in the earlier algorithm while the upper layer salinity was now an unknown to be determined. As before, the thickness of the lower fossil layer was solved via a polynomial equation, which once obtained diagnostically led to knowing the salinity of the upper fossil layer.

In the situation that the diagnosed upper fossil layer salinity is less than the Gaspar or greater than the original fossil, as would occur in the situations depicted in Figs. 4b–d, then the upper fossil layer salinity is reassigned to whichever of these constraining values it lies closer to. A new determination of the lower fossil layer

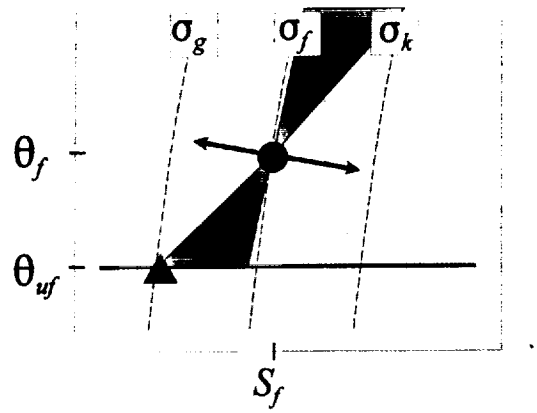

FIG. 5. Schematic based on a temperature–salinity diagram illustrating behavior of present MICOM detrainment scheme for conditions usual to the ice shelf–ocean interaction problem. The thin dashed lines represent the isopycnals of the Gaspar layer σ_g, the fossil layer σ_f, and the isopycnic layer σ_k (which is the recipient of the detrained water). The triangle represents the Gaspar layer, which has properties of θ_g and S_g. The circle positioned with temperature θ_f and salinity S_f represent the fossil layer properties. A built-in constraint of the present MICOM algorithm is that the upper fossil layer temperature is exactly that of the Gaspar layer. The thick, solid horizontal line of fixed temperature θ_{uf} describes this constraint. Since the unmixing of the fossil layer must occur along a straight line, the only possible detrainment lines must lie within the conic structure indicated by the shading. This implies the possibility of creating extremely warm temperature in the lower fossil layer or alternatively not detraining at all, neither behavior being desirable.

thickness is carried out, but with the lower fossil layer temperature and salinity values no longer constrained to be exactly the same as that of the isopycnic layer. While the temperature and salinity of the lower fossil layer now differ from the isopycnic layer, the density of the lower fossil is still constrained to be that of the isopycnic layer. With these new constraints in place, the thickness of the lower fossil layer is once more solved for and the present MICOM algorithm terminates.

In applying this algorithm to the problem of ice shelf–ocean interaction, situations were found where the above algorithm failed to detrain sufficient waters and the waters that were detrained were found to be unacceptably warmed. As the mixed layer in the sub–ice shelf cavity does not undergo a seasonal cycle, which would cycle the waters everywhere in the cavity through an entrainment and detrainment phase, regions of persistent detrainment can lead to the creation of unrealistically warm water masses. Consider for instance, the scenario of detrainment in a polar ocean illustrated in Fig. 5. The fact that the present MICOM algorithm makes the temperature of the upper fossil layer match that of the Gaspar layer results in an excessively warm temperature for the lower fossil layer. A more natural split of the fossil layer would be along the direction "orthogonal" to the isopycnals as suggested in Fig. 5.

Such a split avoids the generation of extreme temperatures but can only be achieved by giving up the constraint that the upper fossil layer temperature must match that of the Gaspar layer. Imposing such a constraint is reasonable in a tropical ocean where density is dominated by temperature. In a polar ocean, where density is dominated by salinity, a more reasonable constraint is that the upper fossil layer adhere to the salinity of the Gaspar layer and not its temperature. What is needed then is a flexible constraint on the upper fossil layer such that it adheres to the Gaspar temperature in tropical oceans but to the Gaspar salinity in polar oceans with a smooth transition between the two in temperate oceans. Such a flexible constraint is possible by introducing the concept of an orthogonal density split of the fossil layer.

2) MODIFIED ALGORITHM

The main difficulty encountered with the present MICOM algorithm stems form the fact that it treats temperature on a special footing as compared to salinity. We argue that it may be better to base a detrainment algorithm on density, with temperature and salinity each proportionally contributing to the algorithm based on their respective thermal expansion and haline contraction coefficients as relevant weighting.

We remove the above constraint that the upper fossil layer be assigned the Gaspar layer temperature. Instead, we argue that the upper and lower fossil layers can each take on arbitrary temperature and salinity values, provided they are constrained by the overall minimum and maximum temperature and salinities present. These extrema come from the properties of the isopycnic layer, the fossil layer (which has the properties of the old mixed layer), and the Gaspar layer. The present MICOM scheme does not "bound" the upper fossil layer by the new Gaspar temperature, but rather sets it equal to it. We argue that the incoming buoyancy fluxes (both of heat and salt) are distributed over the shallower Gaspar layer and not the deeper, initial mixed layer. In this manner the fossil layer retains the initial mixed layer properties while the Gaspar layer has its temperature and salinity set by the incoming heat and salinity fluxes being distributed over the shorter Monin–Obukov length rather than the initial mixed layer depth. The new mixed layer temperature and salinity achieved are then used in defining the properties of the upper fossil layer.

Removing the constraint that the upper fossil temperature must coincide with that of the Gaspar layer reintroduces an extra degree of freedom into the algorithm with the result being that there are an infinite set of choices for splitting the upper and lower fossil layers. We decide then to adhere to two guiding constraints: (i) the upper and lower fossil temperatures and salinities do not go outside the temperature and salinity extremum that we establish, and (ii) the lower fossil temperature and salinity produce a lower fossil density that exactly matches that of the isopycnic layer. While these constraints are superficially similar to that of the present MICOM algorithm, the main difference lies in the

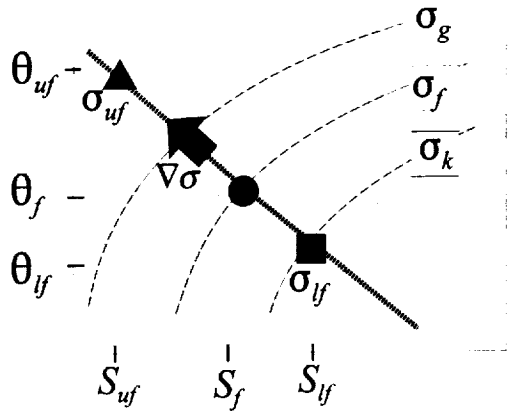

FIG. 6. A schematic of the orthogonal density splitting of the fossil layer illustrated on a temperature–salinity diagram. The thin dashed lines are reference isopycnals showing the density of the Gaspar layer σ_g, the fossil layer σ_f, and the isopycnic layer σ_k. The thick dotted line is aligned with the direction of the gradient vector (shown as the thick, short arrow) of the density contours and passes through the temperature–salinity point of the fossil layer, denoted by the circle symbol. The waters of the fossil layer are ultimately split into an upper fossil layer, denoted by the triangle, which adjoins the Gaspar layer to form the final mixed layer, and a lower fossil layer, denoted by the square, which adjoins the isopycnic layer to form the final isopycnic layer. The determination of the exact orientation of the normal vector and the amount of fossil water going into each of the upper and lower fossil layers is discussed in the text.

choice of the temperature extremum. The MICOM algorithm set the upper fossil temperature to that of the Gaspar layer and places no constraint on the lower fossil temperature. Our approach is different in that we do not impose the upper fossil temperature, rather we solve for the upper and lower fossil temperatures subject to the constraint that no new temperature extremum are created.

3) LOWER FOSSIL PROPERTIES

The new constraint we introduce to replace the present MICOM constraint of assigning the upper fossil layer temperature is to stipulate that the fossil layer is split based on an orthogonal density criterion. This constraint says that the unmixing line for temperature and salinity in the fossil layer occurs along a line that is orthogonal to the isopycnal of the fossil layer (see Fig. 6). Such an orthogonal split has the advantageous property of giving greater weight to the temperature field in tropical oceans while in polar oceans the salinity field controls the splitting of the fossil layer.

To define the direction of such an unmixing line we consider the isopycnals of the temperature–salinity diagram as contours of a scalar field σ. For the few remaining derivations in this section we treat both temperature and salinity as being dimensionless, and we do this so that we can compute a "gradient" in temperature–salinity space with temperature and salinity treated as the independent variables of the density function. Taking the gradient and normalizing by density ρ we arrive at the expression

$$\frac{\nabla\sigma}{\rho} = \beta\hat{\mathbf{i}} - \alpha\hat{\mathbf{j}}, \tag{4.11}$$

where the $\hat{\mathbf{i}}$ and $\hat{\mathbf{j}}$ unit vectors are aligned with the salinity and temperature axes, respectively. In the above equation we have made use of the conventional definitions of the thermal expansion and haline contraction coefficients of seawater (albeit dimensionless for present purposes):

$$\alpha = -\frac{1}{\rho}\frac{\partial\sigma}{\partial\theta} \qquad \beta = \frac{1}{\rho}\frac{\partial\sigma}{\partial S}. \tag{4.12}$$

Given that we know the density of the fossil layer (which is just that of the initial mixed layer), the temperature and salinity of the fossil layer (which is just the temperature and salinity of the initial mixed layer), and the density of the isopycnic layer below, we can determine the orthogonal temperature and salinity of the lower fossil layer so that the layer achieves the same density as the isopycnic layer below as

$$(\theta_{lf}, S_{lf}) = \frac{1}{\rho}\frac{\sigma_k - \sigma_f}{\alpha^2 + \beta^2}(-\alpha, \beta) + (\theta_f, S_f). \tag{4.13}$$

The fossil layer, prior to splitting into upper and lower fossil layers, has a thickness h_f that is the difference between the initial mixed layer thickness and the shallower Gaspar layer thickness:

$$h_f = h_1 - h_g. \tag{4.14}$$

The temperature and salinity of the fossil layer prior to its split is the initial mixed layer temperature θ_1 and salinity S_1. There are six unknowns to be determined in the problem of splitting the fossil layer into an upper and lower fossil layer, namely the temperature, salinity, and thickness of the upper and lower fossil layers. The orthogonal split has set the temperature and salinity of the lower fossil layer reducing the unknowns to four. The conservation of mass for the splitting of the fossil layer sets the lower fossil thickness:

$$h_{lf} = h_f - h_{uf}. \tag{4.15}$$

This leaves us with three unknowns, namely, the temperature, salinity, and thickness of the upper fossil layer.

4) UPPER FOSSIL PROPERTIES

Two constraints we invoke for the fossil layer are that of overall heat and salt conservation:

$$h_f\theta_f = h_{lf}\theta_{lf} + h_{uf}\theta_{uf} \qquad h_fS_f = h_{lf}S_{lf} + h_{uf}S_{uf}, \tag{4.16}$$

which in effect determines the upper fossil layer temperature and salinity. This situation now leaves us but one unconstrained variable, the thickness of the upper fossil layer. To address this last unknown we look at the properties of the final mixed layer, which results

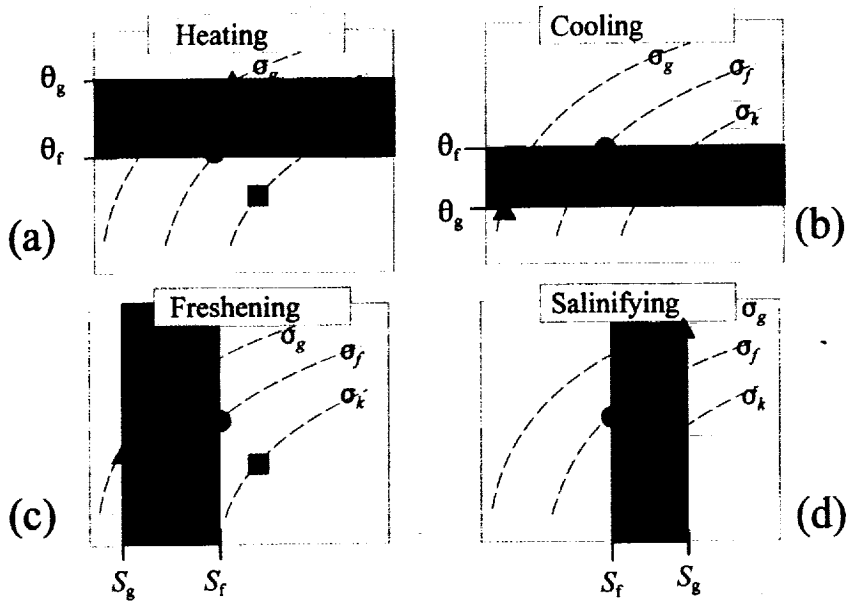

FIG. 7. Bounded constraints on the final mixed layer temperature and salinity under various scenarios of heating/cooling and/or freshening/salinifying. In all panels the Gaspar layer properties are indicated by the triangle, the fossil layer properties by the circle, and the isopycnic density properties by the square. Under (a) surface heating the Gaspar temperature provides the upper bound on the final mixed layer temperature, while under (b) cooling the fossil layer temperature provides the upper bound. (c) Under conditions of surface freshening the Gaspar layer salinity provides the lower bound on salinity, while (d) under salinifying conditions, the fossil layer provides the lower bound on salinity.

when we adjoin the Gaspar layer with the upper fossil layer. Invoking heat and salt conservation for this mixing process produces the constraints

$$h_m\theta_m = h_g\theta_g + h_{uf}\theta_{uf} \qquad h_mS_m = h_gS_g + h_{uf}S_{uf}, \quad (4.17)$$

where from mass conservation the thickness of the new mixed layer is simply

$$h_m = h_g + h_{uf}. \quad (4.18)$$

It appears that we have gained little as we have added two more equations with two more unknowns, namely, the final temperature θ_m and salinity S_m of the final mixed layer. As we shall see, however, we can in fact ultimately combine these equations to solve for the thickness of the upper fossil layer. This amounts to making decisions about the final values that the mixed layer temperature θ_m and salinity S_m will achieve under various scenarios of either net heat gain or loss and similarly for freshwater gain or loss with the objective of maximizing the amount of detrainment. Specifying both the new mixed layer temperature and salinity now puts us in the situation of having one too many equations in relation to the number of unknowns. This situation means that we will obtain two physically valid solutions for the upper fossil layer thickness and we will take the thicker of these as that will represent the most constrained or conservative solution. We now show these two solutions.

Combining the heat conservation equation (4.16) for the fossil mixed layer with the heat conservation equation (4.17) for the final mixed layer leads to an expression for the thickness of the upper fossil layer:

$$h_{uf} = \frac{h_f(\theta_f - \theta_{lf}) + h_g(\theta_g - \theta_m)}{(\theta_m - \theta_{lf})}. \quad (4.19)$$

Similarly, combining the salt conservation equations we obtain

$$h_{uf} = \frac{h_f(S_f - S_{lf}) + h_g(S_g - S_m)}{(S_m - S_{lf})}. \quad (4.20)$$

We cannot evaluate these expressions until we come to a decision as to the final mixed layer temperature and salinity. Our objective is to make the upper fossil layer as thin as possible so as to detrain as much water into the isopycnic layer via the lower fossil layer as is possible, without violating the constraints we impose. This objective will be met by maximizing the difference between the orthogonal temperature and salinity and the final mixed layer temperature and salinity, respectively, while adhering to the overall temperature and salinity constraints that ensure we do not create new temperature or salinity extrema. It turns out that this stipulation of maximum difference depends upon, for temperature, whether we are cooling the Gaspar layer or heating it. Analogously for salinity, we need to know whether the Gaspar layer is freshened or salinified. These situations, depicted in Fig. 7, give us a physical interpretation that

guides the assignment of the final mixed layer temperature and salinity. Briefly stated, if the Gaspar layer is heated, then the final mixed layer temperature will attempt to be the Gaspar layer temperature (Fig. 7a), while if the Gaspar layer is cooled, the final mixed layer temperature will be the warmer fossil layer temperature (Fig. 7b). Analogously for salinity, under conditions of freshwater input to the Gaspar layer via buoyancy forcing then the final mixed layer salinity will attempt to lower to that Gaspar value (Fig. 7c), and vice versa for salt input to the Gaspar layer the final mixed layer salinity will be the fresher fossil layer salinity (Fig. 7d). In this manner the maximum amount of detrainment, while not creating new temperature or salinity extremum, is achieved.

The four scenarios outlined above give four different physically meaningful solutions to the upper fossil layer thickness solutions (4.19) and (4.20). Under the case of heat input (Fig. 7a) at the ocean surface the upper layer fossil thickness is

$$h_{uf} = h_f \frac{\theta_f - \theta_{lf}}{\theta_g - \theta_{lf}}, \tag{4.21}$$

which is a well-behaved solution as we can formally guarantee the desired bounded property of $0 \leq h_{uf} \leq h_f$. Under the case of heat extraction (Fig. 7b) the solution is

$$h_{uf} = h_f - h_g \frac{\theta_f - \theta_g}{\theta_f - \theta_{lf}}, \tag{4.22}$$

which becomes a well-behaved solution as we restrict the permissible solutions to the desired range of $0 \leq h_{uf} \leq h_f$. Under the case of freshwater input (Fig. 7c) the solution is analogous to (4.21) with salinity substituted for temperature. Under the case of salt input (Fig. 7d) the solution is analogous to (4.22) again with salinity substituted for temperature.

Of the two temperature-based upper fossil layer thickness solutions (4.21) and (4.22), only one can be realized at any given instant in time as the Gaspar layer is either being heated or cooled but not both simultaneously. Similarly, only one salinity-based thickness solution is physically relevant at a given instant. This finally leaves us with one temperature-based upper fossil layer thickness estimate and one salinity-based one. Again, we choose the larger upper-fossil thickness as the one to represent the most constrained solution, whether guided by temperature or salinity extremum considerations. This then is the solution of the upper fossil layer thickness. All other dependent quantities of the upper and lower fossil layers are now determined and the algorithm is complete.

The advantage in this approach is clear in that we can always detrain while not altering the isopycnic density of our interior layers, and that we treat tropical water masses and polar water masses on an equal footing with a smooth transition between the two types because our split is on Gaspar density and not on Gaspar temperature.

d. Surface buoyancy fluxes

Because the base of the ice shelf is a thermodynamically active boundary, the waters directly in contact with it will be in a continual state of adjustment toward conditions of thermodynamic equilibrium. We use this fact to diagnose the surface heat and freshwater fluxes that are applied to the mixed layer beneath the ice shelf. The procedure is described in detail by Holland and Jenkins (1999). We use their three-equation formulation, which explicitly accounts for the differing diffusivities of heat and salt in the inner part of the ice–ocean boundary layer, the molecular sublayer. Heat conduction into the ice shelf is parameterized in a way that accounts approximately for both vertical diffusion and constant vertical advection within the ice. The melting and freezing that occur at the ice base are the physical processes responsible for this vertical advection.

Throughout the model domain, whenever we compute the response of the mixed layer to surface forcing, we always convert from potential to in situ temperature before undertaking the calculation. The altered in situ temperature is then converted back to potential temperature for use in all other model calculations, for example, pressure gradients or mixed layer entrainment/detrainment. This back and forth transformation between potential and in situ temperature, which is carried out in double-precision arithmetic, ensures the correct application of surface heat fluxes, regardless of the surface pressure, and does not result in any net drift in temperature.

e. Thermodynamic initialization

The waters throughout the cavity are first assigned properties through lateral extrapolation of values found at the ice front. If the assigned properties of the mixed layer are far removed from a condition of thermodynamic equilibrium with the ice, there will be an initial spike of high melting, which could potentially cause a numerical instability. Therefore, before taking the first model time step, we relax the temperature and salinity of the mixed layer beneath the ice shelf to a state of thermodynamic equilibrium.

We first calculate the in situ freezing point T_f based on the initial assigned temperature T_a and salinity S_a and the pressure at the ice shelf base p_1.

$$T_f = \lambda_1 S_a + \lambda_2 + \lambda_3 p_1, \tag{4.23}$$

where $\lambda_{1,\ldots,3}$ are empirical constants (Millero 1978). The adjustments we make mimic the effects of melting or freezing on the mixed layer properties, so the temperature and salinity are constrained to evolve along a straight line in *T/S* space (Gade 1979) given approximately by

$$\frac{dT}{dS} = \frac{L_f}{c_p S_a}, \tag{4.24}$$

where L_f is the latent heat of fusion and c_p is the specific heat capacity of seawater at constant pressure. The salinity of the mixed layer waters, once they have reached the freezing point, can then be expressed in terms of the initially assigned conditions:

$$S_f = S_a\left[1 - \frac{c_p}{L_f}(T_a - T_f)\right]. \tag{4.25}$$

As a final adjustment, the mixed layer temperature is recomputed with the salinity from (4.25) using (4.23). We emphasize again that the above expressions are all in terms of the in situ temperature, T, rather than the potential temperature, θ.

5. Interactions with topography

a. Layer discontinuity

As a result of the horizontal discretization, surface and bottom topography acquires a stepped structure within MICOM. This raises the possibility of a layer becoming discontinuous, if it is thinner than a particular topographic step is high. In our sub–ice shelf application, this is a particularly strong possibility, because both sea surface and seabed have topography. In particular, the vertical front of the ice shelf introduces a surface step of up to several hundred meters, making it likely that the mixed layer is one of the layers containing a discontinuity. A particular example of this was earlier illustrated in Fig. 1 in the case of the mixed layer.

1) ADVECTION

In principle, there is no difficulty in estimating the mass flow that should pass between grid points that are separated by a topographic discontinuity. The calculation of the Montgomery potential gradient is unaffected by such a discontinuity and will correctly drive flow in the direction that is energetically favorable, that is, dense layers will be forced down bottom slopes, light layers up surface slopes. However, this does not in itself ensure that mass and tracers can be advected across a discontinuity.

The cause of the difficulty arises from the fact that MICOM is discretized on an Arakawa C grid (Arakawa and Lamb 1977) in which the thickness and other scalar properties of layers are defined at grid points horizontally staggered with respect to the points at which the velocity components are defined. A similar problem would also arise if the discretization was performed on the Arakawa B grid. In order to compute the flux of mass or tracer, using (2.5) or (2.6), from one scalar point to a neighboring one, a layer thickness must be assigned to the velocity point that lies between the two neighboring scalar points. The manner in which this assignment is made in the original MICOM code and in our modified code is illustrated in Fig. 8.

Consider the specific example of a two-layer fluid overlying a continental shelf and adjacent deep ocean. The surface of the top layer has a pressure denoted p_1 and the bottom of the bottom layer has a pressure p_3 while the pressure along the mutual interface between the two layers is denoted p_2. We horizontally discretize this fluid environment by considering two "scalar" columns, labeled column a and c, with column a being representative of the shallow layer of fluid on the continental shelf and c representing the deep-ocean column. A scalar column here refers to a column that contains vertically coaligned scalar variables of the Arakawa C grid; a "vector" column refers to vertically coaligned velocity points. Vector columns occur halfway between neighboring scalar columns. In Fig. 8, halfway between the columns a and c we have such a vector column, labeled b. The assignment of layer thicknesses at the vector column requires that we establish the pressure p_2 at the position of the vector column. Referring to Fig. 8, we use X to mark where this pressure is assigned to occur for the original MICOM code and our modified code. In the original MICOM code, p_2 coincides exactly with p_3 at a vector column. The thickness of the bottom layer at the vector column is then zero; that is, the thickness is evaluated as $p_3 - p_2 = 0$. In the modified code, p_2 is assigned to occur higher up in the vector column b such that $p_3 - p_2 \neq 0$, and thus a nonzero thickness of the bottom layer at the vector column is prescribed.

To understand better how this problem can at all occur, it is first necessary to realize that the vector column b has a total column thickness defined by the difference of the deeper of the neighboring surface elevations at columns a and c and the shallower of the two seabed elevations at a and c. Given such a thickness of the vector column b there still remains a degree of freedom in assigning the thickness of the upper and lower layer within this vector column. It is that assignment that is the key difference between the original MICOM code and our modified code.

The algorithm used in the original MICOM code assigns zero layer thickness to the bottom layer at the vector column b. This is so because it uses the maximum "seafloor depth" to evaluate the layer thickness at vector points. Visually one can see this by inspecting the lower-left panel of Fig. 8 and noting that the original MICOM assigns the position of X, which represents the value of p_2 at vector column b, as the average height between p_2 at column a and the p_2 at column c. Mass flux in the bottom layer from column a to column c would then be forced to zero because the bottom layer has zero thickness at the vector column. This would lead to the entrapment of dense water on the continental shelf. In the ice shelf–ocean context, the upside-down version of this problem would occur and buoyant water would be trapped beneath the deeper parts of the ice shelf base with no possibility of floating upward to lower elevations.

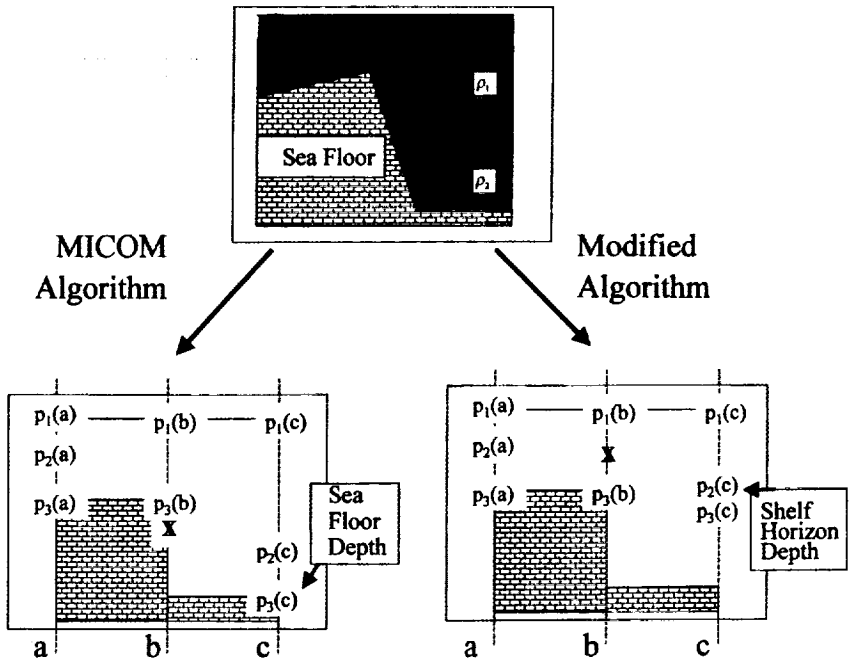

FIG. 8. Illustration of the problem of a dense lens of fluid over a continental shelf being artificially confined to rest on the shelf while in fact the dense plume should flow off the shelf into the deeper waters. The top, centered panel is intended to show a continuum representation of a situation of a two-layer fluid overlying a continental shelf and slope. In the present MICOM algorithm, shown in the leftmost lower panel, the discretization of this scenario leads to a situation whereby there is no "connection" between the fluid overlying the shelf and that in the deeper ocean; consequently there is no flow off the shelf. In the modified algorithm, shown in the rightmost lower panel, there is a connection between shelf and slope waters, and thus the dense lens of water on the shelf can flow off the shelf and into the deep. The key difference is that the modified algorithm uses the concept of a shelf horizon depth instead of a seafloor depth to compute the thickness of the layers at velocity points on the Arakawa C-grid stencil. See the text for further details including an explanation for the various symbols used in the figure.

We introduce the term shelf horizon depth to mean the shallower of the bottom elevation of the two columns a and c, which in this instance occurs at column a. We assign layer thicknesses at vector column b by using the shelf horizon depth concept to produce a nonzero thickness for the bottommost layer, in a physical situation where that is an appropriate assignment. This can be seen visually in the lower-right panel of Fig. 8 where the value of p_2 and p_3 in column c is not allowed to fall below the shelf horizon depth. Our algorithm works to assign the position of the X higher up in the vector column b than in the case of the original MICOM code. Our approach is, however, similar to the original MICOM scheme in that is also ensures that the sum of all the layer thicknesses does not exceed the total water column thickness at the vector column. The distinguishing feature is that any layer with nonzero thickness in either of the neighboring scalar columns a or c is now assigned a nonzero thickness at the vector column b. The result is that gravity currents flow freely both for the case of a dense plume descending a continental slope and that of a buoyant plume ascending the base of an ice shelf.

2) DIFFUSION

While advection is allowed to proceed across a layer discontinuity, diffusive fluxes are modified according to a horizontal "line-of-sight" criterion. If a given layer abuts other isopycnic layers, the diffusivities and viscosity are simply set to zero, whereas if it abuts a solid wall (either ice shelf or seabed), scalar diffusivities are set to zero, while the standard viscosity is used. In this latter case velocity boundary conditions are applied consistent with either free slip or no slip at the solid wall.

If a layer is not completely disjointed by topography, but a partial overlap exists between neighboring scalar grid points, normal diffusive exchange is permitted but fractionally weighted according to the proportion of the layer that is in contact with the solid wall. In this manner there is a smooth transition of the diffusive fluxes if the discontinuity in a layer should gradually appear or disappear.

b. Layer thickness diffusion

As the horizontal resolution of present-day ocean general circulation models is often inadequate to resolve

the detailed structure of baroclinic eddies, a parameterization of their impact is utilized. In the isopycnic framework this is layer thickness diffusion, and is represented by the term on the right-hand side of (2.5). This term acts to flatten our isopycnals, so as to make them coincide with geopotential surfaces, and mimics the way mesoscale eddies remove potential energy from the ocean interior. In the present MICOM code, the flattening of the isopycnals is prohibited once this process would force layer interfaces to go deeper than the bedrock. In the situation of an imposed surface topography, the algorithm is modified so as to also prevent isopycnals passing upward shallower than the base of the ice shelf.

6. Interfacial friction

The horizontal momentum equations (2.8) include a stress term $\tau_k^{\pm}$ that describes the vertical flux of horizontal momentum between neighboring layers. These viscous stresses can occur on the interface between any two adjacent layers or between a layer and an adjacent solid boundary. Such interfacial friction is commonly parameterized in ocean models using a quadratic drag law of the form

$$\tau_k^{\pm} = \rho_o c_d |\Delta \mathbf{v}_k^{\pm}| \Delta \mathbf{v}_k^{\pm}, \tag{6.1}$$

where c_d is a nondimensional and empirical drag coefficient, typically of order 10^{-3}. The velocity jump across the lower + and upper − interfaces bounding layer k are defined

$$\Delta \mathbf{v}_k^{+} = \mathbf{v}_{k+1} - \mathbf{v}_k \quad \text{and} \quad \Delta \mathbf{v}_k^{-} = \mathbf{v}_k - \mathbf{v}_{k-1}. \tag{6.2}$$

In MICOM currently only bottom friction is explicitly included. The velocity at the seabed is assumed to be zero, so the velocity jump appearing in the drag law (6.1) is simply the layer velocity. For simplicity, the drag law is linearized through the use of an effective drag coefficient c_d', based on the velocities from the previous time step, denoted by the "old" superscript:

$$c_d' = \rho_o c_d |\Delta \mathbf{v}_k^{+}|^{\text{old}}. \tag{6.3}$$

We note that this linearization renders the computation of interfacial stress susceptible to numerical instability under certain flow conditions, but we do not offer an alternative. The next step in the MICOM algorithm is to define a viscous thickness scale $(\Delta p)_v$, typically equivalent to 10 m of water, over which the frictional stresses are actually applied. Any fluid, of whatever density, found within this distance of the seafloor is subjected to drag. The viscous stress applied to each isopycnic layer is linearly weighted by the fraction of that layer residing within the bottom $(\Delta p)_v$ of the water column. Although the velocity vector of any layer that is subject to bottom drag will turn away from that of a purely geostrophic flow, the above formulation cannot provide a general parameterization of the bottom Ekman layer, (Ekman 1905), even if there is sufficient model resolution near the seabed.

With the addition of static sea surface topography, surface friction could be introduced in a manner analogous to that described above for bottom friction. The algorithm would be more straightforward, because the mixed layer, aside from being the only nonisopycnic layer, is distinct from the other layers in that it is the only one that has a minimum specified thickness (typically equivalent to 10 m of water). As a consequence, only the mixed layer would experience the surface stress generated at the ice shelf base. For the sake of completeness, we mention that in the open ocean, away from the ice shelf base, the mixed layer experiences a surface stress due to the presence of sea ice and the atmospheric winds.

Aside from surface and bottom stresses, we also wish to consider layer-to-layer interfacial stresses in the ocean interior that arise both from small-scale mixing processes and as a result of the breaking of the internal wave field. At the interface between any two adjacent layers we impose the quadratic drag law, but with a drag coefficient that is much reduced compared with that used for the seabed or surface friction. Our general formulation of the viscous stress is then Eq. (6.1) applied to every layer interface, but with the constant interface drag coefficient, c_d, replaced by a variable drag coefficient, c_d'':

$$c_d'' = c_d\{[e^{-|p_k - p_b|/(\Delta p)_v} + e^{-|p_k - p_b|/(\Delta p)_v}] + 0.001\}. \tag{6.4}$$

This formula has the desired effect of making the effective drag coefficient, c_d'', equal to the standard value, c_d, near the ocean bottom, $p = p_b$, and surface, $p = p_1$, and allowing it to decay gradually to a value two orders of magnitude smaller far away from the boundaries.

For an N-layer ocean model, there are N horizontal velocities. Our algorithm for the application of interfacial stresses is to simultaneously solve (6.1) for all the layer velocities. Applying the boundary conditions of zero velocity at the seabed and ice shelf base, we arrive at a system of N nonlinear equations. We linearize the drag law by adopting an effective drag coefficient based on velocities at the previous time step, in analogy with (6.3). As the net viscous stress acting on any given layer is a function of only the velocities of that layer and of the layers directly above and below it, we then arrive at a system of N linear equations in tridiagonal form. These are conveniently solved using a standard implicit technique, such as Gaussian elimination. It is also noted that this formulation is capable of producing an "Ekman spiral," given sufficient resolution within the physical boundary layer.

7. Model application

a. *Configuration*

We have applied the model to a 10° long × 10° lat × 1000-m-deep box with an idealized ice shelf floating

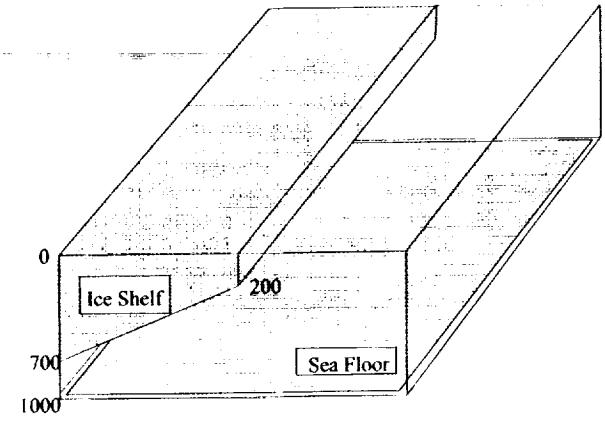

FIG. 9. Idealized box domain with a floating ice shelf in the southern half of the domain (north is to the right). The ice shelf front has a uniform thickness of 200 m while at the grounding line (i.e., where the ice shelf meets the bottom topography) the thickness extends to 700 m. There is a uniform slope between the ice shelf front and the grounding line. The model domain extends south–north over 10° of latitude, or equivalently, about 1000 km; the domain extends west–east over 10° of longitude, or equivalently, about 250 km. The maximum depth of 1000 m of the water column occurs in the open-ocean part of the domain; the minimum depth of 300 m occurs beneath the ice shelf along the grounding line.

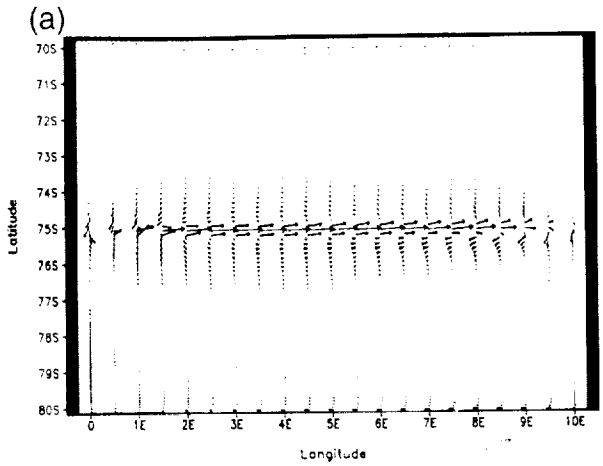

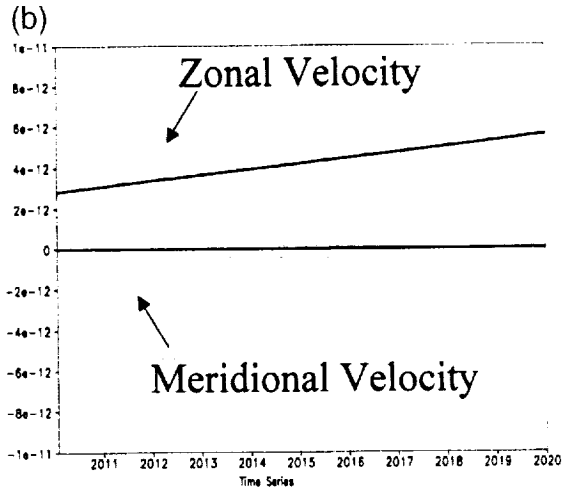

FIG. 10. Homogeneous ocean with no ice shelf base thermodynamical forcing. (a) Depth-averaged flow velocities (cm s^{-1}) at the end of the 20-yr model simulation. The position of the ice shelf front is at 75°S. (b) Time series over the last 10 yr of the model integration of the domain integrated zonal and meridional depth-averaged flows.

in the southern half of the domain (see Fig. 9). The central latitude, which coincides with the ice shelf front, is 75°S, so the horizontal dimensions of the domain are approximately 250 km in width east–west by 1000 km in length north–south. In thickness, the ice shelf itself is wedge shaped with the thickness increasing linearly from 200 m at the front to 700 m at the southern boundary of the domain and being zonally constant. The grid is isotropic with the grid cells having dimensions equivalent to 0.5° of longitude. This gives a horizontal resolution that ranges from approximately 10 km in the southern part of the domain and nearly 20 km in the northern. We divide the water column north of the ice shelf front into 11 layers (10 isopycnic layers plus the mixed layer) of equal thickness and extend the layer interfaces horizontally below the ice shelf. The potential temperature in all the layers is initially −1.8°C, while the salinity increases in equal steps from 34.4 psu in the open ocean mixed layer to 34.8 psu in the bottom layer. Beneath the ice shelf the mixed layer first takes on the properties of the isopycnic layer it displaces, and is subsequently relaxed to the freezing point, as described in section 4e. Restoring conditions are used for the temperature and salinity along the northern wall so as to allow the model to evolve toward a steady state. Without such restoring, the only thermodynamic forcing would be that occurring at the ice shelf base and this in itself would lead to a gradual cooling of all of the waters in the domain.

b. Initial tests

The model setup described above, but with no thermodynamic initialization of the sub–ice shelf mixed layer or any subsequent thermodynamic interaction between ice and ocean, has an exact solution of zero motion for all time. Given that we know of no analytical solutions for buoyancy-driven circulation within a cavity, reproduction of such a motionless state provides us with our one chance of verifying at least some of our model code against a known solution. We show here the results of two such tests, one in which the ocean was completely uniform, with a salinity of 34.8 psu in all layers, and one in which the ocean was stratified in the manner described above.

Depth-averaged velocities at the end of a 20-yr simulation of the homogeneous ocean are shown in Fig. 10a. Peak values of the order 10^{-8} cm s^{-1} occur along the first row of grid points below the ice shelf, while the domain average is four orders of magnitude smaller (Fig. 10b). There is a linear growth in the magnitude

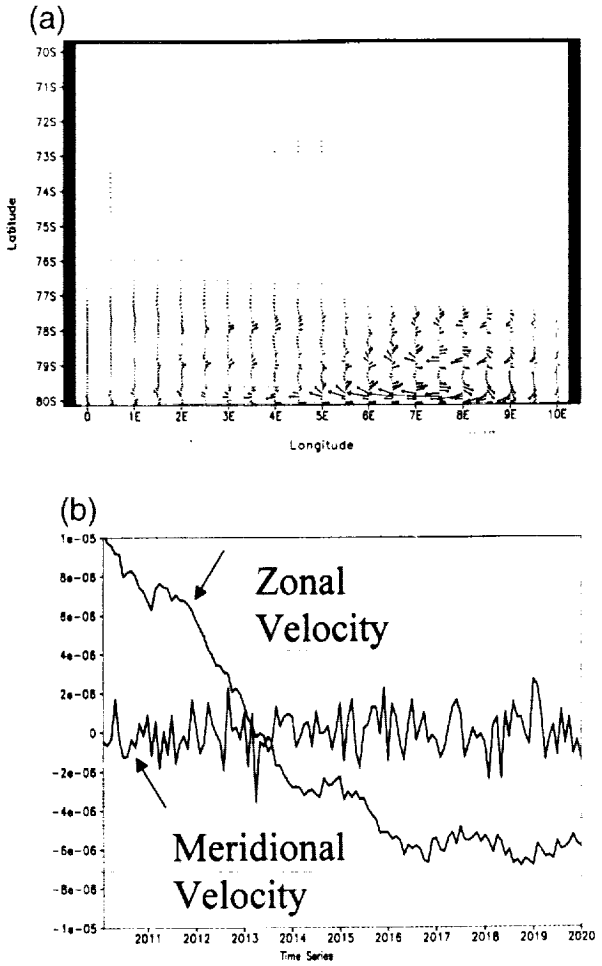

FIG. 11. Stratified ocean with no ice shelf base thermodynamical forcing. (a) Depth-averaged flow velocities (cm s^{-1}) at the end of the 20-yr model simulation. (b) Time series over the last 10 y of the model integration of the domain-integrated zonal and meridional depth-averaged flows.

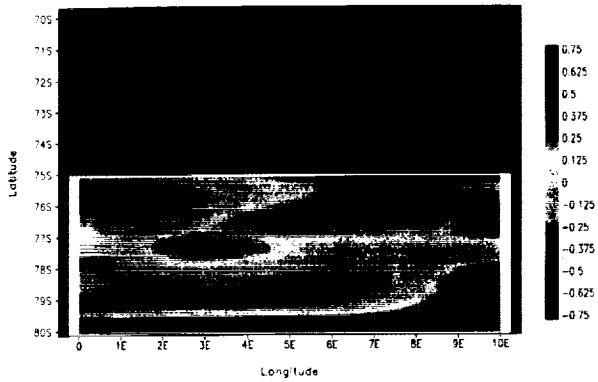

FIG. 12. Plan view of ice shelf basal melt rate (cm yr^{-1}). The northern half of the domain represents the open ocean and the southern half the ice shelf base. The red-shaded areas represent melting zones and the blue represent freezing zones. It is in the later where marine ice accumulates at the ice shelf base. The mean melt rate is 0.5 cm yr^{-1}.

of the zonal component with time, but for any conceivable integration time this noise will remain inconsequential.

Analogous results for the stratified case are shown in Figs. 11a and 11b. In this case peak velocities of the order 1 mm s^{-1} occur along three bands in the most southerly part of the cavity. Once again domain-averaged values are four orders of magnitude smaller. While there is no growth in magnitude over the final 10 yr of the integration, and the general noise level is insignificant, the same cannot be said of the peak values. However, these velocities have a physical origin. They reflect the fact that within the mixed layer, isopycnic surfaces are no longer horizontal, but are effectively vertical. In our discretized space this manifests itself as a sharp density front in the mixed layer wherever its base intersects an isopycnic layer interface. Discretization also leads to steps in the surface topography, and where these cause discontinuities in the mixed layer the front can be preserved. The density gradient within the mixed layer then exactly balances the gradient in Montgomery potential, and the motion remains insignificant. As the horizontal grid resolution increases toward the south, the vertical steps in the topography become smaller. South of 77.2°S the surface steps are less than 10 m, so the mixed layer is continuous in this part of the domain, and the density fronts within it cannot be maintained against diffusion. The exact balance of forces is disrupted and zonal bands of motion develop at the points where isopycnic layer interfaces intersect the mixed layer.

The above results illustrate that genuine noise in the depth-averaged velocity fields is stable at the level of 10^{-5} cm s^{-1} or less. This gives us confidence that we have implemented the surface pressure field and associated model modifications in a manner that has not caused any spurious forcing on the ocean.

c. *Full model*

When the stratified domain is forced by the thermodynamic interaction between the mixed layer and the ice, a circulation pattern emerges that, after 20 yr, leads to net melting of 0.5 cm yr^{-1} averaged over the ice shelf base. There is spatial variability (Fig. 12) with melting, at peak rates of around 10 cm yr^{-1}, concentrated at the southern boundary and broad areas of more gentle melting and freezing to the north. The zone of freezing occupies the central and western portion of the ice shelf base with peak rates of around −0.5 cm yr^{-1} occurring in the northwestern corner. Overall, the thermodynamic interaction with the ice shelf supplies a surface freshwater flux of 22 m^3 s^{-1}, and the resulting thermohaline circulation drives a transport of 0.06 Sv into and out of the sub–ice shelf cavity. The circulation beneath the ice shelf is cyclonic, with inflow concentrated in the east

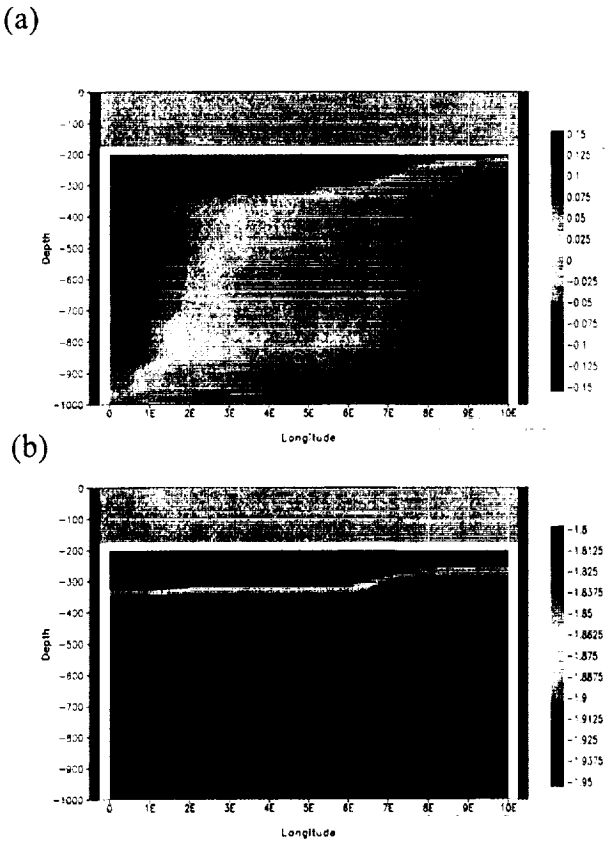

FIG. 13. East–west vertical transects across the ice shelf front. The view is from within the ice shelf cavity and looking northward. (a) The meridional velocity (cm s^{-1}) shows northward flow as red shading in the upper left while the lower right shows southward flow as blue shading. (b) The potential temperature °C showing the presence of supercooled ISW as blue shading near the base of the ice shelf and somewhat concentrated to the western side of the front. The deeper waters continue to hold their initially assigned temperatures of −1.8°C and are shown as red shading.

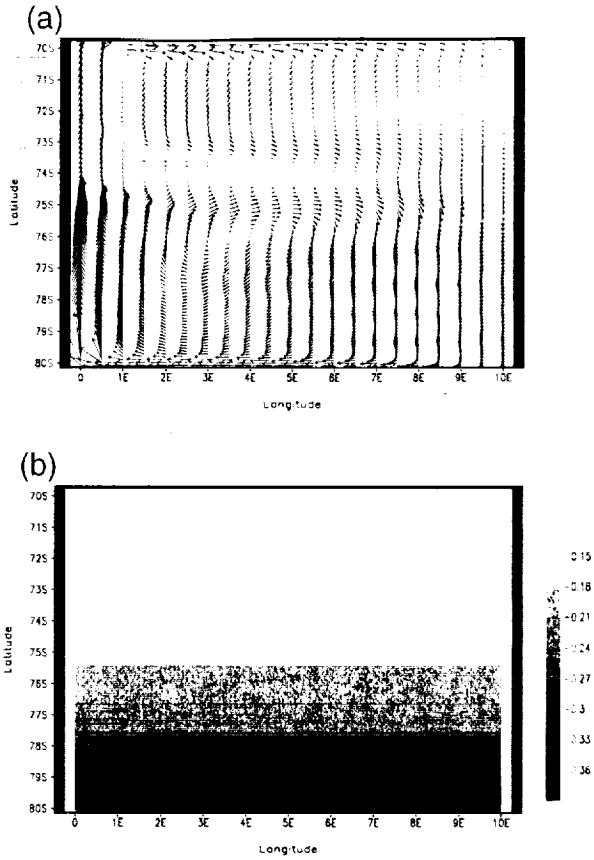

FIG. 14. Barotropic characteristics of the domain and the flow field at the end of the 20-yr model simulation. (a) The depth-averaged velocity field (cm s^{-1}) for the stratified ocean with active thermodynamical forcing at the ice shelf base. (b) The contours of background "barotropic" potential vorticity [1/(ms) × 10^{-7}] emphasize the influence exerted by the ice shelf basal topography.

and outflow in the west. A vertical section of meridional velocity across the ice front (Fig. 13a) shows a level of zero motion sloping down from east to west, consistent with a picture of deep inflow, upwelling within the cavity and outflow along the ice shelf base. Peak velocities reach only a few millimeters per second. Near the ice shelf base the outflowing water has a temperature of around −2°C (Fig. 13b) and is, thus, classed as ISW. Deeper in the water column, much of the outflow has been unaffected by the ice shelf and has retained its initial temperature.

The cyclonic gyre beneath the ice shelf shows up in the depth-mean flow (Fig. 14a). Viewed in this way, the gyre is intensified to the west and is centered just south of the ice shelf front. Although much of the depth-mean flow appears to be steered along the ice front, the step change in water column thickness does not form a complete barrier to the circulation (Fig. 14b). There are broad regions at the east and west where the velocity vectors have a significant component across the ice shelf front. This is not surprising considering that the only forcing on the circulation is the tilting of isopycnic surfaces by the freshwater flux at the ice shelf base. The forcing on an individual model layer is largely independent of that on the other layers, and a nonzero depth-mean flow emerges only because of the influence of friction and the presence of the surface topography itself. This point is well illustrated by the flow of the mixed layer (Fig. 15a), which shows no hint of the gyre, but instead illustrates behavior we would associate with a buoyant plume ascending the ice shelf base. Because the mixed layer remains thin over much of the cavity (Fig. 15b), the dominant balance of forces is between buoyancy and friction, and deflection by the Coriolis acceleration is relatively minor. The mixed layer flow is largely sustained by the entrainment of fluid along the southern boundary, where there is strong horizontal divergence, and the same occurs to a lesser extent along the eastern boundary. This pattern of entrainment gives rise to the regions of strong melting described above. As the waters of the mixed layer ascend the ice shelf

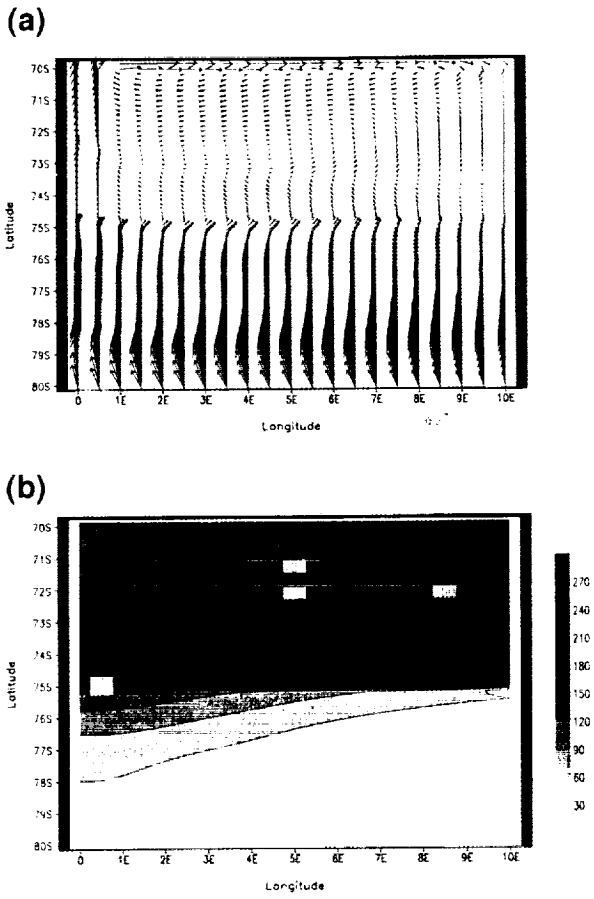

FIG. 15. Mixed layer characteristics at the end of the 20-yr model simulation. (a) Mixed layer flow field (cm s^{-1}) illustrating the northwestward buoyant-plume-like flow regime of the mixed layer circulation beneath the ice shelf. (b) Mixed layer thickness (m) showing a rather thin mixed layer beneath the ice shelf that thickens in the open-ocean portion of the domain.

base the decreasing pressure leads to supercooling and the onset of freezing.

d. Discussion

The sub–ice shelf circulation presented above is broadly similar to that described in earlier studies. The concept of a buoyant flow of ISW ascending the ice shelf base after being initiated by mixing and melting in the deepest parts of the cavity, much like the behavior of our mixed layer, was first introduced by Robin (1979). The idea was subsequently developed by MacAyeal (1984; 1985b) and formed the basis of the one-dimensional models of Jenkins (1991) and Jenkins and Bombosch (1995). Helmer and Olbers (1989) found similar behavior in a two-dimensional, vertical plane model. With the advent of three-dimensional modeling, attention shifted away from the overturning circulation. Determann and Gerdes (1994) and Grosfeld et al. (1997) concluded that the circulation was dominated by a strong depth-averaged horizontal flow. In applications to idealized domains, they found that the depth-integrated transport formed a cyclonic gyre in the cavity, qualitatively similar to the gyre indicated by the depth-averaged flow vectors in Fig. 14a. However, the results we have presented here are quantitatively quite different to those of all the earlier studies. The rates of melting and freezing and the strength of both the horizontal and overturning circulations are all an order of magnitude smaller in our model results.

The likely cause of at least some of these differences is the differing parameterizations of vertical diffusion. In a model where melting at the ice–ocean interface is the only source of forcing, the transport of heat to the ice shelf base is of paramount importance. If vertical heat transfer is easy, melting will be rapid and the circulation will receive strong forcing. However, there is a natural brake on this system in that strong melting suppresses vertical mixing. This brake is incorporated into our model through the use of the TKE budget of the mixed layer to diagnose entrainment rates. In contrast, the three-dimensional models of Determann and Gerdes (1994) and Grosfeld et al. (1997) and the two-dimensional model of Hellmer and Olbers (1989) used constant eddy diffusivities to estimate vertical fluxes, and the one-dimensional models of MacAyeal (1985b), Jenkins (1991), and Jenkins and Bombosch (1995) all used a simple entrainment scheme that did not consider the surface freshwater flux. The impact of the negative feedback of melting on vertical heat transfer is evident in Fig. 12. Only in the vicinity of the grounding line, where entrainment of warm water is driven by horizontal divergence in the mixed layer flow, can melting in excess of 1 cm yr^{-1} be sustained. Introducing an additional source of energy for mixing, such as strong tides, to the model would not necessarily lead to greater or more widespread melting. While a greater supply of TKE should increase the overall depth of the mixed layer, continuous entrainment would still only occur at those locations where it is required to maintain the thickness against thinning driven by horizontal divergence of the mixed layer flow.

Another difference between our model and the three-dimensional models of Determann and Gerdes (1994) and Grosfeld et al. (1997) is the manner in which heat and salt transfer at the ice shelf base is parameterized. The various formulations of this process that have been used in models of sub–ice shelf circulation are discussed by Holland and Jenkins (1999). That used in our model makes the rate of heat and salt transfer dependent on the friction velocity, while that used by both Determann and Gerdes (1994) and Grosfeld et al. (1997) effectively assumes a constant friction velocity. The two formulations would give equal melt rates only if the mixed layer velocity were about 35 cm s^{-1} (Holland and Jenkins 1999). Our weaker flow thus gives much weaker forcing, which once again contributes to the weaker flow.

The results we have presented here differ from those of earlier three-dimensional modeling studies in another important respect. The major conclusion of both Determann and Gerdes (1994) and Grosfeld et al. (1997) was that the circulation beneath the ice shelf remains independent of that in the open ocean unless "f/H" contours cross the ice shelf front. That conclusion is not supported by our results. Our model forcing is confined beneath the ice shelf, but the resulting circulation extends over the entire domain and drives exchange between the cavity in the south and the open ocean to the north.

8. Closing remarks

The study of ocean circulation beneath ice shelves has, of necessity, progressed largely without the aid of the direct observational evidence normally taken for granted in oceanography. There exists a growing database of ship-based observations made along ice fronts, but these features themselves exert a strong influence on the water column. They guide a vigorous coastal current, are the sites of wind-forced upwelling and downwelling (van Heijst 1987) and possibly also of thermohaline convection (Foldvik and Kvinge 1974), and represent sharp changes in water column thickness that induce rectified tidal flows (MacAyeal 1985a; Makinson and Nicholls 1999) and may act as a barrier to some of the flow in the open ocean, such as that forced by the wind (Grosfeld et al. 1997). Using ship-based observations to study sub-ice shelf processes is like trying to understand continental shelf processes based only on data collected along the shelf break. While gross budgets and water mass transformations can be inferred, only theory, supported by a few isolated observations (Jacobs et al. 1979; Nicholls and Makinson 1998), can guide us to the important mechanisms that effect those changes. Yet here we encounter another difficulty. The most tractable theoretical problems in oceanography are those in which the ocean can be assumed to be homogeneous. Although the ocean beneath an ice shelf may appear to be weakly stratified, spatial variations in the stratification are what drives the flow. The assumption of a homogeneous water column yields the null result discussed in section 7b.

Starting with the work of Determann and Gerdes (1994), recent efforts to understand processes beneath ice shelves have involved the application of suitably modified ocean general circulation models to the problem. The model presented in this paper is the first to employ isopycnic coordinates. Such a choice of vertical coordinate is natural for the density-driven flows of interest in this study. It ensures optimum resolution of the water column and allows the introduction of entirely arbitrary topography while avoiding the problems encountered in geopotential coordinates with up- or downslope flows or the difficulties encountered in terrain-following coordinates with estimating pressure gradients. Precise control over diapycnic diffusion and the exact conservation of potential vorticity are also more easily implemented in isopycnic coordinates. The one drawback is the requirement for a nonisopycnic layer, which can admit buoyancy forcing, at the top of the water column. Here some of the advantages outlined above are lost, and the use of an embedded mixed layer model adds complexity, particularly when dealing with the surface topography imposed by an ice shelf. In the early parts of this paper we presented a strategy to overcome these complications.

The idealized runs we presented in section 7 have most in common with the simulations discussed by Grosfeld et al. (1997). Their setup differed slightly in that they imposed a wind field on the open ocean, and their initial conditions were an unstratified ocean with a temperature slightly colder than the one we have used. There are qualitative similarities between the results, namely, the cyclonic flow beneath the ice shelf and the general pattern of melting and freezing, but also distinct differences, particularly in the strength of the circulation. A cursory comparison with observation may suggest that the stronger circulation is closer to reality, but in nature there is considerable extra forcing on the system. For example, the growth and decay of sea ice drives a seasonal cycle of mixing and restratification in the water column to the north of the ice front, and the impact of this on flow beneath an ice shelf has been documented (Nicholls and Makinson 1998). Any process that excites motion in the water could promote more rapid vertical heat transfer, which would provide further forcing on the flow. Thus, the weak response to our idealized forcing may be correct.

If the differences between our results and those of the earlier three-dimensional modeling studies lie in the different parameterizations of vertical heat transfer, we may conclude that a good representation of this process is essential for a realistic simulation of sub–ice shelf circulation. Our other principal conclusion is that the ice front presents less of a dynamic barrier to the buoyancy-driven circulation than has been suggested by the earlier studies. These differences highlight the need for thorough testing and intercomparison of a range of numerical models before more definitive statements can be made about the key processes controlling the circulation beneath ice shelves. We hope that the model we have presented here, both in its current form and with future developments, will prove a useful tool in advancing our currently limited understanding of these processes.

Acknowledgments. The authors gratefully acknowledge support from the Polar Research Program of the National Aeronautical Space Administration (Grant NAG-5-8475) and the Office of Polar Programs of the National Science Foundation (Grants OPP-9901039, OPP-9984966, and OPP-0084286). Supercomputing

time was provided by the Arctic Region Supercomputing Center, University of Alaska, Fairbanks.

REFERENCES

Arakawa, A., and V. R. Lamb, 1977: Computational design of the basic processes of the UCLA general circulation model. *Methods Comput. Phys.*, **17,** 174–265.

Bleck, R., 1998: Ocean modeling in isopycnic coordinates. *Ocean Modeling and Parameterization,* E. P. Chassignet and J. Verron, Eds., Kluwer Academic, 423–448.

——, and D. B. Boudra, 1981: Initial testing of a numerical ocean circulation model using a hybrid (quasi-isopycnic) vertical coordinate, *J. Phys. Oceanogr.*, **11,** 755–770.

——, and L. T. Smith, 1990: A wind-driven isopycnic coordinate model of the north and equatorial Atlantic Ocean. 1. Model development and supporting experiments. *J. Geophys. Res.—Oceans,* **95,** 3273–3285.

——, H. P. Hanson, D. M. Hu, and E. B. Kraus, 1989: Mixed layer thermocline interaction in a three-dimensional isopycnic coordinate model. *J. Phys. Oceanogr.*, **19,** 1417–1439.

——, C. Rooth, D. M. Hu, and L. T. Smith, 1992: Salinity-driven thermocline transients in a wind-forced and thermohaline forced isopycnic coordinate model of the North Atlantic. *J. Phys. Oceanogr.*, **22,** 1486–1505.

Bombosch, A., 1998: Interactions between floating ice platelets and ocean water in the southern Weddell Sea. *Ocean, Ice, and Atmosphere: Interactions at the Antarctic Continental Margin,* S. S. Jacobs and R. F. Weiss, Eds., Amer. Geophys. Union, 257–266.

——, and A. Jenkins, 1995: Modeling the formation and deposition of frazil ice beneath Filchner–Ronne Ice Shelf. *J. Geophys. Res.—Oceans,* **100,** 6983–6992.

Brydon, D., S. Sun, and R. Bleck, 1999: A new approximation of the equation of state for seawater, suitable for numerical ocean models. *J. Geophys. Res.—Oceans,* **104,** 1537–1540.

Determann, J., and R. Gerdes, 1994: Melting and freezing beneath ice shelves: Implications from a three-dimensional ocean circulation model. *Ann. Glaciol.*, **20,** 413–419.

Ekman, V. W., 1905: On the influence of the earth's rotation on ocean currents. *Arch. Math. Astron. Phys.*, **2,** 1–53.

Foldvik, A., and T. Kvinge, 1974: Conditional instability of sea water at the freezing point. *Deep-Sea Res.*, **21,** 169–174.

Gade, H. G., 1979: Melting of ice in sea water: A primitive model with applications to the Antarctic ice shelf and icebergs. *J. Phys. Oceanogr.*, **9,** 189–198.

Gaspar, P., 1988: Modeling the seasonal cycle of the upper ocean. *J. Phys. Oceanogr.*, **18,** 161–180.

Grosfeld, K., R. Gerdes, and J. Determann, 1997: Thermohaline circulation and interaction between ice shelf cavities and the adjacent open ocean. *J. Geophys. Res. Oceans,* **102,** 15 595–15 610.

Hellmer, H. H., and D. J. Olbers, 1989: A two-dimensional model for the thermohaline circulation under an ice shelf. *Antarctic Sci.*, **1,** 325–336.

Higdon, R. L., and A. F. Bennett, 1996: Stability analysis of operator splitting for large-scale ocean modeling. *J. Comput. Phys.*, **123,** 311–329.

Holland, D. M., and A. Jenkins, 1999: Modeling thermodynamic ice ocean interactions at the base of an ice shelf. *J. Phys. Oceanogr.*, **29,** 1787–1800.

Houghton, J. T., L. G. Meira Filho, B. A. Callander, N. Harris, A. Kattenberg, and K. Maskell, Eds., 1996: *Climate Change 1995: The Science of Climate Change.* Cambridge University Press, 572 pp.

Jacobs, S. S., A. L. Gordon, and J. L. Ardai, Jr. 1979: Circulation and melting beneath the Ross Ice Shelf. *Science,* **203,** 439–443.

Jenkins, A., 1991: A one-dimensional model of ice shelf–ocean interaction, *J. Geophys. Res.—Oceans,* **96,** 20 671–20 677.

——, and A. Bombosch, 1995: Modeling the effects of frazil ice crystals on the dynamics and thermodynamics of ice shelf water plumes. *J. Geophys. Res.—Oceans,* **100,** 6967–6981.

MacAyeal, D. R., 1984: Thermohaline circulation below the Ross Ice Shelf: A consequence of tidally induced vertical mixing and basal melting. *J. Geophys. Res.—Oceans,* **89,** 597–605.

——, 1985a: Tidal rectification below the Ross Ice Shelf, Antarctica. *Oceanology of the Antarctic Continental Shelf,* S. S. Jacobs, Ed., Amer. Geophys. Union, 109–132.

——, 1985b: Evolution of tidally triggered meltwater plumes beneath ice shelves. *Oceanology of the Antarctic Continental Shelf,* S. S. Jacobs, Ed., Amer. Geophys. Union, 133–143.

Makinson, K., and K. W. Nicholls, 1999: Modeling tidal currents beneath Filchner–Ronne Ice Shelf and on the adjacent continental shelf: Their effect on mixing and transport. *J. Geophys. Res.—Oceans,* **104,** 13 449–13 465.

McDougall, T. J., and W. K. Dewar, 1998: Vertical mixing and cabbeling in layered models. *J. Phys. Oceanogr.*, **28,** 1458–1480.

Millero, F. J., 1978: Annex 6: Freezing point of seawater. Eighth Report of the Joint Panel of Oceanographic Tables and Standards, UNESCO Technical Papers in Marine Science, 31 pp.

——, C. T. Chen, A. Bradshaw, and K. Schleicher, 1980: A new high pressure equation of state for seawater. *Deep-Sea Res.*, **27,** 255–264.

Montgomery, R. B., 1937: A suggested method for representing gradient flow in isentropic surfaces. *Bull. Amer. Meteor. Soc.*, **18,** 210–212.

Murtugudde, R., M. A. Cane, and V. Prasad, 1995: A reduced-gravity, primitive equation, isopycnic ocean GCM—Formulation and simulations. *Mon. Wea. Rev.*, **123,** 2864–2887.

Nicholls, K. W., and K. Makinson, 1998: Ocean circulation beneath the western Ronne Ice Shelf, as derived from in situ measurements of water currents and properties. *Ocean, Ice, and Atmosphere: Interactions at the Antarctic Continental Margin,* S. S. Jacobs and R. F. Weiss, Eds., Amer. Geophys. Union, 301–318.

Oberhuber, J. M., 1993: Simulation of the Atlantic circulation with a coupled sea ice–mixed layer–isopycnic general circulation model. Part I: Model description. *J. Phys. Oceanogr.*, **23,** 808–829.

Robin, G. de Q., 1979: Formation, flow, and disintegration of ice shelves. *J. Glaciol.*, **24,** 259–271.

Sun, S., 1997: Compressibility effects in the Miami Isopycnic Coordinate Ocean Model. Ph.D. thesis, University of Miami, 138 pp.

van Heijst, G. J. F., 1987: On the oceanic circulation near a shelf-ice edge. *Dynamics of the West Antarctic Ice Sheet,* C. J. van der Veen and J. Oerlemans, Eds., Reidel, 37–56.

Williams, M. J. M., A. Jenkins, and J. Determann, 1998: Physical controls on the ocean circulation beneath ice shelves revealed by numerical models. *Ocean, Ice and Atmosphere: Interactions at the Antarctic Continental Margin,* S. S. Jacobs and R. F. Weiss, Eds., Amer. Geophys. Union, 285–299.

NOTES AND CORRESPONDENCE

The Role of Meltwater Advection in the Formulation of Conservative Boundary Conditions at an Ice–Ocean Interface

ADRIAN JENKINS

British Antarctic Survey, Natural Environment Research Council, Cambridge, United Kingdom

HARTMUT H. HELLMER

Alfred Wegener Institute for Polar and Marine Research, Bremerhaven, Germany

DAVID M. HOLLAND

Courant Institute of Mathematical Sciences, New York University, New York, New York

23 July 1999 and 10 July 2000

ABSTRACT

Upper boundary conditions for numerical models of the ocean are conventionally formulated under the premise that the boundary is a material surface. In the presence of an ice cover, such an assumption can lead to nonconservative equations for temperature, salinity, and other tracers. The problem arises because conditions at the ice–ocean interface differ from those in the water beneath. Advection of water with interfacial properties into the interior of the ocean therefore constitutes a tracer flux, neglect of which induces a drift in concentration that is most rapid for those tracers having the lowest diffusivities. If tracers are to be correctly conserved, either the kinematic boundary condition must explicitly allow advection across the interface, or the flux boundary condition must parameterize the effects of both vertical advection and diffusion in the boundary layer. In practice, the latter alternative is often implemented, although this is rarely done for all tracers.

1. Introduction

Exchanges of heat and freshwater at the surface of the ocean represent the major forcing behind the creation of new water masses. In the polar oceans, the source regions for most of the deep and bottom waters, the processes of exchange are strongly influenced by the presence of ice. If ocean models are to simulate the characteristics and distribution of abyssal waters correctly, they must include an adequate representation of the coupling between ice and ocean. Because melting and freezing entail a transfer of water between the two media, this coupling formally manifests itself in the boundary conditions placed on both the vertical velocity and on the tracer concentrations. However, it is an almost universal practice in numerical modeling of the ocean to regard the sea surface as a permeable, but material, interface—properties may diffuse across it, but no water may be exchanged between the ocean and the overlying medium, be it atmosphere or ice. Huang (1993) criticized such practice, on the grounds that it suppresses the Goldsburgh–Stommel circulation and recommended setting the vertical velocity relative to the upper boundary equal to the precipitation, evaporation, melt, or freeze rate. Here we examine what the assumed nature of the ocean surface implies for the balance equations for tracers under conditions of melting and freezing.

The ice–ocean boundary layer is a region that is distinguished by relatively high gradients in tracer concentrations combined with large changes in the effective diffusivity. It is often the case that the equations used to describe the transport of tracers in the bulk of the oceanic water column are not applicable in the boundary region. This problem can be circumvented by incorporating a simple parameterization of the boundary layer processes into the boundary conditions. Such a formulation invariably entails the diagnosis of conditions at the ice–ocean interface that are distinct from those pertaining at the uppermost model grid point within the

Corresponding author address: Dr. Adrian Jenkins, British Antarctic Survey, Natural Environment Research Council, High Cross, Madingley Rd., Cambridge CB3 0ET, United Kingdom.
E-mail: a.jenkins@bas.ac.uk

sub-ice water column. In the presence of such differences, the advection of meltwater into the bulk of the ocean plays an important role in the balance equations for tracers, but the advective flux is formally absent if the ice–ocean interface is treated as a material surface.

We use a simple, one-dimensional model of the ocean beneath sea ice to demonstrate the role played by meltwater advection in the conservation of tracers. To this model we apply two sets of boundary conditions that differ only in the assumption made about the nature of the ice–ocean interface: material or not. We also discuss the two-dimensional model of thermohaline circulation beneath an ice shelf presented by Hellmer and Olbers (1989) and Hellmer et al. (1998). This model has a material interface at the ice–ocean boundary, but changing the kinematic boundary condition would entail a considerable increase in complexity. Instead, we include the effect of meltwater advection through a modified flux boundary condition and show that this simple fix improves the model performance. Finally, we discuss how the boundary formulations discussed here compare with those used elsewhere.

2. Fundamental equations

Our discussion will focus on the evolution of scalar properties in the upper ocean, and we will use the following generic equation to model this evolution:

$$\frac{\partial X}{\partial t} + \nabla \cdot (\mathbf{u}X) + \frac{\partial}{\partial z}(wX) = -\nabla \cdot \langle \mathbf{u}'X' \rangle - \frac{\partial}{\partial z}\langle w'X' \rangle, \tag{1}$$

where X could be temperature T, salinity S, or any other conservative tracer; boldface variables represent horizontal vectors; primed variables represent turbulent fluctuations; and angle brackets indicate ensemble averaging. In the presence of an ice cover, this equation is forced by the upper boundary conditions placed on the terms describing the vertical advection and diffusion of tracers.

The advective flux at the ice–ocean interface is simply

$$(wX)|_b = w_b X_b, \tag{2}$$

where the subscript b indicates conditions at the ice–water contact. For a nonmaterial surface, the vertical velocity at the boundary is derived from a combination of the motion of the boundary and the advection of fluid across the boundary:

$$w_b = \frac{\partial z_b}{\partial t} + \mathbf{u}_b \cdot \nabla z_b - m, \tag{3}$$

where m indicates the melt rate (negative for freezing) expressed as a thickness of seawater per unit time. For the more commonly encountered material interface, the particles lying on the boundary at one time must lie there at all subsequent times, so their motion must be equal to that of the boundary itself:

$$w_b = \frac{\partial z_b}{\partial t} + \mathbf{u}_b \cdot \nabla z_b. \tag{4}$$

Under this assumption the melt/freeze rate does not impact the continuity equation, a simplification that explains why (4) is generally favored over (3). The price to be paid for this simplification is a slight inconsistency between the continuity and tracer equations because the impact of melting and freezing must be retained in the latter.

We express the diffusive flux at the ice–ocean interface as the product of a turbulent transfer coefficient and the difference in the tracer concentration across the surface boundary layer:

$$\langle w'X' \rangle|_b = \gamma_X (X - X_b), \tag{5}$$

where the transfer coefficient γ_X has the dimensions of velocity (i.e., diffusivity over length). Since the surface boundary layer itself is part of the ocean domain, the precise meaning of the transfer coefficient depends on the form of discretization applied to (1). In a layer model, X in (5) will be a depth-averaged value across the upper layer, part of which will be the boundary layer, and the value of γ_X should reflect this. In a level model, X will be the value at the first level below the boundary, and the value of γ_X should reflect whether this point is within or outside of the boundary layer. At vertical resolutions commonly used in ocean models, these distinctions are unimportant because most of the change in tracer concentration occurs across a very thin viscous sublayer (McPhee 1990). The result is that conditions at the upper level, or within the upper layer, of a model are practically equivalent to the far-field conditions outside the boundary layer.

The application of Eqs. (2) and (5) requires knowledge of the tracer concentration at the ice–ocean interface. We derive this from a consideration of the budget within an infinitesimal control volume that straddles the interface (Mellor et al. 1986). We demand an exact balance between the vertical diffusive fluxes and the sources or sinks of the tracer represented by the consumption or production of meltwater within the control volume:

$$\rho_i k_i \left.\frac{\partial X_i}{\partial z}\right|_b - \rho \gamma_X (X_b - X) = \rho m (X_b - X_i). \tag{6}$$

Here the subscript i indicates ice properties, ρ are densities, and k is a diffusivity. For most tracers, including salinity, stable isotopes and incorporated gases, the diffusivity in ice is negligible, so the first term on the left-hand side of (6) vanishes. This is not so in the case of temperature, for which Eq. (6) becomes

$$\rho_i c_i k_i \left.\frac{\partial T_i}{\partial z}\right|_b - \rho c \gamma_T (T_b - T) = \rho m L_i, \tag{7}$$

where c are specific heat capacities and L a latent heat of fusion.

Complete specification of the boundary problem re-

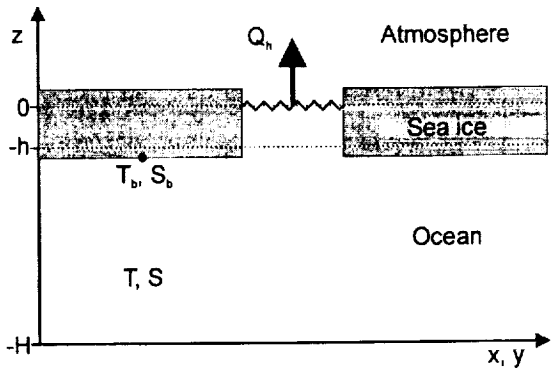

FIG. 1. Schematic of a one-layer ocean beneath sea ice. The ocean layer is characterized by a single temperature and salinity (T, S) and is forced by an atmospheric heat flux (Q_h) that passes through leads. The temperature and salinity at the ice–ocean interface (T_b, S_b) differ from those in the interior, and the differences drive melting and freezing. The sea ice is regarded as a continuum, so the ice–ocean boundary conditions and the atmospheric heat flux are formally applied at the level of the mean ice draft ($z = -h$). The seabed lies at $z = -H$.

quires an expression for the melt/freeze rate. This is determined by the rate at which heat and salt are supplied to, or extracted from, the control volume, and can be calculated from the combination of (7), with an appropriate specification or parameterization of heat conduction through the ice, and the salinity version of (6). A third constraint is that the seawater within the control volume must be at the freezing point, which we define using a linear equation:

$$T_b = \lambda_1 S_b + \lambda_2 + \lambda_3 P_b, \tag{8}$$

where P_b is the pressure at the interface and λ_{1-3} are constants: -0.0573°C/psu, 0.0832°C, and -7.53×10^{-8} °C/Pa, respectively. This relationship is based on that of Millero (1978), with the salinity dependence linearized. Equations (6)–(8) can be solved simultaneously for m, S_b, and T_b, a procedure that is simplified by the use of a linear equation in (8). With the melt rate known the boundary concentration of any other tracer can be calculated from (6) if the concentration in the ice is known.

Boundary conditions of the form given in (5)–(8) were introduced by Josberger (1983) and McPhee (1983). Mellor et al. (1986) recognized the importance of molecular diffusion within the viscous sublayer in determining the melt/freeze rate, and McPhee et al. (1987) and Steele et al. (1989) investigated expressions for the turbulent transfer coefficients that included explicit parameterizations of this process. The magnitudes of the transfer coefficients used in this study are derived from the results of this pioneering work.

3. A simple model of the ocean beneath sea ice

We begin by considering the evolution of a one-layer ocean model (Fig. 1) subject to a symmetric cycle of heating and cooling. We assume horizontal homogeneity and treat the lower boundary as a fixed, insulating surface, thus isolating the upper boundary condition as the only forcing on the model. Under these assumptions integration of Eq. (1) over the depth of the water column leads to

$$\int_{-H}^{-h} \frac{\partial X}{\partial t}\, dz + w_b X_b = -\langle w'X' \rangle|_b. \tag{9}$$

The integral expression can be evaluated as

$$\int_{-H}^{-h} \frac{\partial X}{\partial t}\, dz = \frac{\partial}{\partial t}[(H - h)\overline{X}] + X_b \frac{\partial h}{\partial t}, \tag{10}$$

where the overbar indicates a depth-averaged quantity, and we have made use of the Leibnitz theorem for the differntiation of an integral.

If there were complete ice coverage, the turbulent fluxes at the upper boundary would take the form given in (5) but, if direct ocean–atmosphere exchange can take place through leads, the flux boundary condition at the ice–ocean interface ($z = -h$) becomes

$$\rho\langle w'X' \rangle|_b = A\rho\gamma_X(\overline{X} - X_b) + (1 - A)Q_X, \tag{11}$$

where A is the areal fraction of the surface covered by ice and Q_X is the tracer flux passing through the leads. In the temperature equation, Q_X is replaced by Q_h/c, where Q_h is the heat flux. The two choices for the remaining advective boundary condition are discussed separately below.

We force the model with a sinusoidal variation in the atmospheric heat flux having an amplitude of 500 W m^{-2} over open water and a period of one year. For all other tracers we assume that the flux passing through the leads is zero. The water column thickness ($H - h$) is initially 50 m and the ocean has an initial salinity of 34.5 psu and an initial temperature at the appropriate salinity-dependent freezing point. The initial ice thickness is arbitrary, as we are only concerned with how the melting and freezing cycle influences the bulk ocean properties. The areal coverage of ice is assumed constant at 90% and the model is run for 10 years. We use a turbulent heat transfer coefficient, γ_T, of 5×10^{-5} m s^{-1} and a turbulent salt transfer coefficient, γ_S, of $0.04\gamma_T$. These values are appropriate for a moderate friction velocity of 5×10^{-3} m s^{-1} (McPhee et al. 1987; Holland and Jenkins 1999).

For the purposes of diagnosing the melt/freeze rate and the temperature and salinity at the ice–ocean boundary, we assume that no salt is incorporated into the ice on freezing. We also assume the ice to be sufficiently thick that the heat conducted through it is negligible, which allows us to set the first term on the left-hand side of (7) to zero. The pressure-dependent term in (8) can also be neglected. Note that these assumptions, along with the simple formulations we have used for the heat and salt transfer coefficients, do not affect the form of the equations presented below. They influence only the magnitude of the forcing.

a. With meltwater advection

We first regard the ice–ocean boundary as a nonmaterial interface and apply a kinematic boundary condition of the form given in (3):

$$w_b = -\frac{\partial h}{\partial t} - Am. \tag{12}$$

Applying this and the flux boundary condition given in (11) to (9), the conservation equation for a generic tracer becomes

$$\frac{\partial}{\partial t}[(H - h)\overline{X}] - AmX_b = A\gamma_X(X_b - \overline{X}) - (1 - A)\frac{Q_X}{\rho}. \tag{13}$$

The vertical velocity must vanish at the seabed, so our assumption of zero gradient in the horizontal velocity field implies that the w_b must also be zero, and (12) can be rewritten:

$$\frac{\partial}{\partial t}(H - h) = Am \tag{14}$$

because H is fixed for all time. Using (14) to expand the derivative on the left-hand side of (13), the model equations for salinity and temperature, respectively, become

$$\frac{\partial \overline{S}}{\partial t} = \frac{A(\gamma_S + m)}{(H - h)}(S_b - \overline{S}) \tag{15a}$$

$$\frac{\partial \overline{T}}{\partial t} = \frac{A(\gamma_T + m)}{(H - h)}(T_b - \overline{T}) - \frac{(1 - A)Q_h}{\rho c(H - h)}. \tag{15b}$$

Results obtained with this version of the model are shown in Fig. 2. The annual cycle in ice thickness shows a peak-to-peak range of about 1.5 m, giving rise to ocean salinities that cycle over a range of about 1 psu. Ocean temperatures deviate by up to 0.35°C from the freezing point. The maxima and minima in ice thickness occur about 2.5 weeks after the change in sign of the atmospheric heat flux in spring and autumn (Fig. 2a). The lag is approximately equal to the reaction time, τ, of the oceanic layer:

$$\tau = \frac{(H - h)}{\gamma_{T\text{eff}}}, \tag{16}$$

where $\gamma_{T\text{eff}}$ is the effective heat transfer coefficient, defined by Holland and Jenkins (1999) as

$$\gamma_{T\text{eff}} = \gamma_T\left(1 - \frac{\lambda_1(S_b - S_i)c\gamma_T}{L_i\gamma_S}\right)^{-1}. \tag{17}$$

Continual relaxation towards the freezing point means that the water temperature is a function of the rate at which heat is lost to, or gained from, the atmosphere, subject to the lag mentioned above, so the temperature extremes occur shortly after midsummer and midwinter (Fig. 2b). The salinity is a function of the cumulative

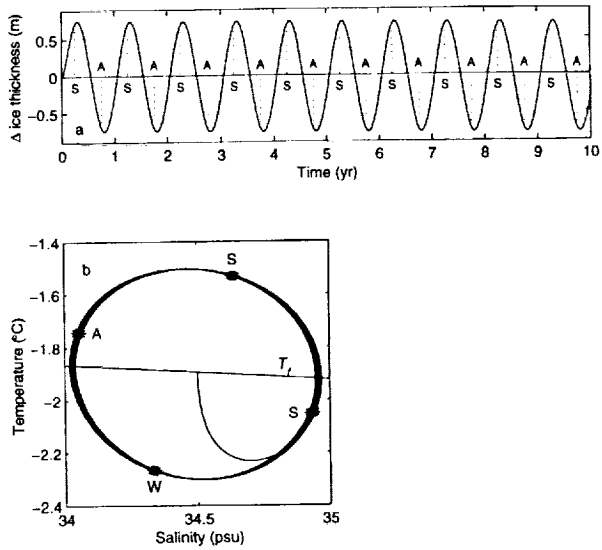

FIG. 2. Results of a ten-year integration of (15): (a) change in ice thickness, (b) temperature, and salinity of the ocean. In (a) the dotted lines indicate the time at which the atmospheric heat flux changes sign in spring (S) and autumn (A). In (b) the stars labeled S (spring), S (summer), A (autumn), W (winter) indicate the times of maximum and zero atmospheric forcing, while the straight line labelled T_f indicates the freezing point at atmospheric pressure.

heat loss or gain throughout a growth or melt season, so the extremes occur when freezing switches to melting, and vice versa. Together these signatures give an annual cycle that traces an ellipse (counterclockwise) in temperature/salinity space. This cycle does not exactly repeat itself. There is a drift of about 0.0025 psu yr^{-1} toward lower salinities, consistent with a reduction in ice thickness of approximately 4 mm yr^{-1}. This drift arises because the ice cover is thicker on average during the spring to autumn period of heating than during the autumn to spring period of cooling (Fig. 2a). In this model formulation the water lost by the ice during melting is gained by the ocean, and vice versa during freezing. The water column is therefore thinner and has a smaller heat capacity, on average, during periods of heating than during periods of cooling, and this allows slightly more melting to occur than freezing.

Despite the simplicity of the model we find some support for such a cycle of ocean properties in observations made during the Arctic Ice Dynamics Joint Experiment. Figure 3 shows mixed layer temperatures and salinities recorded daily between late May 1975 and mid-April 1976 at the Snowbird station (Maykut and McPhee 1995). Many factors not considered in our one-dimensional model, such as drift of the station, horizontal advection of water masses, mixing across the pycnocline, variations in ice concentration, and a variable input of turbulent kinetic energy to the ocean with the passage of weather systems, will all have influenced the observations. Given these complicating factors, the basic shape and phasing of the observed annual cycle

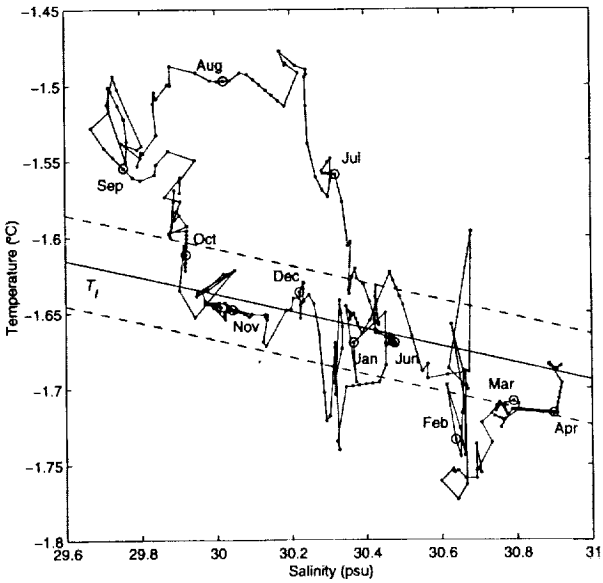

FIG. 3. A 331-day record of temperature and salinity at the Snowbird ice camp. Each dot represents an average value for the upper 25 m of the water column. Data from the first day of each month are circled and labeled. The straight line labeled T_f indicates the freezing point at atmospheric pressure, and the two dashed lines indicate the likely uncertainty in the observed deviation from the freezing point (Maykut and McPhee 1995).

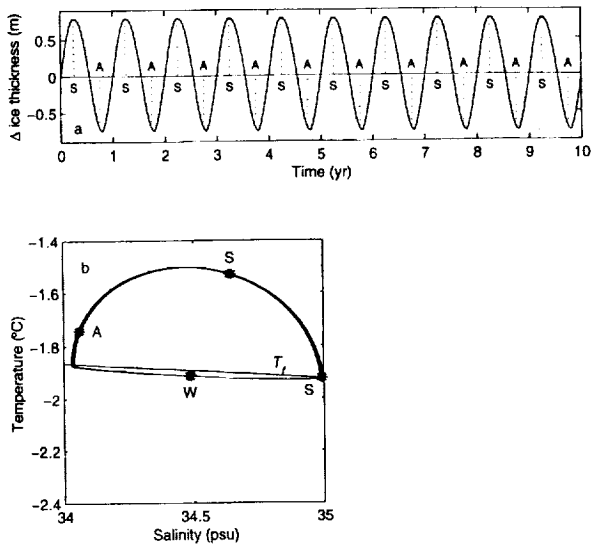

FIG. 4. Same as Fig. 2 but with heat and salt transfer coefficients increased by a factor of 20 when the ocean temperature falls below the freezing point.

in mixed layer properties compare favorably with the model results.

The main qualitative difference between the observations and model results is the lack of any sustained period of supercooling, at levels above the detection threshold of the instrumentation used, in the observational record. A lack of supercooling suggests that the ocean response time is shorter during periods of ice growth than during periods of melting. The reason may be frazil ice production in the water column or fundamentally different behavior within the boundary layer when salt, rather than freshwater, is produced at the phase change interface. Whatever the physical mechanism, we can simulate the effect in the model by increasing the magnitude of the heat and salt transfer coefficients during periods of supercooling. The results are shown in Fig. 4. With the wintertime response of the ocean 20 times faster than before, supercooling is restricted to no more than about 0.02°C, and the peak in supercooling and the transition from melting to freezing are practically coincident with the maximum and the change in sign, respectively, of the atmospheric forcing. Because there is little phase lag between the cycles of atmospheric heat flux and ice growth during half of the year, the drifts in ice thickness and ocean salinity are reduced by a factor of 2.

b. Without meltwater advection

We next treat the ice–ocean boundary as a material surface and apply a kinematic boundary condition analogous to (4):

$$w_b = -\frac{\partial h}{\partial t}. \tag{18}$$

Applying this and the flux boundary condition given in (11) to (9) gives

$$\frac{\partial}{\partial t}[(H - h)\overline{X}] = A\gamma_X(X_b - \overline{X}) - (1 - A)\frac{Q_X}{\rho} \tag{19}$$

for a genetic tracer. Equating w_b to zero yields

$$\frac{\partial}{\partial t}(H - h) = 0, \tag{20}$$

and the model equations for salinity and temperature become

$$\frac{\partial \overline{S}}{\partial t} = \frac{A\gamma_S}{D}(S_b - \overline{S}) \tag{21a}$$

$$\frac{\partial \overline{T}}{\partial t} = \frac{A\gamma_T}{D}(T_b - \overline{T}) - \frac{(1 - A)Q_h}{\rho c D}, \tag{21b}$$

where $D = H - h$ is the, now temporally constant, water column thickness.

The main differences between (15) and (21) arise because the water advected into or out of the ocean in (15), which is absent in (19), has properties equal to those at the boundary. Advection therefore constitutes a tracer flux that is additional to the diffusive fluxes given by (5). Using (21) we obtain a similar evolution of the ice cover to that obtained with (15), but we find a rapid drift of about 0.1 psu yr^{-1} toward higher salinity (Fig. 5). The increase in salinity is what we would anticipate for a net ice growth of 15 cm yr^{-1}, and is clearly in error. It is a result of the missing advective fluxes, which are expressed as the products of the melt rate and

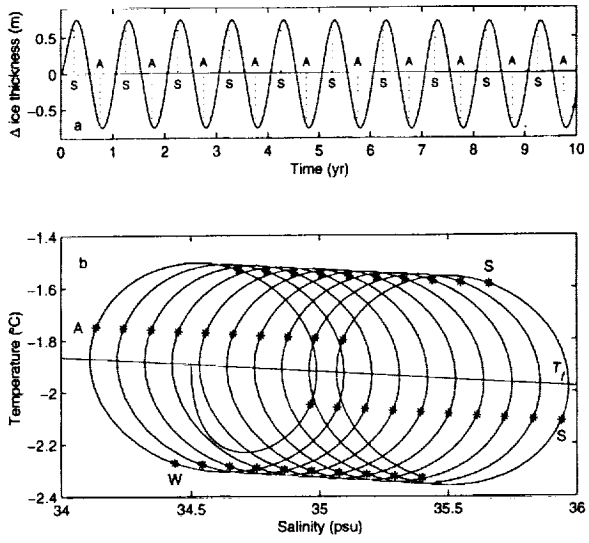

FIG. 5. Results of a ten-year integration of (21): (a) change in ice thickness, (b) temperature, and salinity of the ocean. In (a), the dotted lines indicate the time at which the atmospheric heat flux changes sign in spring (S) and autumn (A). In (b), the stars labeled S (spring), S (summer), A (autumn), W (winter) indicate the times of maximum and zero atmospheric forcing, while the straight line labeled T_f indicates the freezing point at atmospheric pressure.

the difference in tracer concentration between the mixed layer and the ice–ocean interface [Eq. (15)]. The concentration differences are generated by the rejection or uptake of tracers during freezing or melting, so they change sign synchronously with the melt rate (Fig. 6). Hence, the advective fluxes are always of the same sign, and, although they are generally small, their neglect leads to an error that accumulates throughout the annual cycle. With the reaction time of the ocean shortened by

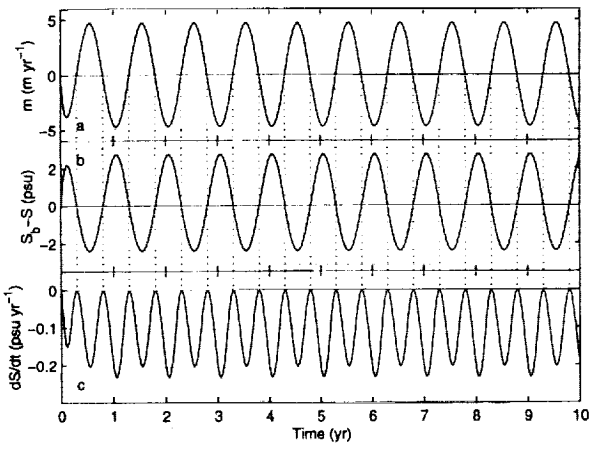

FIG. 6. Illustration of the net dilution induced by advection of meltwater into an ocean layer having a nonmaterial upper boundary: (a) melt rate, (b) salinity difference across the ice–ocean boundary layer, and (c) salinity change that results from the inclusion of meltwater advection on the right-hand side of (15a), defined by $dS/dt = Am(H - h)^{-1}(S_b - \overline{S})$. Dotted lines indicate the times at which the melt rate changes sign.

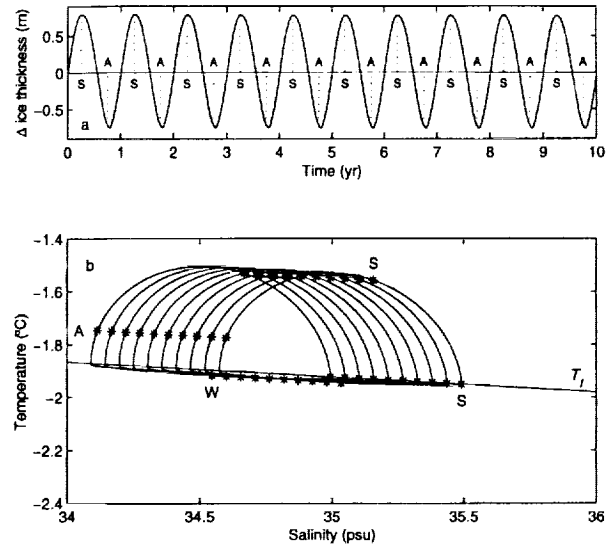

FIG. 7. Same as Fig. 5 but with heat and salt transfer coefficients increased by a factor of 20 when the ocean temperature falls below the freezing point.

a factor of 20 during freezing, the difference in salinity across the boundary layer, and hence the salt flux error, is reduced in winter. The annual drift in salinity is therefore approximately halved (Fig. 7).

Although the net salinity drift is a function of our model setup, in particular the choice of water column thickness, the magnitude of the flux errors are determined only by the nature of the ice–ocean boundary conditions. In the appendix we develop general expressions for the size of the errors and demonstrate that they are approximately proportional to the square of the deviation in water temperature from the freezing point. The errors are most significant for slowly diffusing tracers with small γ_x, the ratio of the excluded advective to included diffusive fluxes being m/γ_x. For this reason the salinity error is much more apparent in Figs. 5 and 7 than the temperature error. The solution could not drift from the freezing point line in any case, but the heat flux error alone would act to reduce the thickness of the ice cover and freshen the mixed layer.

4. A model of thermohaline circulation beneath an ice shelf

We next consider the model of thermohaline circulation beneath an ice shelf described by Hellmer and Olbers (1989). The model domain consists of a vertical plane, oriented perpendicular to the ice front and extending into the cavity beneath the ice shelf. The boundary located at the ice front is open, while the interior boundaries are fixed material surfaces, the upper one corresponding to the ice shelf base. A single equation for the vertical streamfunction replaces the momentum and continuity equations, while the generic equation for tracers, equivalent to our Eq. (1), is written

$$\frac{\partial X}{\partial t} + \frac{\partial}{\partial y}(vX) + \frac{\partial}{\partial z}(wX) = \frac{\partial}{\partial y}\left(K_H \frac{\partial X}{\partial y}\right) + \frac{\partial}{\partial z}\left(K_V \frac{\partial X}{\partial z}\right) + C, \tag{22}$$

where v and w are horizontal and vertical components of velocity, K_H and K_V are horizontal and vertical eddy diffusivities, and C indicates a convective term used to eliminate static instability. Boundary conditions on the streamfunction are specified such that there is no normal flow at the solid boundaries and only normal flow at the open boundary, where the model is forced with an observed vertical profile of temperature and salinity. Where outflow occurs, the observations are overwritten by values advected from the cavity interior. Heat and salt balances at the ice shelf base are specified as in Eqs. (6) and (7), with the first term on the left-hand side of (7) parameterized in a manner appropriate for heat conduction into a melting ice shelf (Nøst and Foldvik 1994; Holland and Jenkins 1999):

$$\rho_i c_i k_i \left.\frac{\partial T_i}{\partial z}\right|_b = \rho m c_i (T_s - T_b), \tag{23}$$

where T_s is the temperature at the surface of the ice shelf.

The model equations are solved on a rectangular grid with regular horizontal and vertical spacing. Staggering of the grid means that the vertical velocity is defined on points that lie half a grid cell above and below the points carrying the tracers. The ice–ocean boundary passes through the velocity points and, since the tracer fluxes ($K_v \partial X/\partial z$) are naturally defined on these points, the diffusive flux boundary condition can simply be written

$$\left. K_V \frac{\partial X}{\partial z}\right|_b = \gamma_X (X_b - X_{1/2}), \tag{24}$$

where the subscript 1/2 indicates conditions at the uppermost grid point within the water column, half a grid box below the interface. The lack of tracer points on the boundary is not a problem because the value X_b is derived from (6) and need not be formally assigned to any grid point.

Application of (24) is equivalent to (21) in that, consistent with the assumption of no normal flow at the boundary, it neglects the advection of meltwater across the ice–ocean interface. However, if the tracer budgets are to be closed correctly, the first grid point in from the boundary must feel the additional sinks of heat and salt associated with the advection of meltwater across the boundary layer. Because Eq. (22) is cast in flux form, it would be simple to impose an advective flux at the ice–ocean interface, but the advection field would then be inconsistent with the velocity field, which is derived on the basis of no normal flow at the boundaries. The problem of nonconservation of tracers would be exacerbated. Instead we apply a modified flux boundary condition that is analogous in form to the terms appearing in our earlier layer-integrated equations 15:

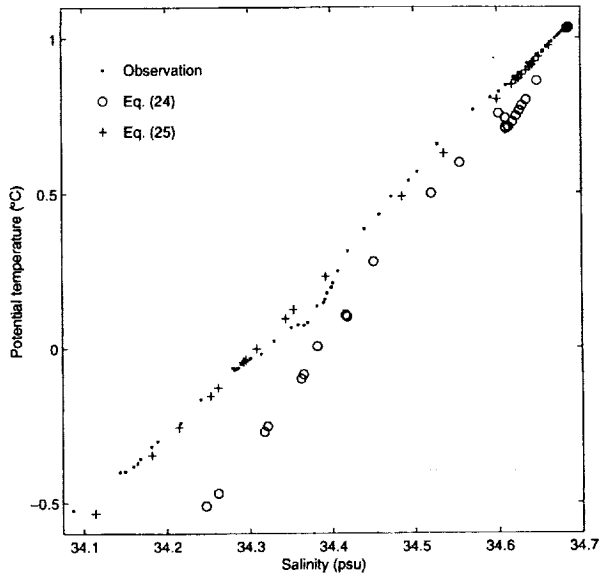

FIG. 8. Potential temperature vs salinity diagram comparing observations made at the calving front of Pine Island Glacier (dots) with the output from a two-dimensional model of thermohaline circulation in the sub-ice cavity (Hellmer et al. 1998). The vertical profiles of potential temperature and salinity used here constitute the open boundary of the model domain. Model results obtained using flux boundary conditions defined as in (24) and (25) are indicated by open circles and crosses, respectively. Both versions of the model were tuned to give net melt rates for the glacier that were consistent with observation.

$$\left. K_V \frac{\partial X}{\partial z}\right|_b = (\gamma_X + m)(X_b - X_{1/2}). \tag{25}$$

Hellmer et al. (1998) applied the two-dimensional model to the water column beneath the 90-km floating extension of Pine Island Glacier, a fast-flowing outlet glacier of the West Antarctic Ice Sheet. Employing flux boundary conditions of the form shown in (25), they were able to obtain good agreement between modeled outflow characteristics and observations made at the calving front of the glacier. Figure 8 shows a comparison between the results of this model run and the observations. The results of a second model run, which employed boundary conditions of the form shown in (24), are also shown in Fig. 8. These latter results are clearly inferior.

The straight line trajectory in potential temperature/salinity space, apparent in Fig. 8, is characteristic of ice melting in seawater. Gade (1979) calculated the gradient of this line to be

$$\frac{\partial T}{\partial S} = \frac{c(T_w - T_b) + L_i + c_i(T_b - T_s)}{c(S_w - S_i)}, \tag{26}$$

where the subscript w indicates the far-field seawater properties and for glacier ice the salinity is zero. The

slope is primarily a function of the water and ice properties and depends only very weakly on the melt rate, through its influence on the boundary temperature. Taking the ratio of heat flux to salt flux, as expressed by (25), substituting from (6), (7), and (23), and setting the salinity of the ice to zero, an expression analogous to (26) is readily obtained. However, writing the fluxes as in (24), a similar procedure leads to

$$\frac{\partial T}{\partial S} = \frac{L_i + c_i(T_b - T_s)}{c(S_b - S_i)}, \tag{27}$$

which represents erroneous forcing on the model. Furthermore, the appearance of the boundary salinity in the denominator makes the slope sensitive to such factors as the melt rate and the magnitude of the turbulent transfer coefficient for salt.

5. Significance for other models

Boundary formulations that include all the effects of meltwater advection are, to our knowledge, uncommon. However, for conditions of low melt/freeze rate and for integrations over short timescales, the errors caused by nonconservation of tracers are probably small. This is the case with most models of the interaction between ice shelves and the ocean, the early versions of which (Hellmer and Olbers 1989; Scheduikat and Olbers 1990; Jenkins 1991) all used boundary formulations analogous to (21) or (24). Later versions of these models (Nicholls and Jenkins 1993; Jenkins and Bombosch 1995; Hellmer et al. 1998) have been corrected, although it is only in the case of the Pine Island Glacier simulations cited in the previous section where melt rates are $\sim$10 m yr^{-1}, an order of magnitude higher than in the other examples, that the correction has had a significant impact on the results.

The literature on coupled sea ice–ocean models is too vast to enable us to present an authoritative survey of all the various boundary formulations in use. In any case, the published descriptions of the models often lack the level of detail required to reveal the use of conservative or nonconservative boundary conditions. Our discussion has centered on what Holland and Jenkins (1999) refer to as three-equation formulations. These employ all of Eqs. (6)–(8) to diagnose the temperature, salinity, and melt/freeze rate at the ice–ocean interface. This type of formulation is not commonly encountered in sea ice models, but where it is, boundary conditions corresponding to (21) and (24) appear to be in use. Two-equation formulations are encountered more often. In these, the salinity at the boundary is assumed equal to that at the upper model level or layer, and only heat transfer through the thermal boundary layer is considered. McPhee et al. (1999) demonstrate that with a suitable choice of effective heat transfer coefficient, such a formulation can yield realistic melt rates. Since the boundary salinity is not explicitly calculated, the conventional choice for the salinity equation is a flux boundary condition of the form

$$K_V \left.\frac{\partial S}{\partial z}\right|_b = m(S_i - S), \tag{28}$$

where S represents the salinity at the uppermost grid point in the water column. This is simply the expression in (25), rewritten using (6), so it is a conservative boundary condition that implicitly includes both advective and diffusive fluxes. However, the analogous boundary condition for temperature, obtained from a combination of (25) and (7),

$$K_V \left.\frac{\partial T}{\partial z}\right|_b = m\left(T_b - T - \frac{L}{c}\right) + \left.\frac{K_i}{\rho c}\frac{\partial T_i}{\partial z}\right|_b, \tag{29}$$

is rarely seen. The conventional version of (29) includes only the latent heat term and the heat conduction through the ice, and therefore conforms to the nonconservative form of (24). Incorporation of meltwater advection into the salt balance eliminates the dominant source of error, but the advection term can rise to several percent of the latent heat term in (29). Although uncertainties in the latent heat term itself may still dominate the overall error in the heat flux, errors resulting from such uncertainty are of opposite sign for melting and freezing, whereas the error arising from neglect of the advective term is independent of the sign of the phase change.

More generally, ice–ocean models often include additional processes such as percolation of surface meltwater through to the ice–ocean interface and precipitation and evaporation at the surface of leads. If percolating meltwater is assumed to have the salinity of the ice and be at the freezing point, Eqs. (6) and (7) become

$$\rho\gamma_S(S - S_b) = \rho(m + m_p)(S_b - S_i) \tag{30}$$

$$\rho_i c_i k_i \left.\frac{\partial T_i}{\partial z}\right|_b + \rho c\gamma_T(T - T_b) = \rho m L_i + \rho c m_p(T_b - T_{fi}), \tag{31}$$

where m_p is the percolation velocity, which is either specified or derived from an ice model, and T_{fi} is the freezing point appropriate for a salinity of S_i. The vertical velocity at the ice–ocean interface, taken as the level of the mean ice draft, is expressed as

$$w_b = \frac{\partial z_b}{\partial t} + \mathbf{u}_b \cdot \nabla z_b - A(m + m_p) - (1 - A)(p - e), \tag{32}$$

where p and e represent the rates of precipitation and evaporation respectively. We could now either apply separate advective and diffusive boundary conditions based on these, as in section 3, or, if we wished to maintain the simplicity of a material ice–ocean interface, we could apply a combined flux boundary con-

dition of the form given in (25). For salinity this would read

$$K_v \frac{\partial S}{\partial z}\bigg|_b = A(\gamma_S + m + m_p)(S_b - S) - (1 - A)(p - e)S. \quad (33)$$

Again we emphasize, by substitution from (30), that this yields the conservative boundary condition:

$$K_v \frac{\partial S}{\partial z}\bigg|_b = A(m + m_p)(S_i - S) - (1 - A)(p - e)S. \quad (34)$$

In contrast, neglect of the meltwater advection terms in (33) yields a boundary condition analogous to (24),

$$K_v \frac{\partial S}{\partial z}\bigg|_b = A\gamma_S(S_b - S) - (1 - A)(p - e)S, \quad (35)$$

and leads, on substitution from (30), to the nonconservative form:

$$K_v \frac{\partial S}{\partial z}\bigg|_b = A(m + m_p)(S_i - S_b) - (1 - A)(p - e)S. \quad (36)$$

In a two-equation formulation (34) would be the natural choice, but we note that the advection of percolating meltwater into the ocean has an impact on the ice–ocean heat flux, equivalent to the addition of the term $m_p(T_{fi} - T)$ to the right-hand side of (29), that is likely to be overlooked. This term would generally be small but, since the interfacial melt rate and percolation velocity are unrelated, it is possible that under certain conditions it could be the dominant term in the ice–ocean heat flux.

Larger-scale ice–ocean models often use a simpler one-equation formulation in which only the freezing point at the upper level or layer of the model is diagnosed. At each time step the computed temperature is reset to the freezing point and an appropriate amount of ice melted or frozen. Once again, because a separate boundary salinity is not calculated, the salinity balance is almost certainly computed correctly, but we suspect that the much smaller errors in the heat balance are routinely made. Of course, none of the errors discussed in this paper will be apparent in models that employ either surface restoring fluxes or diagnosed flux corrections, which are specifically designed to eliminate drift such as that in Figs. 5 and 7.

6. Closing remarks

Mellor et al. (1986) concluded that for small $|m/u_*|$, where u_* is the surface friction velocity, it is possible to neglect the influence of vertical advection in the formulation of boundary conditions at an ice–ocean interface. However, this conclusion was based on an assessment of the likely impact of vertical advection on the structure of the boundary layer. We do not dispute this finding and have implicitly made use of it in our parameterization of diffusion through the boundary layer. Nevertheless, we conclude that meltwater advection does play a role in the balance equations for tracers within a sub-ice water column and that this role may be neglected only if $|m/\gamma_x|$ is small. Since $\gamma_S/u_* \approx 4 \times 10^{-4}$ and the turbulent transfer coefficients for most other dissolved species are of a similar order of magnitude to that of salt, this latter criterion is a much more stringent requirement. We conclude that in general it is not possible to neglect the impact of meltwater advection.

We have presented a formulation of the flux boundary condition at an ice–ocean interface that includes both advective and diffusive fluxes and have demonstrated that inclusion of the advective term is necessary for the conservation of tracers. In practice, the advective fluxes are likely to be excluded only if the application of the boundary conditions involves the explicit diagnosis of the tracer concentration at the ice–ocean interface. There are relatively few models that include this level of sophistication and, although the heat flux error is an exception in that its occurrence is likely in almost all formulations, it is also the least significant of the errors. For other tracers, the commonly used boundary conditions already incorporate both advective and diffusive fluxes, but we believe the foregoing discussion to be of more than academic interest. As computing resources become ever more readily available, more detailed representations of key physical processes are likely to become part of even global-scale models. While our current knowledge of ice–ocean boundary physics is not sufficient to say with confidence that melting and freezing can be calculated more accurately if the boundary salinity is explicitly diagnosed, the inclusion of some additional tracers, in particular stable isotopes, does require the computation of the their boundary concentrations. Also, if the use of a nonmaterial interface at the ocean surface, as recommended by Huang (1993), becomes more commonplace, the distinction between the advective and diffusive parts of the tracer fluxes will become important. If a separate advective boundary condition is applied to the scalar equations, the purely diffusive flux boundary condition (24) must be employed to avoid double-counting of the meltwater advection term. Finally, as efforts are already being made to eliminate the need for flux corrections in coupled ocean–atmosphere general circulation models, it is important to isolate all possible causes of spurious drift in the properties of the ocean.

Acknowledgments. This study would not have been undertaken were it not for the attentive reading and constructive criticism of some of the authors' earlier work by others. Andreas Bombosch and Gregory Lane-Serff independently pointed out the inconsistency in Jenkins (1991). Chris Garrett, in his role as associate editor for an earlier version of Hellmer et al. (1998), asked a number of perceptive questions about the model

behavior. In addressing these we became aware of the possible size of the errors we have described. We gratefully acknowledge this invaluable input. Miles McPhee kindly supplied us with the data from the Snowbird ice station, used to generate Fig. 3, and provided an insightful review of the manuscript. We would like to thank Aike Beckmann, Ralph Timmermann, Keith Nicholls, Chris Doake, and Rupert Gladstone for reading through earlier versions of this paper. Their comments lead to significant clarification of a number of points. Collaborative work that gave rise to this paper was supported by U.S. Department of Energy Grant DE-FG02-93-ER61716 and NASA Polar Programs research Grant NAG5-4028.

APPENDIX

How Large Are the Errors?

The error in the tracer flux, per unit area of ice cover, associated with the use of boundary conditions of the form given in (21) and (24) is

$$Q_{X\mathrm{err}} = -\rho m(X_b - X), \tag{A1}$$

which, using (6) and ignoring the diffusive flux into the ice, can be rewritten:

$$Q_{X\mathrm{err}} = \rho\frac{m^2}{\gamma_X}(X_b - X_i). \tag{A2}$$

For tracers that are rejected from the ice on freezing, the drift will be toward higher concentrations. For equivalent melt/freeze rates the drift will tend to be slightly faster during freezing, when the boundary concentration is raised, than during melting, when the boundary is depleted in the tracer. By substituting for the melt rate from (7) we can express the error as

$$Q_{X\mathrm{err}} = \frac{(X_b - X_i)}{\rho\gamma_X L_i^2}\left[\rho c\gamma_T(T - T_b) + \rho_i c_i k_i\frac{\partial T_i}{\partial z}\bigg|_b\right]^2. \tag{A3}$$

The error in the heat flux is expressed

$$Q_{h\mathrm{err}} = -\rho cm(T_b - T), \tag{A4}$$

and, substituting directly for the melt rate, we obtain

$$Q_{h\mathrm{err}} = \frac{c(T - T_b)}{L_i}\left[\rho c\gamma_T(T - T_b) + \rho_i c_i k_i\frac{\partial T_i}{\partial z}\bigg|_b\right]. \tag{A5}$$

The external factors that determine the melt/freeze rate are the level of turbulence in the mixed layer, how far the temperature of the mixed layer deviates from the freezing point, and the temperature gradient in the ice. We focus on the salt and heat flux errors and seek to express (A3) for salinity and (A5) in terms of the above three factors. The level of turbulence determines the magnitude of the transfer coefficients for heat and salt, an effect that we parameterize by making γ_T a linear function of the friction velocity, u_*,

$$\gamma_T = C_h u_*, \tag{A6}$$

and setting the ratio γ_S/γ_T to a constant value. We take values of 0.01 for the factor C_h and 0.04 for the ratio γ_S/γ_T (McPhee et al. 1999; Holland and Jenkins 1999).

We consider first a situation, such as that addressed in the model described in section 3, in which the heat conduction term is negligible and to a good approximation we can assume melting and freezing to be driven entirely by temperature variations in the water column. Under these conditions, we can ignore the first terms on the left-hand side of both (6) and (7) and hence obtain a simple expression for the ratio of the salinity to temperature difference across the boundary layer:

$$\frac{(S_b - S)}{(T_b - T)} = \frac{(S_b - S_i)c\gamma_T}{L_i\gamma_S}. \tag{A7}$$

We refer to the elevation of the far-field temperature above the freezing point as the thermal driving,

$$T_* = T - \lambda_1 S - \lambda_2 - \lambda_3 P_b, \tag{A8}$$

and, using (8), we relate this to the temperature difference across the boundary layer:

$$T_b - T = \lambda_1(S_b - S) - T_*. \tag{A9}$$

Using (A7) we can rewrite this as

$$T - T_b = \frac{T_*}{\Lambda}, \tag{A10}$$

where

$$\Lambda = 1 - \frac{\lambda_1(S_b - S_i)c\gamma_T}{L_i\gamma_S}. \tag{A11}$$

This rearrangement is the origin of the effective heat transfer coefficient, defined in (17). With (A6) and (A10) substituted into (A3) and (A5) we obtain

$$Q_{X\mathrm{err}} = \frac{C_h(X_b - X_i)}{\rho(\gamma_X/\gamma_T)}u_*\left(\frac{\rho c}{L_i\Lambda}T_*\right)^2, \quad \text{and} \tag{A12}$$

$$Q_{h\mathrm{err}} = \frac{C_h}{\rho L_i}u_*\left(\frac{\rho c}{\Lambda}T_*\right)^2, \tag{A13}$$

where the temperature gradient terms within the parentheses of (A3) and (A5) have been set to zero, consistent with our assumption of negligible heat conduction.

Holland and Jenkins (1999) demonstrate that for thermal driving of <0.5°C, the small variations in boundary salinity have little impact on the effective heat transfer [Eq. (17)]. Taking S_b in (A11) to be constant at 34.5 psu, and taking the ice salinity to be zero, Λ has a constant value of 1.59. The only remaining variables in (A12) and (A13) are then the thermal driving, the friction velocity, and the difference in tracer concentration between the ice and the boundary. To evaluate the salt flux error we make the same approximations for the boundary and ice salinities. We then replace all constants in (A12) and (A13) with their numerical values

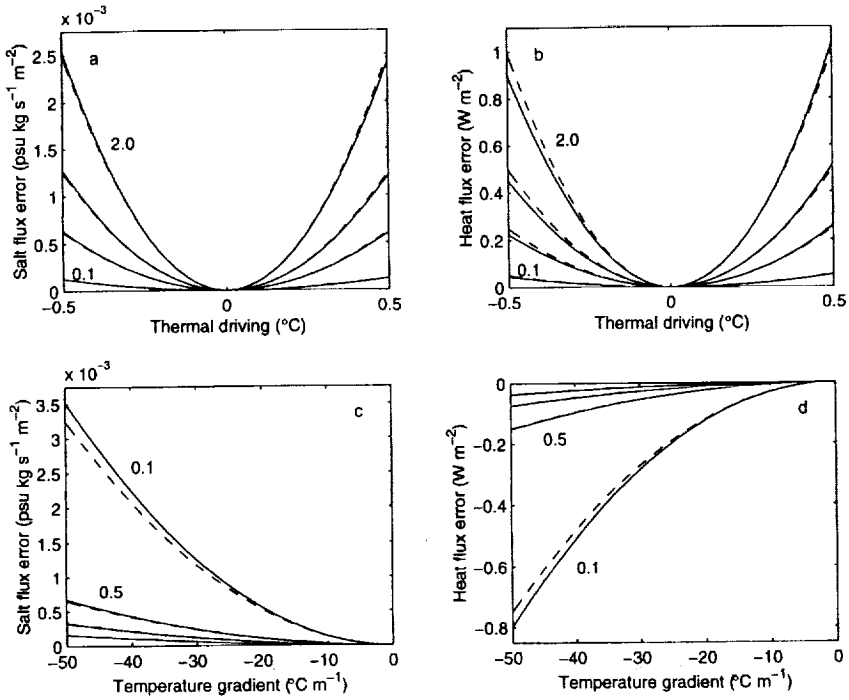

FIG. A1. Salt and heat flux errors induced by the neglect of meltwater advection across an ice–ocean boundary for friction velocities of 0.1, 0.5, 1.0, and 2.0 cm s^{-1}: (a) salt flux errors defined by (A12) (solid line) and by the approximation (dashed line) given in (A14a), (b) heat flux errors defined by (A13) (solid line) and by the approximation (dashed line) given in (A14b), (c) salt flux errors defined by (A17) (solid line) and by the approximation (dashed line) given in (A19a), and (d) heat flux errors defined by (A18) (solid line) and by the approximation (dashed line) given in (A19b).

and express the salt and heat flux errors, respectively, as

$$Q_{Serr} \approx 0.5 u_* T_*^2 \quad [\text{psu kg s}^{-1}\ \text{m}^{-2}] \qquad \text{(A14a)}$$

$$Q_{herr} \approx 200 u_* T_*^2 \quad [\text{W m}^{-2}], \qquad \text{(A14b)}$$

where u_* is in meters per second and T_* is in degrees Celsius.

We next consider the alternative situation where the thermal driving is zero and freezing proceeds as a result of the heat conducted into the cold ice above. Under these conditions we can combine (6) for salinity with (A9) to give an expression for the melt rate,

$$m = \frac{\gamma_S}{\lambda_1 (S_b - S_i)} (T - T_b), \qquad \text{(A15)}$$

and substituting this into (7) we can express the temperature difference across the oceanic boundary layer in terms of the temperature gradient at the base of the ice:

$$T - T_b = \frac{(1 - \Lambda)}{\Lambda} \frac{\rho_i c_i k_i}{\rho c \gamma_T} \left. \frac{\partial T_i}{\partial z} \right|_b . \qquad \text{(A16)}$$

With (A6) and (A16) substituted into (A3) and (A5) we obtain

$$Q_{Xerr} = \frac{(X_b - X_i)}{\rho C_h (\gamma_X / \gamma_T)} \frac{1}{u_*} \left(\frac{\rho_i c_i k_i}{L_i \Lambda} \left. \frac{\partial T_i}{\partial z} \right|_b \right)^2 \quad \text{and} \quad \text{(A17)}$$

$$Q_{herr} = \frac{(1 - \Lambda)}{\rho C_h L_i} \frac{1}{u_*} \left(\frac{\rho_i c_i k_i}{\Lambda} \left. \frac{\partial T_i}{\partial z} \right|_b \right)^2 . \qquad \text{(A18)}$$

Making the same approximations as before, the salt and heat flux errors can be written, respectively

$$Q_{Serr} \approx \frac{1.3 \times 10^{-9}}{u_*} \left(\left. \frac{\partial T_i}{\partial z} \right|_b \right)^2 \quad [\text{psu kg s}^{-1}\ \text{m}^{-2}] \qquad \text{(A19a)}$$

$$Q_{herr} \approx \frac{-3 \times 10^{-7}}{u_*} \left(\left. \frac{\partial T_i}{\partial z} \right|_b \right)^2 \quad [\text{W m}^{-2}], \qquad \text{(A19b)}$$

where, once again, u_* is in meters per second and the temperature gradient is in degrees Celsius.

The salt and heat flux errors given by (A12), (A13), (A14), (A17), (A18), and (A19) are plotted in Fig. A1 for a range of values of friction velocity, thermal driving, and basal temperature gradient. The quadratic dependence on the latter two factors means that the errors are always of the same sign. In the case of (A14) the effects of the errors are counteractive, in that the heat flux error should cause melting and dilution of the mixed

layer, while the salt flux error acts to increase the mixed layer salinity. In the case of (A19), both errors serve to accentuate the effects of freezing. We note that however the errors combine and whichever is dominant, the effect is most evident in the computed salinity because the properties of the seawater are constrained to follow closely the liquidus, which has an almost flat trajectory in temperature/salinity space.

REFERENCES

Gade, H. G., 1979: Melting of ice in sea water: A primitive model with application to the Antarctic ice shelf and icebergs. *J. Phys. Oceanogr.*, **9,** 189–198.

Hellmer, H. H., and D. J. Olbers, 1989: A two-dimensional model for the thermohaline circulation under an ice shelf. *Antarct. Sci.*, **1,** 325–336.

——, S. S. Jacobs, and A. Jenkins, 1998: Oceanic erosion of a floating Antarctic glacier in the Amundsen Sea. *Ocean, Ice, and Atmosphere: Interactions at the Antarctic Continental Margin,* S. S. Jacobs and R. F. Weiss, Eds., Antarctic Research Series, Vol. 75, Amer. Geophys. Union, 83–99.

Holland, D. M., and A. Jenkins, 1999: Modeling thermodynamic ice–ocean interactions at the base of an ice shelf. *J. Phys. Oceanogr.*, **29,** 1787–1800.

Huang, R. X., 1993: Real freshwater flux as a natural boundary condition for the salinity balance and thermohaline circulation forced by evaporation and precipitation. *J. Phys. Oceanogr.*, **23,** 2428–2446.

Jenkins, A., 1991: A one-dimensional model of ice shelf–ocean interaction. *J. Geophys. Res.*, **96,** 20 671–20 677.

——, and A. Bombosch, 1995: Modeling the effects of frazil ice crystals on the dynamics and thermodynamics of Ice Shelf Water plumes. *J. Geophys. Res.*, **100,** 6967–6981.

Josberger, E. G., 1983: Sea ice melting in the marginal ice zone. *J. Geophys. Res.*, **88,** 2841–2844.

Maykut, G. A., and M. G. McPhee, 1995: Solar heating of the Arctic mixed layer. *J. Geophys. Res.*, **100,** 24 691–24 703.

McPhee, M. G., 1983: Turbulent heat and momentum transfer in the oceanic boundary layer under melting pack ice. *J. Geophys. Res.*, **88,** 2827–2835.

——, 1990: Small-scale processes. *Polar Oceanography, Part A: Physical Science,* W. O. Smith Jr., Ed., Academic Press, 287–334.

——, G. A. Maykut, and J. H. Morison, 1987: Dynamics and thermodynamics of the ice/upper ocean system in the marginal ice zone of the Greenland Sea. *J. Geophys. Res.*, **92,** 7017–7031.

——, C. Kottmeier, and J. H. Morison, 1999: Ocean heat flux in the central Weddell Sea during winter. *J. Phys. Oceanogr.*, **29,** 1166–1179.

Mellor, G. L., M. G. McPhee, and M. Steele, 1986: Ice–seawater turbulent boundary layer interaction with melting and freezing. *J. Phys. Oceanogr.*, **16,** 1829–1846.

Millero, F. J., 1978: Annex 6: Freezing point of seawater. Eighth Report of the Joint Panel of Oceanographic Tables and Standards, UNESCO Tech. Paper Mar. Sci. 28, 29–31.

Nicholls, K. W., and A. Jenkins, 1993: Temperature and salinity beneath Ronne Ice Shelf, Antarctica. *J. Geophys. Res.*, **98,** 22 553–22 568.

Nøst, O. A., and A. Foldvik, 1994: A model of ice shelf–ocean interaction with application to the Filchner-Ronne and Ross Ice Shelves. *J. Geophys. Res.*, **99,** 14 243–14 254.

Scheduikat, M., and D. J. Olbers, 1990: A one-dimensional mixed layer model beneath the Ross Ice Shelf with tidally induced vertical mixing. *Antarct. Sci.*, **2,** 29–42.

Steele, M., G. L. Mellor, and M. G. McPhee, 1989: Role of the molecular sublayer in the melting or freezing of sea ice. *J. Phys. Oceanogr.*, **19,** 139–147.

Oceanographic conditions beneath Ronne Ice Shelf: a comparison between model and field data

Adrian Jenkins[1], David M. Holland[2] and Keith W. Nicholls[1]

[1]*British Antarctic Survey, Natural Environment Research Council, High Cross, Madingley Road, Cambridge, CB3 0ET, U.K.*

[2]*Courant Institute of Mathematical Sciences, New York University, 251 Mercer Street, New York City, NY 10012, U.S.A.*

Introduction

Within the cavity beneath Filchner-Ronne Ice Shelf (FRIS), High Salinity Shelf Water (HSSW) is transformed into Ice Shelf Water (ISW) by a combination of melting and freezing at the ice shelf base and mixing within the water column. Evidence of these processes is abundant, both in the distribution of meteoric and marine ice in the ice shelf and in the properties of the water masses occupying the continental shelf. Quantitative information on the rate of water mass transformation is harder to come by, and more elusive still are indications of the rate-controlling factors. Is the circulation primarily "pulled" by the injection of meltwater deep beneath the ice shelf, or "pushed" by the production of dense waters at the ice front? Are there dynamical constraints on the rate of exchange at the ice front? Answers to these questions are highly relevant to the problem of how sensitive the sub-ice cavities are to externally forced climatic change.

During the mid 1990's a series of instrument strings were deployed through FRIS, in and near to the Ronne Depression (Nicholls and Makinson, 1998). Temperature and current records from the two sites within the depression showed a clear seasonality in the strength of the HSSW inflow; evidence of the importance of external forcing even deep within the cavity. The nature of the seasonal cycle, in particular the rapid increase in the HSSW flux associated with wintertime freezing north of the ice front, was further suggestive of some dynamical control on the inflow.

In this paper we attempt to explain some of the key features of the seasonal signal using the results of a three-dimensional numerical model of ocean circulation within the FRIS cavity. We use a version of the Miami Isopycnic Coordinate Ocean Model (MICOM) that we have adapted for sub-ice-shelf domains (Holland and Jenkins, in press). The domain we use in this study is identical to that described by Jenkins and Holland (2000). The forcing is also almost identical, except that we have slightly modified the mid-winter surface salinity (Figure 1) to reflect the lower salinities that are currently generated over Berkner Bank (Nøst and Østerhus, 1998). The model was run for 10 years.

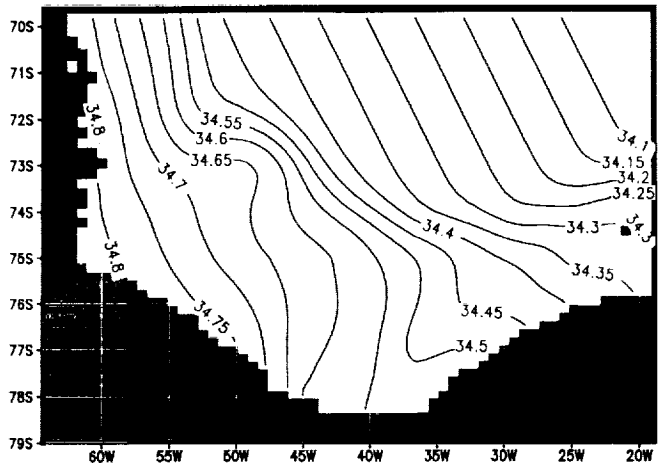

Figure 1: Surface salinity restoring field at the mid-winter maximum.

Time series data from the cavity

We focus on data from sites 2 and 3 (Figure 2). Two year, asynchronous temperature records from instruments suspended 30 to 80 m above the seabed at each site are shown in Figure 3. Both show relatively long periods with high temperatures, approaching the surface freezing point at site 2, followed by a gradual cooling and abrupt warming. Nicholls and Makinson (1998) interpreted the cooling trend as a weakening of the inflow to Ronne Depression, resulting from cessation of HSSW production at the ice front in summer. The warming was interpreted as the arrival of newer HSSW triggered by the onset of sea ice production and overturning of the water column north of the ice front.

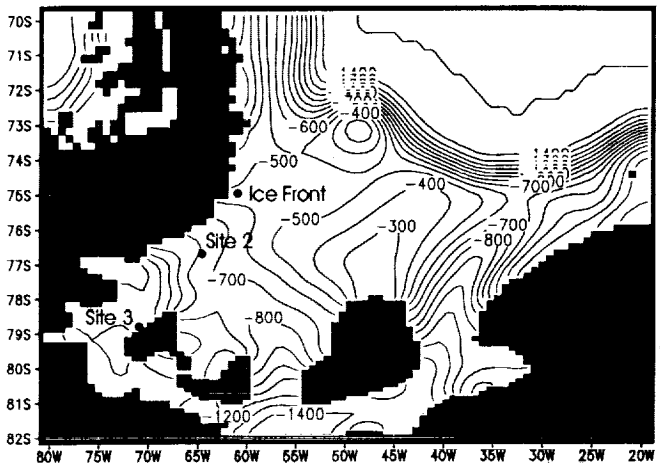

Figure 2: Sites mentioned in the text and bathymetry (m) throughout the model domain.

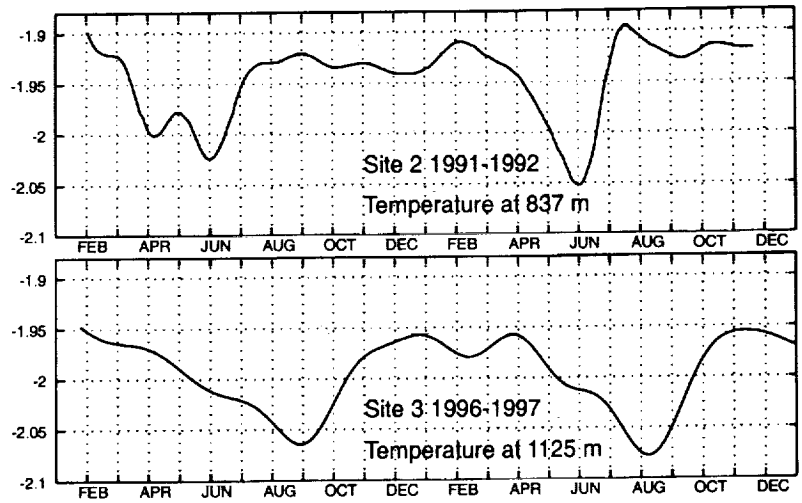

Figure 3: Time series of temperature (°C) recorded near the seabed at sites 2 and 3.

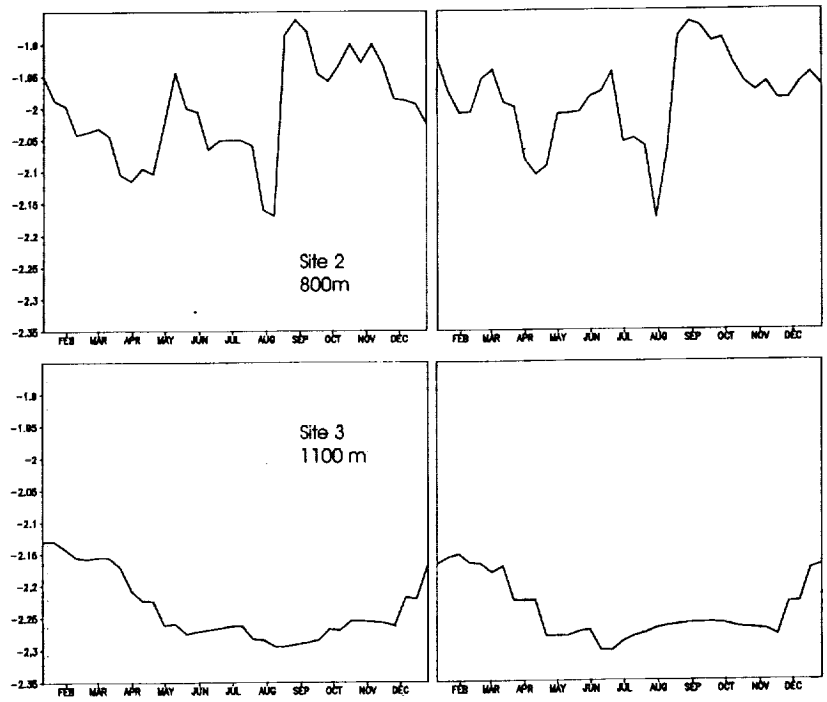

Figure 4: Time series of model temperatures (°C) from grid points close to the seabed at the locations shown in Figure 2.

The changes in temperature were assumed to reflect changes in the thickness of a lower layer of HSSW having relatively constant properties. The cooling was assumed to reflect the sinking of the thermocline past the level of the instrument. Of particular interest are the phasing and abruptness of the warming, associated with a thickening of the lower layer. The delay in arrival of the new HSSW was assumed to be related to the advection timescale from the ice front to the locations of the moorings, but the asymmetry between the abrupt warming and more gradual cooling was not explained.

Figure 4 shows the temperature signal from the last two years of the model run at the grid points corresponding to the positions of the instrumental records described above. While some features of the model results, such as the amplitude of the variability at site 2 and the mean temperature at site 3, do not match the observations, other features, such as the asymmetry of the cycles and relative phasing of the warming at the two sites, show quantitative similarities with the instrumental records. The absolute timing of the model temperature minima is about 2 months out, but this is not surprising given the simple symmetrical forcing that is applied north of the ice front. Given that symmetry in the forcing, the asymmetry in the model response is a particularly interesting feature, the source of which may give insight into the processes affecting the observations.

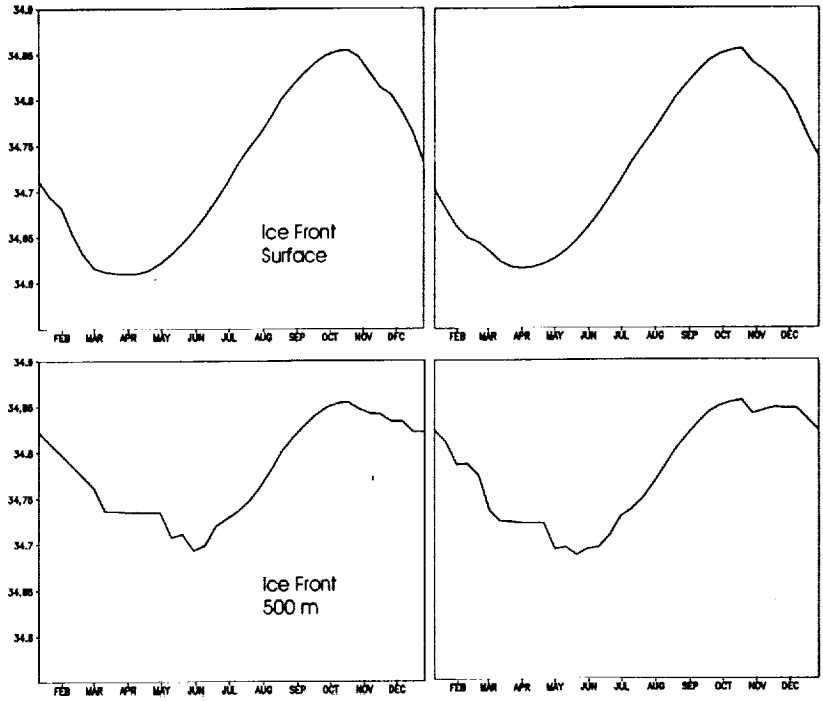

Figure 5: Time series of model salinity for grid points at the surface and near the seabed at the ice front location shown in Figure 2.

Time series data from the ice front

We illustrate the impact of the surface forcing at the ice front with time series of model salinity from 0 and 500 m at a point near the centre of Ronne Depression (Figure 2). The temperature at both levels shows relatively little variability, being held close to the surface freezing point for most of the time. At the surface the salinity deviates only marginally from the sinusoidal restoring cycle, but at 500 m an asymmetry is already apparent (Figure 5). The salinity at any depth in the water column is only forced directly by the atmosphere when the surface mixed layer has deepened sufficiently. At 500 m direct atmospheric forcing is felt only between mid-July and the end of October. After this brief period of HSSW renewal, the springtime retreat of the mixed layer leaves a water column consisting of a stack of isopycnic layers. As the HSSW spreads away from its site of formation, the layers thin and, at the 500 m level, the salinity falls with the sinking of each layer interface past this depth. Convection once again reaches this level when the rising surface salinity of the following winter becomes equal to, and eventually exceeds, the salinity at depth.

The impact of the relatively sharp onset of HSSW production is accentuated beneath the ice shelf by a coincident strengthening of the inflow to the cavity (Figure 6). While the flow is approximately parallel to the ice front during summer and autumn, as convection north of the ice front approaches full depth, the flow rapidly turns beneath the ice front. This is followed by a period of steady flow into the cavity, lasting until the mixed layer starts to retreat, at which time a gradual decrease in the inflow velocity begins. The result is the advection of a blob of new HSSW into the cavity, the front of which is particularly sharp. As the blob moves south along Ronne Depression, the domed isopycnals tend to slump, so that the signature of its arrival becomes progressively more diffuse. This thickening and thinning of the HSSW layer is the origin of the temperature variations shown in Figure 4.

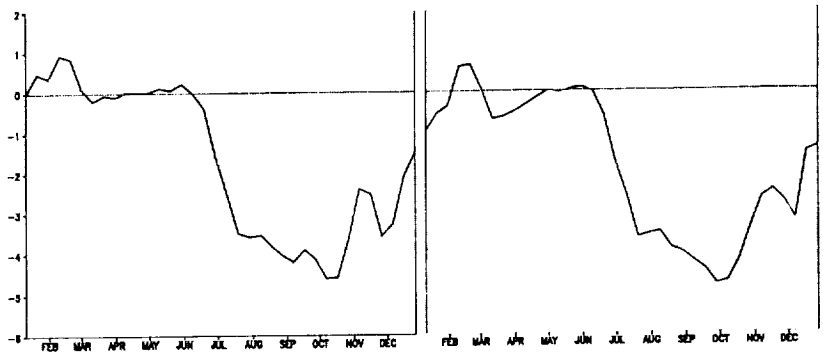

Figure 6: Time series of depth-mean velocity (cm s^{-1}) perpendicular to the ice front at the grid point shown in Figure 2. Negative values indicate flow into the cavity.

Summary

We have explored the propagation of the seasonal signature of HSSW production into the cavity beneath Filchner-Ronne Ice Shelf using MICOM. The focus of our study has been Ronne Depression, from where instrumental records are available for comparison. Agreement between model and observations is not perfect, but the phasing and shape of the annual cycle at two points along the depression is reasonably well simulated. Correct phasing implies that the speed of the inflowing HSSW is about right in the model. The asymmetric response of the model is intriguing, given the simple, symmetric forcing. We find that a combination of two factors is responsible for this. Production of HSSW only occurs for a relatively short period as the surface salinity approaches its maximum. At other times the deep parts of the depression are isolated from the surface buoyancy forcing. As HSSW production begins each year, there is a rapid transition from flow that is predominantly along the ice front, to flow that is directed almost perpendicular to the ice front. The new HSSW propagates into the cavity with a sharp front, that becomes gradually more diffuse with distance from the ice front. The seasonal forcing is felt throughout the model cavity and this, combined with the weak flow reported by Holland and Jenkins (in press) for an ideal cavity with no external forcing, suggests that our sub-ice version of MICOM is more "pushed" than "pulled".

Acknowledgements: This work has received financial support from the U.S. National Aeronautics and Space Administration (grant NAG-5-4028).

References

Holland, D.M. and A. Jenkins. In press. Adaptation of an isopycnic coordinate ocean model for the study of circulation beneath ice shelves, *Mon. Wea. Rev.*

Jenkins, A. and D.M. Holland. 2000. New results from the application of the ocean model MICOM to the Filchner-Ronne Ice Shelf, in *Filchner-Ronne Ice Shelf Programme*, Report No. 13, compiled by H. Oerter, pp. 19–25, Alfred-Wegener-Institute, Bremerhaven, Germany.

Nicholls, K.W. and K. Makinson. 1998. Ocean circulation beneath the western Ronne Ice Shelf, as derived from in situ measurements of water currents and properties, in *Ocean, Ice, and Atmosphere: Interactions at the Antarctic Continental Margin, Antarct. Res. Ser.*, Vol. 75, edited by S.S. Jacobs and R.F. Weiss, pp. 301–318, American Geophysical Union, Washington, D.C., U.S.A.

Nøst, O.A. and S. Østerhus. 1998. Impact of grounded icebergs on the hydrographic conditions near the Filchner Ice Shelf, in *Ocean, Ice, and Atmosphere: Interactions at the Antarctic Continental Margin, Antarct. Res. Ser.*, Vol. 75, edited by S.S. Jacobs and R.F. Weiss, pp. 267–284, American Geophysical Union, Washington, D.C., U.S.A.

Seasonal ventilation of the cavity beneath Filchner-Ronne Ice Shelf Simulated with an Isopycnic Coordinate Ocean Model

Adrian Jenkins[1], David M. Holland[2], Keith W. Nicholls[1], and Michael Schröder[3]

[1]*British Antarctic Survey, Natural Environment Research Council,*

High Cross, Madingley Road, Cambridge, CB3 0ET, U.K.

[2]*Courant Institute of Mathematical Sciences, New York University,*

251 Mercer Street, New York City, NY 10012, U.S.A.

[3]*Alfred-Wegener-Institut für Polar- und Meeresforschung,*

Postfach 120161, D-27515 Bremerhaven, Germany.

Abstract: Although it is isolated from direct atmospheric forcing, the ocean cavity beneath Filchner-Ronne Ice Shelf responds to the seasonal cycle of water mass production in the Weddell Sea. We have investigated the propagation of newly-formed shelf waters into the cavity using a version of the Miami Isopycnic Coordinate Ocean Model. The geographical focus of our study has been Ronne Depression, a seabed trough that crosses the Ronne Ice Front at its western end, and from where instrumental records are available for comparison with model output. Rapid warming is associated with the arrival of the new shelf waters at the instrumented sites beneath the ice shelf, and is followed by a more gradual cooling. The inflow to the cavity is regulated by the density structure in the water column to the north of the ice front, which in turn is controlled by

the seasonal advance and retreat of the mixed layer. Within the Depression, the inflow peaks during the short period around mid-winter when convection reaches full-depth and the densest waters are generated. Once the surface density starts to decline, the deeper parts of the Depression are isolated from the surface buoyancy forcing. Dynamic adjustment of the restratified water column leads to a gradual fall in the bottom salinity and an associated weakening of the inflow.

Introduction

Important water mass conversions take place beneath Antarctica's floating ice shelves. In the Ross and Weddell seas, High Salinity Shelf Water (HSSW) flows beneath the two largest ice shelves. There it is transformed into Ice Shelf Water (ISW), one of the precursors of Antarctic Bottom Water (AABW), by a combination of melting and freezing at the ice shelf base and mixing within the water column. HSSW forms through the enhancement of the shelf water salinity in regions where sea ice grows and is subsequently transported away, allowing further ice growth. While the net surface freshwater flux is determined by the wintertine atmospheric forcing, the properties and quantity of the resulting HSSW are also influenced by the rate at which the newly-formed shelf waters spread from their source region. Similarly, while the exchange of heat and freshwater at the ice shelf base effects the conversion of HSSW into ISW, the properties and quantity of ISW formed are determined by the rate at which HSSW ventilates the sub-ice cavity. Hence, the process of cavity ventilation has implications both for the properties of the abyssal ocean and for the mass budget of the Antarctic Ice Sheet, and represents one way in which the long-term evolution of ice sheet and ocean are linked.

This paper discusses the details of the ventilation process, as revealed by observations and the results of a recently developed model of the circulation beneath Filchner-Ronne Ice Shelf (FRIS).

Early models of sub-ice-shelf circulation [*MacAyeal*, 1984, 1985; *Hellmer and Olbers*, 1989; *Jenkins*, 1991] assumed a free exchange of waters across the ice front, driven by the density difference between the inflow and outflow. Later simulations [*Hellmer and Olbers*, 1991; *Hellmer and Jacobs*, 1992] illustrated how the ice shelf and seabed topography could combine to leave regions of the cavity relatively isolated from the waters beyond the ice front. The first three-dimensional ocean general circulation models to be applied to sub-ice-shelf domains [*Determann and Gerdes*, 1994; *Grosfeld et al.*, 1997] further highlighted the role of topography in guiding the circulation. Strong flows occurred parallel to water column isopachs, with little cross-isopach transport. In these models, the step in water column thickness at the ice front represented a considerable barrier to flow, such that only diffusive exchange occurred between the cavity and open ocean, unless the topography of the seabed and ice shelf base combined to allow continuity of isopachs across the ice front. The implication of these results is that the cavity circulation may be relatively insensitive to the atmospheric forcing north of the ice front, and may therefore be insulated from climatic change.

Observational data are sparse, particularly within the cavities, but suggest that outflows from beneath the Ross and Filchner-Ronne ice shelves each total ~1 Sv [*Foldvik et al.*, 1985; *Jacobs et al.*, 1992]. At this rate the cavity waters could be completely renewed on a timescale of 5-10 years, similar to the residence times inferred from tracer studies of the emerging waters [*Trumbore et al.*, 1991; *Gammelsrød et al.*, 1994]. During

the mid 1990's a series of instrument strings were deployed through FRIS in Ronne Depression, a seabed trough parallel to the western coast of the ice shelf (Figure 1). Temperature and current records from beneath the ice shelf showed a clear seasonality in the strength of the HSSW inflow [*Nicholls and Makinson*, 1998], providing evidence of the importance of external forcing even deep within the cavity. The nature of the seasonal cycle suggested that the dynamical control on the inflow was more complex than could be explained simply by the arrangement of water column isopachs. Current meters deployed at Site FR6, on the western flank of Ronne Depression just north of the ice front (Figure 1), confirmed this as a location of inflowing HSSW [*Woodgate et al.*, 1998]. A pronounced seasonal variation was found in the velocity perpendicular to the ice front. In contrast to the results of the three-dimensional models described above, these observations imply that much of the cavity is impacted by the seasonal atmospheric forcing north of the ice front, and so is likely to react relatively rapidly to changes in that forcing.

Time series observations from Ronne Depression

Two year, asynchronous temperature records from instruments suspended 30 to 80 m above the seabed at sites 2 and 3 (Figure 1) are shown in Figure 2a,b. Both show relatively long periods with high temperatures, approaching the surface freezing point at Site 2, followed by a gradual cooling and abrupt warming. *Nicholls and Makinson* [1998] interpreted these changes as the propagation of a seasonal signal, associated with the wintertime production of HSSW at the ice front, along the Ronne Depression. Following their arguments the cooling trend at each site is a result of the weakening of

the HSSW inflow to the cavity during the summer, while the abrupt warming is triggered by the onset of sea ice production north of the ice front and the inflow of new HSSW.

Nicholls and Makinson [1998] assumed that the changes in temperature reflected changes in the thickness of a lower layer of HSSW that had relatively constant properties. Warming and cooling trends recorded by each instrument were assumed to indicate the rising and falling of a thermocline past the level of the sensor, while periods of relatively constant temperature were thought to indicate the complete immersion of the instrument in the HSSW layer.

Of particular interest are the phasing and abruptness of the warming, associated with the thickening of the lower layer. The delay in arrival of the new HSSW was assumed to be related to the advection timescale from the ice front to the locations of the moorings. This gave an estimate of the inflow velocity that was consistent with estimates derived by other means. The asymmetry between the abrupt warming and more gradual cooling was not explained.

This simple picture of the seasonal intrusion of newly-formed HSSW into the cavity is drawn into question by the observations at Site FR6, where currents were measured at three levels in the water column over a period of about 2 yr. The records indicate a flow that had a relatively constant magnitude throughout the year, but a seasonally varying direction. The component of the velocity perpendicular to the ice front (Figure 2c) peaked in mid-summer and fell close to zero by mid-winter. So the onset of surface freezing in the coastal polynya is associated with a weakening flow into the cavity at this point, and the inflow of new HSSW does not begin to build until late winter, after its apparent arrival at Site 2.

The aim of this paper is to use a three-dimensional numerical model of ocean circulation within and to the north of the FRIS cavity to resolve this apparent discrepancy, and to help explain the character of the signals recorded beneath the ice shelf.

The model

We use a version of the Miami Isopycnic Coordinate Ocean Model (MICOM) that has been adapted for sub-ice-shelf domains [*Holland and Jenkins*, in press]. In this study our model grid covers the entire continental shelf of the southern Weddell Sea (Figure 1) at a resolution of 0.75° of longitude. We use 10 isopycnic layers with equal density steps between them, the density range being chosen to be consistent with that observed within the region covered by the model domain [*Olbers et al.*, 1992]. In addition there is a surface mixed layer, which has a spatially and temporally varying density.

The model is forced by restoring the mixed layer temperature and salinity in the open ocean to a prescribed pattern. The mid-winter surface salinity field is defined to increase both to the south and to the west and to decrease with increasing water depth, giving a pattern that is broadly similar to that of the bottom salinity observed over the shelf during summer [*Foldvik et al.*, 1985]. In this way we ensure that the distribution and properties of the HSSW that we generate in the model approximate those found in nature. The surface temperature is defined to be equal to the salinity-dependent freezing point at all times, consistent with the presence of a perennial ice cover over much of the domain. The mid-summer surface salinity field has a similar pattern to that of mid-winter, and the variation between summer and winter extremes is a simple sinusoid, the

amplitude of which increases to the south and west. This reflects the distribution of winter polynyas, which occur all along the Filchner-Ronne Ice Front, but are most extensive in the west [*Markus et al.*, 1998], where persistent barrier winds drive the ice north. In the model there is no wind forcing anywhere, while beneath the ice shelf the only direct forcing is the melting and freezing that is computed at the ice-ocean interface. Initial conditions are set according to *Olbers et al.* [1992], with simple extrapolation to fill the region beneath the ice shelf. The northern and eastern boundaries of the domain are solid walls, where we restore to initial conditions. The model is run for 10 years

Seasonal response of the cavity interior

Figure 3a shows the temperature signal from the last two years of the model run at the grid points and depths corresponding to the positions of the instrumental records shown in Figure 2a,b. While some features of the model response, such as the amplitude of the variability at Site 2 and the mean temperature at Site 3, do not match the observations, other features, such as the asymmetry of the cycles and the relative phasing of the temperature minima at the two sites, show quantitative similarities with the instrumental records. The times of the model temperature minima are about 2 months late, but this is not surprising given the simple symmetrical forcing that is applied north of the ice front. Given that symmetry in the forcing, the asymmetry in the model response is a particularly interesting feature, the source of which we address in the next section.

The process responsible for the variability shown in Figure 3 is precisely that envisaged by *Nicholls and Makinson* [1998]. HSSW flows along Ronne Depression as a

dense current that hugs the eastern flank (Figure 4). It is thus guided past the locations of the two moorings and the seasonal renewal of the HSSW causes the dense layer to abruptly thicken. This signature becomes progressively delayed and attenuated as it propagates along the Depression. At the location of site 2 the arrival of the new HSSW is accompanied by a 3–4 fold increase in basal melting (Figure 3b). While there is also a distinctive seasonal variation in melting at site 3, the peak is not coincident with the arrival of the HSSW. The warming there seems to be too deep in the water column to have a direct impact on the ice shelf. The phasing of the melt signature is likely to be the result of a further delay while the warming in the deep layers is advected to a site that is more favourable for upwelling, such as a grounding line, and may reflect a regional response to the increased heat supply to the mixed layer at the grounding line.

Forcing and response at the ice front

The net surface freshwater flux required to drive the mixed layer in Ronne Depression through its prescribed salinity cycle is illustrated in Figure 5a. This quantity is directly comparable to the growth rate of sea ice, estimates of which have been made for the entire coastal polynya of the southern Weddell Sea by *Renfrew et al.* [in press]. For the period 1992 to 1998, they estimate that the freezing season started on average in mid- to late February and ended on average in early November. Compared with these results, our model freezing season is of approximately the correct length, but occurs between 1 and 2 months late. The lag in the freezing cycle presumably explains why the temperature variations at sites 2 and 3 in our model appear to lag the observations by a couple of months. Overall the forcing is rather weak, with an average freshwater flux of

7.5 m yr^{-1} over the freezing season compared with over 20 m yr^{-1} estimated by *Renfrew et al.* [in press]. This may reflect the lack of wind forcing in the model, which would tend to drive HSSW northwards away from its site of formation in the coastal polynya. With the winds included in the forcing, we might anticipate that a larger freshwater flux would be required to restore the mixed layer to the prescribed salinity pattern.

We illustrate the impact of the surface forcing at the ice front with time series of model salinity (Figure 5b) from 0 and 500 m depth at the grid point corresponding to Site FR6 (Figure 1). The temperature at both levels shows relatively little variability, being held close to the surface freezing point for most of the time. At the surface the salinity deviates only marginally from the sinusoidal restoring cycle, but at 500 m an asymmetry is apparent. The salinity at any depth in the water column is only forced directly by the atmosphere when the surface mixed layer has deepened sufficiently. At 500 m direct atmospheric forcing is felt only between mid-July and the end of October. After this brief period of HSSW renewal, the springtime retreat of the mixed layer leaves a water column containing significant horizontal and vertical density gradients. Isopycnal surfaces are initially domed around the regions where the densest HSSW has formed. As the HSSW spreads away from its site of formation the isopycnals slump and, at the 500 m level in Ronne Depression, the salinity falls with the sinking of each layer interface past this depth. Convection once again reaches this level when the rising surface salinity of the following winter becomes equal to, and eventually exceeds, the salinity at depth.

The impact of the relatively sharp onset of HSSW production is accentuated beneath the ice shelf by a coincident strengthening of the inflow to the cavity. During the summer and autumn a steady current of ~10 cm s^{-1} carries fresher water from east to west

along the ice front, before turning north along the western coast (Figure 6a). At this time of year the current is confined to the surface layers. Geostrophic adjustment of the deeper layers leads to anti-cyclonic circulation around the regions of maximum salinity (Figure 6b). In the far west, a southerly flow carries HSSW into the cavity. This flow persists until the waters have been drained from the relatively shallow region to the north of FR6 (Figure 1). As convection deepens the mixed layer, more waters are drawn into the current that parallels the ice front until it extends over the full depth of the water column. This combined with the rising salinity in the shallower waters to the north of FR6, means that this current can no longer turn north along the coast, and is forced south beneath the ice shelf (Figure 6c). Melting at the ice front immediately restratifies the incoming water column, and almost unmodified HSSW drains south-west along Ronne Depression (Figure 6d). The melting contributes towards an outflow of ISW around 58°W, which is present in summer also, but is more diffuse then. This outflow is a feature that is common to all observations of oceanographic conditions at the ice front [e.g. *Foldvik at al.*, 1985; *Gammelsrød et al.*, 1994].

Averaged across the width of Ronne Depression the seasonal cycle in the inflow shows a dramatic saw-tooth shape (Figure 7a). The rapid increase in velocity perpendicular to the ice front begins as the surface forcing reaches its maximum and convection reaches full depth at FR6 (Figure 5). The warming at the location of Site 2 follows about one month later (Figure 3). As the surface forcing decays, and the water column restratifies, the decrease in the inflow velocity is more gradual. There is a secondary peak in late summer, corresponding to the final stages of adjustment to the previous winter's convection (Figure 6b). At the westernmost grid point along the ice

front, the seasonal cycle in the inflow (Figure 7b) is dominated by this secondary summer peak, the timing and magnitude of which, at this point, agree favourably with those of the maximum inflow recorded at Site FR6. However, the mid-winter inflow clearly has the greatest impact on the cavity, and the sudden onset and more gradual cessation of this flow is the origin of the asymmetry seen in Figure 3a.

The absence of any significant time lag between the observed and modelled peak inflow at the western end of the ice front probably results from the simplicity of the surface forcing (Figure 5a). Compared with observation [*Renfrew et al.*, in press] the freezing peak is too narrow. The longer, more gradual decline in the model freezing cycle means that the deep layers within the Depression begin their post-convection adjustment too soon. A premature weakening of the mid-winter inflow could also explain why the model temperature records (Figure 2b) fail to reproduce the period of sustained high temperatures that follow the abrupt warming seen in the observations (Figure 2a,b).

Summary and Conclusions

We have explored the propagation of the seasonal signature of HSSW production into the cavity beneath Filchner-Ronne Ice Shelf using MICOM. Agreement between model and observations is not perfect, but the phasing and shape of the annual temperature cycle at two points along Ronne Depression is reasonably well simulated. Correct phasing implies that the speed of the inflowing HSSW is about right in the model. The only direct observations of inflow to the cavity in this region come from the west of the Depression. Once again some of the details of the model results do not match

the observations, but the timing and magnitude of the maximum velocity are simulated reasonably well.

The response of the model cavity is governed by the density structure within the water column to the north of the ice front. Density reaches a maximum for a short period around mid-winter. This is when the most saline shelf waters are renewed and, simultaneously, flow into the cavity increases. These processes are forced directly by the surface freshwater flux, so their onsets are relatively rapid. The new HSSW propagates into the cavity with a sharp front that becomes gradually more diffuse with distance from the ice front. The inflow switches off more gradually as the water column north of the ice front is restratified, leaving the deeper layers once more isolated from the surface buoyancy forcing. This phase of decreasing salinity and generally weakening flow is governed by the dynamic adjustment of the deeper parts of the water column to the earlier forcing. Anti-cyclonic circulation around domed isopycnals tends to carry HSSW northwards in the middle of the Depression, but in the far west drainage into the cavity continues and even increases in strength into the summer. The impact of the seasonal forcing is seen throughout the model cavity, although the phasing is different in different geographical locations and at different levels in the water column.

The above analysis would suggest that the inflow recorded at Site FR6 is of secondary importance for the region further south and west along Ronne Depression, when compared with inflows that occur immediately to the east of the mooring site at other times of the year. This might seem a bold statement, if it were based solely on the results from a crudely-forced, relatively low resolution model, with smoothed and possibly erroneous seabed topography. However, we should re-emphasise that the

observations at sites 2 and 3 are difficult to explain if the main inflow of HSSW to the Ronne Depression peaks in mid-summer. We contend that the model demonstrates a plausible mechanism through which the records from the cavity and that at FR6 may be reconciled.

The exact processes by which the signature of seasonal forcing north of the ice front is transmitted to the interior of the model cavity will be an abstraction of those processes that operate in nature. However, the realistic features of the model response in Ronne Depression lends us confidence in drawing some important, general conclusions. It is clear that even remote parts of the sub-ice-shelf cavity are impacted by external forcing on sub-annual time-scales. This is because the exchange of waters across the ice front is controlled not just by the arrangement of water column isopachs, but by the three-dimensional distribution of density within the water column. We should therefore also anticipate a cavity response to inter-annual variations in sea ice production and to longer-term climatic trends. Such a response has implications for the mass balance of the ice shelf and the production of AABW.

Acknowledgements: This work has received financial support from the U.S. National Aeronautics and Space Administration (grant NAG-5-4028).

References

Determann, J., and R. Gerdes, Melting and freezing beneath ice shelves: Implications from a three-dimensional ocean-circulation model, *Ann. Glaciol.*, *20*, 413–419, 1994.

Foldvik, A., T. Gammelsrød, and T. Tørresen, Circulation and water masses on the southern Weddell Sea shelf, in *Oceanology of the Antarctic Continental Shelf, Antarct. Res. Ser.*, vol. 43, edited by S. S. Jacobs, pp. 5–20, AGU, Washington, D.C., 1985.

Gammelsrød, T., A. Foldvik, O. A. Nøst, Ø. Skagseth, L. G. Anderson, E. Fogelquist, K. Olsson, T. Tanhua, E. P. Jones, and S. Østerhus, Distribution of water masses on the continental shelf in the Southern Weddell Sea, in *The Polar Oceans and Their Role in Shaping the Global Environment*, edited by O. M. Johannesen, R. D. Muench, and J. E. Overland, pp. 159–176, AGU, Washington, D.C., 1994.

Grosfeld, K., R. Gerdes, and J. Determann, Thermohaline circulation and interaction between ice shelf cavities and the adjacent open ocean, *J. Geophys. Res., 102*, 15,595–15,610, 1997.

Hellmer, H. H., and S. S. Jacobs, Ocean interactions with the base of the Amery Ice Shelf, Antarctica, *J. Geophys. Res., 97*, 20,305–30,317, 1992.

Hellmer, H. H., and D. J. Olbers, A two-dimensional model for the thermohaline circulation under an ice shelf, *Antarct. Sci., 1*, 325–336, 1989.

Hellmer, H. H., and D. J. Olbers, On the thermohaline circulation beneath the Filchner-Ronne Ice Shelves, *Antarct. Sci., 3*, 433–442, 1991.

Holland, D. M., and A. Jenkins, Adaptation of an isopycnic coordinate ocean model for the study of circulation beneath ice shelves, *Mon. Wea. Rev.*, in press.

Jacobs, S. S., H. H. Hellmer, C. S. M. Doake, A. Jenkins, and R. M. Frolich, Melting of ice shelves and the mass balance of Antarctica, *J. Glaciol., 130*, 375–387, 1992.

Jenkins, A., A one-dimensional model of ice shelf-ocean interaction, *J. Geophys. Res.*, *96*, 20,671–20,677, 1991.

MacAyeal, D. R., Thermohaline circulation below the Ross Ice Shelf: A consequence of tidally induced vertical mixing and basal melting, *J. Geophys. Res.*, *89*, 597–606, 1984.

MacAyeal, D. R., Evolution of tidally triggered meltwater plumes below ice shelves, in *Oceanology of the Antarctic Continental Shelf, Antarct. Res. Ser.*, vol. 43, edited by S. S. Jacobs, pp. 133–143, AGU, Washington, D.C., 1985.

Markus, T., C. Kottmeier, and E. Fahrbach, Ice formation in coastal polynyas in the Weddell Sea and their impact on oceanic salinity, in *Antarctic Sea Ice: Physical Processes, Interactions and Variability, Antarct. Res. Ser.*, vol. 74, edited by, M. O. Jeffries, pp. 273–292, AGU, Washington, D.C., 1998.

Nicholls, K. W., and K. Makinson, Ocean circulation beneath the western Ronne Ice Shelf, as derived from in situ measurements of water currents and properties, in *Ocean, Ice, and Atmosphere: Interactions at the Antarctic Continental Margin, Antarct. Res. Ser.*, vol. 75, edited by S. S. Jacobs and R. F. Weiss, pp. 301–318, AGU, Washington, D.C., 1998.

Nøst, O. A. and S. Østerhus, Impact of grounded icebergs on the hydrographic conditions near the Filchner Ice Shelf, in *Ocean, Ice, and Atmosphere: Interactions at the Antarctic Continental Margin, Antarct. Res. Ser.*, vol. 75, edited by S. S. Jacobs and R. F. Weiss, pp. 267–284, AGU, Washington, D.C., 1998.

Olbers, D. J., V. Gouretski, G. Seiß, and H. Schröter, Hydrographic Atlas of the Southern Ocean, Alfred-Wegener-Institute, Bremerhaven, Germany, 1992.

Renfrew, I. A., J. C. King, and T. Markus, Coastal polynyas in the southern Weddell Sea: Variability of the surface energy budget, *J. Geophys. Res.*, in press.

Trumbore, S., S. S. Jacobs, and W. Smethie, Jr., Chloroflourocarbon evidence for rapid ventilation of the Ross Sea, *Deep-Sea Res.*, *38*, 845–870, 1991.

Woodgate, R. A., M. Schröder, and S. Østerhus, Moorings from the Filchner Trough and the Ronne Ice Shelf Front: Preliminary results, *in Filchner-Ronne Ice Shelf Programme*, *Report No. 12*, edited by H. Oerter, pp. 85–90, Alfred-Wegener-Institute for Polar and Marine Research, Bremerhaven, 1998.

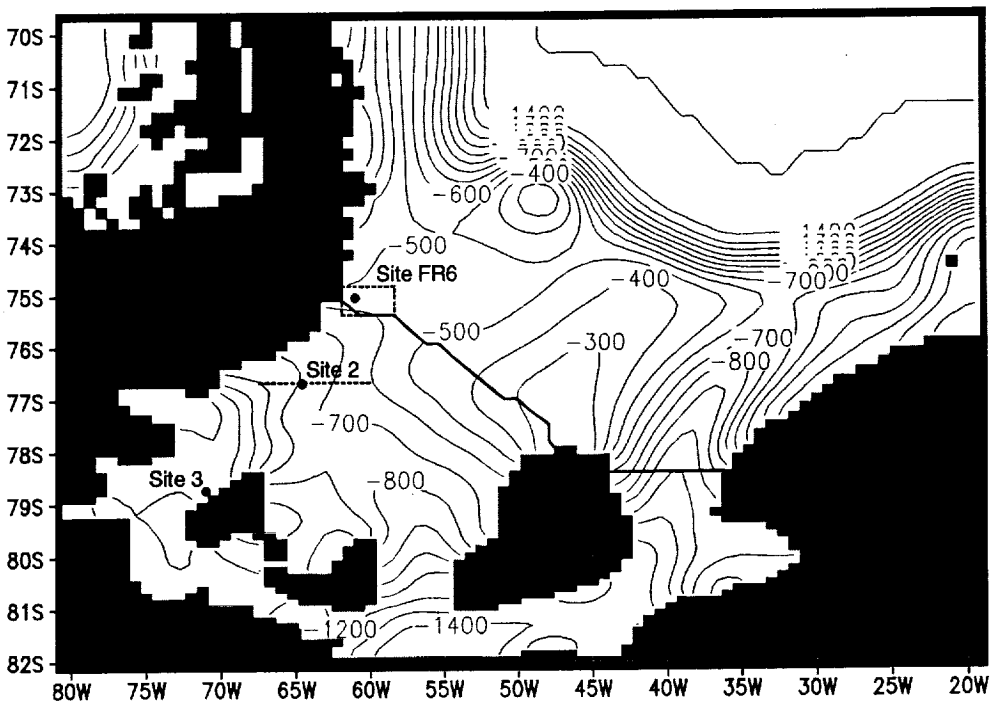

Figure 1: Model domain covering the continental shelf of the southern Weddell Sea. Contour lines indicate seabed depth (m). The region to the south and west of the bold line is covered by Filchner-Ronne Ice Shelf. Labelled solid circles indicate grid points that correspond to the location of moored instruments, the records from which are discussed in the text. The dashed line passing through Site 2 indicates the section plotted in Figure 4. The box shown around Site FR6 indicates the area used to characterise the surface forcing over Ronne Depression (Figure 5), the seabed trough in which all the moorings are located.

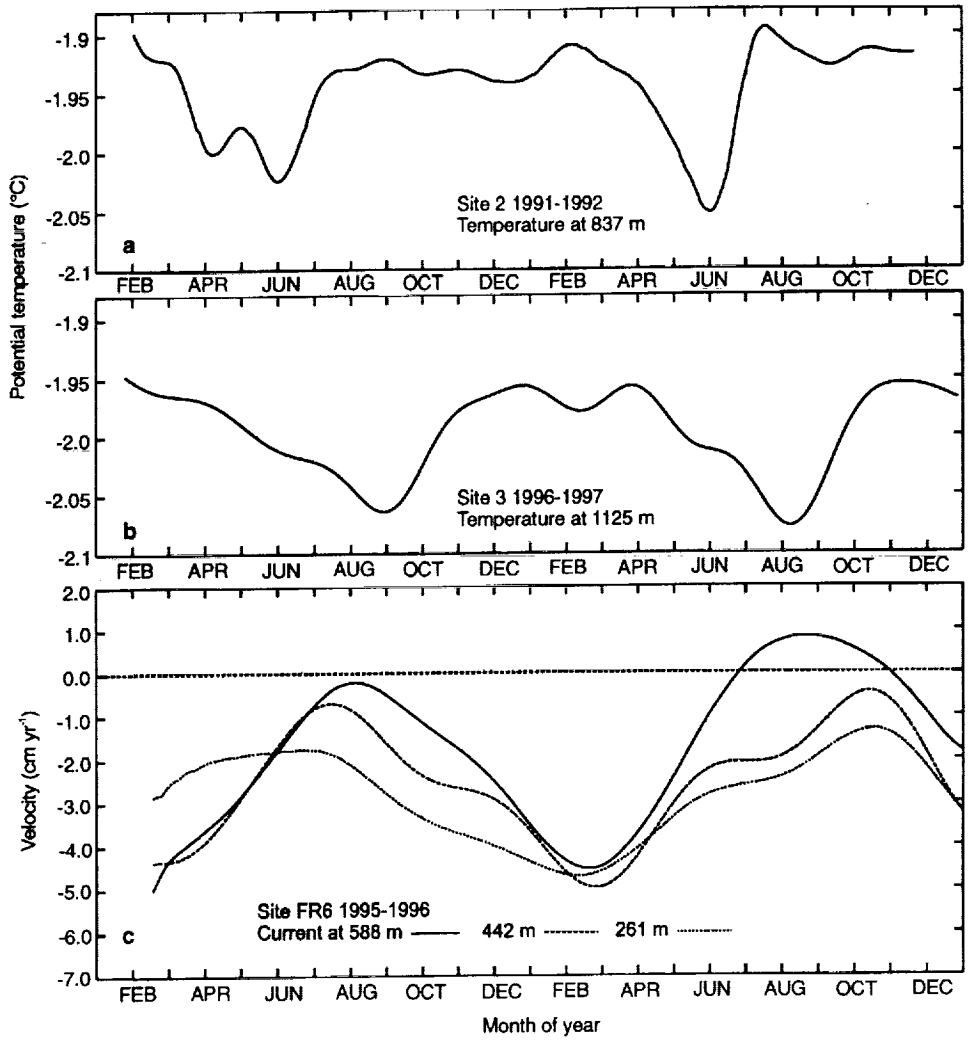

Figure 2: Time series of potential temperature recorded near the seabed at a) Site 2, and b) Site 3. c) Time series of currents perpendicular to the ice front recorded at Site FR6. Negative values indicate flow into the cavity.

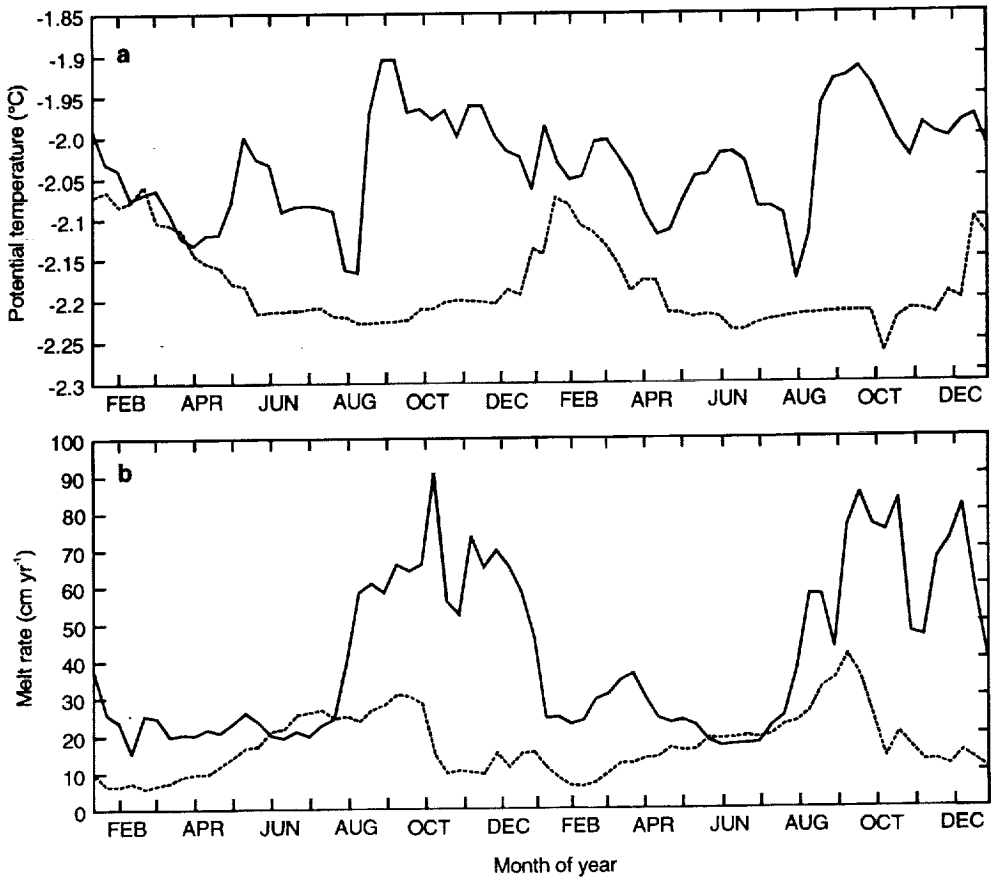

Figure 3: a) Time series of model potential temperature from two of the locations shown in Figure 1. The solid line is an average over the depth range 750 to 850 m below sea level from Site 2, while the dashed line is an average over 1100 to 1200 m at Site 3. b) Time series of modelled melt rate at the ice shelf base for Site 2 (solid line) and Site 3 (dashed line).

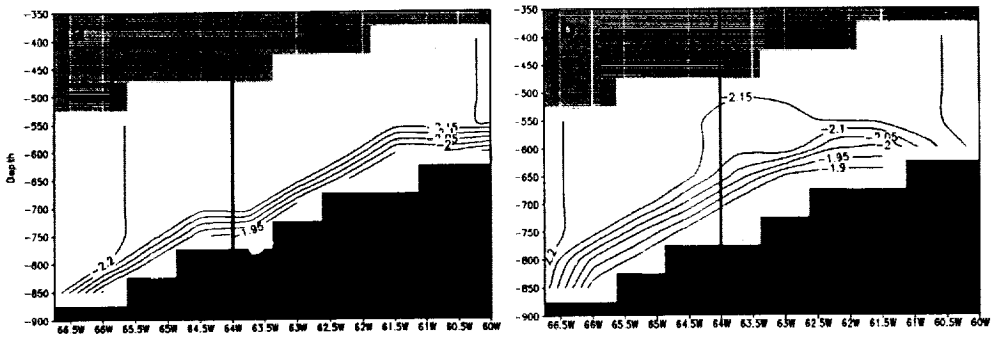

Figure 4: Cross-sections of model potential temperature along the line shown in Figure 1: a) in late July, before the arrival of the HSSW inflow, and b) in late August after the arrival of the inflow. The vertical line indicates the location of Site 2. Light shading denotes the ice shelf, dark shading the seabed.

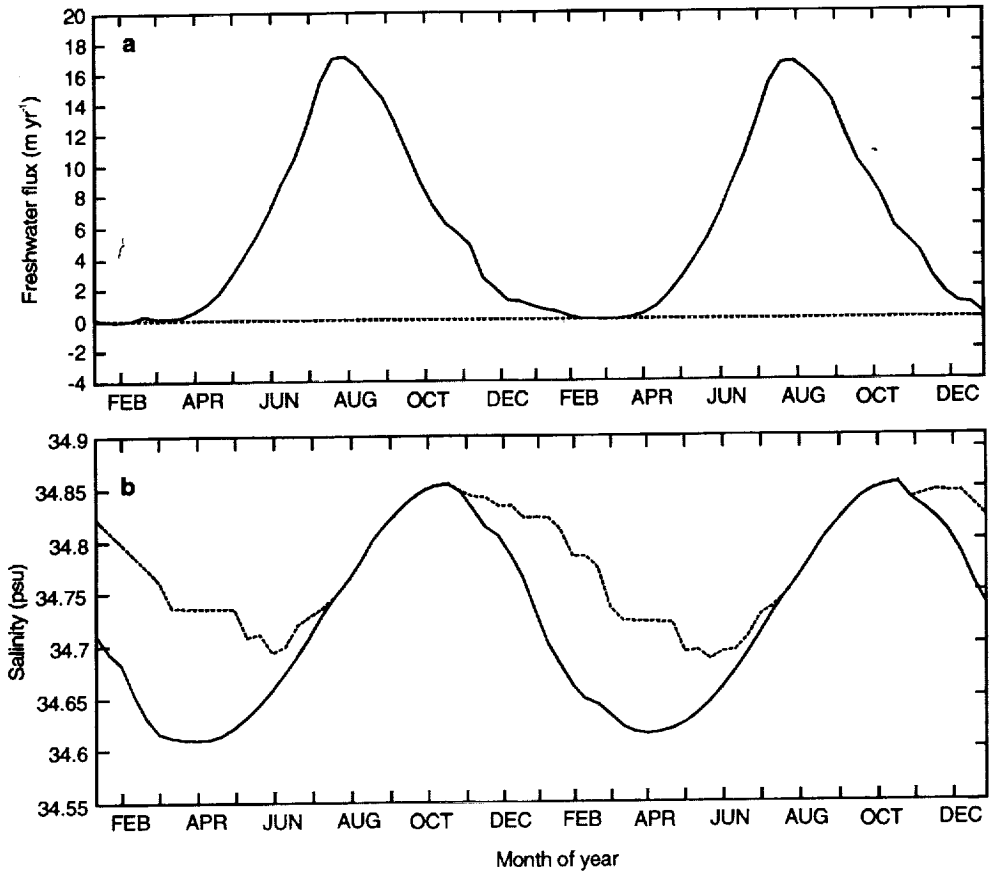

Figure 5: a) Time series of net surface freshwater flux, averaged over the box shown by the dotted outline in Figure 1. Positive values indicate removal of freshwater from the ocean, the model analogue of surface freezing. b) Time series of model salinity for the grid point labelled Site FR6 in Figure 1. The solid line indicates surface values, while the dashed line indicates values at a depth of 500 m.

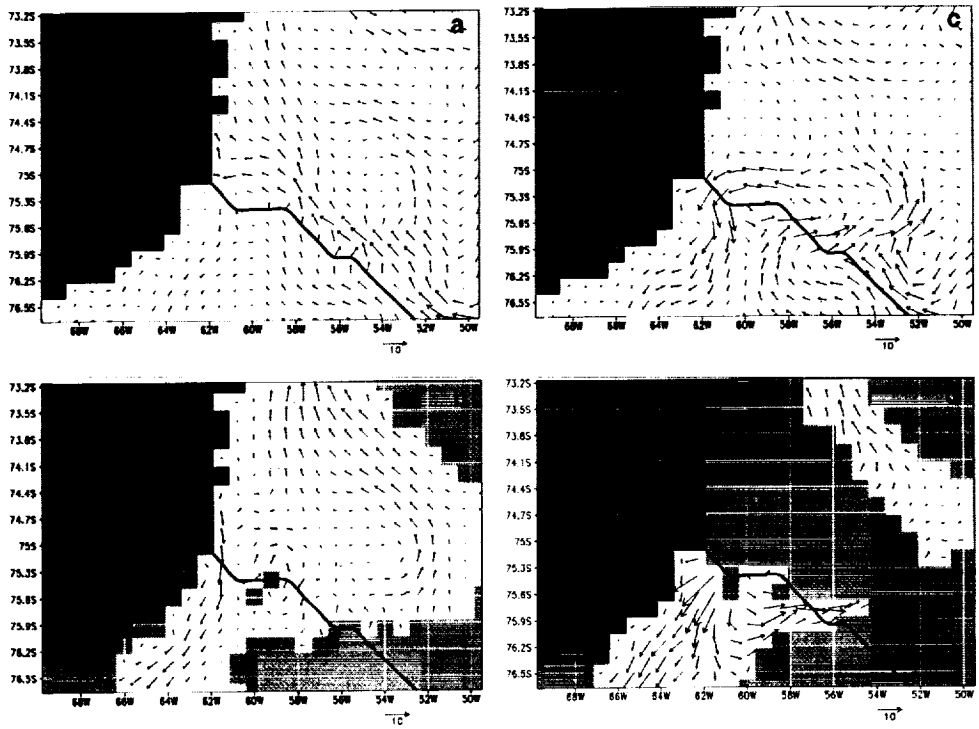

Figure 6: Current vectors showing circulation in a) the mixed layer in late January, b) layer 9 in late January, c) the mixed layer in late September and d) layer 9 in late September. The bold line indicates the ice front, while light shading in b) and d) shows where layer 9 does not exist. Scale (cm s^{-1}) is indicated by the arrows at the bottom right of each panel.

THE WEST ANTARCTIC ICE SHEET: BEHAVIOR AND ENVIRONMENT
ANTARCTIC RESEARCH SERIES, VOLUME 77, PAGES 237-256

A REVIEW OF PINE ISLAND GLACIER, WEST ANTARCTICA: HYPOTHESES OF INSTABILITY VS. OBSERVATIONS OF CHANGE

David G. Vaughan[1], Andrew M. Smith[1], Hugh F. J. Corr[1], Adrian Jenkins[1], Charles R. Bentley[2], Mark D. Stenoien[2], Stanley S. Jacobs[3], Thomas B. Kellogg[4], Eric Rignot[5] and Baerbel K. Lucchitta[6]

The Pine Island Glacier ice-drainage basin has been cited as the part of the West Antarctic ice sheet most prone to substantial retreat on human time-scales. Here we review the literature and present new analyses showing that this ice-drainage basin is glaciologically unusual. Due to high precipitation rates near the coast, Pine Island Glacier basin has the second highest balance flux of any extant ice stream or glacier. Well-defined tributaries flow at intermediate velocities through the interior of the basin and have no regions of rapid velocity increase. The tributaries coalesce to form Pine Island Glacier which has characteristics of outlet glaciers (e.g. high driving stress) and of ice streams (e.g. shear margins bordering slow-moving ice). The glacier flows across a complex grounding zone into an ice shelf. There, it comes into contact with warm Circumpolar Deep Water which fuels the highest basal melt-rates yet measured beneath an ice shelf. The ice front position may have retreated within the past few millennia but during the last few decades it appears to have shifted around a mean position. Mass balance calculations of the ice-drainage basin as a whole show that there is currently no measurable imbalance, although there is evidence that some specific areas within the basin are significantly out of balance. The grounding line has been shown to have retreated in recent years. The Pine Island Glacier basin is clearly important in the context of the future evolution of the West Antarctic ice sheet because theoretically, it has a high potential for change and because observations already show change occurring. There is, however, no clear evidence to indicate sustained retreat or collapse over the last few decades.

1. INTRODUCTION

The West Antarctic ice sheet (Figure 1) drains into the Southern Ocean by three main routes; through the ice streams on the Siple Coast into the Ross Ice Shelf, through the glaciers and ice streams feeding Ronne Ice Shelf, and through the glaciers which debouch, either directly or through small ice shelves, into the Bellingshausen and Amundsen seas. While the dynamics of the Siple Coast ice streams have been studied under the West Antarctic Ice Sheet Initiative (WAIS), and those feeding Ronne Ice Shelf have been studied under the auspices of the Filchner-Ronne Ice Shelf Programme (FRISP), there has been no coordinated effort to understand the dynamics of glaciers feeding the Bellingshausen and Amundsen seas. Consequently, this area is seldom visited and its glaciology is poorly understood.

The largest glaciers in this sector are Pine Island Glacier and Thwaites Glacier. Both transport ice from the interior of the West Antarctic ice sheet to the Amundsen Sea. In terms of the mass of snow accumulating in their

[1]British Antarctic Survey, Natural Environment Research Council, Cambridge, U.K.
[2]Geophysical and Polar Research Center, University of Wisconsin, Madison, Wisconsin
[3]Lamont-Doherty Earth Observatory, University of Columbia, New York
[4]Institute for Quaternary Studies, University of Maine, Orono, Maine
[5]Jet Propulsion Laboratories, Pasadena, California
[6]U.S. Geological Survey, Flagstaff, Arizona

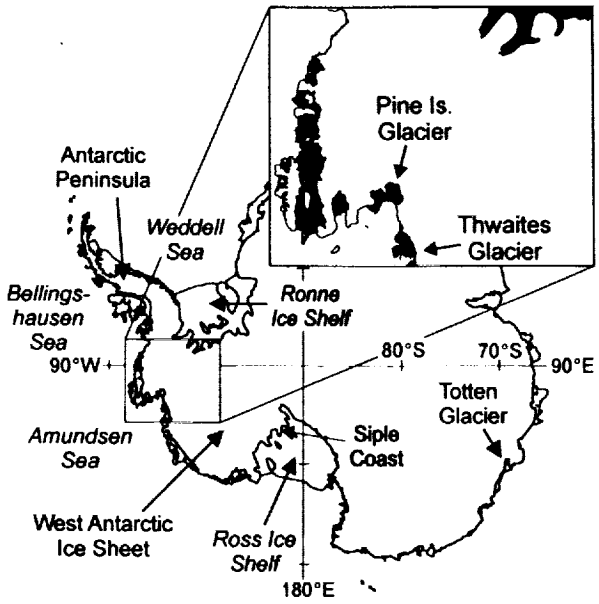

Fig. 1. Location map. Shaded region shows area covered by Figures 2-7.

catchment basins, Pine Island and Thwaites glaciers are respectively, the second and fifth most active basins in Antarctica [*Vaughan and Bamber*, 1998]. Pine Island Glacier alone accounts for around 4% of the outflow from the entire Antarctic Ice Sheet. The ice-drainage basins that feed these glaciers rest on beds as much as 2500 m below sea level, perhaps the deepest in Antarctica, and some authors have suggested that this in itself implies a great potential for rapid collapse [e.g. *Fastook*,1984; *Thomas*, 1984].

Together, Pine Island and Thwaites glaciers may be key to the future evolution of the West Antarctic ice sheet, but in this review, we concentrate on the Pine Island Glacier basin alone. We do this because, in addition to theories of instability, there is a growing body of observations of change and unsteady flow there. After some introductory notes we consider each of the component parts of the basin in turn. We then consider the interactions between the basin and sea into which it flows. We assess the evidence for both long-term and recent changes in the ice cover of the region. Finally, we consider how relevant those observations may be to models which have predicted that Pine Island Glacier might be particularly prone to collapse.

1.1 *Introductory notes on nomenclature*

1.1.1 ***Glaciers, ice streams and outlet glaciers***. The terms *glacier*, *ice stream* and *outlet glacier* are often loosely applied in the scientific literature as well as the non-specialist press. Here we use widely accepted definitions; *ice streams*, being areas of fast-moving ice sheet bounded by slower moving ice; *outlet glaciers*, being fast-moving ice bounded by nunataks or mountain ranges [*Bentley*, 1987; *Swithinbank*, 1954]; and *glaciers*, being a generic term for a "mass of snow and ice continuously moving from higher to lower ground, or if afloat, spreading continuously" [*Armstrong et al.*, 1973]. The distinction between ice streams and outlet glaciers "becomes rather hazy in practice" [*Bentley*, 1987], and is particularly acute in this case, as Pine Island and Thwaites *glaciers* share most of the dynamical characteristics of pure ice streams and need not be considered as inherently different.

1.1.2 ***Floating portion of Pine Island Glacier***. *Hughes* [1980] stated that neither Pine Island Glacier nor Thwaites Glacier are "buttressed by a confined and pinned ice shelf". *Stuiver et al.* [1981] also stated that they "are unimpeded by an ice shelf". At that time, the position of the grounding line of Pine Island Glacier was poorly mapped, and Pine Island Glacier was assumed to calve directly into Pine Island Bay. Airborne radar sounding soon revealed that the seaward ~80 km of the glacier was indeed floating *[Crabtree and Doake*,1982]. The original idea that these glaciers are dynamically different from others in West Antarctica has, however, persisted. Subsequent authors support the original notion, that Pine Island Glacier does not debouch through "an ice shelf" [*Kellogg and Kellogg*, 1987], "a substantial ice shelf" [*Jenkins et al.*, 1997], or "a large ice shelf" [*Rignot*, 1998]. Taking the widely accepted definition of an ice shelf, a "floating ice sheet of considerable thickness attached to a coast" [*Armstrong et al.*, 1973], it is clear that the floating portion of Pine Island Glacier, together with the adjacent floating areas, do constitute an *ice shelf*. Whether the ice shelf is a significant dynamic control on the glacier is, however, still an open question.

1.1.3 ***Pine Island Bay***. Strictly, *Pine Island Bay* is the bay (approximately 75 x 55 km) into which flows the ice from Pine Island Glacier [*Alberts*, 1981], although the term is sometimes applied to a rather wider area.

1.1.4 ***West Antarctic ice sheet***. The West Antarctic ice sheet is not an officially-recognised placename. We follow the accepted usage, meaning the term to refer to the ice sheet that covers West Antarctica, but excluding the Antarctic Peninsula.

1.2 *Introductory note on meteorology*

Since the 1960s, it has been widely recognised that the coastal portions of West Antarctica bordering on the

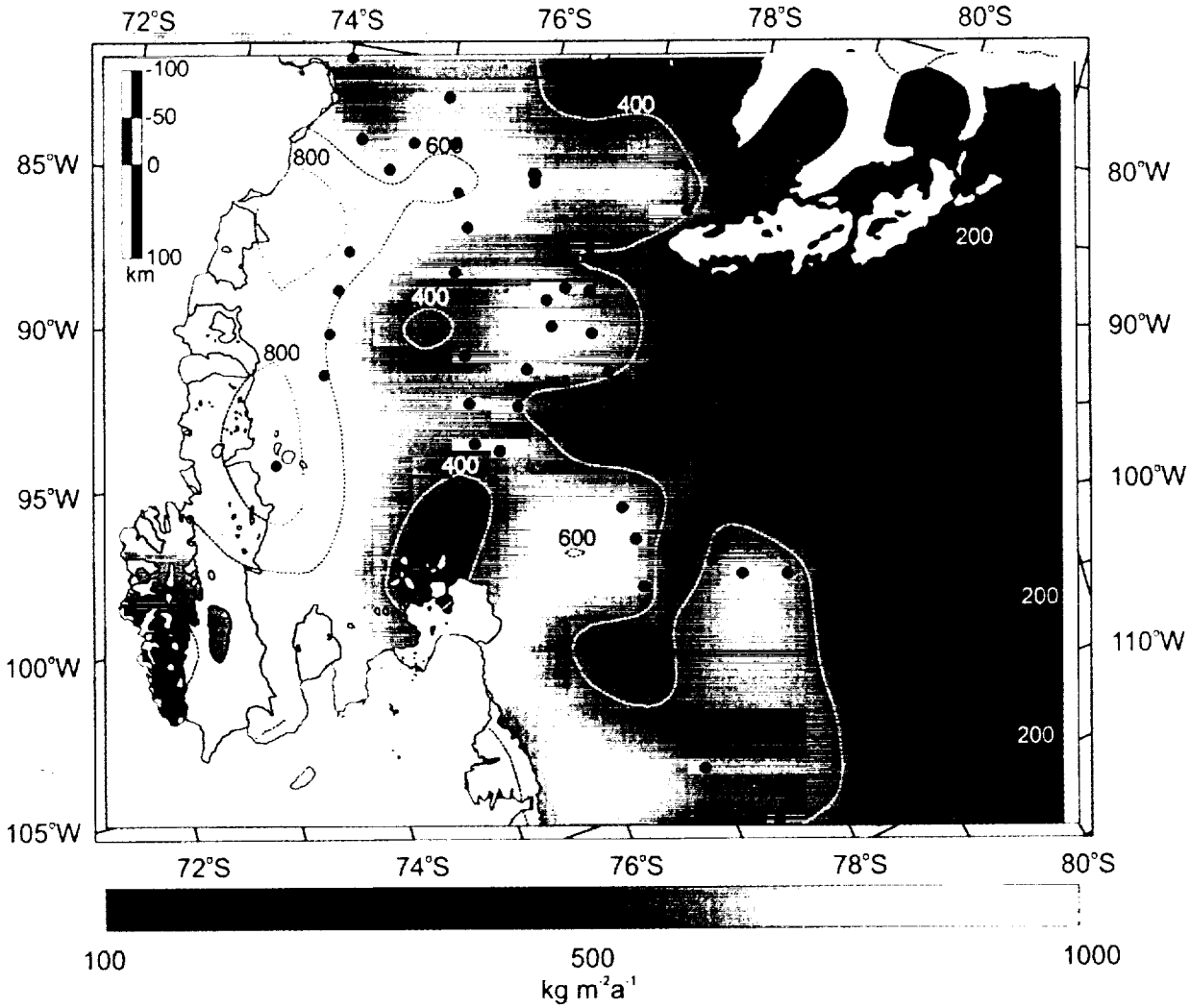

Fig. 2. Map of the area around the ice-drainage basin of Pine Island Glacier showing sites of measured surface mass balance (black dots), and interpreted grid of surface mass balance derived from field measurements and passive microwave satellite data from *Vaughan et al.* [1999].

Amundsen and Bellingshausen seas experience high precipitation rates compared with the rest of Antarctica [*Shimizu*, 1964]. These rates are matched only on the Antarctic Peninsula and around the coast of Wilkes Land [*Giovinetto*, 1964]. A recent compilation of net surface mass balance derived from *in situ* measurements and satellite data [*Vaughan et al.*, 1999] is shown in Figure 2. It agrees broadly with earlier estimates [eg. *Giovinetto and Bentley*, 1985], but shows an increased level of detail.

Meteorologically, the high precipitation rate in this sector results from synoptic-scale cyclones which travel around the Antarctic in the circumpolar trough. The trough is deepest over the Amundsen Sea, and many synoptic-scale cyclones come ashore here, producing considerable precipitation in the coastal zone. The effect is seen in moisture transport calculations [*Bromwich*, 1988] and in precipitation fields derived from General Circulation Models [*e.g., Connolley and King*, 1996]. Precipitation may be particularly high during winter months when the circumpolar trough moves south and more cyclones track across the coastal region [*Jones and Simmonds*, 1993].

There are no meteorological stations in the Bellingshausen/Amundsen Sea sector of West Antarctica. Consequently, direct measurements of decadal climate change (or stasis) have yet to be reported from either the Pine Island Glacier or Thwaites Glacier basins, although it

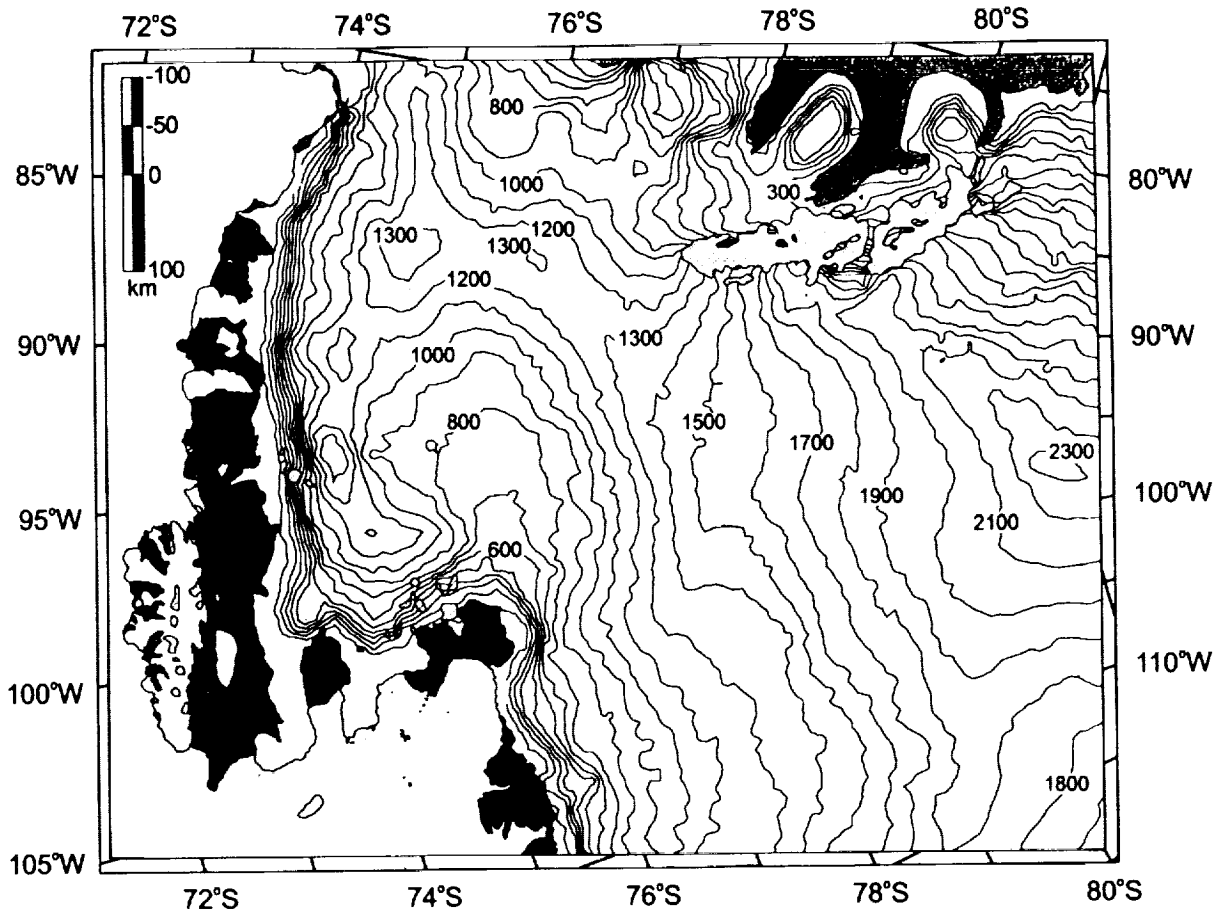

Fig. 3. Map of the area around Pine Island Glacier showing surface-elevation contours (meters above sea level) derived from Geodetic Mission of the ERS-1 satellite on a 5-km grid [*Bamber and Bindschadler*, 1997]. Ice shelves are shaded.

is possible that surface elevation changes (see Section 2.7) do reflect recent anomalous precipitation rates [*Wingham et al.*, 1998]. Offshore, a reduction in sea-ice extent in both the Amundsen and Bellingshausen seas has been noted in all seasons over the two decades prior to 1995 [*Jacobs and Comiso*, 1997]. This perhaps reflects a change in surface temperatures.

2. THE INTERIOR ICE-DRAINAGE BASIN

The interior of ice-drainage basins are sometimes viewed as cisterns, which passively accumulate ice and then supply it to the glacier (or ice stream) at whatever rate the glacier can transport it away. In this section, however, we present evidence that flow in the Pine Island Glacier basin is far from homogeneous. There is no clear distinction between ice-sheet and glacier flow and flow in the basin may have a strong influence on the overall configuration and glacier activity.

2.1 *Delineation of the ice-drainage basin*

Field-measurements of surface elevation in the Pine Island Glacier basin are few, but altimetry from the ERS-1 satellite is available to 81.9°S, which includes the entire basin. This altimetry has been used to create several high-resolution Digital Elevation Models (DEMs) of Antarctica [e.g., *Bamber and Bindschadler*, 1997; *Legresy and Remy*, 1997, *Stenoien*, 1998; *Liu et al.*, 1999].

Here we use a 5 km-resolution ERS-1-derived DEM [*Bamber and Bindschadler*, 1997] (Figure 3) to delineate the Pine Island Glacier basin and its neighbours. For comparison, a 200-m resolution DEM [*Liu et al.*, 1999] was also used to delineate the Pine Island Glacier basin

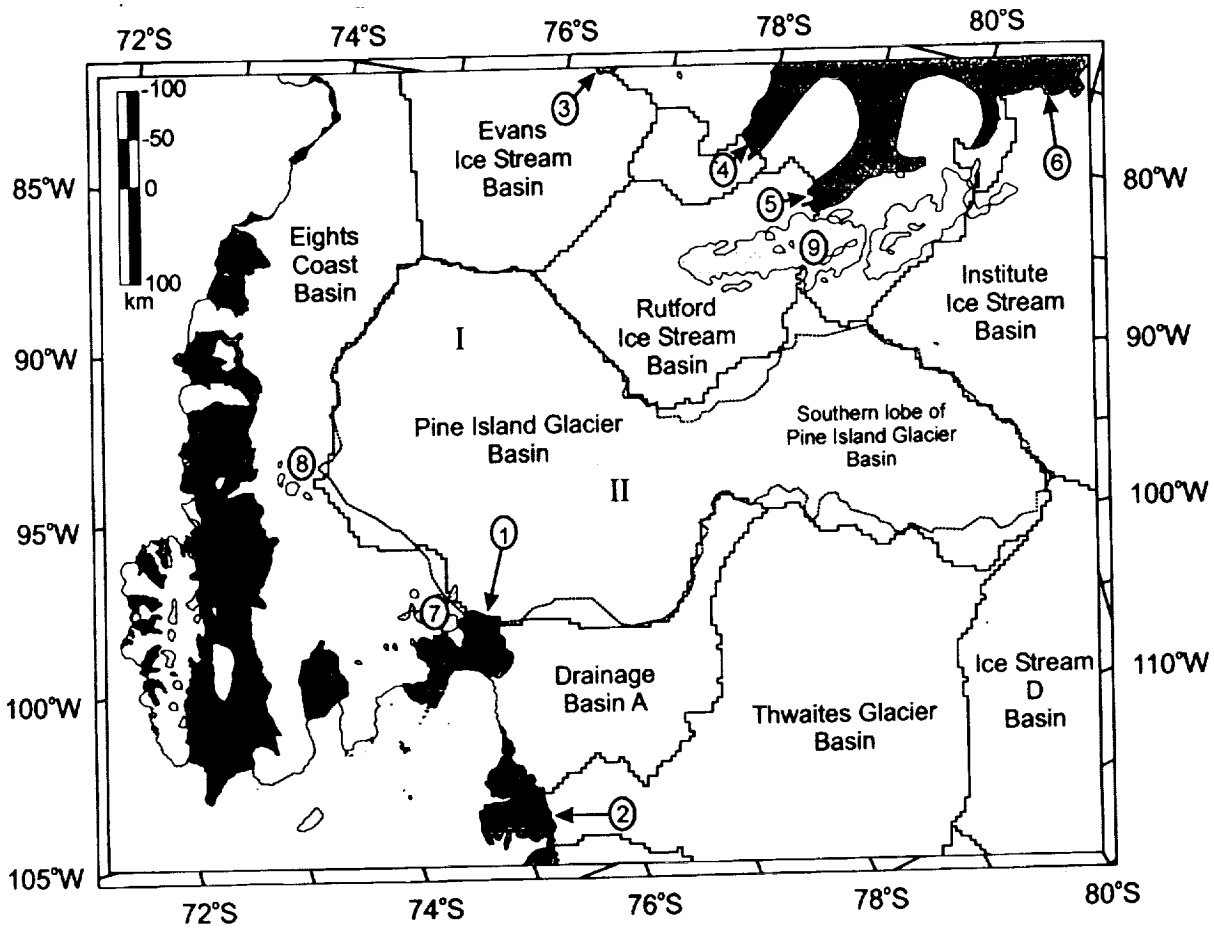

Fig. 4. Map of ice-drainage basins in the vicinity of Pine Island Glacier. Solid lines show basin boundaries derived from *Bamber and Bindschadler* [1997]. Dotted line shows the Pine Island Glacier basin derived from *Liu et al.* [1999]. Major glaciers are numbered and their direction of flow indicated by arrows; 1. Pine Island Glacier, 2. Thwaites Glacier, 3. Evans Ice Stream, 4. Carlson Inlet, 5. Rutford Ice Stream, 6. Institute Ice Stream. Rock outcrops are hatched with the major mountain ranges numbered (7. Hudson Mountains, 8. Jones Mountains, 9. Ellsworth Mountains). I and II indicate regions for which *Stenoien* [1998] presented separate mass-balance calculations. The coastline is derived from the Antarctic Digital Database [SCAR, 1993]. Ice shelves are shaded.

alone (Figure 4). The method used to produce the DEM is described in detail by *Vaughan et al.* [1999]. In summary, we identified segments of grounding line and then delineated the basins that feed them by tracing the line of steepest ascent inland as far as the ice divide. This procedure was limited to the grounded ice sheet as it assumes that ice-flow is parallel to the surface slope.

Table 1 shows the area of the Pine Island Glacier drainage basin measured from the above delineation, using an equal area projection, together with earlier estimates for comparison. There was considerable disagreement between the early estimates. While the more recent ones that rely on ERS-1 data have reduced the uncertainty, some still remains, presumably resulting from the different methods of analysis. For this review, we use an average of the three most recent values (165,000±7000 km^2) as a reasonable estimate of the basin area, although we accept that this may be improved in future by further analysis.

2.2 *Shape of the catchment basin*

The shape of the Pine Island Glacier basin (Figure 4) is similar to earlier delineations. It consists of two lobes, one immediately upstream of Pine Island Glacier and another,

Table 1. Estimates of ice-drainage basin area and balance flux for the Pine Island Glacier basin.

Basin Area (1000 km^2)	Balance Flux (Gt a^{-1})	Source
159	63.4	From DEM by *Liu et al.* [1999] and surface balance compilation of *Vaughan et al.* [1999]
175	69	From DEM by *Bamber and Bindschadler* [1997] and surface balance compilation of *Vaughan et al.* [1999]
159 ± 1	63.9 ± 6	[*Rignot*, 1998]
	76	[*Bentley and Giovinetto*, 1991] (Arithmetic mean of estimates from *Crabtree and Doake* [1982] and *Lindstrom and Hughes* [1984])
182	65.9± 5	[*Lindstrom and Hughes*, 1984]
214 ± 20	86± 30	[*Crabtree and Doake*, 1982]

the *southern lobe*, feeding the first through a neck less than 100 km across. A delineation of the catchment basins of the 70 largest glaciers in Antarctica, by a similar method, showed this configuration is unusual [*Vaughan and Bamber*, 1998]. Generally, ice-drainage basins which drain through glaciers or ice streams, are uniformly convergent. Only the Ice Stream C basin has a similar "necked" shape [*Joughin et al*, 1999]. It is possible that the existence of the *southern lobe* of the Pine Island Glacier basin indicates unsteady conditions in the basin, with this lobe currently being transferred between catchment basins. Alternatively, it may simply reflect unusual bed morphology.

2.3 *Mass input and balance flux*

Overlaying the basins for Pine Island Glacier derived in Section 2.2, on a grid representing the mean surface balance over Antarctica [*Vaughan et al.*, 1999], we have estimated the total rate of snow accumulation in the Pine Island Glacier basin (Table 1). This is the amount of ice that must leave the basin for mass balance to be maintained and is termed the *balance flux*. The aggregate of the three most recent estimates gives a balance flux for Pine Island Glacier of (66 ± 4) Gt a^{-1}. The uncertainty is derived from the spread of the results, but is consistent with the uncertainties in area (± 4%) and accumulation (± 5%) [*Vaughan et al.*, 1999].

A similar process has been used to find the balance fluxes of the other major glaciers of Antarctica, and while many glaciers are fed by basins with larger areas, only one balance flux exceeds that of Pine Island Glacier. Totten Glacier, East Antarctica has a balance flux of around 75 Gt a^{-1} [*Vaughan and Bamber*, 1998]. Outside Antarctica, the most active glacier is Jacobshavns Isbræ, Greenland which supports about half this flux [*Bindschadler*, 1984].

2.4 *Glacier tributaries*

Two techniques employing satellite data and yielding wide coverage allow us to identify areas where ice-flow is concentrated within the interior of the ice-drainage basin. The pattern that emerges is one of great complexity, with many tributaries coalescing to form the main glacier.

2.4.1 ***Satellite Altimetry.*** We can derive some understanding of the distribution of ice flow in the interior of the basin using the DEMs discussed in Section 2.1. The method first calculates the flow-direction for each cell. It then assigns to each cell a numerical value corresponding to the number of other cells whose accumulation will eventually flow through it. The technique is known as *flow-accumulation* and a grey-scale representation of this *flow-accumulation* grid (Figure 5) gives an indication of where flow is more convergent within the basin.

Figure 5 shows a system of tributaries which merge about 100 km above the grounding line to form the single unit of flow which is Pine Island Glacier. These tributaries are identifiable several hundreds of kilometers inland, much further inland than the point where the ice enters a more confined channel, previously suggested to be the start of channelized ice flow [*Lucchitta et al.*, 1995; *Lucchitta et*

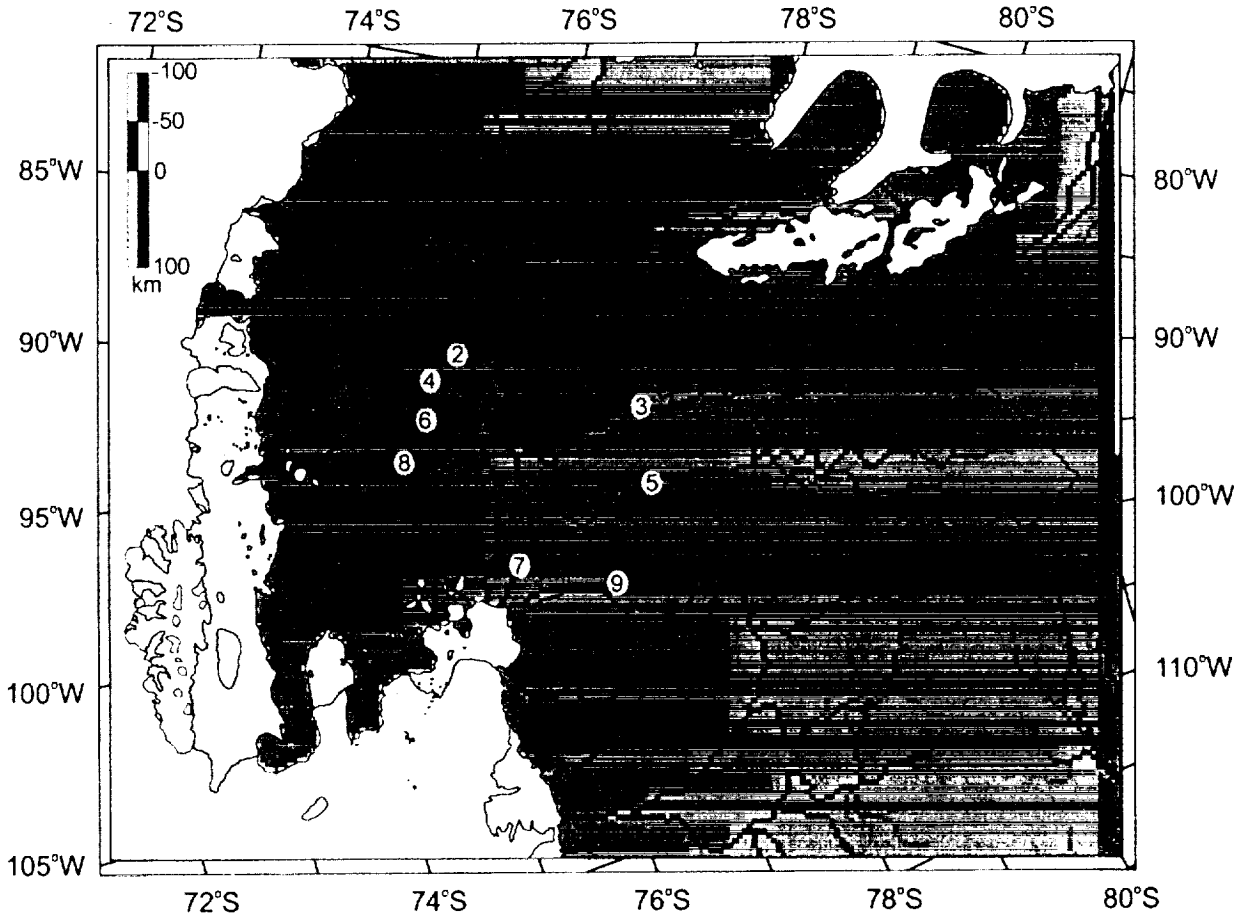

Fig. 5. Map of area around the basin drained by Pine Island Glacier showing flow-accumulation derived from 5-km resolution surface elevation grid. Grid cells are shaded such that cells fed by many others are darker than those fed by only a few. The darker areas thus represent areas into which the flow is channelled. The numbered features are the tributaries as identified by *Stenoien* [1998]. Stenoien's tributaries 1 and 10 are not resolved on this representation.

al., 1994]. This set of tributaries is almost the same as that determined by *Stenoien* [1998] from interferometric Synthetic Aperture Radar (SAR) images (see figure 6.14 of *Stenoien* [1998]) and in Figure 5 they are numbered using Stenoien's designation. One tributary (5) drains much of the southern lobe of the catchment basin described in Section 2.2 Its presence is perhaps not surprising given the narrow neck where the southern lobe joins the rest of the drainage basin.

Stenoien [1998] suggested that similar patterns of tributaries have not been seen elsewhere, and that they are perhaps unique to Pine Island Glacier. There is, however, evidence elsewhere in Antarctica for tributary systems in other basins. Bright margins in ERS-1 SAR data have shown that Evans Ice Stream forms at the confluence of at least five tributaries [*Jonas and Vaughan*, 1996]. Radarsat data shows that Recovery Glacier has two tributaries which extend hundreds of kilometers inland [*Jezek, et al.*, 1998]. Flowlines in Landsat imagery show that Institute Ice Stream also has several tributaries [*Mantripp et al.*, 1996]. Finally, *Joughin et al* [1999] show a tributary system feeding ice streams on the Siple Coast.

The presence of several tributaries in the interior drainage system may imply that Pine Island Glacier is unlikely to respond dramatically to changes in one locality. For example, if "water-piracy" [*Alley et al.*, 1994] or a reduced supply of basal till were to shut-off one of the tributaries, the others would probably be unaffected and the flux in Pine Island Glacier may suffer little change.

2.4.2 ***Interferometric SAR.*** *Goldstein et al.* [1993] used SAR data from the ERS-1 satellite to construct interferometric SAR (InSAR) images of ice flow in

Antarctica. These showed ice movement only along the line of sight to the satellite, but the method has since been refined to produce a 2-dimensional velocity-field for parts of the interior of the Pine Island Glacier basin [*Stenoien*,1998]. The procedure yields an understanding that is more quantitative than that from the satellite altimetry presented above, although coverage of the Pine Island Glacier basin is less complete. *Stenoien's* [1998] 2-dimensional velocity field covers much of the northern part of the drainage basin (see figures 5.14 and 5.15 of *Stenoien* [1998]). The data cover the upstream regions of many of the tributaries (2, 4 and 6 in Figure 5) and the middle regions of two which originate in the southern lobe of the basin (3 and 5 in Figure 5). There are no points of ground control in this area and Stenoien derived an absolute velocity field by assuming that a saddle on the ice divide had zero velocity. Ice speed away from the tributaries is low (0-50 m a^{-1}) but increases within them to more than 150 m a^{-1} upstream of the confluence of tributaries 2, 3 and 5 (Figure 5).

Of interest is Stenoien's observation that none of the tributaries for which data are available shows a rapid increase in ice speed, but rather a gradual increase down the length of each tributary. A similar pattern has also been observed on other West Antarctic ice streams *(Joughin et al.*, 1999) The lack of a sudden velocity increase, suggests notions of a bi-stable state of glacier-flow i.e. fast or slow, may be unrealistic, but rather that a progressive response to changing boundary conditions is possible.

Taken together, InSAR and flow-accumulation show that the interior of the Pine Island Glacier basin is complex with around 10 tributary ice streams coalescing to form a single glacier. None of these tributaries appears to have a well-defined region of rapid velocity increase and what controls their location and longevity remains to be determined. Radar data presented in Section 2.6 suggest that the control may be through basal conditions. However, at present even sophisticated thermomechanical models of the area fail to reproduce this complex flow pattern [e.g. *Payne*, 1999].

2.5 *Subglacial topography*

The bed topography of the West Antarctic ice sheet was first mapped in detail using a combination of traverse data, airborne sounding data and TWERLE balloon altimetry [*Jankowski and Drewry*, 1981]. While this study clearly delineated the major subglacial features of the area, the availability of new data prompts us to repeat the exercise.

Figure 6 shows a new compilation of bed topography beneath the grounded portion of the Pine Island Glacier basin. To create a grid of ice thickness we used (Figure 6a) traverse data [*Bentley and Ostenso*, 1961; *Behrendt*, 1964; *Bentley and Chang*, 1971], airborne radar data [*Jankowski and Drewry*, 1981; British Antarctic Survey unpublished data] and rock outcrops, which were used as an isopleth of zero ice thickness. The resulting grid of ice thickness was subtracted from the ERS-1 derived DEM of surface elevation described in Section 2.1 to produce bed topography (Figure 6b).

The bed topography (Figure 6b) shows clearly the main features identified in earlier compilations: the Bentley Subglacial Trench; the Byrd Subglacial Basin, which here reaches almost 2000 m below sea level; and between these depressions, the "sinuous ridge" described by *Jankowski and Drewry* [1981]. The Ellsworth Subglacial Highlands, are also well-defined. Despite significantly improved data coverage in the Pine Island Glacier basin, Figure 6b shows no new substantial features except a trough 1000 m below sea level, in which Pine Island Glacier and its main tributaries flow.

2.6 *Driving stress*

The *driving stress* in an ice sheet is calculated from the surface slope and ice thickness according to a simple relation [*Paterson*, 1994; page 241]. Here we have calculated the driving stress for the region (Figure 7) using the ERS-1-derived DEM and the ice thickness grid described above. The calculated driving stress is negligible near the ice divide where the surface slopes are low; intermediate (50-110 kPa) on the slow-moving areas between the ice divides and the tributary glaciers; and low (<50 kPa) on the tributary glaciers, but rises to >110 kPa along the main trunk of Pine Island Glacier.

An airborne sortie was flown from the inactive Siple Station (75° 54' S 84° 30' W) to the ice front of Pine Island Glacier in 1998 (the flight-track is shown in Figure 6a). It covered much of the main tributary of Pine Island Glacier (that formed by numbers 2, 4, 6 and 8 in Figure 5). Ice-penetrating radar data from this sortie show that the margin of this main tributary is marked by a downward step in the bed elevation and a change to a smoother ice-base reflection which has an "ice shelf-like" character (Figure 8). This change in reflection character is believed to indicate a transition from a frozen bed (rough) to one which is at the pressure-melting point (smooth). Although the flight track does not follow an ice flow line exactly, the driving stresses derived from the along-track data compare well with those derived from the gridded datasets shown in Figure 7. The driving stress calculated from the along-track topography has four distinct zones (Figure 8); the interior of the basin (50-75 kPa), the main tributary glacier (around 30 kPa), the main trunk of Pine Island Glacier

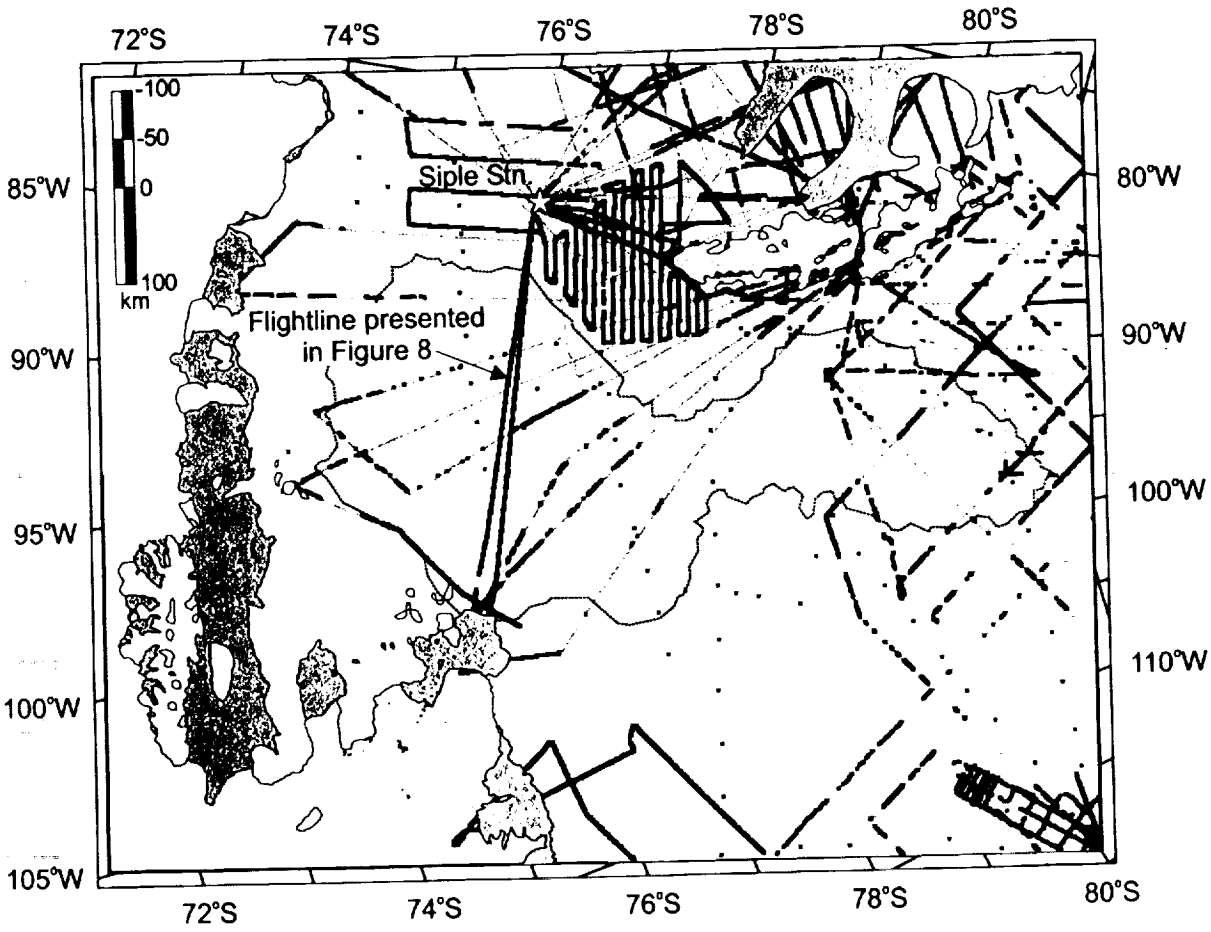

Fig. 6a. Map of the area around the ice-drainage basin of Pine Island Glacier showing measurements of ice thickness from airborne survey and oversnow traverses. Thin grey lines indicate unsuccessful sounding by airborne survey.

(over 100 kPa) and the floating ice (less than 10 kPa). The marked change in bed roughness across the tributary margin may also indicate that the location of the tributary and underlying geological constraints are closely related. The low driving stress suggests that the tributary flows over a well-lubricated bed.

The pattern of driving stresses suggests that the Pine Island Glacier basin is dynamically different from the idealised ice-stream basin. Much of the basin comprises a slow-moving ice sheet which may be cold-based, as suggested by the character of the radar reflection (Figure 8). This ice sheet feeds a number of wet-based (Figure 8), lubricated tributaries with relatively low driving stresses (around 30 kPa). These merge to form Pine Island Glacier, which has a much higher driving stress (>100 kPa), more akin to an East Antarctic outlet glacier, than some of the West Antarctic ice streams [*Bentley*, 1987].

2.7 *Surface elevation change*

ERS-1 satellite altimetry data for the period 1992-1996 were analysed for evidence of surface-elevation change [*Wingham et al.*,1998]. The data covered most of the interior of the Antarctic Ice Sheet north of 82°S. The analysis showed only one region of spatially-coherent surface-elevation change. Thinning at a mean rate of 11.7 ± 1.0 cm per year was indicated in the Pine Island Glacier-Thwaites Glacier basin. *Wingham et al.* [1998] indicated that the change was centered and most significant over the Thwaites Glacier basin (see their Figure 2), rather than the Pine Island Glacier basin, but the trend did appear to extend across both. The simplest interpretation is that the surface lowering resulted from a change in surface mass balance. Alternatively, a change in the glacier flux due to increased discharge or grounding-line retreat might also be

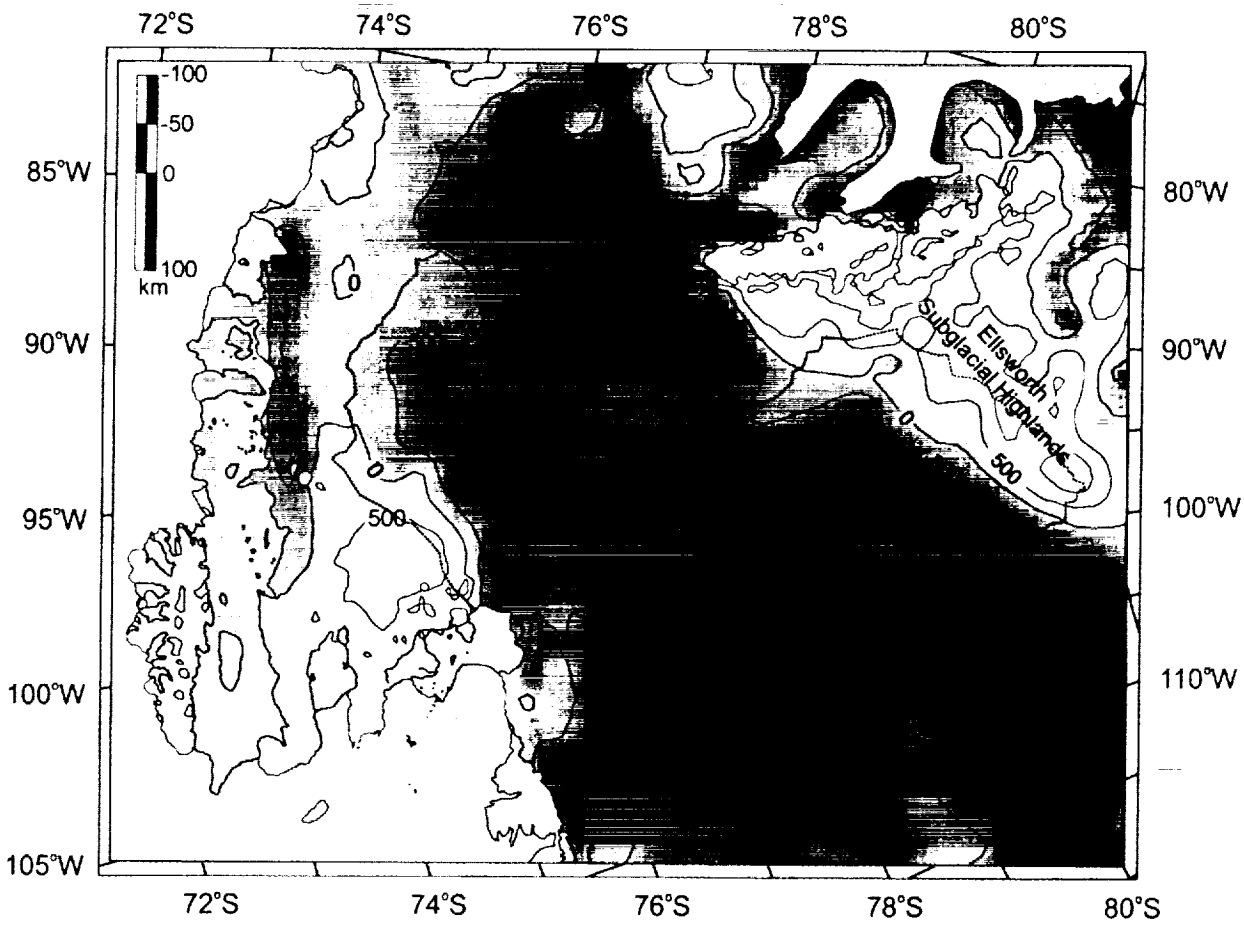

Fig. 6b. Contour map of bed elevation (meters above sea level). A grid of ice thickness was calculated using the measurements shown in Figure 6a. This grid was subtracted from a surface-elevation grid [*Bamber and Bindschadler*, 1997] to produce a grid of bed elevation.

the cause. However, in either case, the shortness of the observation period gives little indication of future behavior. It is hoped that more detailed analysis of the ERS-1 altimetry will refine the pattern of change. NASA's Geoscience Laser Altimeter System (GLAS), scheduled for launch in 2001, will allow similar measurements to be made even in the coastal margin of Antarctica.

3. THE GLACIER

Until the discovery of the network of ice tributaries in the basin [*Stenoien*, 1998; Section 2.4], Pine Island Glacier was generally considered to extend only around 70 km above the grounding line to where the ice is first channelled into parallel flow (Figure 9). This may still be still a useful definition, since it draws some distinction between the tributaries and the main trunk of the glacier and approximately marks the increase in driving stress mentioned in Section 2.6. Thus defined, Pine Island Glacier is bounded to the north by nunataks in the Hudson Mountains and to the south by slow-moving ice sheet.

3.1 *Surface features*

Surface features on Pine Island Glacier revealed by Landsat and SAR imagery have been shown by various authors and are reproduced in Figure 9. Flowlines of the type discussed by *Whillans and Merry* [1993] show considerable convergence at the head of the glacier, around the zone of arcuate "crevasses" revealed by ERS-SAR images (shown in Figure 9 and in greater detail by *Lucchitta et al.* [1995]). These presumably mark a zone of longitudinal extension. *Lucchitta et al.* [1995] noted that these "crevasses" had not been previously described and

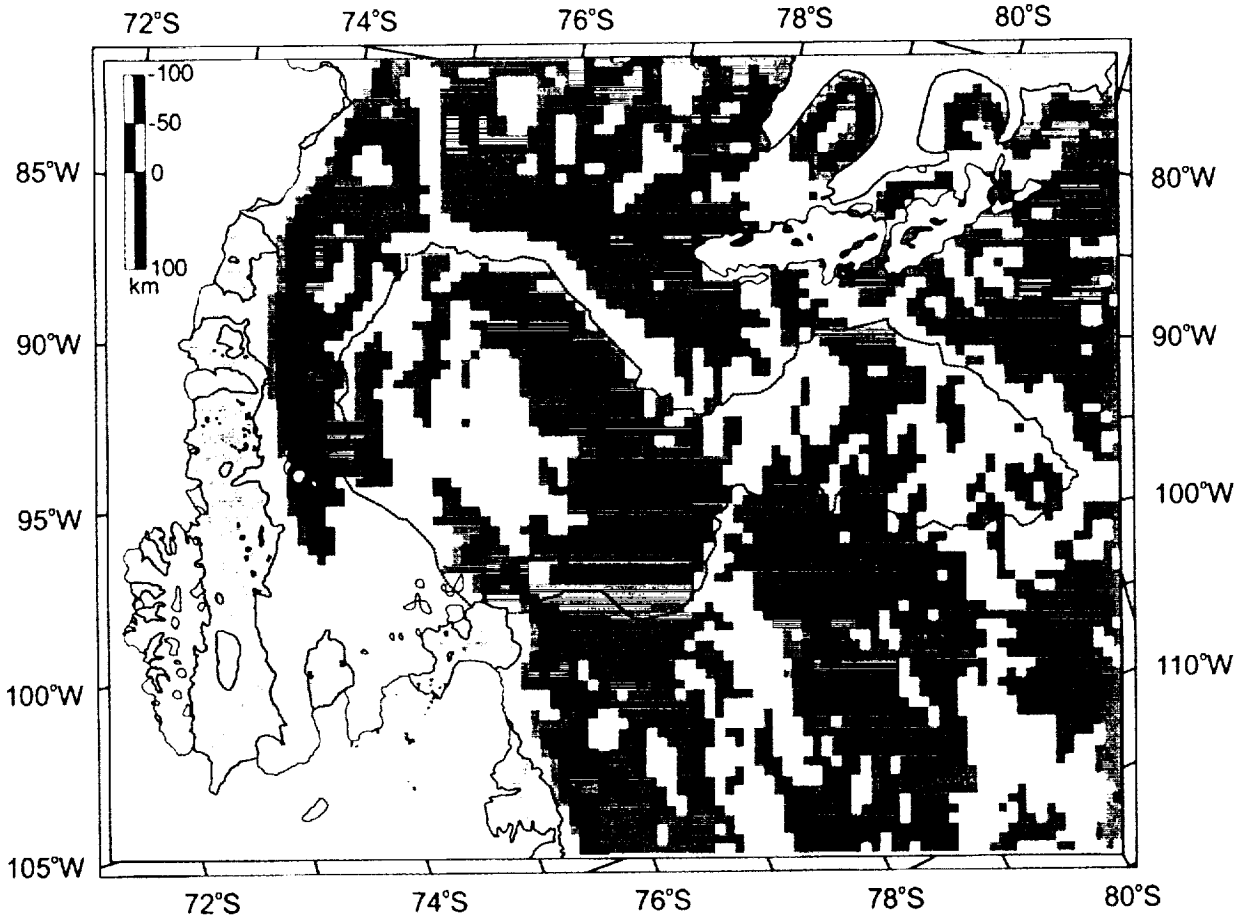

Fig. 7. Map of driving stress for the grounded ice sheet in Pine Island Glacier and neighbouring ice-drainage basins derived from surface elevation (Figure 3) and bed elevation (Figure 6b). Light-grey shading denotes driving stresses in the range 0-50 kPa, mid-grey 50-110 kPa, and dark-grey greater than 110 kPa.

are not shown by visible images, and concluded that they may be covered by a layer of snow.

Below the zone of convergence and arcuate crevasses, flowlines on the glacier are roughly parallel. The surface has smooth, long-wavelength (a few kilometers) undulations that are typical of fast-moving glaciers.

3.2 *Velocity*

Lucchitta and others [*Lucchitta et al.*, 1995; *Lucchitta et al.*, 1994; *Ferrigno et al.*, 1993] have measured the ice velocity on Pine Island Glacier using sequential SAR images acquired by the ERS-1 satellite. They found that on the main trunk of the grounded portion, the center-line speed ranged from about 1 km a^{-1} near the arcuate crevasses, to 1.5 km a^{-1} at the grounding line identified by *Crabtree and Doake* [1982]. The flow speed then rose rapidly to 2.5 km a^{-1} between that grounding line and the one identified by *Rignot* [1998], and then remained approximately constant to the ice front. Their velocity measurements were generally higher than earlier estimates [*Kellogg and Kellogg*, 1987; *Lindstrom and Tyler*, 1984; *Crabtree and Doake*, 1982; *Williams et al.*, 1982] although the data are not adequate to determine if there has been any acceleration.

3.3 *Grounding line*

The grounding line of Pine Island Glacier is not easily discernable on either the Landsat or ERS-1 SAR imagery in Figure 9, but its position was determined by hydrostatic calculations based on airborne data [*Crabtree and Doake*, 1982] (Figure 9). This hydrostatic condition downstream of this grounding line was, however, not entirely clear.

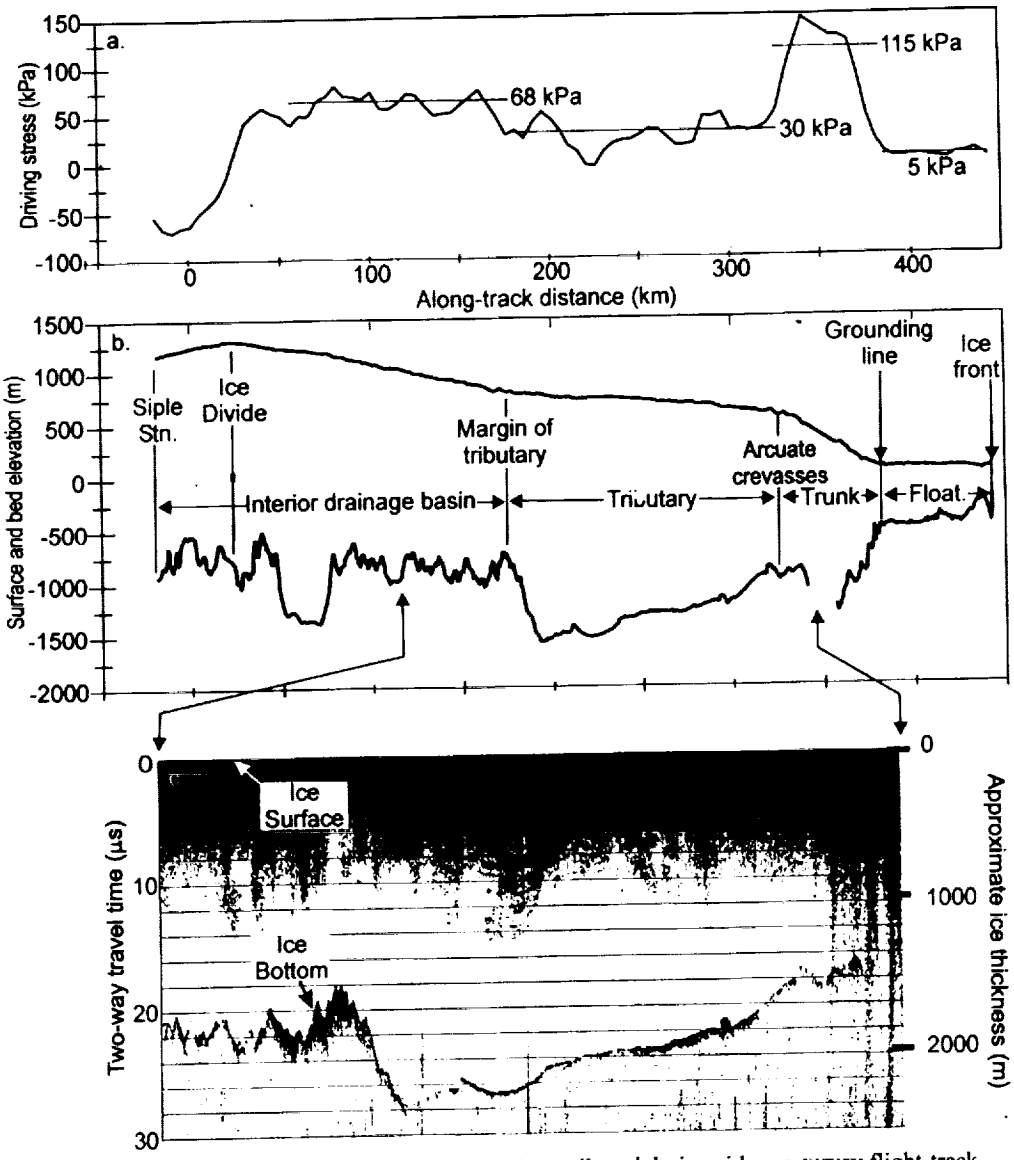

Fig. 8. Driving stress, topography and radar data collected during airborne survey flight-track identified in Figure 6a. a) Driving stress calculated using 10-km smoothing along the flight-track. The driving stress is calculated to be positive in the direction of Pine Island Glacier ice front and is negative where the ice flows into a different basin. b) Ice-surface and bottom topography along the flight-track with ice-flow features marked. c) Section of radar data, showing the difference in character between the ice-bottom return from the interior drainage basin (rough) and from the tributary glacier (smooth). This difference probably reflects the difference between a frozen bed and one that is at the pressure-melting point.

Thomas [1984] argued that a zone of partial grounding might exist for 30 km downstream. This downstream position has now been confirmed, using InSAR to detect the limit of tidal flexing [*Rignot*, 1998]. That analysis also showed that the limit of flexure extends seaward (around 15 km) near the centre of the glacier with a re-entrant on either side (Figure 9). This pattern is possibly an indication of a bedrock obstruction similar to that known to underlie Rutford Ice Stream [*Stephenson*, 1984; *Doake et al*, this volume] or it might be solely due to the glacier being thicker close to its center line.

The position of the limit of flexure was measured at five epochs between 1992 and 1996, which showed that it moved during this period [*Rignot*, 1998]. The simplest

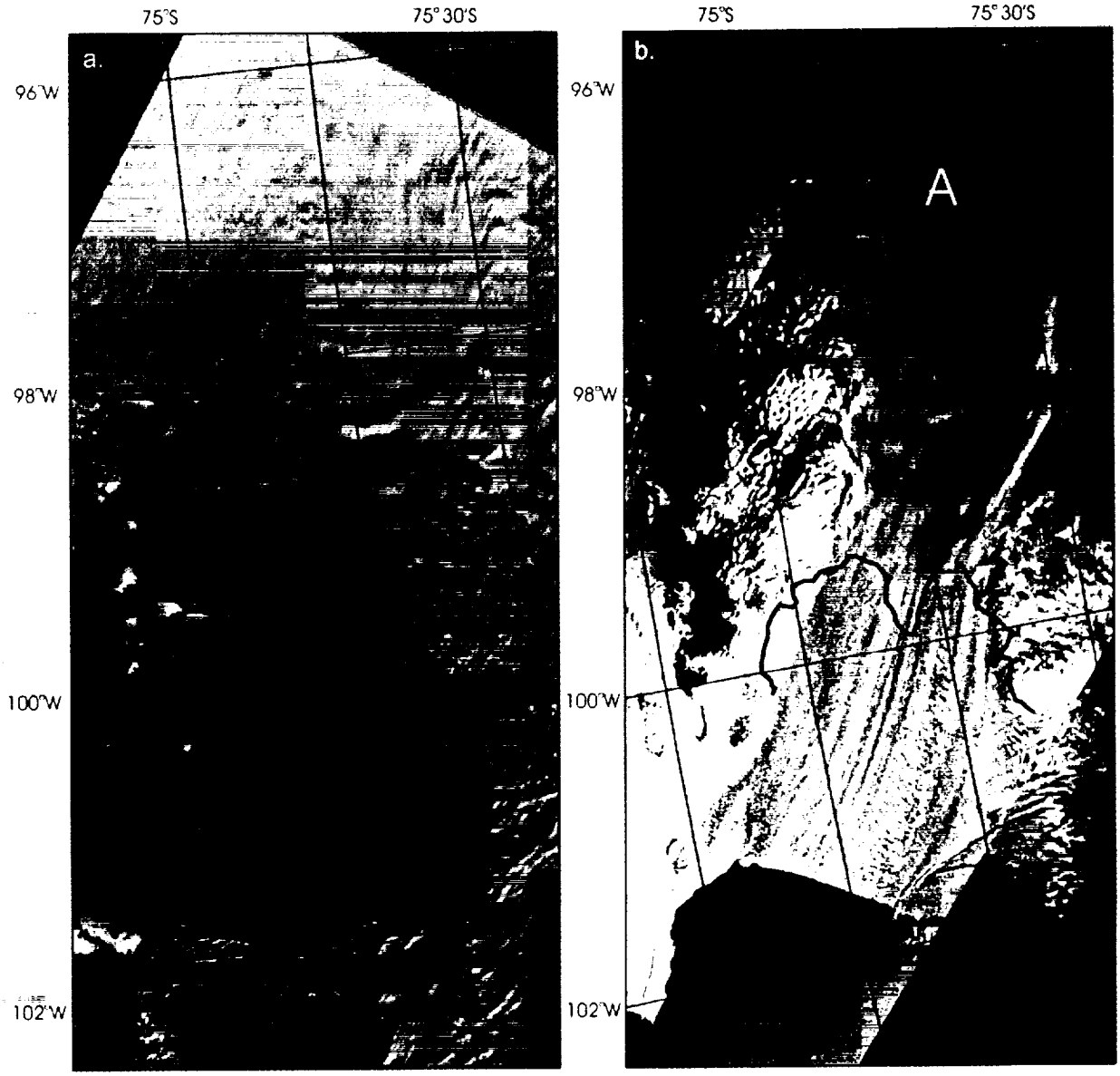

Fig. 9a. Landsat 1 sub-scene of Pine Island Glacier acquired on January 24, 1973 (path 246,row 114). "R" marks the position of the raft of ice discussed in Section 4.1. "U" indicates plumes of ice thickness undulations formed close to the grounding line and dissipating towards the ice front (discussed in Section 4.1). The dotted line marks the grounding line identified by *Crabtree and Doake* [1982] and the black line indicates the limit of tidal flexing determined by *Rignot* [1998] for 21 January 1996.

Fig. 9b. Mosaic of two ERS-1 SAR images (orbit 3174, frames 5193 and 5211) acquired December 4, 1992 showing the same area. "A" marks the set of arcuate crevasses identified by *Lucchitta et al.* [1995].

interpretation is that between 1992 and 1994 there was a retreat in the position of the grounding line in the center of the glacier that averaged 1.2 ± 0.3 km a^{-1}. The pattern of change within the re-entrant parts is not so clear, though Rignot calculated that it could be caused by a thinning rate of 3.5 ± 0.9 m a^{-1}. This is a small fraction of the basal melt rates in this area (see Section 4.2) and thus could result from a relatively small change in the oceanographic conditions. Alternatively, it could also be caused by a thinning of the glacier upstream of the grounding line.

4. THE ICE SHELF

Pine Island Glacier debouches into an ice shelf comprising the ~80 km floating portion of the glacier plus the slow-moving floating ice sheet that surrounds it. The floating portion of Pine Island Glacier is easily identified by plentiful flowlines generated near the grounding line, which continue to the ice front showing little divergence.

4.1 *Surface features*

Kellogg et al. [1985] found that dense (650 kg m^{-3}) "well-sintered" firn predominated at the surface of the floating portion of Pine Island Glacier, close to the ice front. They interpreted this as resulting from strong katabatic winds, producing net sublimation from the ice surface. The extent, persistence or magnitude of this negative net surface mass balance is, however, not well-established.

Landsat and SAR images of the floating portion of Pine Island Glacier (Figure 9) show crevasses formed at the grounding line, moving in plumes to the ice front. Much of the southern side of the floating portion of the glacier is covered by periodic transverse surface undulations visible on the Landsat images. These also form in plumes emanating from the grounding line and dissipating towards the ice front. Airborne radar-sounding data show that these undulations have an amplitude of around 20 m, a horizontal wavelength of around 2.5 km and are hydrostatically compensated by ice thickness changes of 190 m. The ice flow velocity measured on this section of ice shelf was 2.3 - 2.6 km a^{-1} [*Lucchitta et al.*, 1997] which suggests that one undulation is produced each year, although the mechanism that causes them is uncertain.

A former feature of the floating portion of Pine Island Glacier, not previously discussed but clearly visible in Figure 9, was a raft of thicker ice embedded in the ice shelf. In later images, the raft was seen to have been advected downstream at approximately the same speed as the ice-shelf flow. The origin and significance of this raft is unclear and it is no longer available for investigation as it would have calved from the ice shelf in the late-1980s. Similar features have been noted in grounded ice streams [e.g., *Whillans et al.*, 1993] and possibly in floating ice shelves [*Cassasa et al.*, 1991].

4.2 *Basal melting*

In early 1994, the research ship *Nathaniel B. Palmer* entered Pine Island Bay and conducted an oceanographic survey of the area which has led to three studies revealing a most unusual oceanographic regime:

- *Jacobs et al.* [1996] used oceanographic measurements and a "salt-box" calculation to show that the mean basal melt rate beneath the floating portion of Pine Island Glacier was 10-12 m a^{-1}, five times the highest rate previously published (on George VI Ice Shelf [*Bishop and Walton*, 1981]). They concluded that these high melt-rates were driven by relatively warm Circumpolar Deep Water (CDW) flooding this portion of the continental shelf, combined with the deep draft of Pine Island Glacier.
- *Jenkins et al.* [1997] determined that the position of the ice-shelf front showed no persistent trend in the period 1973-1994 (in Figure 10 we extend this series to 1966-1998). Combining this with a flux calculation across the grounding line and with the assumption that it is a steady-state system, they calculated a mean basal melt rate over the ice shelf of 12 ± 3 m a^{-1}.
- *Hellmer et al.* [1998] used analyses of dissolved oxygen and oxygen isotopes to confirm the strong melt-water signal in the outflow and applied a thermohaline model. This suggested that in some areas, the basal melt-rate is twice the mean value and that temporal variations in the temperature of the inflowing CDW could cause substantial changes in the basal melt-rate.

Rapid melting from beneath the floating portion of Pine Island Glacier was later confirmed using satellite measurements of mass balance [*Rignot*, 1998] giving a mean melt-rate of (24±4) m a^{-1} increasing to (50±10) m a^{-1} close to the grounding line. These melt-rates are larger than those calculated by *Jenkins et al.* [1997] due to a new position for the grounding line constrained by InSAR observations of tidal flexing. Using this grounding line position, we increase the estimate of mean melt-rate produced by Jenkins et al. to around 17 m a^{-1}, and that from Jacobs et al. by a similar amount.

These observations of a thick ice shelf coming in contact with relatively warm Circumpolar Deep Water has led to speculation that ice-ocean interactions in Pine Island Bay may be similar to those prevalent during the Last

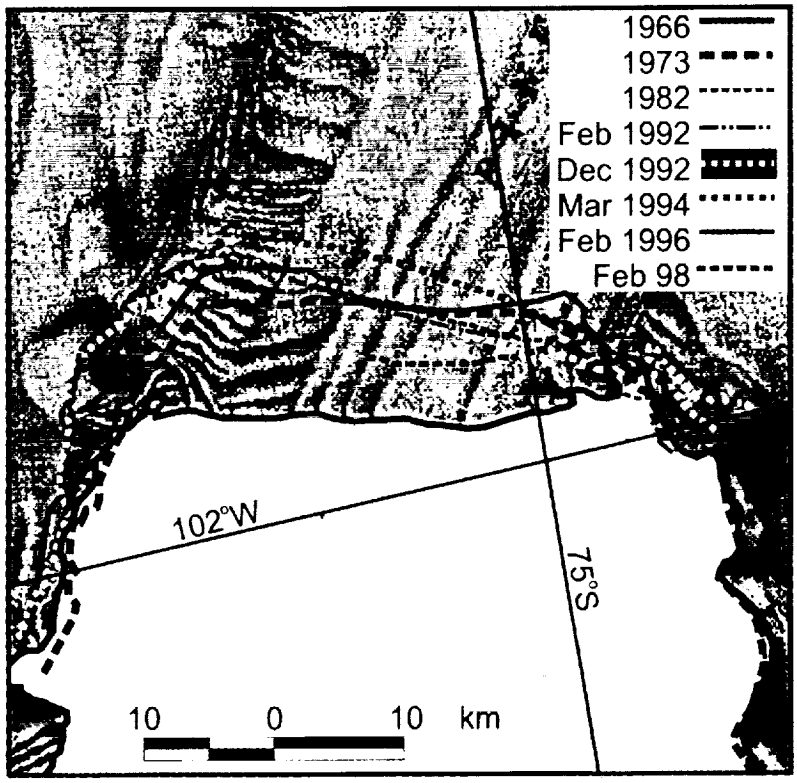

Fig. 10. Map of selected ice-front positions for Pine Island Glacier, between 1966 and 1998 overlaid on an excerpt of a sketch-map drawn from aerial photography collected in 1966 (USGS, 1993; original map prepared in 1967). Sources: 1966, Aerial photography (USGS, 1993); January 24,1973, Landsat 1 (path 246, row 114); January 15, 1982, Landsat image; February 9, 1992, ERS-1 SAR image; December 4, 1992, ERS-1 SAR images (orbit 3174, frames 5193 and 5211); 15 March 1994, ERS-1 SAR image; February, 1996, ERS-1 SAR image; February 13, 1998, flight-track of BAS airborne survey aircraft which flew along the ice front.

Glacial Maximum when much of the West Antarctic ice sheet probably extended out to the edge of the continental shelf and came into contact with similarly warm water [e.g. *Jenkins et al.*, 1997]. In Pine Island Bay we now know that such conditions generate high sub-ice shelf melt-rates and we infer that these rates may have also been prevalent during glacial periods, severely limiting the size of any ice shelves. In addition, the results highlight the importance of oceanographic conditions as a significant control on the present and future configuration of the West Antarctic ice sheet.

4.3 *Ice front stability*

The ice-front position of Pine Island Glacier has been reconstructed by several authors using several sources of data and covering various periods. Figure 10 shows the position of the ice front sporadically since 1966. The pattern suggests a retreat of around 10 km between 1966 and 1973, followed by a period of general stability, and readvance in recent years. However, this simple interpretation should be qualified on two counts. a) The presence of an iceberg just off the ice front on the sketch map drawn from 1966 aerial photography. This indicates that a significant calving had recently occurred, and that prior to this the ice front was even further advanced than the most extreme position shown. The same is true for the 1973 image. b) The ice velocity at the front (>2.5 km a^{-1}) allows for fluctuations within the intervals between the observations, large enough to exceed the extreme positions shown in Figure 10. However, it is interesting that the ice front position *appears* to be relatively stable, despite the high ice velocity. Further monitoring would be required to confirm whether or not this is the case.

Kellogg and Kellogg [1987] have suggested that the Thwaites Iceberg Tongue was not actually formed from

calving of Thwaites Glacier Tongue but might have calved from Pine Island Glacier. This is, however, unlikely, as a profusion of surface transverse lineations on the iceberg tongue matched well with the transverse lineations on Thwaites Glacier, but did not match the longitudinal lineations that predominate on Pine Island Glacier [*Ferrigno et al.*, 1993].

In summary, there are insufficient data available to discern a decadal trend in the ice-front position of Pine Island Glacier, although it is probable that some retreat (~10 km) has occurred in the last 30 years. (Longer-term retreat of the ice shelf front is discussed in Section 5).

5. THE MARINE ENVIRONMENT

5.1 *Retreat of ice in Pine Island Bay*

Seabed sediments provide information on glacier retreat in Pine Island Bay. Results from four cores within Pine Island Bay and from 19 cores on the outer continental shelf and eastern Amundsen Sea have been presented [*Anderson and Myers*, 1981; *Kellogg and Kellogg*, 1987; *Kellogg et al.*, 1987], but their value is limited because they contain very little material suitable for radiocarbon dating. The radiocarbon dates that do exist, only poorly constrain the retreat of the ice sheet in Pine Island Bay to the last few millennia. Prior to this, the ice sheet may have occupied the entire Pine Island Bay, and perhaps butted against the Thwaites Glacier Tongue to form an extensive ice shelf or ice sheet.

Kellogg and Kellogg [1987] suggested the retreat was very recent, with Pine Island Bay being filled with grounded ice only 100 years ago, but this interpretation relied heavily on an ongoing retreat rate of ~0.8 km per year inferred from aerial photography acquired in 1966 and Landsat imagery acquired in 1973. The variable position of the ice front shown in Figure 10 now casts doubt on such an extrapolation.

5.2 *Ice Extent at the Last Glacial Maximum*

The sediment cores collected on the outer continental shelf, near 110°W [*Anderson and Myers*, 1981], and north of Thurston Island between 100°W and 102°W [*Kellogg and Kellogg* 1987; *Kellogg et al.*, 1987] show a thin (0-15 cm) upper layer of sandy mud, probably of Holocene age, containing common planktonic and calcareous benthic foraminifera. Diatoms are relatively rare in this layer despite high abundances in the surface water. A compact, poorly-sorted diamicton underlies the sandy mud. This diamicton is generally more than 2.3 m thick, and probably represents deposition beneath grounded ice that extended to the continental shelf break.

If we assume that the diamicton is a remnant of subglacial basal till, then grounded ice probably remained over most of the Amundsen Sea continental shelf until relatively late in the Holocene. The postglacial sediments on the outer shelf are much thinner in Pine Island Bay than on the outer shelf in the Ross Sea [*Kellogg et al.*, 1979; *Domack et al.*, 1999; *Licht et al.*, 1999; *Shipp et al.*, 1999] which, given similar deposition rates, might suggest an earlier deglaciation in the Ross Sea than in the Amundsen Sea. Finally, if we assume that post-glacial deposition rates were similar to current measured rates (e.g., 10-35 cm a^{-1} beyond coastal Alaskan glaciers [*Molnia and Carlson*, 1999] and ~10 cm a^{-1} in Antarctic Peninsula fjords [*Domack and McClennen*, 1996]), then we can conclude that deglaciation occurred, at most, a few thousand years ago.

6. MASS BALANCE

Comparisons of balance flux (Table 1) and grounding line flux (Table 2) for Pine Island Glacier show a progression toward reduced uncertainty, but significant uncertainty still remains. Our preferred estimate of overall mass balance is -2.4 ± 4 Gt a^{-1} (the difference between the balance flux determined in this study and the grounding line flux calculated by *Rignot* [1998]). This value is not significantly different from zero. Given a catchment basin area of ~170 000 km^2, this would be equivalent to a lowering of surface elevation in the range 1.5 - 3 cm a^{-1}, depending on the density of the layers being lost.

Rignot [1998] determined the ice thickness by inverting the ice-surface elevation at the limit of flexing using a hydrostatic condition but there is evidence that the limit of flexing is often many kilometers upstream of the hydrostatic limit. One example is on Rutford Ice Stream where along the center-line the limit of flexing is 2 km upstream of the hydrostatic point and the surface is 50 m above the hydrostatic condition [*Vaughan*, 1994; *Smith*, 1991]. If a similar situation applies on Pine Island Glacier then the ice flux across the grounding line may have been over-estimated by Rignot. However, as at present we cannot assess the likelihood of this possible error, we use Rignot's grounding line flux for our preferred mass balance estimate.

The mass balance within two regions of the drainage basin has also been calculated (see figure 6.8 and table 6.1 of *Stenoien*, [1998]). The north-eastern part of the basin has a positive mass balance (6.4±3.7 Gt a^{-1}), whereas in the region just north of the narrow neck it is negative

Table 2. Estimates of grounding-line flux for Pine Island Glacier.

Mass (Gt a^{-1})	Source
68.4 ± 2	[*Rignot*, 1998]
> 56 ± 6	[*Jenkins et al.*, 1997]
70	[*Lucchitta et al.*, 1995]
25.5 ± 5	[*Lindstrom and Hughes*, 1984]

(-7.7±4.7 Gt a^{-1}). These values were calculated using a hand-drawn map of mean surface mass balance, but repeating the calculation using an updated map of surface mass balance [*Vaughan et al.*,1999], gave the same answer. Distributed evenly across the areas, these imbalances represent changes in surface elevation of (23±14) cm a^{-1} and (-51±31) cm a^{-1}, respectively.

There is thus a contradiction between mass balance calculations and measurements of change in surface elevation [*Wingham et al.*,1998; see Section 2.7] which seems to imply one of three possibilities; a) substantial changes in the density-depth relation in the snow in the period 1992-1996, b) unusually low precipitation accumulation in the period 1992-1996 or, c) one, or both of the analyses is substantially in error.

7. DISCUSSION AND CONCLUSIONS

The Pine Island Glacier ice-drainage basin is an area of particular interest and in some ways, may be unique. The shape of the basin is unusual. It comprises two lobes joined by a narrow neck less than 100 m across. The southern lobe has a higher ice-surface elevation and does not appear to correlate with any significant bed feature. Surface elevation in the ice-drainage basin dropped over four years [*Wingham et al.*, 1998], though the reasons for this are uncertain. Precipitation rates are high and the basin has the second-highest balance flux of any extant ice stream or glacier (66±4 Gt a^{-1}). Although there are indications that the ice sheet may be out of balance locally [*Stenoien*, 1998], mass balance calculations of the basin as a whole show that there is currently no measurable, significant imbalance. The tributaries which drain the basin flow at intermediate speeds (50-150 m a^{-1}) and show no regions of marked velocity increase. They coalesce to form Pine Island Glacier which has high driving stresses (>100 kPa) similar to East Antarctic outlet glaciers, but also shear margins bordering slow-moving ice, often typical of West Antarctic ice streams. The bed of the slow-moving ice in the drainage basin appears to be frozen. In the tributaries, the bed is at the pressure-melting point and is well-lubricated, presumably associated with the reduction observed in the driving stress. This thawed bed continues into Pine Island Glacier. The glacier flows over a complex grounding zone where *Rignot* [1998] measured a grounding line retreat along the center of the glacier of a few kilometers over a period of a few years. Once afloat, the base of the glacier comes into contact with warm Cicumpolar Deep Water which generates basal melt-rates of 10-20 m a^{-1} or more [*Jacobs et al.*, 1996; *Jenkins et al.*, 1997; *Hellmer et al.*, 1998; *Rignot*, 1998], the highest rates yet measured beneath any ice shelf. The front of the ice sheet or shelf in Pine Island Bay may have retreated significantly in the last few millennia [*Kellog and Kellog*, 1987], but over the last few decades it appears to have been more stable, shifting back and forth no more than a few kilometers.

These observations summarize what is known about Pine Island Glacier and its drainage basin. Several of them indicate evidence of change in this part of the West Antarctic ice sheet on time scales varying from millennia to a few years. However, at present we are cautious as to the long-term significance of these changes. Although we note that the unusual basin shape could indicate ongoing transfer of the southern lobe between catchments, there is no evidence to support this and the shape may simply be reflecting the bed topography in some way. We are uncertain as to the whether the observed surface-elevation change is the result of changing precipitation or else changing ice flow. In addition, the apparent local imbalances do not seem to concur with the changes in surface elevation. We do not understand yet if the recent grounding line retreat has been associated with a significant change in the force-balance of the glacier. Although the ice-ocean interaction in Pine Island Bay appears to be unusually dynamic, we cannot be sure of the past or future nature of the intrusion of warm water which is responsible. Finally, more radio-carbon dating and better

discrimination between ice-rafted, sub-ice shelf and sub-ice sheet sediments are required to improve our confidence in the indications of ice-front retreat over the past millennia. Hence, as yet, none of the observed changes make a strong case for ongoing basin-scale ice-sheet change or readjustment and certainly, none suggest that the ice sheet in this area has entered a phase of significant collapse or retreat.

At a time when the paradigm of marine-ice-sheet instability is being questioned, our observations of change, perhaps appear ambiguous and inconclusive. Interpreting them as precursors of collapse would clearly be unjustified. They are certainly not yet sufficient to rigorously test the various theoretical models and ideas of ice sheet stability and collapse which have been discussed over the years [e.g. *Weertman*, 1974; *Mercer*, 1978; *Hughes*, 1980; *Fastook*, 1984; *MacAyeal*, 1992; *Hindmarsh*, 1993; *Bentley*, 1998]. This is the case, even though Pine Island Glacier has occupied a central position in discussions regarding the stability of the West Antarctic ice sheet. It can be argued that research has made relatively poor progress in the Pine Island Glacier region, particularly when compared to the Siple Coast ice streams or those which drain into the Ronne Ice Shelf. This shortcoming suggests that we should prepare field and remote sensing experiments that will allow us to determine the causes of change in the ice sheet. Only such an understanding will lead us to a sound foundation for predicting future behaviour.

Acknowledgments. We thank Howard Conway and Robert Bindschadler for constructive reviews. SSJ acknowledges support of the NASA Polar Research Program for the LDEO contribution (#6034).

REFERENCES

Alberts, F.G., *Geographic names of the Antarctic*. National Science Foundation, Washington. 1981

Alley, R.B., S. Anandakrishnan, C.R. Bentley and N. Lord, A water-piracy hypothesis for the stagnation of Ice Stream C, Antarctica, *Ann. Glaciol.*, 20, 187-194, 1994.

Anderson, J.B. and M.C. Myers, USGSC Glacier Deep Freeze 81 Expedition to the Amundsen Sea and Bransfield Strait, *Antarct. J. U.S.*, 16, 5, 1981

Armstrong, T., B. Roberts and C.W.M. Swithinbank, *Illustrated glossary of snow and ice*, Scott Polar Research Institute, Cambridge, 1973.

Bamber, J.L. and R.A. Bindschadler, An improved elevation dataset for climate and ice-sheet modelling: validation with satellite imagery, *Ann. Glaciol.*, 25, 439-444, 1997.

Behrendt, J.C., Distribution of narrow-width magnetic anomalies in Antarctica, *Science*, 144, 3621, 993-994, 1964.

Bentley, C.R., Antarctic ice streams: a review, *J. Geophys. Res.*, 92, 8843-8858, 1987.

Bentley, C.R., Rapid sea-level rise from a West Antarctic ice-sheet collapse: a short-term perspective, *J. Glaciol.*, 44, 157-163, 1998.

Bentley, C.R. and N.A. Ostenso, Glacial and subglacial topography of West Antarctica. *J. Glaciol.*, 3, 882-911. 1961.

Bentley, C.R. and F.K. Chang, Geophysical exploration in Marie Byrd Land, Antarctica, in *Antarctic Snow and Ice Studies 2, Antarct. Res. Ser.* vol 16, edited by A.P. Crary, pp 1-38, AGU, Washington, D.C., 1971.

Bindschadler, R., Jakobshavn Glacier drainage basin: a balance assessment, *J. Geophys. Res.*, 89, 2066-2072, 1984.

Bishop, J.F. and J.L.W. Walton, Bottom melting under George VI Ice Sheet, Antarctica, *J. Glaciol.*, 27, 429-447, 1981.

Bromwich, D. Snowfall in high southern latitudes, *Rev. Geophys.*, 26, 149-168, 1988.

Cassasa, G., K.C. Jezek,, J. Turner and I.M. Whillans, Relict flow stripes on the Ross Ice Shelf. *Ann. Glaciol.*, 15, 132-138, 1991

Connolley, W.M. and J.C. King, A modelling and observational study of East Antarctic surface mass balance, *J. Geophys. Res.*, 101, 1335-1343, 1996.

Crabtree, R.D. and C.S.M. Doake, Pine Island Glacier and its drainage basin: Results from radio-echo sounding, *Ann. Glaciol.*, 3, 65-70, 1982.

Doake, C.S.M., H.F.J. Corr, A. Jenkins, K. Makinson, K.W. Nicholls, C. Nath, A.M. Smith and D.G. Vaughan, Rutford Ice Stream, Antarctica, *this volume*.

Domack, E. W. and C. E. McClennen, Accumulation of glacial marine sediments in fjords of the Antarctic Peninsula and their use as late Holocene palaeoenvironmental indicators, in *Foundations for Ecological Research West of the Antarctic Peninsula, Antarct. Res. Ser.* vol 70, edited by R.M. Ross et al., pp 135-154, AGU, Washington, D.C., 1996.

Domack, E.W., E.A. Jacobson, S. Shipp and J.B. Anderson, Late Pleistocene-Holocene retreat of the West Antarctic Ice-Sheet system in the Ross Sea: Part 2 - Sedimentologic and Stratigraphic Signature, *Geological Society of America Bulletin*, 111, 1517-1536, 1999.

Fastook, J.L., West Antarctica, the sea-level controlled marine instability: past and future, in *Climate Processes and Climate Sensitivity, Geophys. Mono.* vol 29, edited by J.E. Hansen and T. Takahashi, pp 275-287, AGU, Washington, D.C., 1984.

Ferrigno, J.G., B.K. Lucchitta, K.F. Mullins, A.L. Allison, R.J. Allen, and W.G. Gould, Velocity measurements and changes in the position of Thwaites Glacier/iceberg tongue from aerial photography, Landsat images and NOAA AVHRR data, *Ann Glaciol.*, 17, 239-244, 1993.

Giovinetto, M.B., The drainage systems of Antarctica: Accumulation, in *Antarctic Snow and Ice Studies, Antarct Res. Ser.* vol 2, edited by M. Mellor, pp 127-155, AGU, Washington, D.C., 1964.

Giovinetto, M.B. and C.R. Bentley, Surface balance in ice drainage systems of Antarctica, *Antarct. J. US.*, 20, 6-13, 1985.

Goldstein, M., H. Engelhardt, B. Kamb, and R.M. Frolich, Satellite radar interferometry for monitoring ice sheet motion: application to an Antarctic ice stream, *Science*, 262, 1525-1530, 1993.

Hellmer, H.H., S.S. Jacobs, and A. Jenkins, Ocean erosion of a floating Antarctic Glacier in the Amundsen Sea, in *Ocean, Ice and Atmosphere: Interactions at the Antarctic Continental Margin, Antarct. Res. Ser.* vol 75, edited by S.S. Jacobs and R.F. Weiss, pp 83-100, AGU, Washington, D.C., 1998.

Hindmarsh, R.C.A., Qualitative dynamics of marine ice sheets, in *Ice in the Climate System, NATO ASI.Series* vol I 12, edited by W.R. Peltier, pp 68-99, Springer-Verlag, Berlin Heidelberg, 1993.

Hughes, T.J., The weak underbelly of the West Antarctic Ice Sheet, *J. Glaciol.*, 27, 518-525, 1980.

Jacobs, S.S., H.H. Hellmer, and A. Jenkins, Antarctic ice sheet melting in the Southeast Pacific, *Geophys. Res. Lett.*, 23, 957-960, 1996.

Jacobs, S.S. and J.C. Comiso, Climate variability in the Amundsen and Bellingshausen Seas, *J. Clim.*, 10, 697-709, 1997.

Jankowski, E.J. and D.J. Drewry, The structure of West Antarctica from geophysical studies, *Nature*, 291, 17-21, 1981.

Jenkins, A., D.G. Vaughan, S.S. Jacobs, H.H. Hellmer, and J.R. Keys, Glaciological and oceanographic evidence of high melt rates beneath Pine island glacier, West, Antarctica, *J. Glaciol.*, 43, 114-121, 1997.

Jezek, K.C., H.G. Sohn and K.F. Noltimier, The Radarsat Antarctic Mapping Project, *IGARSS '98 - 1998 International Geoscience and Remote Sensing Symposium, Proceedings*, Vol 1-5, Chapter 888, 2462-2464, 1998.

Joughin, I., L. Gray, R. Bindschadler, S. Price, D. Morse, C. Hulbe, K. Matter and C. Werner, Tributaries of West Antarctic Ice Streams Revealed by RADARSAT Interferometry, *Science*, 286, 283-286, 1999.

Jonas, M. and D.G. Vaughan, ERS-1 SAR mosaic of Filchner-Ronne-Schelfeis, *Filchner Ronne Ice Shelf Programme Reports*, 10, edited by H. Oerter, 47-49, AWI, Bremerhaven, Germany, 1996.

Jones D.A. and I. Simmonds, A climatology of Southern Hemisphere extratropical cyclones, *Climate Dynamics*, 9, 135-145, 1993.

Kellogg, T.B., R.S. Truesdale, and L.E. Osterman, Late quaternary extent of the West Antarctic Ice Sheet: new evidence from Ross Sea cores, *Geology*, 7, 249-253, 1979.

Kellogg, T.B., D.E. Kellogg, and T.J. Hughes, Amundsen Sea sediment coring, *Antarct. J. U.S.*, 20, 79-81, 1985.

Kellogg, T.B. and D.E. Kellogg, Recent glacial history and rapid ice stream retreat in the Amundsen Sea., *J. Geophys. Res.*, 92, 8859-8864, 1987.

Kellogg T.B., D.E. Kellogg, E.D. Waddington, and J.S. Walder., Late Quaternary deglaciation of the Amundsen Sea: implications for ice sheet modelling, in *The physical basis of ice sheet modelling, IAHS Pub. 170*, edited by E.D. Waddington and J.S. Walder, pp 349-357,Int. Assoc. of Hydrol. Sci., Wallingford, England, 1987.

Legresy, B. and F. Remy, Altimetric observations of surface characteristics of the Antarctic Ice Sheet, *J. Glaciol.*, 43, 265-275, 1997.

Licht, K.J., N.W. Dunbar, J.T. Andrews, and A.E. Jennings, Distinguishing subglacial till and glacial marine diamictons in the western Ross Sea, Antarctica: implications for a last glacial maximum grounding line, *Bulletin of the Geological Society of America*, 111, 91-103, 1999.

Lindstrom, D. and D. Tyler, Preliminary results of Pine Island and Thwaites Glaciers Study, *Antarct. J. U.S.*, 19, 53-55, 1984.

Liu, H., K. Jezek, and B. Li, Development of an Antarctic digital elevation model by integrating cartographic and remotely sensed data: A geographic information system based approach., *J. Geophys. Res.*, 104, 99-23,213, 1999.

Lucchitta, B., C. Rosanova, and K. Mullins, Velocities of Pine Island and Thwaites Glacier, West Antarctica, from ERS-1 SAR images, *Ann. Glaciol.*, 21, 277-283, 1995.

Lucchitta B.K., C.E. Smith, J. Bowell, and K.F. Mullins, Velocities and mass balance of Pine Island Glacier, West Antarctica, derived from ERS1-SAR. *ESA Publication SP-361*, 147-151, 1994.

Lucchitta B.K., and C.E. Rosanova, Velocities of Pine Island and Thwaites Glaciers, West Antarctica, from ERS1-SAR images. *ESA Publication SP-414*, 819-824, 1997.

MacAyeal, D.R., Irregular oscillations on the West Antarctic Ice Sheet, *Nature*, 359, 29-32, 1992.

Mantripp, D.R., J. Sievers, H. Bennat, C.S.M. Doake, K. Heidland, J. Idhe, M. Jonas, B. Reidel, A.V. Robinson, R. Scharroo, H.W. Shenke, U. Shirmer, F. Stefani, D.G. Vaughan and D.J. Wingham, *Topographic map (satellite image map), Filchner-Ronne-Shelfeis (2nd Edition). Map at 1 : 2 000 000*, Institut für Angewandte Geodäsie, Frankfurt am Main, Germany, 1996.

Mercer, J.H., West Antarctic Ice Sheet and CO_2 greenhouse effect: A threat of disaster, *Nature*, 271, 321-325, 1978.

Molnia, B.F. and P.R. Carlson, Surface sedimentary units of northern Gulf of Alaska continental shelf, *Bulletin of the American Association of Petroleum Geologists*, 62, 633-643, 1999.

Paterson, W.S.B., *The physics of glaciers*, Elsevier Science, Oxford, 480pp, 1994.

Payne, A.J., A thermomechanical model of ice flow in West Antarctica. *Climate Dynamics*, 15, 115-125, 1999.

Rignot, E.J., Fast recession of a West Antarctic Glacier, *Science*, 281, 549-551, 1998.

SCAR, *Antarctic digital database user's guide and reference manual*, Scientific Committee on Antarctic Research, Cambridge, xi+156pp, 1993.

Shimizu, H., Glaciological studies in West Antarctica, in *Antarctic Snow and Ice Studies, Antarct. Res. Ser.* vol 2, edited by M. Mellor, pp 37-64, AGU, Washington, D.C., 1964.

Shipp, S., J. Anderson and E. Domack, Late Pleistocene-Holocene retreat of the West Antarctic Ice-Sheet system in the Ross Sea: Part 1 - Geophysical Results, *Geological Society of America Bulletin*, 111, 1486-1516, 1999.

Smith, A.M., The use of tiltmeters to study the dynamics of Antarctic ice-shelf grounding lines, *J. Glaciol.*, 37, 51-58, 1991.

Stenoien M.D., *Interferometric SAR observations of the Pine Island Glacier catchment area*, Unpublished Ph.D. thesis, University of Wisconsin-Madison, 127pp, 1998.

Stuiver, M., G.H. Denton, T.J. Hughes and J.L. Fastook, History of the marine ice sheet in West Antarctica during the last glaciation: a working hypothesis, in *The Last Great Ice Sheets*, edited by G.H. Denton and T.J. Hughes, Wiley-Interscience, New York, 1981.

Stephenson, S.N., Glacier flexure and the position of grounding lines: Measurements by tiltmeter on Rutford Ice Stream, Antarctica, *Ann. Glaciol.*, 5, 165-169, 1984.

Swithinbank C.W.M., Ice streams, *Polar Record*, 7, 185-186, 1954.

Thomas, R.H., Ice sheet margins and ice shelves. In: J.E. Hansen and T. Takahashi (Eds), Climate Processes and Climate Sensitivity, in *Climate Processes and Climate Sensitivity, Geophys. Mono.* vol 29, edited by J.E. Hansen and T. Takahashi, pp 265-274, AGU, Washington, D.C., 1984.

USGS, *Antarctica Sketch Map, Thurston Island - Jones Mountains, 1:500,000*, USGS, Washington, D.C., 1993.

Vaughan, D.G., Investigating tidal flexure on an ice shelf using kinematic GPS, *Ann. Glaciol*, 20, 372-376, 1994.

Vaughan, D.G., J.L. Bamber, M. Giovinetto, J. Russell, and A.P.R. Cooper, Reassessment of net surface mass balance in Antarctica, *J. Clim.*, 12, 933-946, 1999.

Vaughan D.G. and J.L. Bamber, Drainage basin analysis and improved calculation of balance fluxes for West Antarctic ice streams and glaciers, in *Abstracts, AGU Chapman Conference on the West Antarctic Ice Sheet, Orono, Sept.1998*, 1998.

Weertman, J., Stability of the junction of an ice sheet and an ice shelf, *J. Glaciol.*, 13, 3-11, 1974.

Whillans, I.M. and C.J. Merry, Ice-flow features on Ice Stream B, Antarctica, revealed by SPOT HRV imagery, *J. Glaciol.*, 39, 515-527, 1993.

Whillans, I.M., M. Jackson and Y-H Tseng, Velocity pattern in a transect across Ice Stream B, Antarctica, *J. Glaciol.*, 39, 562-572, 1993.

Williams, R.S., J.G. Ferrigno, T.M. Kent, and J.W. Schoonmaker, Landsat images and mosaics of Antarctica for mapping and glaciological studies, *Ann. Glaciol.*, 3, 321-326, 1982.

Wingham, D.J., A.J. Ridout, R. Scharroo, R.J. Arthern, and C.K. Schum, Antarctic elevation change from 1992 to 1996, *Science*, 282, 456-458, 1998.

C. R. Bentley and M.D. Stenoien, Geophysical and Polar Research Center, University of Wisconsin - Madison, Madison, Wisconsin 53706, USA. (email: bentley@geology.wisc.edu)

S. S. Jacobs, Lamont-Doherty Earth Observatory, University of Columbia, Palisades, New York 10964, USA. (email: sjacobs@ldeo.columbia.edu)

T. B. Kellogg, Institute for Quaternary Studies, University of Maine, Orono, Maine 04469, USA. (email: tomk@iceage.umeqs.maine.edu)

B.K. Lucchitta, U.S. Geological Survey, Flagstaff, Arizona 86001, USA. (email: blucchitta@flagmail.wr.usgs.gov)

E. Rignot, Jet Propulsion Laboratory, Pasadena, California 91109, USA. (email: eric@adelie.jpl.nasa.gov)

D. G. Vaughan, A.M. Smith, H. F. J. Corr, A. Jenkins, British Antarctic Survey, Natural Environment Research Council, Cambridge CB3 0ET, U.K. (email: d.vaughan@bas.ac.uk)